Dissertation

Alkali metal ortho thioaluminates, -silicates and -phosphates as solid electrolytes for all-solid-state batteries

Sascha Patric Harm

München 2020

Dissertation zur Erlangung des Doktorgrades
der Fakultät für Chemie und Pharmazie
der Ludwig–Maximilians–Universität München

Alkalimetall ortho-Thioaluminate, -silikate und -phosphate als Ionenleiter für Festkörperbatterien

Sascha Patric Harm

aus

Speyer, Deutschland

2020

Erklärung

Diese Dissertation wurde im Sinne von § 7 der Promotionsordnung vom 28. November 2011 von Frau Prof. Dr. Bettina V. Lotsch betreut.

Eidesstattliche Versicherung

Diese Dissertation wurde eigenständig und ohne unerlaubte Hilfe erarbeitet.

München, den 21. Mai 2020

Sascha Patric Harm

Dissertation eingereicht am:	22.05.2020
1. Gutachterin:	Prof. Dr. Bettina V. Lotsch
2. Gutachter:	P.D. Dr. Constantin Hoch
Mündliche Prüfung am:	15.06.2020

Danksagung

Zuallererst möchte ich meiner Doktormutter, Prof. Dr. Bettina Lotsch, für ihre Offenheit, fortwährende Unterstützung auch in nicht wissenschaftlichen Themen, und die Freiheit das zu untersuchen was mich interessierte, danken.

Des Weiteren, möchte ich P.D. Dr. Constantin Hoch für seine motivierende Art und für die Zeit die er sich nahm nicht nur wissenschaftliche sondern, wenn nötig, auch zwischenmenschliche Probleme bei einem Kaffee oder einem Feierabendbierchen zu besprechen, danken.

Außerdem, möchte ich Prof. Dr. Wolfgang Schnick und seiner ganzen Gruppe für ihre Unterstützung und die Möglichkeiten Laborplätze und –geräte, trotz der gelegentlichen olfaktorischen Beeinträchtigung, mitverwenden zu können, danken.

Bedanken möchte ich mich auch für die sehr gute Zusammenarbeit und die wertvollen Diskussionen mit allen Koautoren, Kooperationspartnern vom AK Zeier, Janek, Kwade und Dinnebier, und meinen Bachelor und F-Praktikanten Sonja, Sebastian, Pamina, Simon, Christina, Verena und Lucas.

Ebenfalls möchte ich noch Peter Wagatha, Arthur Haffner, Thomas Miller, Juliane Stahl, Christian Minke, Otto Zeman und Dr. Thomas Bräuninger für ihre Unterstützung bei XRD, REM und NMR Messungen danken. Vielen Dank an Wolfgang Wünschheim für seine Hilfe bei Problemen mit Hard- und Software.

Außerdem möchte ich dem gesamten AK Lotsch für das wunderbare Arbeitsklima danken. Ich bin sehr froh, dass ich in eine so harmonische Gruppe reingerutscht bin. Vielen Dank auch an Claudia Kamella für den steten herzlichen Empfang am MPI FKF und, zusammen mit Sigrid Fuhrmann, die Unterstützung bei bürokratischen Belangen.

Ein besonderer Dank geht an meine drei Mitstreiter aus dem 103er Labor, Jonathan "that's-not-my-name" Sappl, Fabian "Seeräuberopa Fabian" Keßler und die beste Koautorin der Welt, Anna-Katharina "Queen Banäna" Hatz. Es war wirklich ein wahnsinniges Glück euch kennen lernen und mit euch arbeiten zu dürfen.

Natürlich möchte ich auch all meinen Freunden danken. Hierbei muss ich besonders meine

Band Sunset Point und die "Summer Breeze Gruppe" erwähnen, da sie meine Leidenschaft für Musik teilen und mich wenn nötig immer aufgebaut haben oder für die nötige Ablenkung sorgten um wieder kreativ zu sein.

Ein ganz besonderer Dank geht an Jasmin Dums die mich die komplette Dauer dieser Promotion ausgehalten hat, mich in allem unterstützte und damit den nötigen Rückhalt gab diese Arbeit anzufertigen.

Zuletzt möchte ich mich natürlich noch bei meiner Familie bedanken. Ihr habt immer an mich geglaubt und deshalb habe ich diesen Weg einschlagen können. Vielen Dank.

There is a theory which states that
if ever anyone discovers exactly
what the universe is for and why it
is here, it will instantly disappear
and be replaced by something even
more bizarre and inexplicable.
There is another theory which
states that this has already
happened.

– Douglas Adams,
Hitchhiker's Guide to the Galaxy

Contents

Danksagung **x**

List of figures **xx**

List of tables **xxiii**

Abstract **xxv**

1 Introduction **1**
1.1 Lithium ion batteries 1
1.1.1 Conventional lithium ion batteries 2
1.1.2 All-solid-state lithium ion batteries 4
1.2 Sodium ion batteries 6
1.3 Solid electrolytes 7
1.3.1 Solid lithium ion electrolytes 9
1.3.2 Solid sodium ion electrolytes 13

2 Selected experimental methods **25**
2.1 Powder X-ray diffraction 25
2.1.1 Rietveld analysis 25
2.1.2 Structure determination from PXRD data 27
2.2 Electrochemical impedance spectroscopy 28
2.3 Bond valence energy landscape calculations 30

3 A Lesson learned from NMR: characterization and ionic conductivity of LGPS-like Li_7SiPS_8 **35**
3.1 Abstract 35
3.2 Introduction 36
3.3 Experimental procedure 37
3.3.1 Synthesis 37
3.3.2 Powder X-ray diffraction 37
3.3.3 Single crystal X-ray diffraction 38
3.3.4 Solid-state NMR spectroscopy 38
3.3.5 Electrochemical impedance spectroscopy (EIS) 38

3.3.6 Raman spectroscopy . . . 39
3.3.7 Scanning electron microscopy and energy-dispersive X-ray spectroscopy 39
3.4 Results and discussion . . . 40
3.4.1 X-ray diffraction . . . 40
3.4.2 MAS NMR spectroscopy . . . 44
3.5 Quantitative phase analysis . . . 45
3.5.1 Pulsed field gradient NMR . . . 46
3.5.2 Electrochemical impedance spectroscopy (EIS) . . . 47
3.6 Conclusion . . . 49
3.7 Acknowledgement . . . 50
3.8 Assotiated content . . . 50

4 Chemical modification on *tetra*-LSiPS 55
4.1 Aliovalent substitution in *tetra*-$Li_{7+x}Si_{1-x}Al_xPS_8$ . . . 55
4.1.1 Experimental procedure . . . 55
4.1.2 Results and Discussion . . . 57
4.1.3 Conclusion and Outlook . . . 62
4.2 Impact of LiCl on the phase composition in *tetra*-LSiPS . . . 63
4.2.1 Experimental procedure . . . 64
4.2.2 Results and discussion . . . 64
4.2.3 Conclusion and Outlook . . . 65

5 Finding the right blend: Interplay between structure and sodium ion conductivity in the system Na_5AlS_4 – Na_4SiS_4 71
5.1 Abstract . . . 71
5.2 Introduction . . . 72
5.3 Experimental Section . . . 73
5.3.1 Synthesis . . . 73
5.3.2 Powder X-ray Diffraction . . . 73
5.3.3 Single Crystal X-ray Diffraction . . . 74
5.3.4 Solid-state Nuclear Magnetic Resonance Spectroscopy . . . 74
5.3.5 Differential Scanning Calorimetry . . . 74
5.3.6 Energy Dispersive X-Ray Analysis . . . 74
5.3.7 Bond Valence Energy Landscape Calculations . . . 74
5.3.8 Electrochemical Impedance Spectroscopy . . . 75
5.4 Results and Discussion . . . 76
5.4.1 X-Ray Diffraction . . . 76
5.4.2 NMR spectroscopy . . . 80
5.4.3 Bond Valence Energy Landscape Calculations . . . 80
5.4.4 Electrochemical Impedance Spectroscopy . . . 84
5.4.5 Discussion . . . 85
5.5 Conclusion . . . 87

6 Summary and Outlook 93

A Supporting Information for "A Lesson learned from NMR: characterization and ionic conductivity of LGPS-like Li_7SiPS_8" 97
A.1 Crystallographic Data . . . 98
A.2 Energy-dispersive X-ray Analysis . . . 105
A.3 Scanning Electron Microscopy . . . 106
A.4 Quantitative phase analysis . . . 107
A.5 Raman spectroscopy . . . 109
A.6 Estimation of the electronic contribution to the conductivity . . . 110
A.7 Comparison of different fitting models for the impedance spectrum of *tetra*-LSiPS at -80°C . . . 112
A.8 Room-temperature EIS measurements of *tetra*-LSiPS . . . 113

B Supporting Information for "Finding the right blend: Interplay between structure and sodium ion conductivity in the system $Na_5AlS_4 - Na_4SiS_4$" 115
B.1 Crystallographic data for Na_5AlS_4 . . . 116
B.2 Crystallographic data for Na_4SiS_4 . . . 119
B.3 Crystallographic data for $Na_{8.5}(AlS_4)_{0.5}(SiS_4)_{1.5}$ . . . 124
B.4 Thermal analysis . . . 132
B.5 Electron microscopy . . . 134
B.5.1 BVEL calculations . . . 136
B.5.2 BVEL calculations of Na_5AlS_4 . . . 137
B.5.3 BVEL calculations of Na_4SiS_4 . . . 138
B.5.4 BVEL calculations of $Na_9(AlS_4)(SiS_4)$ . . . 139
B.6 Electrochemical characterization . . . 140
B.6.1 Galvanostatic polarization measurements . . . 140
B.7 Electrochemical impedance spectroscopy . . . 141
B.7.1 Activation Energies . . . 145

C Additional supporting information 147
C.1 Additional data for Chapter 1 . . . 147
C.2 Additional data for Chapter 4.1 . . . 148
C.2.1 Electrochemical impedance data . . . 148
C.2.2 Crystallographic data . . . 149
C.3 Additional data for Chapter 4.2 . . . 153
C.3.1 Electrochemical impedance data . . . 153
C.3.2 Crystallographic data . . . 154

D List of publications and author contributions 157

E List of presentations **159**
E.1 Oral presentations 159
E.2 Poster presentations 159

List of Figures

1 Tetragonal Li_7SiPS_8 is a glassy ceramic, where the amorphous phase impedes the ionic conductivity. . . . xxv

2 The right blend of aluminum and silicon enables high sodium ion conduction in the solid solution series $Na_{5-x}Al_{1-x}Si_xS_4$. . . . xxvi

1.1 Schematic representation of a conventional lithium ion cell. . . . 3

1.2 Schematic representation of a all-solid-state lithium ion cell. . . . 5

1.3 Overview of selected lithium ion conductors. . . . 10

1.4 Predicted ionic conductivities for the tetragonal L*M*PS system. . . . 11

1.5 Crystal structure of LGPS. . . . 12

2.1 Scheme of the unmodified charge flipping algorithm. . . . 28

2.2 Exemplary Nyquist plot. . . . 29

3.1 textitleft: PXRD measurements of the obtained products at indicated temperatures (radiation: Cu-$K_{\alpha 1}$); *right*: Time-dependent high temperature PXRD measurements of quenched *ortho*-LSiPS, inset graph shows the mass fraction of *tetra*-LSiPS (black) and *ortho*-LSiPS (red) plottet against time (radiation: Mo-$K_{\alpha 1}$, temperature: 823 K). . . . 40

3.2 **(a)**: Structure of *ortho*-LSiPS (Li_7SiPS_8) viewed along the *c*-axis. Li atoms are omitted for better visibility. Black rectangles mark the unit cell, the red lines outline the pseudo-hexagonal unit cell of the underlying hcp (hexagonal close packing) of S atoms; **(b)**: Pseudo-hexagonal unit cell depicted in red with all atoms. Not all coordination polyhedra for Li are depicted for better visibility. Li-ellipsoids were drawn at 50% probability. . . . 41

3.3 Rietveld refinement of *tetra*-LSiPS annealed at 823 K. The square root of the intensity is given for better visibility. . . . 42

3.4 **(a)**: Structure of *tetra*-LSiPS (Li_7SiPS_8) viewed along the *c*-axis. Black squares mark the tetragonal primitive unit cell, the red square marks the underlying fcc (face-centered cubic) unit cell; **(b)**: Pseudo-cubic fcc unit cell marked by red lines. . . . 42

3.5 *left:* ^{31}P MAS NMR spectra of *ortho*- and *tetra*-LSiPS; right: ^{29}Si MAS NMR spectrum of *tetra*-LSiPS. Peaks were colored according to the respective phases (orange: *tetra*-LSiPS, yellow: *ortho*-LSiPS, grey: amorphous) and labeled according to the respective Wyckoff positions of the P atoms. . 44

3.6 PFG NMR measurements of *tetra*-LSiPS annealed at 823 K. Two different diffusion times, defined by the time between the gradient pulses Δ_{NMR} were employed to probe diffusion processes at shorter (10 ms) and longer (100 ms) ranges. 46

3.7 The low-temperature EIS of *ortho*-LSiPS shows two slightly depressed semicircles and was fit with the model given in the inset. 47

3.8 **(a)** Low-temperature EIS of *tetra*-LSiPS modeled by four processes attributed to grain boundary processes (R_1C_1, R_2CPE_2, and R_3CPE_3) and electrode polarization (CPE_4); **(b)** Arrhenius plot comparing of the total conductivity of R_1+R_2+R_3 of *tetra*-LSiPS yielding an activation energy of 0.27 eV with the respective activation energies obtained by PFG NMR and of *ortho*-LSiPS. 48

4.1 Lattice parameters in $Li_{7+x}Si_{1-x}Al_xPS_8$. 57

4.2 ^{27}Al MAS NMR spectrum of $Li_{7.1}Si_{0.9}Al_{0.1}PS_8$. 58

4.3 ^{31}P and ^{29}Si MAS NMR spectra of *tetra*-LSiPS and *tetra*-LSiAlPS 58

4.4 Total conductivities and respective activation energies of the solid solution series $Li_{7+x}Si_{1-x}Al_xPS_8$ ($(0 \leq x \leq 0.15)$). 59

4.5 Comparison of the calculated BVEL Maps for *tetra*-LSiPS and tetragonal $Li_{7.1}Si_{0.9}Al_{0.1}PS_8$. 61

4.6 Reaction scheme between the amorphous side phase of *tetra*-LSiPS, Li_2S and LiCl · 63

4.7 Results from Rietveld refinements from samples with different amounts of additional Li_2S and LiCl. 65

4.8 **(a)**: Total conductivities and **(b)**: activation energies for ion conduction of samples with increasing Li_2S and LiCl content. Blue bars depict the estimated deviation for the specific ionic conductivity and activation energy for different tetra-LSiPS samples. As a reference the respective values for the lithium argyrodite Li_6PS_5Cl are also depicted. 66

4.9 Deconvoluted ^{31}P MAS NMR spectra of a sample with 15 awt% amorphous Li_3PS_4 and a typical *tetra*-LSiPS sample. Deconvoluted peaks are color coded to their respective phase. Orange represents crystalline tetra-LSiPS, yellow ortho-LSiPS, blue the Li-argyrodite and gray an amorphous phase. The percentage of the respective integrated areas is given for each peak. The envelope of the overall fit function is depicted in red. Measured data is given as a black line. 66

5.1 **(a)**: Normalized volume of the observed crystalline phases obtained by Rietveld refinement displayed against substitution value x; error bars represent 3σ and the red lines are a guide to the eye to illustrate the Vegard-like dependence on x. **(b)**: PXRDs (Mo-$K_{\alpha 1}$ radiation) of all samples in the $Na_{5-x}Al_{1-x}Si_xS_4$ ($0 \leq x \leq 1$) substitution series. 76

5.2 **(a)**: Rietveld refinement of Na_5AlS_4 ($x = 0$) measured using Cu-$K_{\alpha 1}$ radiation; black dots depict the measured data, red lines the Rietveld fit, gray lines the difference plot and black lines the respective reflection positions. **(b)**: [AlS_4]-tetrahedral sublattice in Na_5AlS_4 viewed along a. **(c)**: Perspective view of the [AlS_4]-tetrahedral and [$Na2S_6$] octrahedral arrangement parallel to b. **(d)**: Complete Na_5AlS_4 structure with [AlS_4]-tetrahedral arrangement viewed along b; maroon curved lines represent sodium ion diffusion pathways determined by BVEL calculations. 77

5.3 **(a)**:Rietveld refinement of Na_4SiS_4 ($x = 1$) measured using Mo-$K_{\alpha 1}$ radiation, the super-structure reflection is marked by an asterisk; black dots depict the measured data, red lines the Rietveld fit, gray lines the difference plot and black lines the respective reflection positions. **(b)**: Na_4SiS_4 crystal structure parallel to c; **(c)**: Na_4SiS_4 structure viewed along a; **(d)**: [SiS_4]-tetrahedra (blue) and [NaS_5]-pyramidal (red) arrangement viewed parallel to c, showing the [NaS_5]-pyramids in a one-up-two-down-pattern; maroon curved lines represent sodium ion diffusion pathways determined by BVEL calculations. 78

5.4 **(a)**: [Si/AlS_4]-tetrahedral and [$Na13S_6$]-octahedral arrangement viewed along c and infinite [Si/AlS_4]-[$Na13S_6$]-rods viewed parallel to a. **(b)**: $Na_9(AlS_4)(SiS_4)$ crystal structure viewed along b; blue polyhedra depict [Si/AlS_4]-tetrahedra, orange polyhedra depict [$Na13S_6$]-octahedra, red, dark red and yellow atoms depict Na, and blue atoms depict Si/Al; ellipsoids were drawn at 80% probability. **(c)**: Deconvoluted ^{27}Al MAS NMR spectrum of $Na_9(AlS_4)(SiS_4)$ ($x = 0.5$); purple line shows the overall fit, colored dashed lines represent the contributing pseudo-Voigt peaks, relative intensities are given with their respective standard deviation in parentheses. **(d)**:^{29}Si MAS NMR spectrum of $Na_9(AlS_4)(SiS_4)$; colored dotted lines show a tentative signal distribution. 79

5.5 **(a)**: Na_5AlS_4 crystal structure viewed along b direction. Bond valence energy landscape at isoenergy value of $-2.40\,\text{eV}$ ($E_{min}^{global} = -3.71\,\text{eV}$, $E_{min}^{path} = -3.43\,\text{eV}$, $E_{mig}^{path} = -2.58\,\text{eV}$,$\Delta E_{3D} = 0.83\,\text{eV}$). The unit cell is divided along the crystallographic c direction into alternating sections **A** and **B**. **(b)**: Na_5AlS_4 unit cell with sections **A** and **B**. **(c)**: Section **A** ($c = 0.9-1.1$) viewed along b and c. **(d)**: Section **B** ($c = 0.6 - 0.9$) viewed along b and c. 81

5.6 Crystal structure of Na_4SiS_4 (simplified model without superstructure) with sodium atoms drawn in red and sulfur atoms drawn in yellow. Bond valence energy landscape at isoenergy values of **(a)**: $-2.40\,eV$ and **(b)**: $-1.80\,eV$ are drawn in gray ($E_{min}^{global} = -3.73\,eV$, $E_{min}^{path} = -3.73\,eV$, $E_{mig}^{path} = -2.68\,eV$, $\Delta E_{2D} = 1.05\,eV$). Red arrows depict sodium ion diffusion pathways. Numbers denote crystallographic sodium sites. 82

5.7 Crystal structure of $Na_9(AlS_4)(SiS_4)$ along **(a)**: a and **(b)**: c direction. The bond valence energy landscape at isoenergy value of $-2.60\,eV$ is drawn in gray ($E_{min}^{global} = -4.02\,eV$, $E_{min}^{path} = -3.86\,eV$, $E_{mig}^{path} = -2.64\,eV$, $\Delta E_{3D} = 1.22\,eV$). 83

5.8 **(a)**: Sodium ion conductivity in the phase system $Na_{5-x}Al_{1-x}Si_xS_4$ with ($0 \leq x \leq 1$) as a function of the substitution factor x (visualized by dashed line). In the range of $x = 0.50$ – 0.75, where the material crystallizes in the $Na_9(AlS_4)(SiS_4)$-structure, the highest average conductivity of $2.04 \cdot 10^{-5}\,S\,cm^{-1}$ was observed. The unsubstituted phases Na_5AlS_4 and Na_4SiS_4 show a significantly lower ionic conductivity of $1.64 \cdot 10^{-7}\,S\,cm^{-1}$-$1.77 \cdot 10^{-7}\,S\,cm^{-1}$, respectively. The error bars include the standard deviation of the sample and the error of the measurement of about 8%. **(b)**: Temperature dependent sodium ion conductivities calculated from R1 of all phases for a selection of measurements (all parameters for these particular measurements are given in Table S12 and Table S13). The different colors indicate the different crystal structures: Na_5AlS_4-structure (blue), $Na_9(AlS_4)(SiS_4)$-structure (black) and Na_4SiS_4-structure (red) 85

A.1 SEM image of *tetra*-LSiPS with an acceleration voltage of 20.0 kV showing a morphology resembling a glassy matrix with embedded crystallites. . . . 106

A.2 ^{31}P MAS NMR spectra and peak deconvolutions for all samples containing *tetra*-LSiPS. Relative intensity values were extracted from peak areas and are given in the respective images as percentage values. 107

A.3 Rietveld fits for all samples containing *tetra*-LSiPS. Black reflection markers indicate peak positions of the internal standard Si, blue markers of *tetra*-LSiPS and green markers of *ortho*-LSiPS. The square root of the intensity is shown for better visibility of all phases. 108

A.4 Raman spectra of *tetra*-LSiPS (black) and *ortho*-LSiPS (red). 109

A.5 Equivalent circuit model of an ionic and electronic conducting sample with a grain boundary process between two ion blocking electrodes. 110

A.6 *a)* and *b)* DC galvanostatic polarization measurements of *ortho*- and *tetra*-LSiPS performend at 298 K with blocking electrodes Pt|LSiPS|Pt 111

A.7 Comparison of three different models of the impedance spectrum of *tetra*-LSiPS at -80 °C showing that model #3 fits the data best. 112

A.8 Room-temperature impedance spectrum of *tetra*-LSiPS showing a total resistance of about 180 Ω resulting in an ionic conductivity of 2 $mScm^{-1}$. . . 113

B.1 Sodium ion coordination in $Na_{8.5}(AlS_4)_{0.5}(SiS_4)_{1.5}$. Na–S-distances are given in Å. Sodium atoms are depicted in orange, sulfur atoms in yellow. Ellipsoids are drawn at 80% probability. 131

B.2 DSC measurement of Na_4SiS_4 and Na_5AlS_4; green and blue lines represent the heating and cooling ramps of Na_4SiS_4, respectively, measured at 5 $Kmin^{-1}$, black and red lines represent the heating and cooling ramps of Na_5AlS_4, respectively, measured at 2 $Kmin^{-1}$. 132

B.3 DSC measurement of $Na_{5-x}Al_{1-x}Si_xS_4$, $x = 75\%$; the measurement corresponds to the cooling of the sample at a rate of 5 $Kmin^{-1}$ after annealing it at 600 °C for 3 h. 133

B.4 Crystal structure of Na_5AlS_4 with Na atoms drawn in red (migrating ions) and orange (isolated ions), Al atoms drawn in blue and sulfur atoms depicted in yellow. Bond valence energy landscape at different isoenergy values are drawn in grey. 137

B.5 Crystal structure of Na_4SiS_4 with Na atoms drawn in red, Si atoms drawn in blue and sulfur depicted in yellow. Bond valence energy landscape at different isoenergy values are drawn in grey. 138

B.6 Crystal structure of $Na_9(AlS_4)(SiS_4)$ with Na atoms drawn in red (migrating ions) and orange (isolated ions). Bond valence energy landscape at different isoenergy values are drawn in grey. 139

B.7 Galvanostatic polarization measurement of $Na_{5-x}Al_{1-x}Si_xS_4$ with $x = 0.05$ with a current of 0.5 nA shows an electronic conductivity of $6x10^{-11} S\,cm^{-1}$ and a transference number of 0.9998. The material is clearly a mainly ionic conducting material. 140

B.8 For each member of the series $Na_{5-x}Al_{1-x}Si_xS_4$ with $(0 \leq x \leq 1)$ a representative impedance spectrum with fit and equivalent circuit model at 25 °C is given. The according values for conductivity, capacitance, activation energy and the prefactor are given in TableB.12 and TableB.13. For x=0.625,0.75and1.00 the inclusion of a low frequency semicircle into the model leads to overfitting. Thus, the best fitting model consists only of one RC- or RCPE-element in series to an CPE. 142

B.9 Ionic conductivities calculated exclusively from the resistance of the high frequency semicircle (R1) excluding resistive processes occurring for some member of in $Na_{5-x}Al_{1-x}Si_xS_4$ with $(0 \leq x \leq 1)$. The error bars denote the error and the standard deviation of the values. 144

B.10 The measured activation energies range from 0.30-0.38 eV for the whole substitution range of $Na_{5-x}Al_{1-x}Si_xS_4$ with $(0 \leq x \leq 1)$. The lowest activation energy can be found in the double salt at x=0.75. The error bars denote the error and the standard deviation of the values. 145

C.1 Representative Nyquist plot of electrochemical impedance spectra measured at $-70\,^{\circ}\mathrm{C}$ of $Li_{7+x}Si_{1-x}Al_xPS_8$ ($x = 15\%$). Black dots depict the measured data, red lines represent the fit of the equivalent circuit model depicted in the insets. 148
C.2 Representative Nyquist plots of electrochemical impedance spectra measured at $-20\,^{\circ}\mathrm{C}$ of **(a)**: a sample with 8 awt% amorphous and **(b)**: 15 awt% amorphous. Black dots depict the measured data, red lines represent the fit of the equivalent circuit model depicted in the insets. 153

List of Tables

2.1 Possible interpretations of observed capacitance values given by Irvine *et al.* 30

3.1 Crystallographic data and information about the Rietveld analysis for *tetra*-LSiPS tempered at 823 K. Standard deviations are given in parentheses. . 43
3.2 Phase composition of various LSiPS samples determined by powder X-Ray diffraction with an internal standard (Si) and MAS NMR spectroscopy. The standard deviation is given in parentheses 45

4.1 Results of BVEL calculations performed on *tetra*-LSiPS and tetragonal $Li_{7.1}Si_{0.9}Al_{0.1}PS_8$. 60

A.1 Crystallographic information and data for the structure solution and refinement of orthorhombic Li_7SiPS_8 on the basis of single crystal data. 98
A.2 Fractional atomic coordinates in standardized setting and equivalent isotropic displacement parameters of orthorhombic Li_7SiPS_8. 99
A.3 Anisotropic displacement parameters of orthorhombic Li_7SiPS_8. 99
A.4 Interatomic distances in orthorhombic Li_7SiPS_8 100
A.5 Fractional atomic coordinates and equivalent isotropic displacement parameters for *tetra*-Li_7SiPS_8 from Rietveld refinement. 102
A.6 Interatomic distances in tetragonal Li_7SiPS_8 103
A.7 EDX measurements on *tetra*-LSiPS. All data are given in relative atom% . 105
A.8 Observed Raman modes of *tetra*-LSiPS compared with vibrational modes of tetragonal LGPS-like $Li_{10}SnP_2S_{12}$ and orthorhombic β-Li_3PS_4. 109

B.1 Crystallographic data and information for the structure solution and refinement from powder X-ray diffraction data for Na_5AlS_4. 116
B.2 Standardized fractional atomic coordinates[4] and isotropic displacement parameters for Na_5AlS_4. 117
B.3 Interatomic distances in Na_5AlS_4. 118
B.4 Crystallographic data and information for the structure solution and refinement from powder X-ray diffraction data for Na_4SiS_4. 119
B.5 Standardized fractional atomic coordinates[4] and isotropic displacement parameters for Na_4SiS_4. 120
B.6 Interatomic distances in Na_4SiS_4. 121

B.7 Crystallographic data and information for the structure solution and refinement from powder X-ray diffraction data for $Na_{8.5}(AlS_4)_{0.5}(SiS_4)_{1.5}$. . . . 124
B.8 Standardized fractional atomic coordinates[4] and equivalent isotropic displacement parameters for $Na_{8.5}(AlS_4)_{0.5}(SiS_4)_{1.5}$. 125
B.9 Anisotropic displacement coefficients for $Na_{8.5}(AlS_4)_{0.5}(SiS_4)_{1.5}$. 126
B.10 Interatomic distances in $Na_{8.5}(AlS_4)_{0.5}(SiS_4)_{1.5}$. 127
B.11 Results of EDX measurements for $Na_{8.5}Al_{0.5}Si_{1.5}S_8$ ($x = 0.75$) in atom% normalized to the sum of Al and Si being 4. SEM micrographs depict the positions on the sample. 135
B.12 Ionic conductivities calculated from R_1 and R_{Tot} (=R_1+R_2) and the respective capacitances of representative measurements shown in Figure B.8 at 25 °C of $Na_{5-x}Al_{1-x}Si_xS_4$ with ($0 \leq x \leq 1$). The electrode area was 0.20 cm^2 and the thickness of the pellets in the range of 0.35-0.75 mm. 141
B.13 Pellet density of $Na_{5-x}Al_{1-x}Si_xS_4$ with ($0 \leq x \leq 1$) samples shown in Figure B.8 and their activation energies with prefactor σ_0 averaged over several temperature cycles. 141
B.14 Ionic conductivity data calculated from R_{Tot} and averaged over all samples measured for each member of the series $Na_{5-x}Al_{1-x}Si_xS_4$ with ($0 \leq x \leq 1$) at 25 °C. The activation energies $\sigma(R_{Tot})$ were averaged over all samples and several temperature cycles for each sample. The electrode area was 0.20 cm^2 and the thickness of the pellet in the range of 0.35-0.75 mm. 143
B.15 Ionic conductivity data calculated from R_1 and averaged over all samples measured for each member of the series $Na_{5-x}Al_{1-x}Si_xS_4$ with ($0 \leq x \leq 1$) at 25 °C. The activation energies $\sigma(R_1)$ were averaged over all samples and several temperature cycles for each sample. The electrode area was 0.20 cm^2 and the thickness of the pellet in the range of 0.35-0.75 mm. 143

C.1 Total ionic conductivities at room temperature and the respective activation energies for selected lithium solid electrolytes. This data was used to create Figure 1.3. 147
C.2 Crystallographic data and information on the Rietveld refinement from powder X-ray diffraction data for $Li_{7.05}Si_{0.95}Al_{0.05}PS_8$ using Si as an internal standard. Standard deviations are given in parentheses. 149
C.3 Crystallographic data and information on the Rietveld refinement from powder X-ray diffraction data for $Li_{7.1}Si_{0.9}Al_{0.1}PS_8$ using Si as an internal standard. Standard deviations are given in parentheses. 150
C.4 Crystallographic data and information on the Rietveld refinement from powder X-ray diffraction data for $Li_{7.15}Si_{0.85}Al_{0.15}PS_8$ using Si as an internal standard. Standard deviations are given in parentheses. 151
C.5 Crystallographic data and information on the Rietveld refinement from powder X-ray diffraction data for $Li_{7.2}Si_{0.8}Al_{0.2}PS_8$ using Si as an internal standard. Standard deviations are given in parentheses. 152

C.6 Crystallographic data and information on the Rietveld refinement from powder X-ray diffraction data for a LSiPSCl sample, assuming 2.5 wt% amorphous content, using Si as an internal standard. The phase content of the internal standard was omitted and the given data scaled accordingly. Standard deviations are given in parentheses. 154
C.7 Crystallographic data and information on the Rietveld refinement from powder X-ray diffraction data for a LSiPSCl sample, assuming 8 wt% amorphous content, using Si as an internal standard. The phase content of the internal standard was omitted and the given data scaled accordingly. Standard deviations are given in parentheses. 155
C.8 Crystallographic data and information on the Rietveld refinement from powder X-ray diffraction data for a LSiPSCl sample, assuming 15 wt% amorphous content, using Si as an internal standard. The phase content of the internal standard was omitted and the given data scaled accordingly. Standard deviations are given in parentheses. 156

Abstract

All-solid-state batteries represent promising next-generation battery systems. They offer the possibility of fast charging, improved capacity and energy density, as well as a drastically reduced fire risk by replacing the flammable liquid electrolyte by one or more solid ion conductors. Sulfides are among the potential candidates to be employed in all-solid-state batteries, because of their high specific ionic conductivities, being essential for fast charging of the resulting battery, combined with their mechanical softness, allowing for cold pressing of the electrolyte powder without the need for further high temperature annealing. Since not only conductivity and chemical stability, but also production costs and weight are important factors that determine the choice of a solid electrolyte, the scope of this work is to expand the field of low-cost sulfide based solid electrolyte materials utilizing only earth abundant main group elements while showing high ionic conductivities.

For the lithium based solid electrolytes, this work shows the synthesis and characterization of Li_7SiPS_8 (LSiPS), a new member of the tetragonal LGPS ($Li_{10}GeP_2S_{12}$)-type family of ultrafast Li^+ solid electrolytes. The crystal structure, phase stability, as well as Li^+ conductivity of tetragonal and orthorhombic LSiPS are reported. The tetragonal modification shows a total specific ionic conductivity of $2 \cdot 10^{-3}\,\mathrm{S\,cm^{-1}}$. While being fast in absolute terms, the observed conductivity is unexpectedly low compared to other members of the tetragonal LGPS-type family. Using a combination of different solid-state NMR techniques, quantitative phase analysis and impedance spectroscopy an amorphous thiophosphate side phase with low Si content was identified that impedes the intergrain conductivity and therefore masks a potentially higher bulk ionic conductivity. This case study highlights the importance of analyzing solid electrolytes, especially thiophosphates, beyond the crystalline fractions to gain insights into the structure-property relationships of these glassy ceramics.

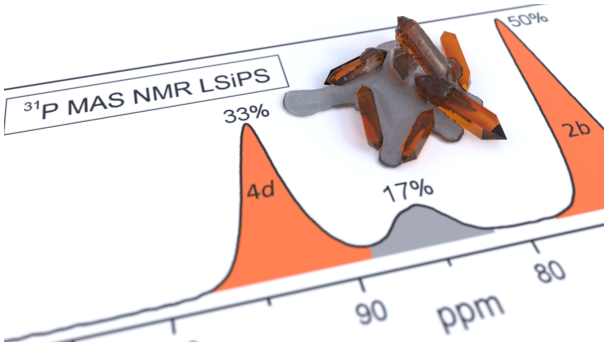

Figure 1: Tetragonal Li_7SiPS_8 is a glassy ceramic, where the amorphous phase impedes the ionic conductivity.

In addition, this thesis shows the successful aliovalent substitution of silicon by aluminum

in $Li_{7+x}Si_{1-x}Al_xPS_8$. The increased charge carrier density combined with a flatter energy landscape resulting from this substitution should increase the total ionic conductivity of the material, which is corroborated by bond valence energy landscape calculations presented in this work. However, a slight decrease in conductivity with increasing substitution ratio x was observed which was attributed to a change in the composition of the amorphous side phase detected by solid state NMR. First investigations showed that upon addition of lithium chloride and lithium sulfide the formation of these amorphous side phases can almost completely be inhibited by forming, amongst others, lithium argyrodite $Li_{7+x-y}P_{1-x}Si_xS_{6-y}Cl_y$. The resulting mixture shows an ionic conductivity of $4 \cdot 10^{-3}\,S\,cm^{-1}$ with an activation energy of 0.17 eV, doubling the previously reported conductivity.

Furthermore, new sodium ion electrolytes in the substitution series $Na_{5-x}Al_{1-x}Si_xS_4$ ($0 \leq x \leq 1$) are reported in this work. These exhibit ionic conductivities ranging from $1.64 \cdot 10^{-7}\,S\,cm^{-1}$ for Na_4SiS_4 to $2.04 \cdot 10^{-5}\,S\,cm^{-1}$ for $Na_{8.5}(AlS_4)_{0.5}(SiS_4)_{1.5}$ ($x = 0.75$). The crystal structures of the Na^+-ion conductors Na_4SiS_4 as well as hitherto unknown Na_5AlS_4 and $Na_9(AlS_4)(SiS_4)$ are reported. Using these experimental data, Na^+-ion conduction pathways for all new structures were calculated by the bond valence energy landscape (BVEL) method. These highlight the influence of the local coordination symmetry of sodium ions on the energy landscape within this family of compounds. The findings reported in this work show that the interplay of charge carrier concentration and low site symmetry of sodium ions can enhance the conductivity by several orders of magnitude.

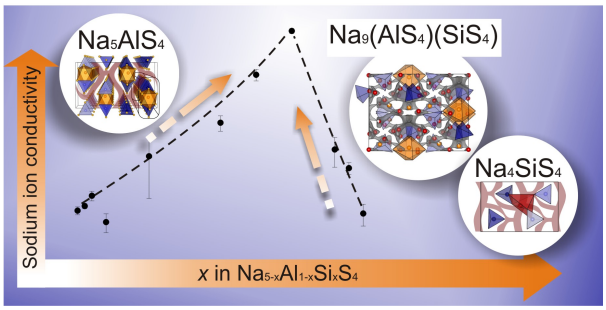

Figure 2: The right blend of aluminum and silicon enables high sodium ion conduction in the solid solution series $Na_{5-x}Al_{1-x}Si_xS_4$.

Chapter 1

Introduction

Since the re-invention of the first battery by Alessandro Volta in 1799, a stack of metallic copper and zinc discs separated by brine soaked cloth,[1,2] the importance of energy storage has drastically increased and is nowadays dominated by the lithium ion (secondary) battery. Today, these devices are found in nearly all mobile electrical devices, such as laptops, cell phones or power-tools. Especially, electric vehicles are dependent on the high energy density lithium ion batteries offer. These batteries are heavily in the spotlight of politics and industry because they offer, with proper infrastructure and recycling, a way to decrease CO_2 and NO_x emissions world-wide.[3] Safety, energy density, and hence the distance the vehicle can travel without re-charging, and price are key concerns for the lithium ion batteries employed in electric vehicles. The first two can potentially be tackled by substitution of the flammable liquid electrolyte by one or more solids. However, the resulting all-solid-state lithium ion batteries (ASSLiBs) require a lithium metal anode to outperform conventional lithium ion batteries in terms of energy density.[4]
Sulfide based solid electrolytes are one of the potential candidates to be employed in such ASSLiB systems, because of their softness and therefore processability by enabling cold pressing. Additionally, sulfides offer high ionic conductivities, which is essential for fast-charging of the resulting all-solid-state batteries. However, long-term stability of the solid electrolyte against the electrode materials is a major concern impacting lifetime and safety of this type of batteries. Possible solutions to this problem are protective coatings of the electrode materials or a combination of a multitude of solid electrodes tailored to the specific electrode materials.[5] The scope of this work is to expand the materials space of sulfide based lithium and sodium solid electrolytes as well as study the impact of crystal- and micro-structure on the conductivity. The following sections give a more thorough insight into the topics mentioned above, starting with the conventional lithium ion battery.

1.1 Lithium ion batteries

The following section deals with the history and setup of conventional batteries, i.e. batteries employing a liquid electrolyte, and all-solid-state lithium ion batteries, followed by

an overview of state-of-the-art solid electrolytes with potential to be used in future battery applications.

1.1.1 Conventional lithium ion batteries

The term 'battery' was coined by Benjamin Franklin in 1748 to denote an array of Leyden jars, water filled glass jars with two metal electrodes serving as capacitors to store charge from electrostatic generators.[6] After the discovery of the Voltaic pile in 1799, its improvement and commercialization by John F. Daniell and the invention of the lead-acid-battery in 1859 by Gaston Plante, batteries were categorized in primary (one use) and secondary (rechargeable) batteries. In contrast to the Leyden jars or capacitors, batteries store electrical energy as chemical energy in the electrodes. These are denoted as cathode and anode for primary and secondary batteries alike. The cathode is defined as the electrode where a reduction reaction takes place during the discharge of the battery. Consequently, the anode designates the electrode where an oxidation reaction takes place during discharge. The electrical output of a battery is a current $I = dq/dt$ with a voltage V for a time Δt. The electrical energy stored in a battery is given by:[7]

$$\int_0^{\Delta t} I \cdot V dt = \int_0^Q V dq \tag{1.1}$$

with the battery capacity:

$$Q = \int_0^{\Delta t} I dt = \int_0^Q dq \tag{1.2}$$

The chemical reaction in a battery has an electronic and an ionic component. The electrolyte and if necessary a separator enables ionic transport between the electrodes but hinders electronic transport, forcing a current to flow outside the battery through a resistance. In equilibrium the open-circuit potential of a cell $V_{OC} = E_{cell}$ of a battery is given by the Nernst equation:[8]

$$E_{cell} = E^{\circ}_{cell} - \frac{RT}{zF} \ln Q_r \tag{1.3}$$

with a reaction coefficient:

$$Q_r = \frac{\prod_j a_j^{\nu_j}}{\prod_i a_i^{\nu_i}} \tag{1.4}$$

where E_{cell} is the cell voltage at a given temperature T for the cell voltage at standard conditions E°_{cell} for a specific reaction coefficient Q_r. a_j and a_i are the reaction product and starting material activities, respectively, with their specific stoichiometric coefficients ν_j and ν_i.
The stability 'window' of an electrolyte is roughly estimated by the energy gap $E_g = E(LUMO) - E(HOMO)$ between the lowest unoccupied molecular orbital (LUMO) and

the highest occupied molecular orbital (HOMO) of the solvent molecule(s). A cathodic electrochemical potential higher than the LUMO, or an anodic electrochemical potential lower than the HOMO can reduce or oxidize the electrolyte respectively. Hence, E_g of the electrolyte effectively limits the maximum open circuit potential of one cell and therefore the energy density of the whole battery, which is one of the key performance indicators of a battery, especially for mobile applications.

In aqueous solutions this voltage limit is given by the redox couple $O_2|H_2O|H_2$ with $E_g = 1.23\ V$. Kinetic energy barriers (overpotential) can in some cases increase this limit up to $V_{OC} \approx 2\ V$, like in the case of the lead-acid-battery.[7,9] However, to harness higher voltages per electrochemical cell the transition from protons as charge carriers to the also small and light lithium ion was made. Lithium metal offers the highest anodic electrochemical potential energy and its salts (e.g. $LiPF_6$) can be dissolved in organic carbonate esters like propylene carbonate showing specific Li-ion conductivities of $\sigma_{Li} > 10^{-2}\,S\,cm^{-1}$.[10] Moreover, the addition of ethylene carbonate enabled the formation of a stable solid electrolyte interface (SEI) on the lithium metal anode.[11] These SEIs kinetically hinder the decomposition of the electrolyte and make cells feasible with $V_{OC} \leq 5\ V$ vs. Li, although the degradation is initiated at $V_{OC} > 4\ V$.[12]

Whittingham *et al.* explored layered materials such as TiS_2 as cathode materials for lithium ion batteries. They showed, that TiS_2 can reversibly intercalate lithium ions between its layers forming Li_xTiS_2 $(0 \leq x \leq 1)$ in the process. Using TiS_2 as cathode material, lithium metal as anode and the above mentioned solution of $LiPF_6$ in propylene carbonate a working, rechargeable battery was demonstrated in 1976 ($V_{OC} \approx 2\ V$ vs. Li).[13–15] The discovery of $LiTmO_2$ $(Tm = Co, Ni)$ as suitable cathode materials by Goodenough *et al.* enabled the construction of high voltage lithium ion battery cells showing $V_{OC} \approx 4\ V$ vs. Li.[16–18] However, the formation of dendrites using lithium metal as anode on repeated cycling, causing the cells to short-circuit, was a safety hazard. The utilization of graphite as an anode material[19,20] made the handling of these first Li-ion batteries much safer and lead to their commercialization. Figure 1.1 shows a schematic representation of the $LiCoO_2$||C-cell patented by Yoshino *et al.* in 1985.[21] During charging Li^+-ions deintercalate from the cathode material $Li_{1-x}CoO_2$ $(0 \leq x \leq 0.5)$ by oxidizing Co^{III} to Co^{IV}, diffuse through the elec-

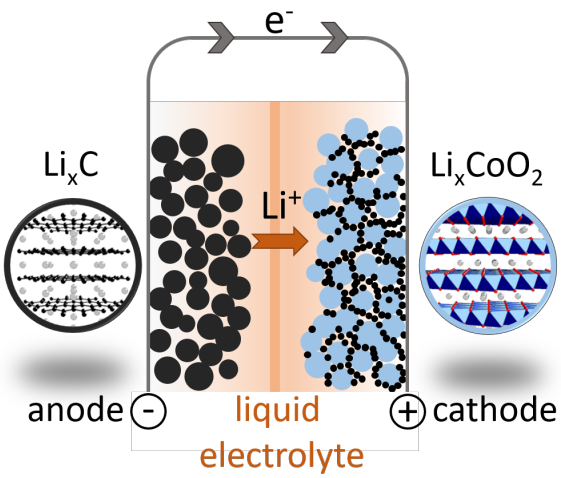

Figure 1.1: Schematic representation of a conventional lithium ion cell. The electrodes are made of intercalation compounds: the cathode is $LiCoO_2$, the anode is graphite and the liquid electrolyte is e.g. a solution of 1 M $LiPF_6$ in a mixture of ethylene carbonate and dimethyl carbonate (EC/DC).

trolyte and subsequently intercalate into a partially reduced graphite anode to form Li_xC_6 ($0 \leq x \leq 1$). Following these discoveries Sony corporation marketed the first cell phone which ultimately mobilized our every-day life.

Lithium ion batteries were gradually improved upon until this day, to increase their specific (volumetric and gravimetric) energy density as well as their power density but the overall design stayed the same. This improvement was achieved mainly through processing of the utilized electrode materials, e.g. nanostructuring, optimization of the liquid electrolyte solution and the discovery of new cathode materials. The nowadays utilized cathode materials can be sorted into three groups of materials: Layered transition metal oxides, such as $LiCoO_2$ (LCO) and nickel, manganese or aluminum substituted versions, e.g. $LiNi_{0.33}Co_{0.33}Mn_{0.33}O_2$ (NCM111) or $LiNi_{0.8}Co_{0.15}Al_{0.05}O_2$ (NCA), spinels like $LiMn_2O_4$ (LMO) and nickel substituted $LiNi_{0.5}Mn_{1.5}O_4$ (LNMO), and olivines, such as $LiFePO_4$ (LFP). The layered transition metal oxides show the highest specific capacities compared to the other cathode materials and are therefore preferred for the use in electric vehicles (EVs). Whereas LFP shows high specific power, enabling fast charging, as well as high lifetimes, the spinels on the other hand offer high energy density, achieved through higher electrochemical potentials up to 4.7 V *vs.* Li, although they show comparatively low specific capacities.[22] Both olivines and spinels, being comprised of earth-abundant elements resulting in cheaper batteries, are therefore mainly used in batteries intended for consumer goods, e.g. cell phones.
The temperature of large lithium ion battery packs, which are for example employed in EVs, has to be monitored and controlled by separate heating or cooling systems, especially during charging and discharging.[23] Overheating of battery cells can cause a thermal runaway event by which temperatures can reach as high as 500 °C.[24] This can lead to a chain reaction inside the battery causing the whole battery pack to catch fire, fueled by the flammable organic electrolyte.[25,26] The replacement of the liquid electrolyte by a solid not only minimizes this safety concern by introducing more chemically and mechanically robust materials, it also offers the benefit of improved volumetric and gravimetric energy density of the whole battery pack, because of cell design and also the reduced complexity of temperature management systems. The concept of the all-solid-state lithium ion battery is discussed in further detail in the following section.

1.1.2 All-solid-state lithium ion batteries

Conventional lithium ion batteries are highly optimized devices and, by being subject to intense research for decades, are slowly approaching their physicochemical limits at least in terms of volumetric energy density in their current designs.[4] Replacing the liquid electrolyte used in conventional lithium ion batteries by one or more solids offers the possibility to keep reliable, high energy electrode materials as well as their respective manufacturing procedures. Furthermore, hitherto impossible cell designs can potentially improve the energy density of the resulting batteries and additionally eliminate safety concerns with the liquid electrolyte.

The all-solid-state lithium ion battery (ASSLIB) is not a new concept. The first ASSLIBs, being lithium-iodine batteries, can be found in pacemakers and are nowadays also employed in low power devices such as RFID chips. The lithium-iodine batteries are comprised of a lithium metal sheet as anode wrapped around a iodine containing poly-2-vinyl pyridine cathode.[27] On contact lithium iodide is formed which acts as separator and electrolyte. Because of the low conductivity of the electrolyte LiI, these batteries show low specific power and are therefore not applicable for high power uses such as powering an EV.

Modern ASSLIB designs are derived from conventional LIBs introduced above, but offer the prospect of improved energy density, achieved by substituting the carbon anode by metallic lithium, and improved power density, by utilizing solid electrolytes with high specific conductivities.[28] Additionally, for large battery packs, used for example in EVs, bi-polar stacking of battery cells and less complex thermal management systems, as was discussed above, is envisioned to provide higher volumetric energy densities, resulting in more compact lithium ion batteries compared to conventional designs. First working bi-polar stacked ASSLIB designs utilizing lithium metal as anode were already demonstrated.[29] A schematic representation of an ASSLIB cell is given in Figure 1.2. The choice of solid electrolyte used in these battery cells is key to their performance and there is a plethora of suitable materials available including borides, phosphides, oxides, sulfides and organic polymers. This work, however, only focuses on sulfides because of their superior ionic conductivities and mechanical properties. It is also uncertain which specific cell design will become accepted in the future. However, to be compatible with conventional LIB designs and to maximize the energy and power densities that can be achieved, it seems to be established that lithium metal as anode has to be employed.[4] Therefore, the solid electrolyte in future ASSLIBs has to be either thermodynamically stable or kinetically inert in contact with lithium metal and high energy cathode materials, which could be achieved by an electrolyte forming stable SEIs, or both anode and cathode materials have to be coated and therefore provide an artificial SEI.[5] Another alternative is to use suitable combinations of electrolytes, each forming stable SEIs at the cathode and anode side, respectively. Section 1.3.1 will give a more in-depth overview of state-of-the-art lithium ion electrolytes.

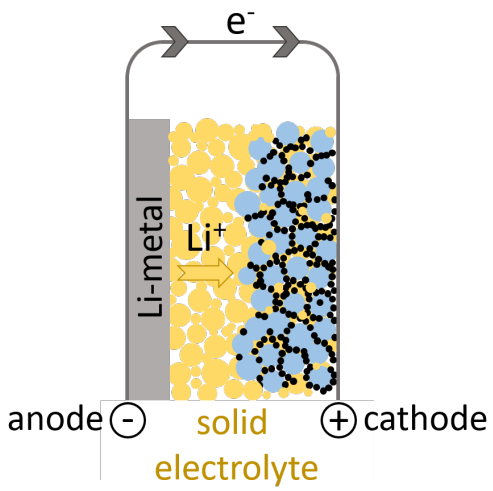

Figure 1.2: Schematic representation of a all-solid-state lithium ion cell. The electrodes are made of lithium metal and $LiCoO_2$ as anode and cathode, respectively. The electrolyte is a powdered solid which allows for lithium ion diffusion.

1.2 Sodium ion batteries

In spite of many reports of future lithium shortages resulting from the increasing production of EVs, estimations on the availability and demand for at least the next 30 years of growing battery production show no concerning results.[30–32] However, regardless whether conventional or solid-state battery technology is employed, the price of lithium will play a more substantial role in battery production than at this point in time. Combined with geopolitical considerations, alternatives to a lithium-based technology should be explored.[33–35]
In general, since its commercialization far more resources have been spent to improve conventional LIB technology compared to sodium ion batteries (SIB). Both technologies experienced a similar development in the 1970s and 80s and just recently the results of that time were taken up again.[36] Unfortunately, with sodium being a less electropositive and heavier metal than lithium, energy densities of the resulting batteries are bound to be lower ($Na/Na^+ = 2.71\ V$ *vs.* $Li/Li^+ = 3.04\ V$). Additionally, since sodium shows a bigger ionic radius than lithium ($r_{Na^+} = 1.02\,\text{Å}$ *vs.* $r_{Li^+} = 0.76\,\text{Å}$),[37] different electrode materials are required than those used for LIBs. For instance, sodium does not readily form intercalation compounds with graphitic carbon as lithium does. However, amorphous 'hard carbon' appears to be a viable alternative.[38] Similar to LIBs transition metal oxides were explored as cathode materials for SIBs as well. Delmas *et al.* identified numerous promising $Na_x TmO_2$ ($0.5 \leq x \leq 1$; $Tm = Cr, Mn, Co$) compounds in this regard.[36,39,40] In addition to these sodium transition metal oxides, silicates and sodium vanadium phosphates have also been considered, but by and large no large-scale technology has been established yet.[36]
For stationary energy storage systems the sodium-sulfur secondary battery is a well-known alternative to the lithium systems. Developed in the 1970s, this type of battery was one of the first using a solid electrolyte, β-alumina (cf. below), combined with two liquid electrode materials. However, molten sodium and sulfur require the battery to be operated at around 300 °C which renders the battery too impractical and unsafe to be handled in mobile applications, especially considering the brittle nature of the oxide electrolyte. Additionally, the need to non-stop heat the battery, which can be considered as self-discharge, makes this technology only feasible for large-scale storage facilities where the specific surface area and therefore heat-loss of the battery is minimized.
There are recent approaches trying to adapt the Na/S battery technology to room temperature by using a S/C-cathode, sodium metal anode, $NaCF_3SO_3$ in tetraethylene glycol dimethyl ether (TEGDME) as electrolyte and Na-β"-alumina as separator.[41] This hybrid between solid-state and conventional battery showed high capacity of over 600 mAh/g with a coulombic efficiency close to 100%.
In addition to the systems presented, pure solid-state battery systems have already been presented. For instance, Liu *et al.* showed that an all-solid-state battery utilizing the transition metal oxide $Na_{0.66}Ni_{0.33}Mn_{0.67}O_2$ as cathode, Na-β"-alumina as electrolyte and sodium metal as anode can give a battery system with high reversibility. This battery showed a voltage range between 2.5 – 3.8 V with a cycle life of 10'000 with 90% capacity retention at 6 C ($I_{charge/discharge} = C\text{-}rate \cdot Q/3600\ s$), albeit with a capacity of only $Q = 80\,\text{mAh}$ at 70 °C.[42] Elevated temperatures were used to inhibit dendrite growth on

the sodium metal during cycling, which would ultimately result in shorting of the battery cell. This is also common practice for ASSLIBs.
For all-solid-state sodium ion battery cells the same considerations as made for the ASSLIBs (cf. above) regarding energy density and the stability of the employed electrolyte materials are true. By and large, sodium battery technology is not yet as mature as that for lithium, but great efforts have been made in recent years to compensate for this. Considering the promising results with manganese cathode materials, this technology may allow us to dispense not only with lithium but also with electrode materials containing cobalt, decreasing cost and increasing safety, especially paired with all-solid-state technology.

1.3 Solid electrolytes

To be applicable for battery applications a solid electrolyte should possess the following properties:

- high specific ionic conductivity, comparable to modern liquid electrolytes, at room temperature ($\sigma_{RT,ion} \geq 1\ mScm^{-1}$);
- very low partial electronic conductivity to minimize self discharge of the battery;
- inert against lithium metal and high-voltage cathode materials;
- mechanically soft to withstand volume change during cycling and handling of the battery (e.g. vibrations in EVs) and reduce grain-boundary resistances by current constriction effects (cf. 3) without the need of high temperature sintering.

The next section gives a short introduction to the structure-property relationships affecting the ionic conductivity of a solid.
Typically, the diffusion of an ion through a solid is a vacancy driven one. It has to hop from one possible coordination site to the next which has to be empty at the arrival time of the ion. This hopping can occur through edges or, more favorably, faces of its respective coordination polyhedron.[43] The movement of the ion away from its energetically favorable position is associated with an activation energy E_a. The dependence of the specific conductivity σ on temperature T can be expressed by the Arrhenius equation 1.5:

$$\sigma = \frac{\sigma_0}{T} e^{-E_a/k_B T} \tag{1.5}$$

with an Arrhenius pre-factor:[44,45]

$$\sigma_0 = \frac{zn(Ze)^2}{k_B} e^{\Delta S_m/k_B} a_0^2 \nu_0 \tag{1.6}$$

where z is a geometrical factor (for different geometries, includes correlation factors), charge carrier density n and their charge Ze, entropy of migration ΔS_m,[46] jump distance a_0 and jump frequency ν_0.

Equation 1.5 shows that to obtain a solid electrolyte with sufficiently high specific ionic conductivity (cf. below) the activation energy for ion migration E_a has to be low and the Arrhenius pre-factor σ_0 has to be high. The first is usually considered to be the most important factor for high ionic conductivity and is mainly influenced by the coordination of the diffusing ions, i.e. their percolation pathway through the crystal, and the polarizability of the anion sublattice. In this regard, Ceder *et al.* showed that the lowest activation energies are to be expected, in the case of lithium, for jumps of the cation between face-sharing tetrahedra in a body centered cubic (*bcc*) sulfur packing.[47] The famous tetragonal $Li_{10}GeP_2S_{12}$ (LGPS, cf. section 1.3.1), one of the fastest ion conductors, crystallizes with a slightly distorted variant of this anion packing. Another favorable arrangement of the anion sub-lattice is the tetragonal close packing (*tcp*),[48,49] a distorted variant of the hexagonal close packing (*hcp*) with a sphere density of 71.87%, which offers double the amount of octahedral and tetrahedral voids than in a *hcp*, albeit very distorted, and by being connected by faces and corners, the respective coordination polyhedra offer energetically facile diffusion paths for the cation.[43] An anion arrangement in between a *hcp* and *tcp* is for example realized in the lithium superionic conductor (LISICON) $Li_{2+2x}Zn_{1-x}GeO_4$.[50] Distorted coordination polyhedra, which occur for example in the *tcp*, typically flatten out the energy landscape of the ion occupying the polyhedron and therefore not only influence the activation barrier for ion migration but also influence the entropy of migration S_m and therefore the Arrhenius pre-factor in Equation 1.6.[45,51] DiSteffano *et al.* showed recently for $LiTi_2(PS_4)_3$ that this effect can lead to a frustrated energy landscape, which is predicted to result in very high ionic conductivities.[52]

Many of the effects discussed above can be influenced by substitution of one or more elements in a given ion conducting compound to influence its properties. Anion substitution can increase the polarizability of the anion lattice, by for example substituting with a heavier homologue, resulting in a decrease in E_a which should result in an increase in ionic conductivity. However, Krauskopf *et al.* showed that for $Na_3PS_{4-x}Se_x$ this does not have to be the case, due to ion-phonon interactions affecting the jump frequency ν_0 of the diffusing ion.[45] A softer lattice is a more polarizable one, which makes for a material with lower activation energy of ion migration and a more favorable mechanical behaviour. However, this also decreases the phonon energy of the lattice, decreasing the attempt frequency of ion hopping, which can in turn lower the ionic conductivity. This is in accordance with the empirical Meyer-Neldel rule, stating that $log\sigma_0$ shows a positive linear correlation to the activation energy E_a.[53,54]

Anion substitution can also affect the chemical stability of the electrolyte. In general, lighter homologues are more electronegative and therefore harder to oxidize. Additionally, Kanno *et al.* showed improved stabilities of tetragonal $Li_{9.42}Si_{1.02}P_{2.1}S_{9.96}O_{2.04}$ against anodic reduction in contact with lithium metal.[55] In addition to the isovalent substitutions discussed above, aliovalent substitution of either the anion or cation, in an at least ternary system, can also affect the charge carrier density n, which allows for the creation of vacancies or the occupation of interstitial sites in a given crystal structure in addition to the effects discussed above. According to Equation 1.6, small changes in n should only have a small influence, since the Arrhenius prefactor only scales linearly. However, correlation

effects can amplify this effect by several orders of magnitude.
Like many diffusion processes with high concentrations of charge carriers, the diffusion of e.g. an alkaline cation in a solid electrolyte is prone to correlation effects. The measure for the existence of these effects is the Haven ratio $H_R = D^{tr}/D_\sigma$, relating the measured diffusion coefficient of a tracer atom or ion D^{tr} to the diffusion coefficient calculated from the conductivity of the diffusing species through the sample D_σ in absence of ion-ion correlations $H_R = 1$. Here, the Nernst-Einstein equation (Eq. 1.7) links the diffusion coefficient of an ion to the conductivity:

$$\sigma = \frac{Dnz^2e^2}{k_BTH_R} \tag{1.7}$$

D^{tr} can be experimentally determined for example by pulsed field gradient nuclear magnetic resonance (cf. Chapter 3). However, the Haven ratio H_R alone does not give information about the type of correlation occurring during the diffusion process.[56]
Since alkali metal sulfides, in particular with small complex anions like thio-phosphates, offer a combination of beneficial factors discussed above (polarizability, lattice dynamics,...) which can result in high ionic conductivities (cf. Chapter 1.3.1) combined with mechanical softness, which is advantageous for the processability and battery life time, they are the primary focus of this work. The next sections give an overview of state-of-the-art solid electrolytes containing lithium and sodium, focusing primarily on sulfides since they are most relevant for this work.

1.3.1 Solid lithium ion electrolytes

One of the first fast lithium ion conductors, orthorhombic $Li_{14}Zn(GeO_4)_4$, was found by Hong in 1978 and became known, in reference to the sodium superionic conductors (NASICON, cf. Chapter 1.3.2), as LISICON.[50]
This finding together with the commercialization of the conventional LIB started the search for new materials rivaling liquid electrolytes in conductivity. The most prominent oxide materials that showed specific ionic conductivities in the $1 \cdot 10^{-3}\,\mathrm{S\,cm^{-1}}$ range were found in the perovskite-like lithium lanthanum titanate (LLTO, $Li_{3x}La_{2/3-x}\square_{1/3-2x}TiO_3$, $0.06 \leq x \leq 0.16$), NASICON-like lithium aluminum titanium phosphate (LATP, $Li_{1.3}Al_{0.3}Ti_{1.7}(PO_4)_3$) and garnet-type lithium lanthanum zirconate (LLZO, $Li_7La_3Zr_2O_{12}$) with specific bulk ionic conductivities of $1.4 \cdot 10^{-3}\,\mathrm{S\,cm^{-1}}$,[57] $3 \cdot 10^{-3}\,\mathrm{S\,cm^{-1}}$,[58] and up to $1 \cdot 10^{-3}\,\mathrm{S\,cm^{-1}}$,[59] respectively. These oxide materials show very high stability against oxidation ($> 6\ V$ vs. Li) and are in part inert against metallic lithium.[60] As was discussed before, the specific ionic conductivity and the electrochemical stability of a solid electrolyte play an important role for its application in solid-state batteries, but they are not the only important factors. Mechanical properties of the electrolytes, i.e. their plasticity and softness, determines how well the grains of a compacted powder are contacted after pressing and weather cracking of the electrolyte can easily occur during cycling of a solid-state battery. In the case of the above mentioned oxides, sintering with temperatures above 800 °C of compacted powders must be employed to reduce grain boundary resistances to

yield total ionic conductivities in a useful range for battery applications. However, this procedure is incompatible with high energy cathode materials.

Substituting the oxide anion by the heavier chalcogenide sulfur is supposed to not only give a softer, i.e. polarizable, and therefore an energetically favorable lattice for ion movement (cf. above) but also a mechanically softer lattice.[68] Indeed, most sulfur electrolytes show very little detrimental grain boundary contribution to the total ionic conductivity, even for cold pressed powders. The substitution of oxygen by sulfur in lithium phosphates and subsequent tuning of lithium interstitial sites by aliovalent substitution of phosphorus by germanium led to the discovery of the orthorhombic $Li_{3+x}P_{1-x}Ge_xS_4$ (*ortho*-LGPS) by Kanno *et al.* with a total ionic conductivity at room temperature of $2.2 \cdot 10^{-3}\,S\,cm^{-1}$ for $x = 0.25$.[69] Because of the similarities of the anion sub-lattices of *ortho*-LGPS and LISICON, namely a packing in between a *hcp* and *tcp*, this new class of fast lithium ion conductors was called thio-LISICONs. The end members of the solid-solution series $Li_{3+x}P_{1-x}Ge_xS_4$, $\beta - Li_3PS_4$ (LPS) and Li_4GeS_4 crystallize homeotypically, where in the case of the latter additional octahedral voids are filled by lithium. Furthermore, Murayama *et al.* showed the flexibility of this system to iso- and aliovalent substitution on the phosphorous position, influencing the charge carrier density and polarizability of the anion lattice.[70] However, higher conductivities than $6 \cdot 10^{-4}\,S\,cm^{-1}$ ($Li_{3.4}Si_{0.4}P_{0.6}S_4$) could not be achieved. With the discovery by Mitsui *et al.* of an ordered double salt in the solid-solution series $Li_{3+x}P_{1-x}Ge_xS_4$ with $x = \frac{1}{3}$ and a specific ionic conductivity at room temperature of 12 mS/cm,[64] solid lithium ion conductors outperformed organic liquid electrolytes for the first time and started to move into the focus of solid-state electrolyte research.

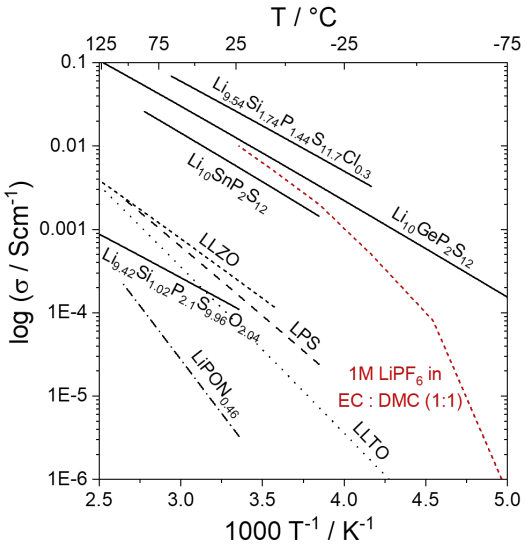

Figure 1.3: Overview of selected lithium ion conductors. For compounds crystallizing homeotypically the same line type was chosen. The total ionic conductivities and respective activation energies to create this graph are given in Table C.1.[55,60–67]

$Li_{10}GeP_2S_{12}$ (LGPS) crystallizes in the tetragonal space group $P4_2/nmc$ (Fig. 1.5), with $a = 8.719(3)$ Å and $c = 12.639(4)$.[71] The topology of its sulfur sublattice, in contrast to the end members of its solid solution series $Li_{3+x}P_{1-x}Ge_xS_4$, is a distorted variant of the *bcc* packing. This was shown to be energetically advantageous for hops of cations between tetrahedral voids.[47] In the case of LGPS, these hops take place between lithium atom Li1 and Li3 situated in channels running parallel to *c*, which subsequently show the lowest activation energy for ion hopping. Additional tetrahedrally coordinated lithium atoms (Li4)

interconnect these 1D channels and enable 3D diffusion. The octahedrally coordinated Li2 shows the highest activation barrier and is usually considered to be immobile at room temperature.[72–76] Additionally, the crystal structure features two phosphorous positions, one (P2) is occupied solely by phosphorous, the other (P1) shows a mixed occupation with the tetrel atom Ge of 50%. Both are tetrahedrally coordinated by four sulfur atoms forming $[PS_4]^{3-}$ and $[GeS_4]^{4-}$ anions, which are edge- or corner-sharing to $[Li2S_6]$-octahedra, respectively. The topology of these anions closely resembles the LiO_2 structure type, which is shown in more detail in Chapter 3.

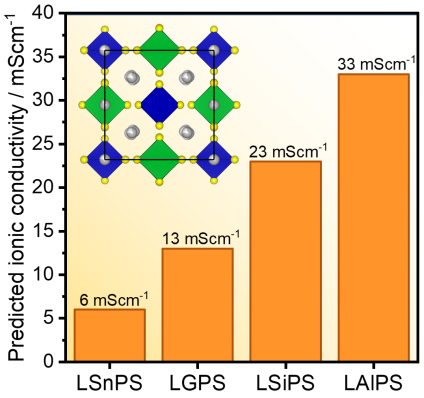

Figure 1.4: Predicted specific ionic conductivities at room temperature for the tetragonal LMPS ($Li_{10\pm1}\,TtP_2S_{12}$, M = Sn, Ge, Si, Al) system.[77]

It was shown later, that the tetragonal LGPS phase can be obtained in a compositional range of $\frac{1}{3} \leq x \leq \frac{1}{2}$ in $Li_{3+x}P_{1-x}Ge_xS_4$, resulting in Li_7GePS_8 as one of the end members of this series with a specific ionic conductivity of 6 mS/cm.[78] Furthermore, Kanno *et al.* have shown that tetragonal LGPS constitutes a low-temperature phase in the $Li_{3+x}P_{1-x}Ge_xS_4$ solid-solution series, which shows a peritectic phase separation into the thio-LISICON (*ortho*-LGPS) phases described above at temperatures around 550 °C.[79] Additionally, Ge can be substituted by other tetrel atoms (Si, Sn), resulting in superionic conductors containing only earth-abundant elements.[60,67,71,78,80–84] However, the possible substitutional range decreases from Si ($\frac{1}{3} \leq x \leq \frac{2}{3}$) to Sn ($x \approx \frac{1}{3}$) in $Li_{3+x}P_{1-x}\,Tt_xS_4$. However, $Li_{11}Si_2PS_{12}$ ($x = \frac{2}{3}$) could only be synthesized by pressures exceeding 4 GPa.[81] In this regard, $Li_{11}Si_2PS_{12}$, which was found by Kuhn *et al.*, showed higher lithium ion-diffusivities than tetragonal LGPS. These findings follow the predictions by Ceder *et al.* obtained by *ab initio* molecular dynamics (AIMD) simulations.[77] They report a trend which predicts increasing conductivities in the series $Tt = Sn \rightarrow Ge \rightarrow Si$ for $Li_{10}\,TtP_2S_{12}$ (Fig. 1.4). However, the total conductivities of the silicon containing compounds synthesized by conventional solid-state synthesis with $\sigma_{RT} \approx 2\ mScm^{-1}$ falls behind these expectations.[67,83,84] Chapter 3 gives a more thorough description of the assumed underlying problem of an amorphous side phase impeding the total ionic conductivity ubiquitous to at least all tetragonal LSiPS compounds.

According to the AIMD simulations by Ceder *et al.* the highest conductivities of 33 mS/cm for a tetragonal LGPS-type compound can be achieved by substituting Ge by Al to form '$Li_{11}AlP_2S_{12}$'.[77] Amaresh *et al.* showed that only partial substitution of Ge by Al is possible, up to $x \leq 0.3$ in $Li_{10+x}Ge_{1-x}Al_xP_2S_{12}$, which gave a maximum specific ionic conductivity of 1.7 mS/cm for $x = 0.3$.[85] These same limitations were found by Roling *et al.* for $Li_{10+x}Sn_{1-x}Al_xP_2S_{12}$, resulting in a very similar total specific ionic conductivity of 2 mS/cm for $x = 0.3$.[67] Hitherto, a solid solution series containing Si did not yield the

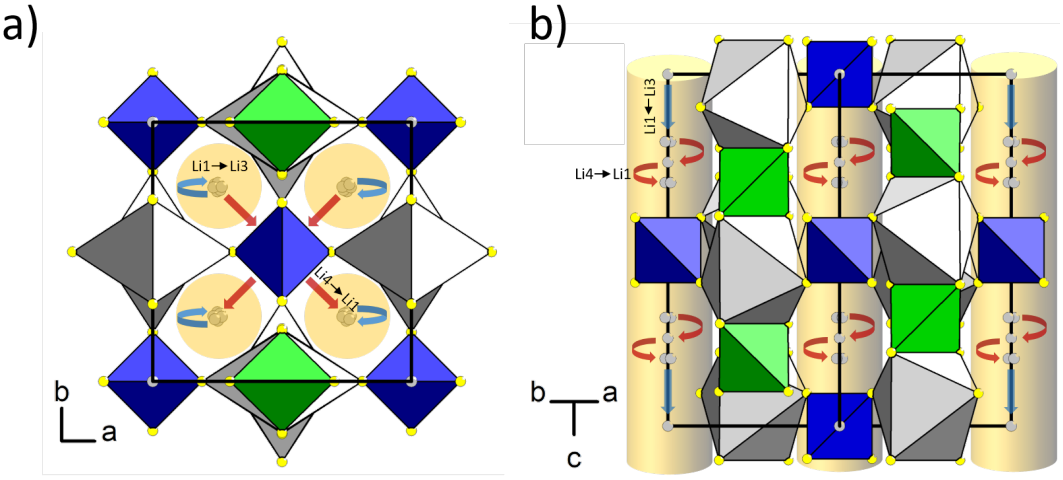

Figure 1.5: Crystal structure of LGPS. **a:** View parallel to c; **b:** View parallel to [110]; Blue and green tetrahedra depict $[P2S_4]$- and $[P1/Ge1S_4]$-anions, respectively, grey octahedra depict $[Li2S_6]$-units, grey atoms represent lithium. The main diffusion channels running parallell to c are represented by yellow rods. Jumps between Li1 and Li3 inside the channels or Li1 and Li4 between the channels are represented by blue or red arrows, respectively.

desired tetragonal LGPS-like phase.[70] More information on this substitution series can be found in Chapter 4.1.

The currently fastest lithium ion solid electrolyte material $Li_{9.54}Si_{1.74}P_{1.44}S_{11.7}Cl_{0.3}$ was found by Kanno *et al.* and shows a specific ionic conductivity at room temperature of 25 mS/cm, although the existence of a supposedly less conducting side phase (cubic Li_6PS_5Cl) was observed.[55] Recent theoretical studies attribute this jump in conductivity by one order of magnitude from the diverse LSiPS materials to the higher polarizability of the $[PS_3Cl]^{2-}$-anion which enhances cooperative migration of lithium ions.[86] Another explanation for this dramatic increase, which is given in more detail in Chapter 4.2, is a decrease of the high grain boundary resistivity observed in LSiPS materials compared to other LGPS-like materials[67] by formation of an $Li_{7-x}P_{1-x}Si_xS_{5-x}Cl_x$ argyrodite phase acting as a more conductive interface between the crystalline grains of the electrolyte.

Lithium argyrodites ($Li_{7-x}PnCh_{6-x}X_x$, $Pn = P, As$, $Ch = S, Se$, $X = Cl, Br, I$) were just recently identified as fast sulfur or selenide based lithium ion conductors with ionic conductivities up to 10^{-2} S cm^{-1}.[87–90] Similar to the mineral Ag_8GeS_6, cubic Li argyrodites are double salts consisting of $[PnCh_4]^{3-}$-anions, whose topology closely resembles that of the cubic Laves phase $MgCu_2$ with additional sulfur anions, which can be partially substituted by halogenide ions, and lithium cations situated in tetrahedral voids.[60,91–94] Furthermore, the ionic conductivity of this class of materials shows a strong dependence on the S – X disorder, which can be influenced by doping and cooling rate during the synthesis.[95] Zeier *et al.* showed that, similar to the LGPS-system, a substitution of P by Ge is possible, further enhancing the ionic conductivity up to 18 mS/cm for $x = 0.7$ in $Li_{6+x}P_{1-x}Ge_xS_5I$

by affecting the S – I disorder, charge carrier concentration and polarizability of the anion sublattice.[96]
Besides the thio-ortho-phosphates, complex phosphates (pyro-, meta- or hypho-) are also of scientific interest, but by and large have not yet reached the conductivities of the former.[90,97,98] One prominent exception, is the glassy ceramic $Li_7P_3S_{11}$ which features a specific ionic conductivity of 17 mS/cm.[99]
Furthermore, there is a plethora of interesting compounds from different material classes, the enumeration and description of which would however go beyond the scope of this work and can be found elsewhere.[60,100,101]

1.3.2 Solid sodium ion electrolytes

When talking about solid sodium ion electrolytes one has to mention the Na-β-alumina system which was found by Beevers and Ross more than 80 years ago.[102] Its composition can be expressed as $Na_2O \cdot n(Al_2O_3)$ with $5 \leq n \leq 11$. This set of compounds is famously employed as the solid electrolyte in the sodium-sulfur battery (cf. above). The structure of β-alumina can be described as being comprised of so-called spinel blocks, in which Al^{3+} is tetrahedrally and octahedrally coordinated by oxide anions forming a *ccp* lattice, and Na – O layers interrupting these blocks featuring mobile sodium ions. The number of interrupting layers, and therefore charge carriers, is directly dependent on n, where compounds with $n = 11$ or $n = 5$ are denoted β- or β''-alumina, respectively. All other possible compositions with n in between 5 and 11 yield materials showing coherent intergrowth between those two structures. Since Na-β''-alumina shows the highest charge carrier concentration it consequently also shows the highest specific ionic conductivity at room temperature in this system of up to 14 mS/cm.[103–106] Another important system of solid electrolytes showing 3D sodium diffusion, rather than the 2D- diffusion in layers of mobile ions in β-alumina, is the NASICON system. This class of materials was found by Hong and Goodenough 1976 as $Na_{1+x}Zr_2Si_xP_{3-x}O_{12}$ ($0 \leq x \leq 3$).[107] Considering the abundance of available materials, a general formula $AM(SiO_4)_z(PO_4)_{3-z}$ results, where the A-site cation is octahedrally coordinated by oxygen and can be occupied by a mono-, di-, tri-, or tetravalent atom, the M-site cation is also octahedrally coordinated and can be occupied by either a di-, tri-, tetra- or pentavalent atom, where in the latter case the A-site cation has to be vacant to maintain charge neutrality.[108] Guin and Tietz report a plethora of existing compounds for sodium occupying the A-site alone, resulting in $Na_{1+2w+x-y+z}M_w^{(II)}M_x^{(III)}M_y^{(V)}M_{2-w-x-y}^{(IV)}(SiO_4)_z(PO_4)_{3-z}$.[109] Due to the abundance of possible iso- and aliovalent substitution in this system, the charge carrier concentration and polarizability of the anion sub-lattice can be carefully tuned, resulting in a maximum ionic conductivity at room temperature of 5 mS/cm for $Na_{2.96}Nb_{0.04}Zr_{1.96}(SiO_4)_2(PO_4)$.[110]
However, the mentioned materials exhibit the same problems already discussed for the lithium solid electrolytes, where oxide materials generally show high grain boundary resistances requiring high sintering temperatures to give sufficiently high total conductivities. In this regard, sulfide materials offer an advantage in processability by allowing for simple cold-pressing of the powdered materials. One of the most promising materials in this class

is Na_3PS_4. This material shows two modifications, a low-temperature tetragonal and a high-temperature cubic one with a transformation from α- to β-Na_3PS_4 at 261 °C.[111] This high temperature phase was thought to be obtainable at room temperature by mechanical milling, improving the conductivity of the tetragonal α-phase by two orders of magnitude from $10^{-6}\,S\,cm^{-1}$ to $4.6 \cdot 10^{-4}\,S\,cm^{-1}$.[112,113] However, Zeier *et al.* showed that this phase's local structure is better described by the tetragonal α-phase and that the jump in conductivity results from the higher defect concentration introduced by the mechanical stress of the milling process.[114] The topology of the crystal structure of α-Na_3PS_4 can be described as a slightly distorted NaCl-packing of Na^+-cations and $[PS_4]^{3-}$-anions, where the tetrahedral anions are rotated in a way that allows for rows or zig-zag lines of sodium atoms to form diffusion paths.[111] Noteworthy is the tolerance of this structure to substitution, which allows for a wide diversity of compounds in this system. By isovalent substitution of S by Se, values up to $1.16 \cdot 10^{-3}\,S\,cm^{-1}$ can be achieved for Na_3PSe_4.[45,115,116] Additionally, isovalent substitution on the pnictogen position by antimony gives air stable Na_3SbS_4 showing a conductivity of up to 3.1 mS/cm, which in addition to a solid-state reaction can also be obtained by liquid synthesis.[117]

Similar to the LGPS-system, phosphorus can also be aliovalently substituted by the tetrel elements Si and Sn. In the case of silicon only a partial substitution is possible. Tanibata *et al.* reported a maximum conductivity of $7.4 \cdot 10^{-4}\,S\,cm^{-1}$ for a glass ceramic of composition $94(Na_3PS_4) \cdot 6(Na_4SiS_4)$.[118] Substitution by tin on the other hand results in a double salt with very similar topology to tetragonal LGPS, with conductivities varying from $4 \cdot 10^{-5}\,S\,cm^{-1}$ for $Na_{10}SnP_2S_{12}$ to $4 \cdot 10^{-3}\,S\,cm^{-1}$ for $Na_{11}Sn_2PS_{12}$.[80,119,120]

The highest measured sodium ion conductivity so far was found for $Na_{2.9}Sb_{0.9}W_{0.1}S_4$ by Zeier *et al.* with 41 mS/cm.[121] The isotypic phosphorus containing compound $Na_{2.9}P_{0.9}W_{0.1}S_4$ shows also a very high specific ionic conductivity of 13 mS/cm. These jumps in conductivity by more than one order of magnitude are explained by a decrease in activation energy from 0.25 eV to below 0.20 eV by substitution of $[PnS_4]^{3-}$ $(Pn = P, Sb)$ by the more polarizable $[WS_4]^{2-}$-anion, which also leads to an increase in sodium vacancies, and, in the case of $Na_{2.9}Sb_{0.9}W_{0.1}S_4$, a phase transition to the cubic high temperature phase.

Similar to the lithium ion solid electrolytes, a wide variety of different sodium ion solid electrolytes are available beside those which are mentioned here, including materials from the class of polymers, phosphides, and borides, to only name a few. The enumeration and description of these materials is however beyond the scope of this work and can be found elsewhere.[101,122,123]

Bibliography

(1) Keyser, P. T. The purpose of the Parthian Galvanic cells: a first-century A.D. electric battery used for analgesia. *J. Near East. Stud.* **1993**, *52*, 81–98.

(2) Volta, A. On the Electricity Excited by the Mere Contact of Conducting Substances of Different Kinds. *Philos. Trans. RoyalSoc.* **1800**, *90*, 403–431.

(3) Unterstaller, A. Electric vehicles: a smart choice for the environment `https://www.eea.europa.eu/articles/electric-vehicles-a-smart` (accessed 08/30/2019).

(4) Janek, J.; Zeier, W. G. A solid future for battery development. *Nat. Energy* **2016**, *1*, 16141.

(5) Culver, S. P.; Koerver, R.; Zeier, W. G.; Janek, J. On the Functionality of Coatings for Cathode Active Materials in Thiophosphate-Based All-Solid-State Batteries. *Adv. Energy Mater.* **2019**, *9*, 1900626.

(6) Bellis, M. History and Timeline of the Battery `https://www.thoughtco.com/battery-timeline-1991340` (accessed 09/18/2019).

(7) Goodenough, J. B. Rechargeable batteries: challenges old and new. *J. Solid State Electrochem.* **2012**, *16*, 2019–2029.

(8) Atkins, P. W., *Physikalische Chemie*; Wiley-VCH: Weinheim, 2013, pp 242–253.

(9) Winter, M.; Brodd, R. J. What Are Batteries, Fuel Cells, and Supercapacitors? *Chem. Rev.* **2004**, *104*, 4245–4270.

(10) Xu, K. Nonaqueous Liquid Electrolytes for Lithium-Based Rechargeable Batteries. *Chem. Rev.* **2004**, *104*, 4303–4418.

(11) Aurbach, D.; Gofer, Y.; Langzam, J. The Correlation Between Surface Chemistry, Surface Morphology, and Cycling Efficiency of Lithium Electrodes in a Few Polar Aprotic Systems. *J. Electrochem. Soc.* **1989**, *136*, 3198–3205.

(12) Edström, K.; Gustafsson, T.; Thomas, J. The cathode–electrolyte interface in the Li-ion battery. *Electrochim. Acta* **2004**, *50*, Polymer Batteries and Fuel Cells:Selection of Papers from First International Conference, 397–403.

(13) Whittingham, M. S. Electrointercalation in Transition-Metal Disulphides. *J. Chem. Soc., Chem. Commun.* **1974**, 328–329.

(14) Whittingham, M. S.; Gamble, F. R. The Lithium Intercalates of the Transition Metal Dichalcogenides. *Mater. Res. Bull.* **1975**, *10*, 363–371.

(15) Whittingham, M. S. Electrical Energy Storage and Intercalation Chemistry. *Science* **1976**, *192*, 1126–1127.

(16) Li_xCoO_2 ($0 < x < -1$): A new cathode material for batteries of high energy density. *Mater. Res. Bull.* **1980**, *15*, 783–789.

(17) Solid-solution oxides for storage-battery electrodes. *Jpn. J. Appl. Phys.* **1980**, *19*, 305–313.

(18) Lithium mobility in the layered oxide $Li_{1-x}CoO_2$. *Solid State Ionics* **1985**, *17*, 13–19.

(19) M. S. Whittingham, A. J. J., *Intercalation chemistry*; Academic: New York, 1982, pp 19–53.

(20) Yazami, R.; Touzain, P. A reversible graphite-lithium negative electrode for electrochemical generators. *J. Power Sources* **1983**, *9*, 365–371.

(21) Yoshino, A., US Patent No. 4, 668, 595 and JP9769585, 1985.

(22) Julien, C.; Mauger, A.; Zaghib, K.; Groult, H. Comparative Issues of Cathode Materials for Li-Ion Batteries. *Inorganics* **2014**, *2*, DOI: 10.3390/inorganics2010132.

(23) Hannan, M. A.; Hoque, M. M.; Hussain, A.; Yusof, Y.; Ker, P. J. State-of-the-Art and Energy Management System of Lithium-Ion Batteries in Electric Vehicle Applications: Issues and Recommendations. *IEEE Access* **2018**, *6*, 19362–19378.

(24) Bandhauer, T. M.; Garimella, S.; Fuller, T. F. A Critical Review of Thermal Issues in Lithium-Ion Batteries. *J. Electrochem. Soc.* **2011**, *158*, R1–R25.

(25) Wang, Q.; Ping, P.; Zhao, X.; Chu, G.; Sun, J.; Chen, C. Thermal runaway caused fire and explosion of lithium ion battery. *J. Power Sources* **2012**, *208*, 210–224.

(26) Miao, Y.; Hynan, P.; von Jouanne, A.; Yokochi, A. Current Li-Ion Battery Technologies in Electric Vehicles and Opportunities for Advancements. *Energies* **2019**, *12*, 1074.

(27) Crompton, T. R., *Lithium — Iodine Batteries. In: Small Batteries*; Palgrave: London, 1982, pp 196–197.

(28) Robinson, A. L.; Janek, J. Solid-state batteries enter EV fray. *MRS Bulletin* **2014**, *39*, 1046–1047.

(29) Wei, Z.; Chen, S.; Wang, J.; Wang, Z.; Zhang, Z.; Yao, X.; Deng, Y.; Xu, X. A large-size, bipolar-stacked and high-safety solid-state lithium battery with integrated electrolyte and cathode. *J. Power Sources* **2018**, *394*, 57–66.

(30) Gruber, P.; Medina, P.; Keoleian, G. Global Lithium Availability: A Constraint for Electric Vehicles. *J. Ind. Ecol.* **2011**, 1–16.

(31) Grosjean, C.; Miranda, P. H.; Perrin, M.; Poggi, P. Assessment of world lithium resources and consequences of their geographic distribution on the expected development of the electric vehicle industry. *Renewable Sustainable Energy Rev.* **2012**, *16*, 1735–1744.

(32) Speirs, J.; Contestabile, M.; Houari, Y.; Gross, R. The future of lithium availability for electric vehicle batteries. *Renewable Sustainable Energy Rev.* **2014**, *35*, 183–193.

(33) Vikström, H.; Davidsson, S.; Höök, M. Lithium availability and future production outlooks. *Appl. Energy* **2013**, *110*, 252–266.

(34) Habib, K.; Hamelin, L.; Wenzel, H. A dynamic perspective of the geopolitical supply risk of metals. *J. Cleaner Prod.* **2016**, *133*, 850–858.

(35) Narins, T. P. The battery business: Lithium availability and the growth of the global electric car industry. *The Extractive Industries and Society* **2017**, *4*, 321–328.

(36) Sun, Y.; Guo, S.; Zhou, H. Exploration of Advanced Electrode Materials for Rechargeable Sodium-Ion Batteries. *Adv. Energy Mater.* **2019**, *9*, 1800212.

(37) Shannon, R. D. Revised effective ionic radii and systematic studies of interatomic distances in halides and chalcogenides. *Acta Crystallogr. Sect. A* **1976**, *32*, 751–767.

(38) Chen, X.; Zheng, Y.; Liu, W.; Zhang, C.; Li, S.; Li, J. High-performance sodium-ion batteries with a hard carbon anode: transition from the half-cell to full-cell perspective. *Nanoscale* **2019**, *11*, 22196–22205.

(39) Delmas, C.; Fouassier, C.; Hagenmuller, P. Structural classification and properties of the layered oxides. *Physica B+C* **1980**, *99*, 81–85.

(40) Braconnier, J.; Delmas, C.; Hagenmuller, P. Etude par desintercalation electrochimique des systemes Na_xCrO_2 et Na_xNiO_2. *Mater. Res. Bull.* **1982**, *17*, 993–1000.

(41) Kim, I.; Park, J.-Y.; Kim, C. H.; Park, J.-W.; Ahn, J.-P.; Ahn, J.-H.; Kim, K.-W.; Ahn, H.-J. A room temperature Na/S battery using a β"-alumina solid electrolyte separator, tetraethylene glycol dimethyl ether electrolyte, and a S/C composite cathode. *J. Power Sources* **2016**, *301*, 332–337.

(42) Liu, L.; Qi, X.; Ma, Q.; Xiaohui, R.; Hu, Y.-S.; Zhou, Z.-B.; Li, H.; Huang, X.; Chen, L. Toothpaste-like Electrode: A Novel Approach to Optimize the Interface for Solid-State Sodium-Ion Batteries with Ultralong Cycle Life. *ACS Applied Materials & Interfaces* **2016**, *8*, DOI: 10.1021/acsami.6b11773.

(43) West, A. R.; Bruce, P. G. Tetragonal-Packed Crystal Structures. *Acta Crystallogr.* **1982**, *38*, 1891–1896.

(44) Tilley, R. J. D., *Defects in Solids*; John Wiley & Sons: 2008.

(45) Krauskopf, T.; Pompe, C.; Kraft, M. A.; Zeier, W. G. Influence of Lattice Dynamics on Na^+ Transport in the Solid Electrolyte $Na_3PS_{4-x}Se_x$. *Chem. Mater.* **2017**, *29*, 8859–8869.

(46) Dobson, T. W.; Wager, J. F.; Van Vechten, J. A. Entropy of migration for atomic hopping. *Phys. Rev. B* **1989**, *40*, 2962–2967.

(47) Wang, Y.; Richards, W. D.; Ong, S. P.; Miara, L. J.; Kim, J. C.; Mo, Y.; Ceder, G. Design principles for solid-state lithium superionic conductors. *Nat. Mater.* **2015**, *14*, 1026–1031.

(48) Baur, W. H. A three dimensionally periodic, eleven coordinated, dense packing of symmetry equivalent spheres. *Mater. Res. Bull.* **1981**, *16*, 339–345.

(49) Periodic arrays of identical ions packed with 10, 11, and 12 nearest neighbors. *J. Solid State Chem.* **1983**, *50*, 235–239.

(50) Hong, H.-P. Crystal structure and ionic conductivity of Li14Zn(GeO4)4 and other new Li+ superionic conductors. *Mater. Res. Bull.* **1978**, *13*, 117–124.

(51) Almond, D.; West, A. The activation entropy for transport in ionic conductors. *Solid State Ionics* **1987**, *23*, 27–35.

(52) Di Stefano, D.; Miglio, A.; Robeyns, K.; Filinchuk, Y.; Lechartier, M.; Senyshyn, A.; Ishida, H.; Spannenberger, S.; Prutsch, D.; Lunghammer, S.; Rettenwander, D.; Wilkening, M.; Roling, B.; Kato, Y.; Hautier, G. Superionic Diffusion through Frustrated Energy Landscape. *Chem.* **2019**, *5*, 2450–2460.

(53) Meyer, W.; Neldel, H. Über die Beziehung zwischen der Energiekonstanten und der Mengenkonstanten *a* in der Leitwerts-Temperaturformel bei oxydischen Halbleitern. *Z. Tech. Phys.* **1937**, *18*, 588.

(54) Dalvi, A.; Reddy, N. P.; Agarwal, S. The Meyer–Neldel rule and hopping conduction. *Solid State Commun.* **2012**, *152*, 612–615.

(55) Hori, S.; Suzuki, K.; Hirayama, M.; Kato, Y.; Kanno, R. Lithium Superionic Conductor $Li_{9.42}Si_{1.02}P_{2.1}S_{9.96}O_{2.04}$ with $Li_{10}GeP_2S_{12}$-Type Structure in the Li_2S - P_2S_5 – SiO_2 Pseudoternary System: Synthesis, Electrochemical Properties, and Structure–Composition Relationships. *Front. Energy Res.* **2016**, *4*, 38.

(56) Vargas-Barbosa, N. M.; Roling, B. "Dynamic Ion Correlations in Solid and Liquid Electrolytes: How do they affect Charge and Mass Transport? *Chem. Electro. Chem.*, *0*, 10.1002/celc.201901627, DOI: 10.1002/celc.201901627.

(57) Itoh, M.; Inaguma, Y.; Jung, W.-H.; Chen, L.; Nakamura, T. High lithium ion conductivity in the perovskite-type compounds $Ln_{12}Li_{12}TiO_3$ (Ln=La,Pr,Nd,Sm). *Solid State Ionics* **1994**, *70-71*, 203–207.

(58) Aono, H.; Sugimoto, E.; Sadaaka, Y.; Imanaka, N.; Adachi, G. Ionic conductivity of the lithium titanium phosphate ($Li_{1+x}M_xTi_{2-x}(PO_4)_3$, M=Al, Sc, Y, and La) systems. *J. Electrochem. Soc.* **1989**, *136*, 590.

(59) Thangadurai, V.; Pinzaru, D.; Narayanan, S.; Baral, A. K. Fast Solid-State Li Ion Conducting Garnet-Type Structure Metal Oxides for Energy Storage. *J. Phys. Chem. Lett.* **2015**, *6*, 292–299.

(60) Lotsch, B. V.; Maier, J. Relevance of solid electrolytes for lithium-based batteries: A realistic view. *J. Electroceram.* **2017**, *38*, 128–141.

(61) Inaguma, Y.; Liquan, C.; Itoh, M.; Nakamura, T.; Uchida, T.; Ikuta, H.; Wakihara, M. High ionic conductivity in lithium lanthanum titanate. *Solid State Commun.* **1993**, *86*, 689–693.

(62) Yu, X.; Bates, J. B.; Jellison, G. E.; Hart, F. X. A Stable Thin-Film Lithium Electrolyte: Lithium Phosphorus Oxynitride. *J. Electrochem. Soc.* **1997**, *144*, 524–532.

(63) Murugan, R.; Thangadurai, V.; Weppner, W. Fast Lithium Ion Conduction in Garnet-Type $Li_7La_3Zr_2O_{12}$. *Angew. Chem. Int. Ed.* **2007**, *46*, 7778–7781.

(64) Kamaya, N.; Homma, K.; Yamakawa, Y.; Hirayama, M.; Kanno, R.; Yonemura, M.; Kamiyama, T.; Kato, Y.; Hama, S.; Kawamoto, K.; Mitsui, A. A lithium superionic conductor. *Nat. Mater.* **2011**, *10*, 682–686.

(65) Liu, Z.; Fu, W.; Payzant, E. A.; Yu, X.; Wu, Z.; Dudney, N. J.; Kiggans, J.; Hong, K.; Rondinone, A. J.; Liang, C. Anomalous High Ionic Conductivity of Nanoporous β-Li_3PS_4. *J. Am. Chem. Soc.* **2013**, *135*, 975–978.

(66) Kato, Y.; Hori, S.; Saito, T.; Suzuki, K.; Hirayama, M.; Mitsui, A.; Yonemura, M.; Iba, H.; Kanno, R. High-power all-solid-state batteries using sulfide superionic conductors. *Nat. Energy* **2016**, *1*, 16030.

(67) Bron, P.; Dehnen, S.; Roling, B. $Li_{10}Si_{0.3}Sn_{0.7}P_2S_{12}$ – A low-cost and low-grain-boundary-resistance lithium superionic conductor. *J. Power Sources* **2016**, *329*, 530–535.

(68) Wakamura, K. Roles of phonon amplitude and low-energy optical phonons on superionic conduction. *Phys. Rev. B* **1997**, *56*, 11593–11599.

(69) Kanno, R.; Murayama, M. Lithium Ionic Conductor Thio-LISICON: The Li_2S - GeS_2 - P_2S_5 System. *J. Electrochem. Soc.* **2001**, *148*, A742.

(70) Murayama, M. Synthesis of New Lithium Ionic Conductor Thio-LISICON—Lithium Silicon Sulfides System. *J. Solid State Chem.* **2002**, *168*, 140–148.

(71) Kuhn, A.; Köhler, J.; Lotsch, B. V. Single-crystal X-ray structure analysis of the superionic conductor $Li_{10}GeP_2S12$. *Phys. Chem. Chem. Phys.* **2013**, *15*, 11620.

(72) Mo, Y.; Ong, S. P.; Ceder, G. First Principles Study of the $Li_{10}GeP_2S_{12}$ Lithium Super Ionic Conductor Material. *Chem. Mater.* **2012**, *24*, 15–17.

(73) Du, F.; Ren, X.; Yang, J.; Liu, J.; Zhang, W. Structures, Thermodynamics, and Li^+ Mobility of $Li_{10}GeP_2S_{12}$: A First-Principles Analysis. *J. Phys. Chem. C* **2014**, *118*, 10590–10595.

(74) Hori, S.; Taminato, S.; Suzuki, K.; Hirayama, M.; Kato, Y.; Kanno, R. Structure–property relationships in lithium superionic conductors having a $Li_10GeP_2S_12$-type structure. *Acta Crystallogr., Sect. B* **2015**, *71*, 727–736.

(75) Weber, D. A.; Senyshyn, A.; Weldert, K. S.; Wenzel, S.; Zhang, W.; Kaiser, R.; Berendts, S.; Janek, J.; Zeier, W. G. Structural Insights and 3D Diffusion Pathways within the Lithium Superionic Conductor $Li_{10}GeP_2S_{12}$. *Chem. Mater.* **2016**, *28*, 5905–5915.

(76) Krauskopf, T.; Culver, S. P.; Zeier, W. G. Bottleneck of Diffusion and Inductive Effects in $Li_{10}Ge_{1-x}Sn_xP_2S_{12}$. *Chem. Mater.* **2018**, *30*, 1791–1798.

(77) Ong, S. P.; Mo, Y.; Richards, W. D.; Miara, L.; Lee, H. S.; Ceder, G. Phase stability, electrochemical stability and ionic conductivity of the $Li_{10\pm1}MP_2X_{12}$ (M = Ge, Si, Sn, Al or P, and X = O, S or Se) family of superionic conductors. *Energy Environ. Sci.* **2013**, *6*, 148–156.

(78) Kuhn, A.; Duppel, V.; Lotsch, B. V. Tetragonal $Li_{10}GeP_2S_{12}$ and Li_7GePS_8 – exploring the Li ion dynamics in LGPS Li electrolytes. *Energy Environ. Sci.* **2013**, *6*, 3548.

(79) Hori, S.; Kato, M.; Suzuki, K.; Hirayama, M.; Kato, Y.; Kanno, R. Phase Diagram of the Li_4GeS_4 – Li_3PS_4 Quasi-Binary System Containing the Superionic Conductor $Li_{10}GeP_2S_{12}$. *J. Am. Ceram. Soc.* **2015**, *98*, ed. by Sprenkle, V., 3352–3360.

(80) Bron, P.; Johansson, S.; Zick, K.; Schmedt auf der Günne, J.; Dehnen, S.; Roling, B. $Li_{10}SnP_2S_{12}$: An Affordable Lithium Superionic Conductor. *J. Am. Chem. Soc.* **2013**, *135*, 15694–15697.

(81) Kuhn, A.; Gerbig, O.; Zhu, C.; Falkenberg, F.; Maier, J.; Lotsch, B. V. A new ultrafast superionic Li-conductor: ion dynamics in $Li_{11}Si_2PS_{12}$ and comparison with other tetragonal LGPS-type electrolytes. *Phys. Chem. Chem. Phys.* **2014**, *16*, 14669–14674.

(82) Kato, Y.; Saito, R.; Sakano, M.; Mitsui, A.; Hirayama, M.; Kanno, R. Synthesis, structure and lithium ionic conductivity of solid solutions of $Li_{10}(Ge_{1-x}M_x)P_2S_{12}$ (M = Si, Sn). *J. Power Sources* **2014**, *271*, 60–64.

(83) Whiteley, J. M.; Woo, J. H.; Hu, E.; Nam, K.-W.; Lee, S.-H. Empowering the Lithium Metal Battery through a Silicon-Based Superionic Conductor. *J. Electrochem. Soc.* **2014**, *161*, A1812–A1817.

(84) Kato, Y.; Hori, S.; Saito, T.; Suzuki, K.; Hirayama, M.; Mitsui, A.; Yonemura, M.; Iba, H.; Kanno, R. High-power all-solid-state batteries using sulfide superionic conductors. *Nat. Energy* **2016**, *1*, 16030.

(85) Amaresh, S.; Karthikeyan, K.; Kim, K. J.; Lee, Y. G.; Lee, Y. S. Aluminum based sulfide solid lithium ionic conductors for all solid state batteries. *Nanoscale* **2014**, *6*, 6661–6667.

(86) Zhang, B.; Yang, L.; Wang, L.-W.; Pan, F. Cooperative transport enabling fast Li-ion diffusion in Thio-LISICON $Li_{10}SiP_2S_{12}$ solid electrolyte. *Nano Energy* **2019**, *62*, 844–852.

(87) Kong, S.-T.; Deiseroth, H.-J.; Reiner, C.; Gün, Ö.; Neumann, E.; Ritter, C.; Zahn, D. Lithium Argyrodites with Phosphorus and Arsenic: Order and Disorder of Lithium Atoms, Crystal Chemistry, and Phase Transitions. *Chem. Eur. J.* **2010**, *16*, 2198–2206.

(88) Boulineau, S.; Courty, M.; Tarascon, J.-M.; Viallet, V. Mechanochemical synthesis of Li-argyrodite Li_6PS_5X ($X = Cl, Br, I$) as sulfur-based solid electrolytes for all solid state batteries application. *Solid State Ionics* **2012**, *221*, 1–5.

(89) Chen, H. M.; Maohua, C.; Adams, S. Stability and ionic mobility in argyrodite-related lithium-ion solid electrolytes. *Phys. Chem. Chem. Phys.* **2015**, *17*, 16494–16506.

(90) Dietrich, C.; Sadowski, M.; Sicolo, S.; Weber, D. A.; Sedlmaier, S. J.; Weldert, K. S.; Indris, S.; Albe, K.; Janek, J.; Zeier, W. G. Local Structural Investigations, Defect Formation, and Ionic Conductivity of the Lithium Ionic Conductor $Li_4P_2S_6$. *Chem. Mater.* **2016**, *28*, 8764–8773.

(91) Eulenberger, G. Die Kristallstruktur der Tieftemperaturmodifikation von Ag_8GeS_6. *Monatsh. Chem.* **1977**, *108*, 901–913.

(92) Kuhs, W.; Nitsche, R.; Scheunemann, K. The argyrodites - A new family of tetrahedrally close-packed structures. *Mater. Res. Bull.* **1979**, *14*, 241–248.

(93) Gaudin, E.; Deiseroth, H.; Zaiß, T. The argyrodite $\gamma - Ag_9AlSe_6$: a non-metallic filled Laves phase. *Z. Kristallogr. – Cryst. Mater.* **2009**, *216*, 39–44.

(94) Bernges, T.; Culver, S. P.; Minafra, N.; Koerver, R.; Zeier, W. G. Competing Structural Influences in the Li Superionic Conducting Argyrodites $Li_6PS_{5-x}Se_xBr$ ($0 \leq x \leq 1$) upon Se Substitution. *Inorg. Chem.* **2018**, *57*, 13920–13928.

(95) Gautam, A.; Sadowski, M.; Prinz, N.; Eickhoff, H.; Minafra, N.; Ghidiu, M.; Culver, S. P.; Albe, K.; Fässler, T. F.; Zobel, M.; Zeier, W. G. Rapid Crystallization and Kinetic Freezing of Site-Disorder in the Lithium Superionic Argyrodite Li_6PS_5Br. *Chem. Mater.* **2019**, *31*, 10178–10185.

(96) Kraft, M. A.; Ohno, S.; Zinkevich, T.; Koerver, R.; Culver, S. P.; Fuchs, T.; Senyshyn, A.; Indris, S.; Morgan, B. J.; Zeier, W. G. Inducing High Ionic Conductivity in the Lithium Superionic Argyrodites $Li_{6+x}P_{1-x}Ge_xS_5I$ for All-Solid-State Batteries. *J. Am. Chem. Soc.* **2018**, *140*, 16330–16339.

(97) Dietrich, C.; Weber, D. A.; Sedlmaier, S. J.; Indris, S.; Culver, S. P.; Walter, D.; Janek, J.; Zeier, W. G. Lithium ion conductivity in Li_2S – P_2S_5 glasses – building units and local structure evolution during the crystallization of superionic conductors Li_3PS_4, $Li_7P_3S_11$ and $Li_4P_2S_7$. *J. Mater. Chem. A* **2017**, *5*, 18111–18119.

(98) Schoop, L. M.; Eger, R.; Pielnhofer, F.; Schneider, C.; Nuss, J.; Lotsch, B. V. Synthesis and Characterization of Three New Lithium-Scandium Hexathiohypodiphosphates: $Li_{4-3x}Sc_xP2S6$ ($x = 0.358$), *m*-$LiScP_2S_6$, and *t*-$LiScP_2S_6$. *Z. anorg. allg. Chem.* **2018**, *644*, 1854–1862.

(99) Seino, Y.; Ota, T.; Takada, K.; Hayashi, A.; Tatsumisago, M. A sulphide lithium super ion conductor is superior to liquid ion conductors for use in rechargeable batteries. *Energy Environ. Sci.* **2014**, *7*, 627–631.

(100) Zhao, W.; Yi, J.; He, P.; Zhou, H. Solid-State Electrolytes for Lithium-Ion Batteries: Fundamentals, Challenges and Perspectives. *Electrochem. Energ. Rev.* **2019**, *2*, 574–605.

(101) Ohno, S.; Banik, A.; Dewald, G. F.; Kraft, M. A.; Krauskopf, T.; Minafra, N.; Till, P.; Weiss, M.; Zeier, W. G. Materials design of ionic conductors for solid state batteries. *Prog. Energy* **2020**.

(102) Beevers, C. A.; Ross, M. A. S. The Crystal Structure of "Beta Alumina" $Na_2O \cdot 11Al_2O_3$. *Z. Kristallogr. – Cryst. Mater.* **1937**, *97*, 59–66.

(103) Yamaguchi, G.; Suzuki, K. On the Structures of Alkali Polyaluminates. *Bull. Chem. Soc. Jpn.* **1968**, *41*, 93–99.

(104) Kummer, J. β-Alumina electrolytes. *Prog. Solid State Chem.* **1972**, *7*, 141–175.

(105) Briant, J.; Farrington, G. Ionic conductivity in Na^+, K^+, and Ag^+ β"-alumina. *J. Solid State Chem.* **1980**, *33*, 385–390.

(106) Zhao, C.; Liu, L.; Qi, X.; Lu, Y.; Wu, F.; Zhao, J.; Yu, Y.; Hu, Y.-S.; Chen, L. Solid-State Sodium Batteries. *Adv. Energy Mater.* **2018**, *8*, 1703012.

(107) Goodenough, J.; Hong, H.-P.; Kafalas, J. Fast Na+-ion transport in skeleton structures. *Mater. Res. Bull.* **1976**, *11*, 203–220.

(108) Anantharamulu, N.; Koteswara Rao, K.; Rambabu, G.; Vijaya Kumar, B.; Radha, V.; Vithal, M. A wide-ranging review on Nasicon type materials. *J. Mater. Sci.* **2011**, *46*, 2821–2837.

(109) Guin, M.; Tietz, F. Survey of the transport properties of sodium superionic conductor materials for use in sodium batteries. *J. Power Sources* **2015**, *273*, 1056–1064.

(110) Takahashi, T.; Kuwabara, K.; Shibata, M. Solid-state ionics - conductivities of Na^+ ion conductors based on NASICON. *Solid State Ionics* **1980**, *1*, 163–175.

(111) Jansen, M.; Henseler, U. Synthesis, structure determination, and ionic conductivity of sodium tetrathiophosphate. *J. Solid State Chem.* **1992**, *99*, 110–119.

(112) Hayashi, A.; Noi, K.; Sakuda, A.; Tatsumisago, M. Superionic glass-ceramic electrolytes for room-temperature rechargeable sodium batteries. *Nat. Commun.* **2012**, *3*, 855–856.

(113) Hayashi, A.; Noi, K.; Tanibata, N.; Nagao, M.; Tatsumisago, M. High sodium ion conductivity of glass–ceramic electrolytes with cubic Na_3PS_4. *J. Power Sources* **2014**, *258*, 420–423.

(114) Krauskopf, T.; Culver, S. P.; Zeier, W. G. Local Tetragonal Structure of the Cubic Superionic Conductor Na_3PS_4. *Inorg. Chem.* **2018**, *57*, 4739–4744.

(115) Zhang, L.; Yang, K.; Mi, J.; Lu, L.; Zhao, L.; Wang, L.; Li, Y.; Zeng, H. Na_3PSe_4: A Novel Chalcogenide Solid Electrolyte with High Ionic Conductivity. *Adv. Energy Mater.* **2015**, *5*, 1501294.

(116) Krauskopf, T.; Muy, S.; Culver, S. P.; Ohno, S.; Delaire, O.; Shao-Horn, Y.; Zeier, W. G. Comparing the Descriptors for Investigating the Influence of Lattice Dynamics on Ionic Transport Using the Superionic Conductor $Na_3PS_{4-x}Se_x$. *J. Am. Chem. Soc.* **2018**, *140*, 14464–14473.

(117) Gamo, H.; Phuc, N. H. H.; Matsuda, R.; Muto, H.; Matsuda, A. Multiphase Na_3SbS_4 with high ionic conductivity. *Mater. Today Energy* **2019**, *13*, 45–49.

(118) Tanibata, N.; Noi, K.; Hayashi, A.; Tatsumisago, M. Preparation and characterization of highly sodium ion conducting Na_3PS_4 – Na_4SiS_4 solid electrolytes. *RSC Adv.* **2014**, *4*, 17120–17123.

(119) Richards, W. D.; Tsujimura, T.; Miara, L. J.; Wang, Y.; Kim, J. C.; Ong, S. P.; Uechi, I.; Suzuki, N.; Ceder, G. Design and synthesis of the superionic conductor $Na_{10}SnP_2S_{12}$. *Nat. Commun.* **2016**, *7*, 11009.

(120) Duchardt, M.; Ruschewitz, U.; Adams, S.; Dehnen, S.; Roling, B. Vacancy-Controlled Na^+ Superion Conduction in $Na_{11}Sn_2PS_{12}$. *Angew. Chemie Int. Ed.* **2018**, *57*, 1351–1355.

(121) Fuchs, T.; Culver, S. P.; Till, P.; Zeier, W. G. Defect-Mediated Conductivity Enhancements in $Na_{3-x}Pn_{1-x}W_xS_4$ (Pn = P, Sb) Using Aliovalent Substitutions. *ACS Energy Lett.* **2020**, *5*, 146–151.

(122) Haffner, A.; Hatz, A.-K.; Moudrakovski, I.; Lotsch, B. V.; Johrendt, D. Fast Sodium-Ion Conductivity in Supertetrahedral Phosphidosilicates. *Angew. Chem. Int. Ed.* **2018**, *57*, 6155–6160.

(123) Wang, Y.; Song, S.; Xu, C.; Hu, N.; Molenda, J.; Lu, L. Development of solid-state electrolytes for sodium-ion battery–A short review. *Nano Mater. Sci.* **2019**, *1*, 91–100.

Chapter 2

Selected experimental methods

2.1 Powder X-ray diffraction

Powder X-ray diffraction (PXRD) is a versatile tool to determine phase composition of a crystalline mixture in powder form. Since nearly all products were obtained as micro crystalline powders, it was the primary analytical method in this work to characterize samples. This section will give a brief theoretical background on the methods used to analyze the obtained data of PXRD measurements. This includes especially Rietveld refinement as a tool to determine exact phase compositions, including amorphous content, and in combination with charge flipping and simulated annealing implemented in TOPAS v. 5 the determination of crystal structures from PXRD data. For a more in-depth description on the following subjects the reader is pointed to the textbooks by Massa[1] and Dinnebier.[2]

2.1.1 Rietveld analysis

The Rietveld method is used to fit the intensities of a measured crystalline sample obtained from a diffraction experiment using either X-rays or neutrons. This is done by the least squares method minimizing the weighted difference between the in i steps measured intensities $I_{obs,i}$ and the calculated intensities $I_{calc,i}$ (Equ. 2.1):[3]

$$\sum_i (w_i(I_{obs,i} - I_{calc,i})) \rightarrow Min \tag{2.1}$$

For powder X-ray data the intensities are calculated by Equation 2.2:[3]

$$I_{calc,i} = \sum_p (S_p \sum_{\mathbf{s}(p)} (|F_{calc,\mathbf{s},p}|^2 \Phi_{\mathbf{s},p,i} Corr_{\mathbf{s},p,i})) + Bkg_i \tag{2.2}$$

with:[4]

$$F(\mathbf{s}) = \sum_{j=0}^{n} t_j(\mathbf{s}) f_j(\mathbf{s}) e^{2\pi i \mathbf{s}\mathbf{x}_j} \tag{2.3}$$

Where S_p is the scale factor of the respective phase p. The reciprocal scattering vector $\mathbf{s}$ can be expressed as a function of the reciprocal lattice vectors $\mathbf{a}^*, \mathbf{b}^*, \mathbf{c}^*$ using the integer Miller indices : $\mathbf{s} = (ha^*, kb^*, lc^*)$. $F_{calc,\mathbf{s},p}$ is the calculated structure factor of one crystalline phase as a sum over all atomic form factors $f_j(\mathbf{s})$ (ignoring anomalous scattering) of atom j with their respective displacement parameter t_j at position $\mathbf{x}_j = (x, y, z)$ as a vector of its fractional coordinates. $\Phi_{\mathbf{s},p,i}$ is the profile function of the respective reflection of a specific phase being a convolution of the instrumental resolution function and microstructural parameters of the respective phase, i.e. crystallite size and micro-strain. Bkg_i is a function to fit the background of the measurement caused by e.g. non-coherent elastic scattering from an amorphous phase. In this work Chebyshev polynomials were used. $Corr_{\mathbf{s},p,i}$ are correction functions. The for PXRD data most commonly used ones are given in Equation 2.4:[5]

$$Corr(\mathbf{s}) = M(\mathbf{s})LP(s)A(s)PO(\mathbf{s})E(\mathbf{s})... \tag{2.4}$$

$M(\mathbf{s})$ is the multiplicity of the reflection, $LP(s)$ is the solely geometrical Lorenz-polarization factor, $A(s)$ is the linear absorption coefficient ,PO($\mathbf{s}$) is a correction for a preferred orientation of crystallites and $E(\mathbf{s})$ a correction for extinction for highly crystalline samples.
The fit quality of a Rietveld refinement is, similar to single crystal structure refinements, expressed in agreement factors the so-called R-factors. These are given in the following equations:[6]

profile R-factor:

$$R_p = \frac{\sum_i |I_{obs,i} - I_{calc,i}|}{\sum_i I_{obs,i}} \tag{2.5}$$

weighted profile R-factor:

$$R_{wp} = \sqrt{\frac{\sum_i w_i (I_{obs,i} - I_{calc,i})^2}{\sum_i I_{obs,i}^2}} \tag{2.6}$$

expected R-factor:

$$R_{exp} = \sqrt{\frac{N - P}{\sum_i w_i I_{obs,i}^2}} \tag{2.7}$$

Goodness of fit:

$$Gof = \chi^2 = \left(\frac{R_{wp}}{R_{exp}}\right)^2 = \left(\sqrt{\frac{\sum_i w_i (I_{obs,i} - I_{calc,i})^2}{N - P}}\right)^2 \tag{2.8}$$

where N are the number of data points and P are the number of parameters.

As was stated above the phase composition of a mixture of crystalline products can be determined. The weight fraction of a phase W_α can be calculated by Equation 2.9, knowing the formula units per unit cell Z, the molecular weight M and the volume per unit cell V of all crystalline phases i:[7]

$$W_\alpha = \frac{S_\alpha Z_\alpha M_\alpha V_\alpha}{\sum_i S_i Z_i M_i V_i} \tag{2.9}$$

Using a fully crystalline internal standard with a similar absorption coefficient as the sample and known weight fraction $W_{std}(known)$ the with Equation 2.9 calculated weight fractions $W_\alpha(calc)$ can be corrected using Equation 2.10 to obtain the absolute values $W_\alpha(abs.)$. Since the obtained values should sum up to 1.0, Equation 2.11 gives the absolute weight fraction of unknown material $W_{unknown}(abs.)$ of the measured sample. In this work this relation was used to determine the amorphous content of samples:[7]

$$W_\alpha(abs.) = W_\alpha(calc)\frac{W_{std}(known)}{W_{std}(calc)} \tag{2.10}$$

$$W_{unknown}(abs.) = 1.0 - \sum_i W_i(abs.) \tag{2.11}$$

2.1.2 Structure determination from PXRD data

Structure determination from PXRD data was performed using the program Topas v. 5[8] and was done in the following steps:

- Indexing of the diffraction data and selection of meaningful results, i.e. unit cell dimensions
- Integration of the reflection intensities by performing a Pauli fit using selected result and generation of *hkl*-file
- Phase retrieval and generation of electron densities by applying the *charge flipping* algorithm (CFA) implemented in Topas.[9–11] Figure 2.1 shows a scheme of the the unmodified CFA. The CFA constructs initial electron densities ρ from the Fourier magnitudes calculated from observed reflection intensities and randomly generated phases. By flipping the electron density below a defined threshold δ, typically 0.1 of the electron density of the respective light atom in the crystal structure,[9] positivity of the electron density is enforced, excluding random noise. After Fourier transformation the Fourier magnitudes of the new structure factors are replaced by the observed ones and structure factors for not observed reflections are set to zero. By inverse Fourier transformation new electron densities are calculated. If the convergence criterion is not met the algorithm starts another iteration.

  Topas uses a modified version of this algorithm improving stability and convergence time by e.g. including symmetry operations and combination of the CFA with the

tangent formula from the classical *direct methods*.[11,12] This alteration is necessitated by the typically poor data quality of PXRD data compared to single crystal data.

- Rietveld refinement using the from *charge flipping* obtained atom positions.
- Difference Fourier synthesis to obtain light atom positions or, if this failed, *simulated annealing* within reasonable barriers.[13]

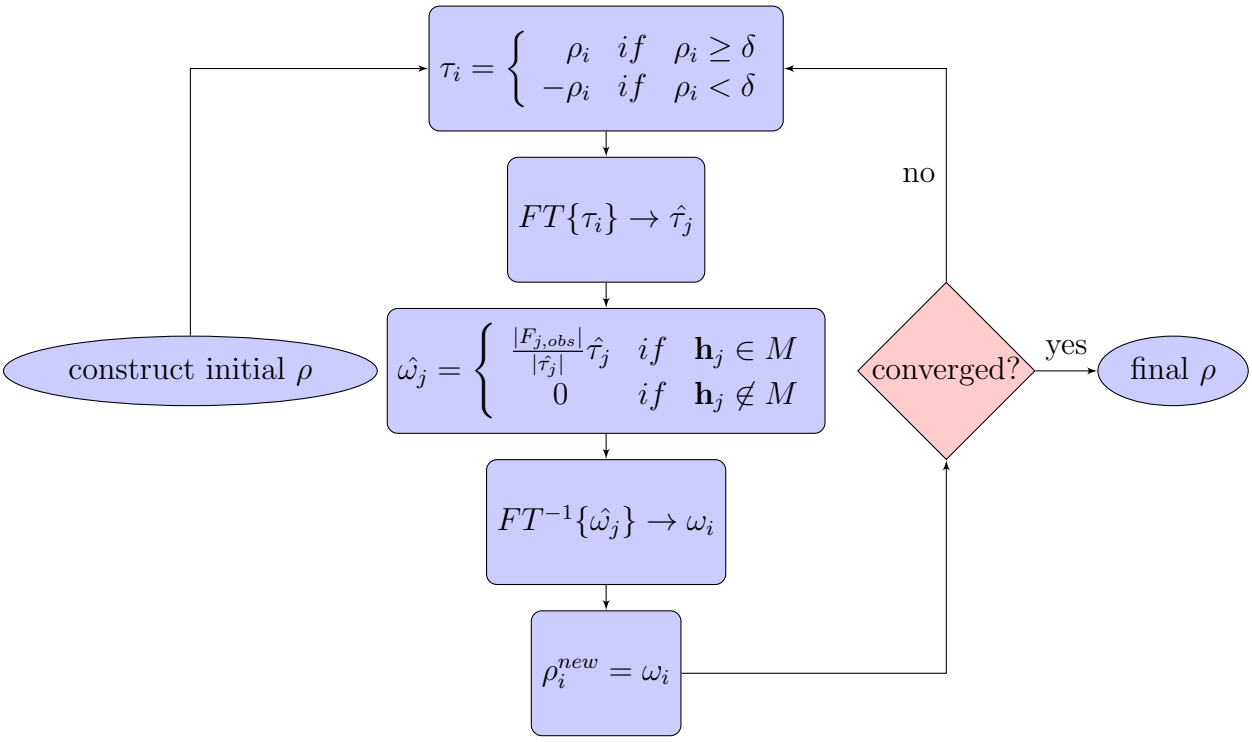

Figure 2.1: Scheme of the unmodified charge flipping algorithm. τ, ω are intermediate electron densities ρ, and $\hat{\tau}$ and $\hat{\omega}$ are their Fourier transforms respectively, δ is the charge flipping threshold, $\mathbf{h}_j$ is the Miller index of a reflection j, M is the set of observed reflections and $|F_{j,obs}|$ are their respective Fourier magnitudes. This scheme was reproduced from Palatinus.[11]

2.2 Electrochemical impedance spectroscopy

The following section gives a short introduction to electrochemical impedance spectroscopy. For more detailed information on the topic the reader is pointed to the book by Orazem and Tribollet.[14]

Electrochemical impedance spectroscopy was used to assess the specific ionic conductivity of a solid electrolyte at a given temperature. The conductivity is determined by measuring

the impedance of the sample. The impedance is the complex electrical resistance a sample induces on an alternating current (AC) flowing through it. It is determined by measuring for instance the current response of a sample excited by a sinusoidal voltage of given frequency f. The impedance is dependant on this frequency and describes not only the relation between the voltage excitation and current response, but also a phase shift ϕ between these signals. Therefore, the impedance is typically expressed as a vector consisting of a real component $Z^{'}$ and a complex component $iZ^{''}$ (cf. Equ. 2.12 and 2.13).[15]

$$\hat{Z} = \frac{\hat{U}}{\hat{I}} = Z^{'} + iZ^{''} = |Z|e^{i\phi} = |Z|(cos(\phi) + isin(\phi)) \tag{2.12}$$

, where:

$$|Z| = \sqrt{Z'^2 + iZ''^2} \tag{2.13}$$

An electrochemical impedance spectrum can be obtain by exciting a sample by multiple voltage signals of varying frequency. Whereas a low enough amplitude must be applied to ensure linearity of the current response. The resulting spectrum can only be interpreted in a meaningful and physical sense by comparing it to a chosen equivalent circuit model, where each circuit element represents a physical phenomenon.[16,17] This is typically done by fitting the impedance spectrum of the equivalent circuit model to the experimental data, utilizing established least-squares algorithms (e.g. Levenberg-Marquardt).

The fitting function is obtained by combining the impedance of electrical components, such as resistors ($Z = R$), capacitors ($Z = (i2\pi fC)^{-1}$) and inductors ($Z = i2\pi fL$), where the resistance R, the capacitance C and the inductance L are free parameters. Capacitors and inductors induce a constant phase shift of the current response of $-90°$ and $90°$, respectively. However, inhomogeneities of the electrode surface, high surface roughness or the overlapping of multiple processes can reduce the apparent phase angle. Therefore, an empirical circuit element, the constant phase element (CPE, $Z = (Q(i2\pi f)^{-\alpha})^{-1}$), is utilized, introducing another fit parameter α, which can vary from $-1 \leq \alpha \leq 1$ and Q.[18] This element becomes equal to a resistor, capacitor, inductor or Warburg element, which describes the impedance caused by infinite linear diffusion, with values of $\alpha = 0$, $\alpha = 1$, $\alpha = -1$ or $\alpha = 0.5$, respectively. In this work, when

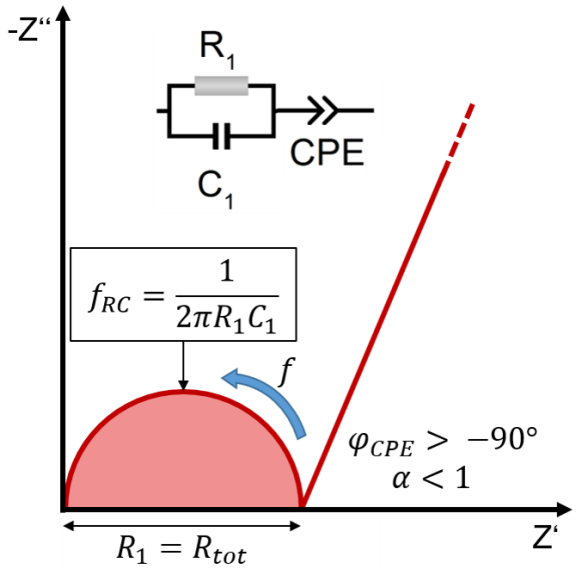

Figure 2.2: Exemplary Nyquist plot of a (RC)-CPE element. f_{RC} denotes the characteristic frequency or inverse relaxation time τ^{-1} of the (RC)-element.

a CPE was used, the corresponding influences to the impedance were exclusively capacitive in nature. Therefore, α was restrained to be $0.5 \leq \alpha \leq 1$.
Being a complex number, the impedance is commonly depicted in a Nyquist or Argand plot. Here, the imaginary part of the impedance is plotted against the real part and the excitation frequency is only implied.[19] Since solid electrolytes do not contribute inductively to the impedance, the sign of the ordinate is typically flipped for convenience. Figure 2.2 shows an exemplary Nyquist plot depicting a common EIS for a solid electrolyte. In this case, $R1$ is interpreted as the resistance encountered by the moving ion during conduction. Its inverse normalized by the geometric factors of the sample is therefore its specific conductivity σ. The capacitive behaviour of the sample is expressed as a capacitance C_1, which depends on the dielectric constant of the sample. These two circuit elements in parallel ((RC)-element) result in a semicircle in the Nyquist plot. If more than one (RC)-element is needed to fit the experimental data, an estimation of the expected capacitances can help to assign the observed processes. Table 2.1 gives expected ranges of capacitances for different conduction processes.

Table 2.1: Possible interpretations of observed capacitance values given by Irvine *et al.*[20]

Capacitance [F]	Responsible phenomenon
10^{-12}	bulk
10^{-11}	minor phase
$10^{-11} - 10^{-8}$	grain boundary
$10^{-10} - 10^{-9}$	bulk ferroelectric
$10^{-9} - 10^{-7}$	surface layer
$10^{-7} - 10^{-5}$	sample-electrode interface
10^{-4}	electrochemical reaction

The expression for the effective capacitance of a CPE in series or parallel to a resistor derived by Brug *et al.* is given in Equation 2.14:[18,21]

$$C_{eff} = Q^{\frac{1}{\alpha}} R^{(\frac{1}{\alpha}-1)} \tag{2.14}$$

Furthermore, for a solid electrolyte to be applicable in a battery it is important to determine the contribution of the electronic conductivity to the total conductivity. Chapter A gives a short introduction how the partial electronic conductivity is estimated.

2.3 Bond valence energy landscape calculations

Bond valence energy landscape (BVEL) calculations were performed with the 3DBVSMapper[22] program available for the Materials Studio software-suite. The BVEL method is based on the work of Adams and Rao, who introduced conversion terms to scale bond valence sum (BVS) mismatch into energy and additionally introduced coulombic repulsion terms.[23] It was shown before that the paths of lowest BVS mismatch, i.e. pseudo-potential

energy, in an ion conducting compound correlate well with the diffusion paths determined by *ab-initio* molecular dynamics (AIMD) simulations and can therefore be used as a computationally cheap way to gain fundamental understanding of the ion conduction mechanism.[24,25] The BVEL in 3DBVSMapper is calculated according to Equation 2.15 and 2.16 by first removing all test ions, e.g. lithium ions, in a given crystal structure and placing one test ion at all voxel points of the given unit cell.[22] The number and position of voxel points is defined by the desired resolution of the resulting map.

$$BVEL_{+/-} = \sum_{j=1}^{N} \left(m_j D_0 \{ exp[\alpha(R_{min} - d_j)] - 1 \}^2 - 1 \right) \tag{2.15}$$

and for ions of equal charge:

$$BVEL_{+/+} = \sum_{j=1}^{N} \left\{ ConvEV \frac{m_j}{d_j} \frac{|V_{TI}||V_j|}{(n_{qn,TI} n_{qn,j})^{1/2}} \left[erfc\left(\frac{d_j}{\rho}\right) - erfc\left(\frac{d_{cutoff}}{\rho}\right) \right] \right\} \tag{2.16}$$

where d_j is the distance to the jth ion of occupancy m_j, N is the number of ions inside the cut-off distance d_{cutoff} (here: 8 Å), D_0, R_{min} and α are empirical constants dependent on the type of test ion and its jth neighbour, $ConvEV$ is a conversion factor to eV, $V_{TI/j}$ is the oxidation states and $n_{qn,TI/j}$ the quantum numbers of the test ion and its jth neighbour, respectively, $erfc$ is the complementary error function and $\rho = 0.74(r_{TI} + r_j)$, where r_{TI} and r_j are the covalent radii of the test ion and its jth neighbour, respectively.
Activation energies of ion conduction are subsequently calculated by finding the lowest energy of an infinitely connected path through the unit cell inside the BVEL map. Although, 3DBVSMapper removes all test ions during the calculation and therefore vastly overestimates these activation energies, Avdeev *et al.* could show that the activation energies calculated with the BVEL method show a linear correlation to those obtained from AIMD simulations for a large number of ion conducting compounds.[26] A step-by-step description of the data handling and the limitations of the calculation method are given in chapter B.

Bibliography

(1) Massa, W., *Kristallstrukturbestimmung*; B.G. Teubner Verlag: Wiesbaden, 2007, 49ff.

(2) Dinnebier, R.; Leineweber, A.; Evans, J., *Rietveld Refinement. Practical Powder Diffraction Pattern Analysis using* Topas; De Gruyter: Berlin, Boston, 2018.

(3) Dinnebier, R.; Leineweber, A.; Evans, J., *Rietveld Refinement. Practical Powder Diffraction Pattern Analysis using* Topas; De Gruyter: Berlin, Boston, 2018, p 17.

(4) Dinnebier, R.; Leineweber, A.; Evans, J., *Rietveld Refinement. Practical Powder Diffraction Pattern Analysis using* Topas; De Gruyter: Berlin, Boston, 2018, p 33.

(5) Dinnebier, R.; Leineweber, A.; Evans, J., *Rietveld Refinement. Practical Powder Diffraction Pattern Analysis using* Topas; De Gruyter: Berlin, Boston, 2018, p 36.

(6) Dinnebier, R.; Leineweber, A.; Evans, J., *Rietveld Refinement. Practical Powder Diffraction Pattern Analysis using* Topas; De Gruyter: Berlin, Boston, 2018, pp 77–78.

(7) Dinnebier, R.; Leineweber, A.; Evans, J., *Rietveld Refinement. Practical Powder Diffraction Pattern Analysis using* Topas; De Gruyter: Berlin, Boston, 2018, p 134.

(8) Coelho, A. A. TOPAS and TOPAS-Academic : an optimization program integrating computer algebra and crystallographic objects written in C++. *J. Appl. Crystallogr.* **2018**, *51*, 210–218.

(9) Oszlányi, G.; Süto, A. *Ab initio* structure solution by charge flipping. *Acta Crystallogr., Sect. A* **2004**, *60*, 134–141.

(10) Oszlányi, G.; Sütő, A. The charge flipping algorithm. *Acta Crystallogr.* **2008**, *A64*, 123–134.

(11) Palatinus, L. The charge-flipping algorithm in crystallography. *Acta Crystallogr., Sect. B* **2013**, *69*, 1–16.

(12) Coelho, A. A. A charge-flipping algorithm incorporating the tangent formula for solving difficult structures. *Acta Crystallogr., Sect. A* **2007**, *63*, 400–406.

(13) Dinnebier, R.; Leineweber, A.; Evans, J., *Rietveld Refinement. Practical Powder Diffraction Pattern Analysis using* Topas; De Gruyter: Berlin, Boston, 2018, pp 183–195.

(14) Orazem, M. E.; Tribollet, B., *Electrochemical Impedance Spectroscopy*; John Wiley & Sons, Ltd: 2008.

(15) Orazem, M. E.; Tribollet, B., *Electrochemical Impedance Spectroscopy*; John Wiley & Sons, Ltd: 2008; Chapter 4, pp 61–72.

(16) Orazem, M. E.; Tribollet, B., *Electrochemical Impedance Spectroscopy*; John Wiley & Sons, Ltd: 2008; Chapter 5, pp 73–96.

(17) Orazem, M. E.; Tribollet, B., *Electrochemical Impedance Spectroscopy*; John Wiley & Sons, Ltd: 2008; Chapter 9, pp 153–162.

(18) Orazem, M. E.; Tribollet, B., *Electrochemical Impedance Spectroscopy*; John Wiley & Sons, Ltd: 2008; Chapter 13, pp 233–263.

(19) Orazem, M. E.; Tribollet, B., *Electrochemical Impedance Spectroscopy*; John Wiley & Sons, Ltd: 2008; Chapter 1, pp 1–21.

(20) Irvine, J. T. S.; Sinclair, D. C.; West, A. R. Electroceramics: Characterization by Impedance Spectroscopy. *Adv. Mater.* **1990**, *2*, 132–138.

(21) Brug, G.; van den Eeden, A.; Sluyters-Rehbach, M.; Sluyters, J. The analysis of electrode impedances complicated by the presence of a constant phase element. *J. Electroanal. Chem. Interfacial Electrochem.* **1984**, *176*, 275–295.

(22) Sale, M.; Avdeev, M. *3DBVSMAPPER*: a program for automatically generating bond-valence sum landscapes. *J. Appl. Cryst.* **2012**, *45*, 1054–1056.

(23) Adams, S.; Rao, R. P. High power lithium ion battery materials by computational design. *Phys. Status Solidi A* **2011**, *208*, 1746–1753.

(24) Adams, S. Modelling ion conduction pathways by bond valence pseudopotential maps. *Solid State Ionics* **2000**, *136-137*, Proceedings of the 12th International Conference on Solid State Ionics, 1351–1361.

(25) Brown, I. D. Recent Developments in the Methods and Applications of the Bond Valence Model. *Chem. Rev.* **2009**, *109*, PMID: 19728716, 6858–6919.

(26) Avdeev, M.; Sale, M.; Adams, S.; Rao, R. P. Screening of the alkali-metal ion containing materials from the Inorganic Crystal Structure Database (ICSD) for high ionic conductivity pathways using the bond valence method. *Solid State Ionics* **2012**, *225*, 43–46.

Chapter 3

A Lesson learned from NMR: characterization and ionic conductivity of LGPS-like Li_7SiPS_8

Sascha Harm, Anna-Katharina Hatz, Igor Moudrakovski, Roland Eger, Alexander Kuhn, Constantin Hoch, Bettina V. Lotsch

Published in: *Chemistry of Materials*, **2019**, *31*, 1280-1288.
DOI: 10.1021/acs.chemmater.8b04051
https://pubs.acs.org/doi/10.1021/acs.chemmater.8b04051

3.1 Abstract

We report on the facile solid-state synthesis and characterization of Li_7SiPS_8, a new member of the tetragonal LGPS ($Li_{10}GeP_2S_{12}$)-type family of ultrafast Li^+ solid electrolytes. We analyze the structure, phase stability, as well as Li^+ conductivity of tetragonal and orthorhombic LSiPS by pulsed field gradient NMR and impedance spectroscopy, which show conductivities at RT of up to 2 $mScm^{-1}$. While ranking tetragonal LiSiPS as an ultrafast solid electrolyte, the observed conductivity is unexpectedly low compared to other members of this solid solution system. Utilizing solid-state NMR, quantitative phase analysis, and impedance spectroscopy we identify an amorphous thiophosphate side phase with low Si content, which limits the intergrain conductivity and, hence, a potentially higher total conductivity. This case study thus highlights the need for comprehensive structure analysis of LGPS-type materials beyond the crystalline fractions to fully characterize the structure - property relationships in these glass ceramic compounds.

3.2 Introduction

All-solid-state lithium ion batteries (ASSLiBs) have been identified as promising candidates for future mobile battery applications. This is due to inherent safety issues with conventional lithium-ion battery systems utilizing liquid electrolytes and the promise of a substantial gain in energy and power density as the application of ASSLiBs allows for much more compact setups in combination with lithium metal anodes.[1] The solid-state electrolytes (SSEs) used in these battery systems need to fulfill several important requirements. High ionic and low electronic conductivity are key prerequisites, along with high electrochemical and structural stability, as well as low production costs.[2] Regarding conductivity, some of the best solid state electrolytes are sulfides and were discovered just recently.[3–7] Their high conductivities as compared to most oxide SSEs is supposed to be due to the high polarizability of the sulfide ion enabling fast lithium movement and, at least for the thio-LISICON (lithium superionic conductor) family, a structure that is derived from a strongly distorted hexagonal close packed sulfur sub-lattice featuring many distorted face and edge sharing tetrahedral and octahedral voids, also facilitating lithium hopping.[8–10] Tetragonal $Li_{10}GeP_2S_{12}$ (lithium thiogermanate thiophosphate, LGPS) is one of the most promising thio-LISICON materials. It was first introduced by Mitsui *et al.* in 2011 and shown to exceed the conductivity values of the hitherto best crystalline lithium ion conductors by one order of magnitude.[7,11] The LGPS system can be described as a solid solution $Li_{11-x}\,Tt_{2-x}P_{1+x}S_{12}$ (L*Tt*PS) with *Tt* = Si, Ge, Sn. For a solid solution of lithium ortho tetrelates and phosphates a quasi-binary phase diagram can be established in the sense of $Li_4\,TtS_4$ - Li_3PS_4. The respective system with *Tt* = Ge was investigated by Kanno *et al.* showing that tetragonal LGPS undergoes a peritectic phase separation at temperatures exceeding 550 °C (823 K).[12] One of the products obtained by this decomposition is the solid solution $Li_{3+x}P_{1-x}Ge_xS_4$ which crystallizes homeotypically to the parent phases Li_4GeS_4 and Li_3PS_4 in the orthorhombic crystal system and exhibits a specific conductivity in the order of ~ 1 mS cm^{-1}.[13] Theoretical studies by Ceder *et al.*[14] for the tetragonal L*Tt*PS system predicted decreasing activation energies for the lithium ion diffusion process and increasing ionic conductivity in the series *Tt* = Sn→Ge→Si, which is in accordance with recent findings for the lithium diffusivity measured *via* NMR.[5,15] However, the ionic conductivity probed by electrochemical impedance spectroscopy (EIS) does not follow this trend for the $Li_{11-x}Si_{2-x}P_{1+x}S_{12}$ compounds. Some works on this system noticed the presence of small amounts of orthorhombic $Li_{3+x}P_{1-x}Si_xS_4$ as a side phase and and suggested that this compound likely impedes the measured total ionic conductivity.[8,16–18]

The first tetragonal LGPS-type material containing Si instead of Ge was synthesized by Kuhn *et al.* under high-pressure conditions as $Li_{11}Si_2PS_{12}$ with a higher tetrel content.[15] It crystallizes in the tetragonal space group $P4_2/nmc$ (no. 137) with $a = 8.6905(14)$ Å and $c = 12.5703(20)$ Å. The material showed the highest lithium ion diffusivity values compared to other tetragonal LGPS like material known at the time. Kanno *et al.* added two new members to the LSiPS family by conventional solid-state synthesis. The first one, $Li_{10.35}Si_{1.35}P_{1.65}S_{12}$, is closely related to the LSiPS compound presented in this work, the second one a chlorine-containing $Li_{9.54}Si_{1.74}P_{1.44}S_{11.7}Cl_{0.3}$, is the best lithium ion con-

ductor to date with a specific conductivity of 25 mS cm^{-1}.[4,8] However, LGPS-type materials containing Si, Ge, or Sn suffer from poor stability against metallic lithium due to the formation of electrically conducting lithium tetrelides promoting the reduction of the electrolyte material and ultimately short-circuiting the battery.[19,20] Zeier *et al.* proposed that utilizing glassy ceramic composites can be beneficial for the stability of these solid state electrolytes.[21] Yet, a glass phase with high impedance can also limit the performance of such materials shown recently in NASICON (sodium superionic conductor)-like $Li_{1-x}Ti_{2-x}Sc_x(PO_4)_3$.[22] In this paper, we report on the facile solid-state synthesis of Li_7SiPS_8, a new LGPS-like superionic conductor. It exhibits an overall ionic conductivity of 2 $mScm^{-1}$, which, while being fast in absolute terms, is unexpectedly low for this kind of electrolyte material. We show that conductivity is strongly impeded by one or more amorphous side phases remaining unrecognized in conventional powder X-ray analysis, rendering this material a glassy ceramic rather than a (fully) crystalline SSE.

3.3 Experimental procedure

3.3.1 Synthesis

Tetragonal (*tetra-*) and orthorhombic (*ortho-*) Li_7SiPS_8 (LSiPS) were prepared by heating Li_2S (Alfa Aesar, 99.9%), Si (Alfa Aesar, 99.999%), red P (Merck, 99%) and S (sublimed *in vacuo*) in stoichiometric amounts in a glassy carbon crucible sealed in a quartz glass ampoule under vacuum to 1223 K for 2 h. Subsequently, the ampoule was quenched in ice water and annealed for 5 d at 848, 823, 798, 773, or 748 K. Cooling rates of the samples after annealing showed no significant influence on side-phase formation and samples were therefore left in the oven after the end of the annealing program until the temperature was below 373 K. The resulting products were moisture-sensitive red or slightly yellow microcrystalline powders. All analytical procedures were therefore conducted in an argon-filled glovebox or in argon-filled sealed containers.

3.3.2 Powder X-ray diffraction

Powder X-ray diffraction (PXRD) experiments were carried out using a Stoe STADI P diffractometer (Mo-$K_{\alpha1}$ or Cu-$K_{\alpha1}$ radiation, Ge-(111) monochromator, Mythen 1 K Detector) in Debye-Scherrer geometry. All samples were sealed in glass capillaries with a diameter of 0.3 to 0.5 mm under argon. Subsequent Rietveld refinements were carried out with the program Topas Academic v. 5.[23] For determining phase purity and amorphous content by quantitative phase analysis, ball-milled silicon (Alfa Aesar, 99.999%) powder was added as an internal standard.

3.3.3 Single crystal X-ray diffraction

Single crystals were grown by slow-cooling of LSiPS melts from 1173 K to 873 K with 10 K/h in a glassy carbon crucible sealed in a quartz glass ampoule under argon. Crystals were then isolated under paraffin oil and sealed in glass capillaries under argon. Measurements were carried out with a STOE IPDS-II diffractometer using Mo-K_α radiation. The structure solution and refinement were performed with the programs SHELXS97 and SHELXL97, respectively.[24]

3.3.4 Solid-state NMR spectroscopy

Solid-state NMR spectra were measured on a BRUKER Avance III instrument at a magnetic field of $B_0 = 9.4\,T$. Magic-angle spinning (MAS) experiments were performed in ZrO_2 spinners at a spinning speed of 10 kHz using a Bruker 4 mm triple-channel probe. ^{29}Si and ^{31}P spectra were externally referenced to tetramethyl silane ($Si(CH_3)_4$, $\delta_{iso} = 0.0\ ppm$) or 85 % phosphoric acid (H_3PO_4, $\delta_{iso} = 0.0\ ppm$), respectively. ^{7}Li pulsed field gradient (PFG) diffusion NMR experiments utilized a diff60 single gradient diffusion probe allowing for pulsed field gradients g of up to 30 $T\ m^{-1}$ and temperatures up to 150 °C. The experiments used a stimulated echo pulse sequence.[25] The diffusion coefficient D was obtained by fitting the experimental echo attenuation curves $S(g, \delta, \Delta)$ by the Stejskal-Tanner equation: $S(g, \delta, \Delta) = -\gamma^2\delta^2 g^2 D(\Delta - \frac{\delta}{3})$,[26] where $\gamma = 1.398 \cdot 10^8\ Hz\ T^{-1}$ is the ^{7}Li gyromagnetic ratio, δ is the duration of the pulse field gradient g, and Δ is the time interval between field gradient pulses defining the diffusion time. Measurements were conducted at gradient strengths varying between 0.1 and 30 Tm^{-1}, fixed $\delta = 1.0\ ms$, and Δ varied between $10 - 100\ ms$.

3.3.5 Electrochemical impedance spectroscopy (EIS)

Electrochemical impedance spectroscopy and galvanostatic polarization measurements were performed with an IVIUM compactstat.h (24 bit instrument) in a two-electrode setup using a home-built impedance cell kept under argon atmosphere during all measurements. The applied rms AC voltage was 10 mV. The analysis of the impedance spectra was carried out with the RelaxIS software from rhd instruments. Before measuring, the samples were ground thoroughly and compacted to a pellet of about 1 mm thickness and 5 mm diameter by uniaxial cold pressing (500 MPa). For *ortho*-LSiPS a density of 94% and 88% for *tetra*-LSiPS was obtained. For impedance spectroscopy, the pellets were sandwiched between indium foil (ALFA AESAR, 0.127 mm thick, 99.99% (metals basis)) to enhance the contact with the measuring cells. No reaction between In and the samples were observed. For galvanostatic polarization measurements, the samples were sputtered on both sides with Pt.

3.3.6 Raman spectroscopy

Raman spectra were registered on a Jobin Yvon Typ V 010 labram single grating spectrometer, equipped with a double super razor edge filter and a Peltier-cooled CCD camera (Jobin Yvon). The incident Laser wavelength was 632 nm. All samples were measured after the PXRD measurements and therefore sealed in the same glass capillaries as described above.

3.3.7 Scanning electron microscopy and energy-dispersive X-ray spectroscopy

Elemental composition was determined by energy-dispersive X-ray spectroscopy (EDX; detector: Oxford Instruments Inca Energy) and an image of the morphology was obtained using a Jeol JSM 6500 F scanning electron microscope (SEM; field emission gun, acceleration voltage 20 kV).

3.4 Results and discussion

3.4.1 X-ray diffraction

The Si-derivative of tetragonal LGPS was obtained by pre-reaction of the precursors by melting of the samples, subsequent quenching and annealing, which was found to be key to minimize the amount of crystalline side phases. To study the influence of annealing temperature a series of samples was annealed at 25 K steps. All products of the annealing series were investigated using powder X-ray diffraction (PXRD). Samples quenched from 1223 K exhibit the orthorhombic LGPS (*ortho*-LGPS) structure (cf. Fig. 3.2).[13] Annealing temperatures exceeding 773 K are required to form tetragonal LGPS like Li_7SiPS_8 (*tetra*-LSiPS) which is confirmed by PXRD and subsequent Rietveld refinement (Fig. 3.1, left; Fig. 3.3).[7] Products annealed at 848 K and above show an increasing amount of *ortho*-LSiPS. On the XRD level no other phases could be detected. Time-dependent high-temperature PXRD measurements were conducted to study the phase transformation time needed to form *tetra*-LSiPS from *ortho*-LSiPS at 823 K. A complete transformation is visible after three hours (Fig. 3.1, right).
Single crystals grown from slow-cooling of LSiPS melts crystallize in the orthorhombic crystal system with space group *Pnma* (Nr. 62) with $a = 13.348(3)$ Å, $b = 7.9703(16)$ Å and $c = 6.1343(12)$ Å. The compound can be regarded as a solid solution of lithium ortho-thiophosphate and an ortho-thiosilicate. The topology of the crystal structure is similar to the ones of $\beta - Li_3PS_4$ and Li_4GeS_4 regarding the PS_4^{3-}/SiS_4^{4-} anion arrangement. However, the Lithium atom positions differ slightly.[27,28] This formation of a solid solution of Li_4SiS_4 and Li_3PS_4 was previously reported by Murayama *et al.*, yet no lithium positions were refined.[29]

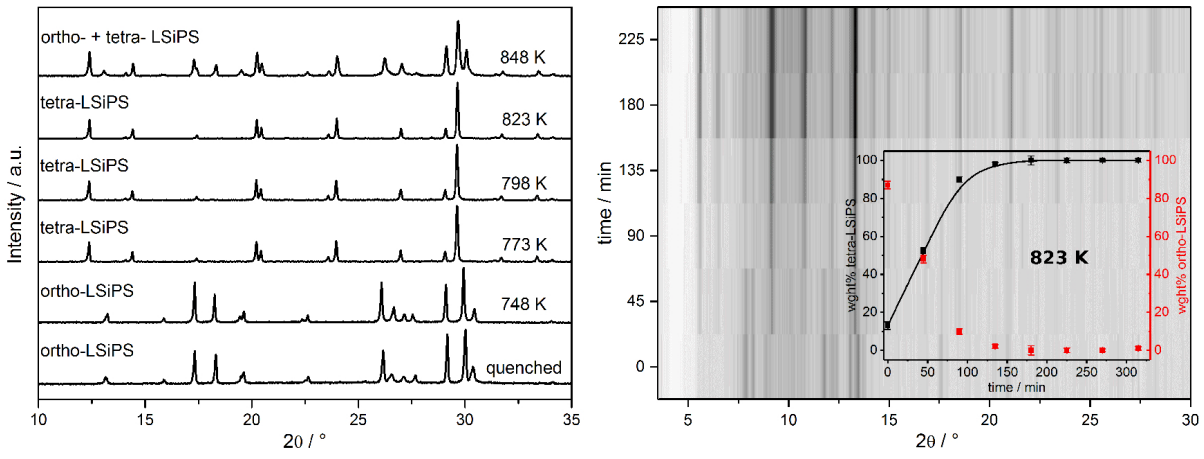

Figure 3.1: textitleft: PXRD measurements of the obtained products at indicated temperatures (radiation: Cu-$K_{\alpha 1}$); *right*: Time-dependent high temperature PXRD measurements of quenched *ortho*-LSiPS, inset graph shows the mass fraction of *tetra*-LSiPS (black) and *ortho*-LSiPS (red) plottet against time (radiation: Mo-$K_{\alpha 1}$, temperature: 823 K).

The crystal structure of *ortho*-LSiPS shows one crystallographically independent P site which is partially occupied by Si (50%) and tetrahedrally coordinated by four S atoms. The mixed occupancy influences the P-S distances of 2.07 - 2.09 Å to be slightly larger than that observed for $\beta - Li_3PS_4$ with 2.01 - 2.06 Å due to the larger cation radius of Si^{4+} (Si = 0.26 Å; P = 0.17 Å).[30] The Lithium cations are located between the PS_4 and SiS_4 tetrahedra, occupying tetrahedral and octahedral voids [LiS_4] and [LiS_6] with Li-S distances reasonable for their respective coordination sphere (cf. crystallographic information in SI). All Lithium positions are partially occupied, most likely due to the close proximity of these sites, giving rise to Coulombic repulsion. The topology of the crystal structure can be described as a distorted hexagonal closest packing of S atoms with Li and P/Si filling the tetrahedral voids and Li also filling half of the octahedral voids (cf. Fig. 3.2).

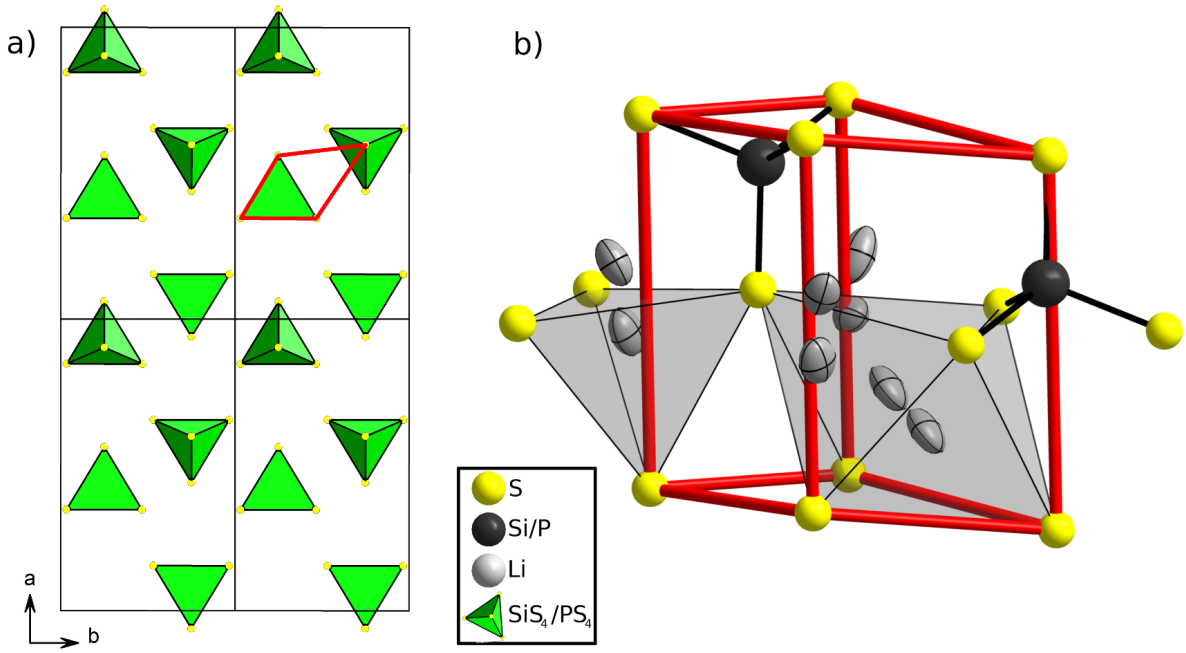

Figure 3.2: **(a)**: Structure of *ortho*-LSiPS (Li_7SiPS_8) viewed along the *c*-axis. Li atoms are omitted for better visibility. Black rectangles mark the unit cell, the red lines outline the pseudo-hexagonal unit cell of the underlying hcp (hexagonal close packing) of S atoms; **(b)**: Pseudo-hexagonal unit cell depicted in red with all atoms. Not all coordination polyhedra for Li are depicted for better visibility. Li-ellipsoids were drawn at 50% probability.

Rietveld refinement of the sample annealed at 823 K is shown in Fig. 3.3. *Tetra*-LSiPS crystallizes in the tetragonal space group $P4_2/nmc$ (no. 137) with $a = 8.6734(2)$ Å and $c = 12.5412(2)$ Å. Similar to *ortho*-LSiPS this compound is also a solid solution of lithium ortho-thiophosphate and an ortho-thiosilicate. However, it is partially ordered in respect to the PS_4/SiS_4 tetrahedra and is isotypic to tetragonal Li_7GePS_8.[6] The structure shows two crystallographically distinct P sites, both tetrahedrally coordinated by four S atoms. Shown by MAS NMR, the P1 ($4d$) site is partially occupied by Si causing a larger P-S distance of 2.11 - 2.12 Å than the P-S distances for the P2 ($2b$) site, which are very similar to those observed in Li_3PS_4 with 2.02 Å. The different P-S distances suggest a higher occupation by Si of the P1 site than observed in *ortho*-LSiPS and no mixed Si occupation for the P2 site, as corroborated by ^{31}P MAS NMR spectroscopy.

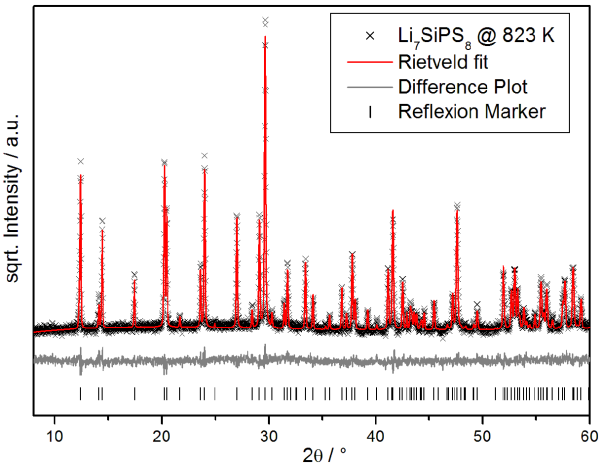

Figure 3.3: Rietveld refinement of *tetra*-LSiPS annealed at 823 K. The square root of the intensity is given for better visibility.

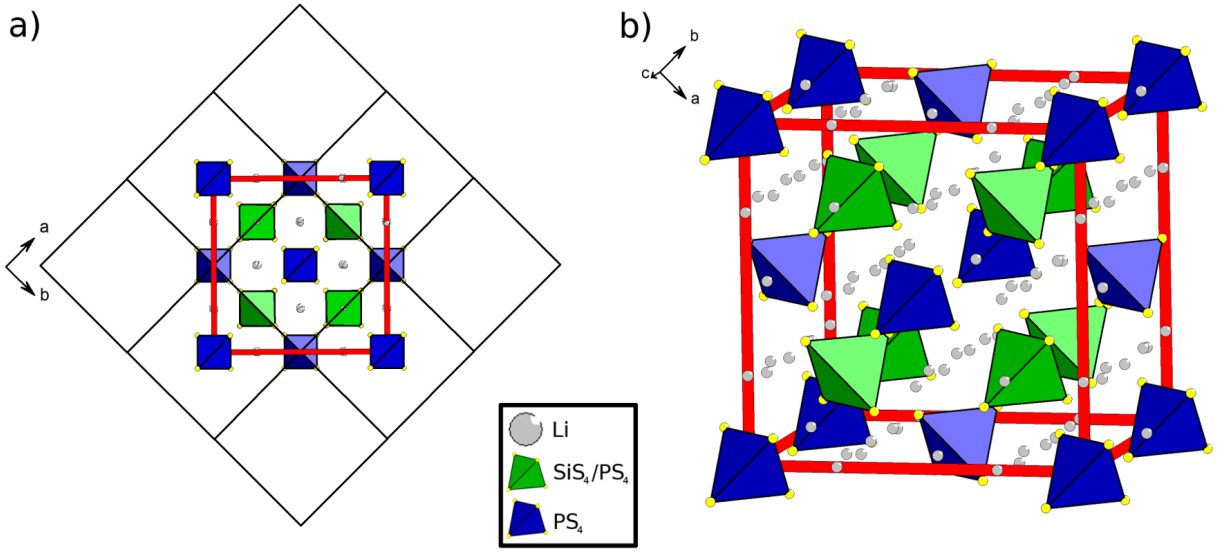

Figure 3.4: **(a)**: Structure of *tetra*-LSiPS (Li_7SiPS_8) viewed along the c-axis. Black squares mark the tetragonal primitive unit cell, the red square marks the underlying fcc (face-centered cubic) unit cell; **(b)**: Pseudo-cubic fcc unit cell marked by red lines.

Table 3.1: Crystallographic data and information about the Rietveld analysis for *tetra*-LSiPS tempered at 823 K. Standard deviations are given in parentheses.

	Li_7SiPS_8
Crystal system	tetragonal
Space group	$P4_2/nmc$, (Nr. 137)
Lattice constants [Å]	$a = 8.6734(2)$
	$c = 12.5412(2)$
Volume [Å^3]	943.44(6)
Formula units	4
Calculated density [gcm^{-3}]	1.923(9)
Diffractometer	*Stoe* STADI P, Debye-Scherrer geometry
	Cu-$K_{\alpha 1}$ radiation, Ge-(111) monochromator
Temperature [K]	295
Absorption coefficient [mm^{-1}]	14.794(1)
Refined 2θ region [°]	8.0 - 90.0
R_{exp}	12.21%
R_p	9.49%
R_{wp}	12.21%
Correction	absorption (geometric)
Number of independent parameters	41
Number of background parameters	6
GooF	1.001
R_{Bragg}	3.82%

This mixed occupancy of Si vs. P at the $4d$ site was not refined because of the similar atomic scattering factors. The two sets of isolated PS_4^{3-} and SiS_4^{4-} anions are connected by tetrahedrally and octahedrally coordinated Li^+ cations. These are only partially occupied with very small distances between the tetrahedrally coordinated Li atoms. The Li occupancy factors were constrained to obtain charge neutrality. However, the composition Li_7SiPS_8 was confirmed by EDX measurements (cf. SI table 9), and the smaller cell volume of this phase compared to $Li_{11}Si_2PS_{12}$ is in accordance with the assumption of a lower silicon content.[15] Selected crystallographic data from the Rietveld refinement is shown in Table 3.1 and additional information is given in the SI. The topology of the crystal structure of *tetra*-LSiPS can be described as a slightly distorted cubic structure (cf. Fig. 3.4). Considering the two sets of differently sized PS_4 tetrahedra, the structure is very similar to the CaF_2 structure-type with the smaller $P2S_4$ tetrahedra building a face centered cubic lattice and the bigger $P1S_4$ tetrahedra occupying all tetrahedral voids. Considering the completely different topologies of the crystal structures of *ortho*- and *tetra*-LSiPS a phase transition from the low-temperature phase (*tetra*-LSiPS) to the high-temperature phase (*ortho*-LSiPS) is supposed to be reconstructive. We assume this partial ordering of the PS_4/SiS_4 tetrahedra and the reconstruction of the sulfur sublattice is the reason for the high temperature and therefore high activation energy to form *tetra*-LSiPS from *ortho*-LSiPS.

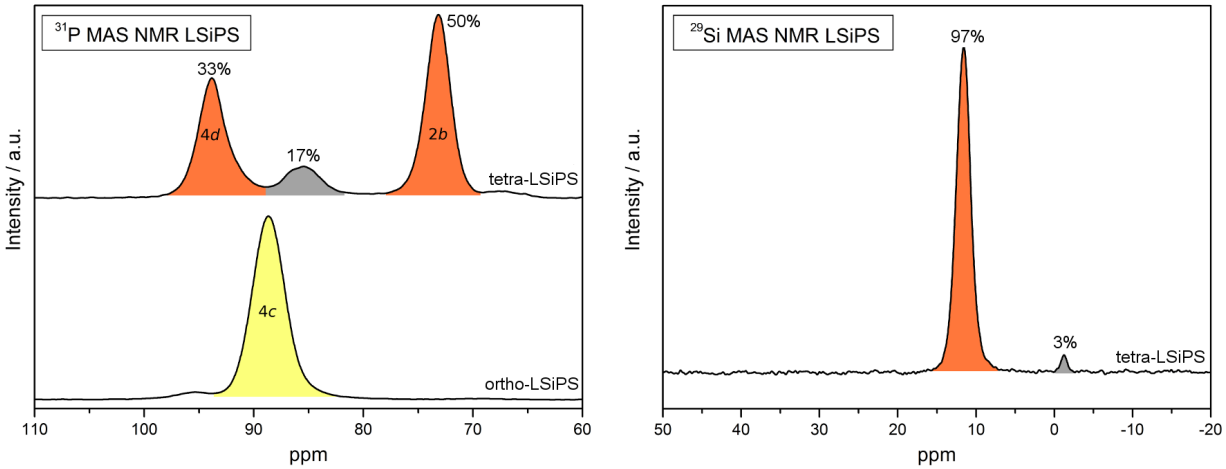

Figure 3.5: *left:* ^{31}P MAS NMR spectra of *ortho-* and *tetra*-LSiPS; right: ^{29}Si MAS NMR spectrum of *tetra*-LSiPS. Peaks were colored according to the respective phases (orange: *tetra*-LSiPS, yellow: *ortho*-LSiPS, grey: amorphous) and labeled according to the respective Wyckoff positions of the P atoms.

3.4.2 MAS NMR spectroscopy

Figure 3.5(left) shows the ^{31}P MAS NMR spectra of *tetra*-LSiPS and *ortho*-LSiPS, which also supports the silicon substitution on the 4*d* phosphorous site for *tetra*-LSiPS, similar to other tetragonal LGPS-type compounds. In addition to PXRD, NMR spectroscopy reveals detectable amounts of an unwanted phosphorus-containing side phase. A side phase with a similar chemical shift was reported for *tetra*-LGPS and previously attributed by us to small impurities of *ortho*-LGPS.[6] *ortho*-LSiPS shows a single peak with a slightly different chemical shift as compared to that of the observed side phase. However, the chemical shift of the observed side phase is in good accordance with values given by Zeier *et al.*[21] for orthorhombic β-Li_3PS_4. Further information on the composition of the unknown side phase is obtained by ^{29}Si MAS NMR. Assuming silicon substitution only on the 4*d* P site in the majority phase *tetra*-LSiPS, as is known for other LGPS phases,[15] only one peak in the ^{29}Si MAS NMR spectrum (Fig. 3.5, right) is expected. Yet a second peak is visible in the spectrum, which is attributed to the side phase. We therefore identify the side phase as a Si-doped ortho-thiophosphate with a local structure that is similar to β-Li_3PS_4. By ^{29}Si MAS NMR spectroscopy it was determined that 3 atom% of the overall silicon in the material is present in the side phase. Regarding the absence of Bragg reflections for this second phase, we assume *tetra*-LSiPS crystals to be embedded in an amorphous matrix, rendering this material a glass ceramic. The glass like appearance of the material in the SEM (cf. SI figure 1) further corroborates this assumption. However, a thorough analysis of the grains *via* electron microscopy was not possible due to severe damage when the material is exposed to the electron beam.

3.5 Quantitative phase analysis

The mass fraction of the amorphous side phase (Table 3.2) was calculated from signal intensities in ^{31}P MAS NMR spectra and Rietveld analysis with an internal standard (Si) on all samples containing *tetra*-LSiPS (cf. SI). Relative signal intensities in MAS NMR spectra were extracted by deconvolution of the measured spectra by pseudo Voigt functions. The obtained relative intensities correspond to atomic percent of the overall phosphorus content. Quantitative phase analysis by Rietveld refinement yields weight percentage values for the respective crystalline phases, which is at first sight not comparable with the results obtained from MAS NMR, since quantitative NMR yields information on the relative elemental content and, hence, atom%. Since the exact composition of the side phases is not known, a conversion to weight percent can be achieved by assuming it to be a thio-ortho-phosphate, which is reasonable due to the observed chemical shift and Si content being negligible. The mass fraction of the amorphous side phase(s) for all samples containing *tetra*-LSiPS were below 10%. Considering the respective errors the combined data of both methods reveal no discernible trend with the synthesis temperature. However, by quantifying the mass fraction of all phases present in the samples, we suggest the following formula of the side phase: $Li_{3.2}Si_{0.2}P_{0.8}S_4$. The fact that this amorphous phase is only present after annealing and formation of *tetra*-LSiPS and does not share the same stoichiometry with the crystalline phase could hint at a peritectic phase separation and partial melting of the sample, similar to tetragonal LGPS,[12] assuming that the amorphous side phase constitutes the solidified melt. This melt could also play a role in the phase transition of *ortho*-LSiPS to *tetra*-LSiPS by facilitating the crystallization of the tetragonal phase.

Table 3.2: Phase composition of various LSiPS samples determined by powder X-Ray diffraction with an internal standard (Si) and MAS NMR spectroscopy. The standard deviation is given in parentheses

Synthesis Temperature [K]	w% *tetra*-LSiPS	w% *ortho*-LSiPS	w% amorphous (XRD)	w% amorphous (NMR)
773	91.5(7)%	-	8.5(7)%	7(2)%
798	94.4(6)%	-	5.7(8)%	8(2)%
823	93(1)%	-	7(1) %	9(2)%
848	49.9(6)%	42.1(6)%	8(1)%	5(2)%

3.5.1 Pulsed field gradient NMR

Temperature-dependent pulsed field gradient (PFG) NMR spectroscopy was used to determine ^{7}Li diffusion coefficients and activation energies for lithium diffusion in LSiPS annealed at 823 K for 5 d. The two datasets (Fig. 3.6) were measured with the spacings between the gradient pulses Δ_{NMR} of 10 and 100 ms, yielding shorter diffusion lengths at reduced diffusion time. In a first approximation, the probed diffusion length can be estimated by calculating the isotropic diffusion radius: $r_{rms} = \sqrt{2D^{tr}_{NMR}\Delta_{NMR}}$,[31] resulting in values of the same order of magnitude ($r_{rms} \approx 200\ nm$) for both measurements at room temperature. This hints at a fast diffusion process confined in small domains. Taking into account that the crystalline phase should exhibit the higher ionic conductivity,[29] and considering the mean grain size of a ground material is in the order of a few μm, we assume the isotropic diffusion radius to be the mean crystallite size. The increased ion diffusivity and reduced activation energy for shorter diffusion times hints at a mixed intra- and intergrain diffusion process which is in agreement with our structural model of a highly ion conductive material embedded in a less conductive amorphous matrix. Conductivity values at room temperature were calculated from PFG NMR ($\Delta = 10\ ms$) and Rietveld data with the Nernst-Einstein equation: $\sigma_{NMR} = \frac{D^{tr}_{NMR} n z^2 e^2}{k_B T}$, where σ_{NMR} is the conductivity derived from diffusion coefficients D^{tr}_{NMR} determined by PFG NMR spectroscopy, n is the concentration of charge carriers, z the charge of charge carriers, e the elementary charge, k_B the Boltzmann constant and T temperature. Assuming uncorrelated lithium motion and that the Li2 site does not contribute to the conductivity mechanism at room temperature, which was discussed in several earlier works for tetragonal LGPS,[14,32–36] 17 lithium atoms per unit cell are available, resulting in a calculated conductivity value σ_{NMR} at room temperature of $5 \pm 1\ mS\ cm^{-1}$. With a Haven ratio $D^{tr}_{NMR}/D^{\sigma} = H_R$ of 1 (D^{tr}_{NMR}: tracer diffusion coefficient from PFG NMR, D^{σ}: conductivity diffusion coefficient, H_R: Haven ratio), this value can be considered a lower limit for the diffusivity of the crystalline phase, since other LGPS-like materials show a strongly correlated jump process of the cation sublattice and therefore Haven ratios smaller than 1, which would imply an even higher charge diffusion coefficient and therefore conductivity value.[37] Additionally, the process probed by PFG NMR even at short pulse spacings may be a mixed intra- and intergrain lithium diffusion which would also imply that the obtained value can be even higher if the diffusion is still limited by

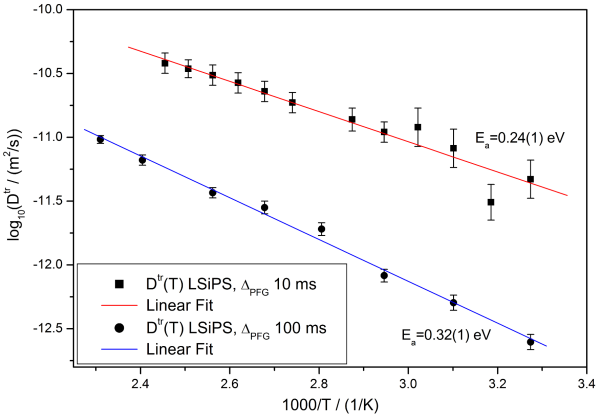

Figure 3.6: PFG NMR measurements of *tetra*-LSiPS annealed at 823 K. Two different diffusion times, defined by the time between the gradient pulses Δ_{NMR} were employed to probe diffusion processes at shorter (10 ms) and longer (100 ms) ranges.

grain-boundaries or side phases in the calculated radius of approximately 200 nm.

3.5.2 Electrochemical impedance spectroscopy (EIS)

Lithium-ion conductivities of *ortho*- and *tetra*-LSiPS were determined in a blocking-electrode configuration by EIS in the frequency range between 1 MHz and 0.01 Hz. The impedance spectra of low-temperature measurements were analyzed in terms of an equivalent circuit analysis. DC galvanostatic polarization measurements indicate only a negligible amount of electronic conductivity contributing to the overall conductivity for both phases (cf. SI figure 5). Thus, they can be treated as predominantly ionic conductors.

In Figure 3.7, the complex impedance spectrum of *ortho*-LSiPS, measured at -60°C, exhibits two slightly depressed semicircles at high- and mid-frequencies and a clear polarization spike at low frequencies. The spectrum was modeled with a serial connection of two parallel arrangements of a resistor (R) and a constant phase element (CPE), representing the conductive and capacitive behavior of the solid ionic conductor, respectively.[38,39] The polarization is modeled by an additional CPE.[38,39] In general, a CPE accounts for a dispersion of relaxation times, caused by e.g. surface roughness of the sample or electrodes, or by non-uniform current distribution in the sample.[40] The impedance of this empirical parameter is given by $Z_{CPE} = \frac{1}{Q(j\omega)^{\alpha}}$.[41]

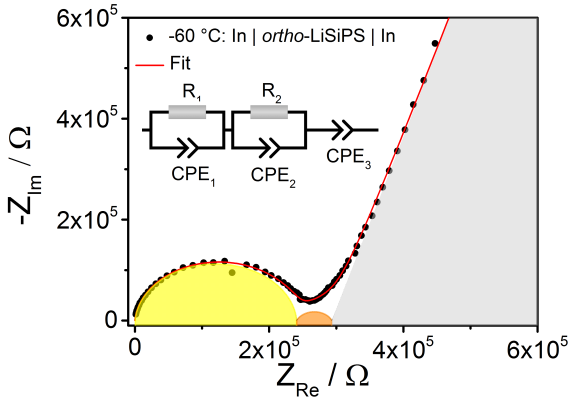

Figure 3.7: The low-temperature EIS of *ortho*-LSiPS shows two slightly depressed semicircles and was fit with the model given in the inset.

Where Q is the CPE's admittance value, j is $\sqrt{-1}$, ω is the angular frequency and α is the CPE's exponential factor. If the CPE is connected in parallel to a resistance, an effective capacitance C_{eff} can be calculated by the Brug formula $C_{eff} = Q^{\frac{1}{\alpha}} R^{(\frac{1}{\alpha}-1)}$.[42,43] The high frequency arc in Figure 3.7 (yellow) has a capacitance in the 10 pF range, thus probably stemming from the bulk properties of the material.[15,38] The bulk conductivity is calculated as the inverse of the resistance R_1, the total sample thickness (L) and the surface area of the electrodes (A): $\sigma = \frac{L}{AR}$.[42,44] As shown in Figure 3.8b, the activation energy of the bulk process is 0.29 eV. The mid-frequency arc (orange) has a similar activation energy and a capacitance in the nF range, thus about three orders of magnitude higher than the grain capacitance. This is typical for geometrical current constriction at grain-to-grain contacts due to the moderate compactness of the sample of 94%.[45] At room temperature, both processes overlap and *ortho*-LSiPS exhibits a total ionic conductivity of 0.13 $mS\ cm^{-1}$. The total conductivity at room temperature and activation energy are comparable to the findings of Murayama *et al.*[29] for the solid solution series of $Li_{4-x}Si_{1-x}P_xS_4$ ($x = 0 - 0.8$).

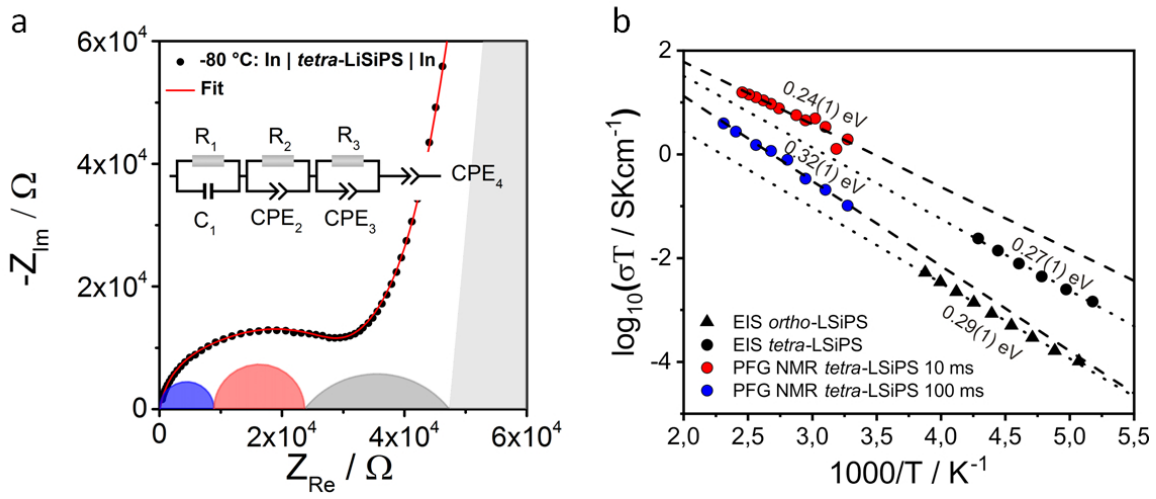

Figure 3.8: **(a)** Low-temperature EIS of *tetra*-LSiPS modeled by four processes attributed to grain boundary processes (R_1C_1, R_2CPE_2, and R_3CPE_3) and electrode polarization (CPE_4); **(b)** Arrhenius plot comparing of the total conductivity of R_1+R_2+R_3 of *tetra*-LSiPS yielding an activation energy of 0.27 eV with the respective activation energies obtained by PFG NMR and of *ortho*-LSiPS.

The low-temperature spectrum of cold-pressed *tetra*-LSiPS in Figure 3.8 is much more distorted than the spectrum of cold-pressed *ortho*-LSiPS. Sintering of the pellets was not possible due to decomposition reactions as reported previously.[15,16,18] The data were fit by the model given in Figure 3.8 containing four different contributions. The capacitances of the blue and red semicircles range from 0.2 to 0.7 nF, respectively. The capacitance of the grey semicircle is higher by one order of magnitude (7 nF). Those values are in the typical range for grain boundary processes.[6,18,45] The resistances (R_1, R_2, R_3) are all on the same order of magnitude and the activation energies for the single processes in the model are all very similar $(0.25 - 0.29$ eV) with an activation energy of the total conductivity of 0.27 eV. Thus, a clear distinction of the bulk process from other contributions is difficult. Such contributions for instance stem from (highly resistive) grain boundaries, geometrical current constriction effects and the presence of a second ion conducting phase that considerably complicates the analysis as reported for the presence of an orthorhombic by-phase in $Li_{10}SiP_2S_{12}$.[18,40,45] Notably, no extremely high activation energy pointing to a highly resistive grain boundary layer was observed. Besides, current constriction originating for example from a small contact area between the grains caused by low compactness of the cold-pressed powder (about 88%), or by a less conductive second phase at the grain boundary, could contribute to the spectrum. Derived from $\frac{R_x}{R_1} = \frac{\sqrt{\frac{\alpha_{max}}{\alpha}}-1}{1+\frac{1}{2}\sqrt{\frac{\alpha}{\alpha_{max}}}}$ with $R_x = R_2$ the average fraction of contacted area between the grains α is estimated to be about 14% and with $R_x = R_3$ only 6%.[45] For comparison, assuming the low frequency semicircle in *ortho*-LSiPS arises from current constriction effects, a much larger fraction of contact area

of 56% is obtained. However, the compactness of *ortho*-LSiPS is similar to the compactness of *tetra*-LSiPS. Thus, the small fraction of contact area in *tetra*-LSiPS suggests that the ion transport is likely limited by an effect that significantly reduces the contact area between the grains. This observation is in line with an ionic conductor that is embedded in a less conducting amorphous matrix. For a more in-depth analysis a model with more precise information about the complete microstructure of the glassy ceramic would be necessary. Yet, cross section images by focused ion beam (FIB) and transmission electron microscopy (TEM) could not be obtained for this material due to substantial beam damage during the measurements.

At temperatures above 0 °C, only one semicircle can be observed for *tetra*-LSiPS (cf. SI Fig. 7). The total ionic conductivity at room temperature of the new *tetra*-Li_7SiPS_8 is about 2 mS cm^{-1} (cf. SI Figure 7). This is very similar to the conductivity of tetragonal $Li_{10}SiP_2S_{12}$[16,18] and distinctly higher than the conductivity of the orthorhombic phase with 0.13 mS cm^{-1}. The activation energy of the total conductivity of 0.27 eV is on the same order of magnitude as the activation energy obtained by PFG NMR (cf. Figure 3.8). The activation energies of $Li_{10}SiP_2S_{12}$ were between 0.20 eV[16] and 0.30 eV,[18] and thus again similar to *tetra*-LSiPS. Unfortunately hitherto, tetragonal LGPS-like LSiPS compounds except high pressure $Li_{11}Si_2PS_{12}$[15] have not reached the high specific conductivity of more than 10 mS cm^{-1} proposed by Ceder *et al.*.[14] while in tetragonal $Li_{10}SiP_2S_{12}$[18] the presence of the orthorhombic modification increases the impedance. This work suggests that in *tetra*-LSiPS an amorphous side phase is at the heart of a higher than expected impedance in this glass ceramic material.

3.6 Conclusion

We have introduced tetragonal Li_7SiPS_8 as a new member of the LGPS-type family of superionic conductors. The material was obtained by solid-state synthesis at ambient pressure. Using a combination of PXRD and NMR, we have shown that tetragonal Li_7SiPS_8 is a glass-ceramic rather than a fully crystalline material, since at least one amorphous side phase is present at all explored temperatures. This side phase does not share the same stoichiometry with the crystalline phase, suggesting a peritectic phase separation of the tetragonal phase similar to tetragonal LGPS.[12] Since tetragonal LGPS shows a higher decomposition temperature, this would indicate that the silicon containing phase presented here is less stable than the one with the heavier homologue Ge at elevated temperatures. The fact that the amorphous side phase is very hard to detect suggests that it may be ubiquitous in this family of compounds and also limit the performance of other LGPS-type compounds. This calls for characterization of LGPS-like materials by methods which are sensitive not only to crystalline phases, but also to amorphous fractions, such as solid-state NMR spectroscopy.

Author Contributions

SH, CoH and BVL conceived and designed this study; SH conducted the synthesis, measured PXRD and performed Rietveld analysis; SH and AKH were responsible for measuring EIS; AKH analysed measured EIS data; IM performed ssNMR spectroscopy; SH and IM analysed obtained ssNMR data; RE and AK were responsible for growing single crystals of *ortho*-LSiPS; AK performed the structure determination from SCXRD data; CoH helped in interpretation of crystal structure data; SH and AKH wrote sections of the manuscript; All authors wrote and commented on the manuscript.

3.7 Acknowledgement

We like to thank Christian Minke for his assistance in collecting SEM/EDX data. Financial support was granted by the German Federal Ministry of Research and Education (BMBF), project 03XP0177B.

3.8 Assotiated content

The Supporting Information is available free of charge on the ACS Publications website at DOI: 10.1021/acs.chemmater.8b04051.
Crystallographic data, EDX analysis, SEM micrographs, quantitative phase analysis, Raman spectroscopy, estimation of the electronic contribution to the conductivity, comparison of different fitting models for the impedance spectrum of *tetra*-LSiPS at -80°C, room-temperature EIS measurements of *tetra*-LSiPS.

Bibliography

(1) Goodenough, J. B. Rechargeable batteries: challenges old and new. *J. Solid State Electrochem.* **2012**, *16*, 2019–2029.

(2) Lotsch, B. V.; Maier, J. Relevance of solid electrolytes for lithium-based batteries: A realistic view. *J. Electroceram.* **2017**, *38*, 128–141.

(3) Holzmann, T.; Schoop, L. M.; Ali, M. N.; Moudrakovski, I.; Gregori, G.; Maier, J.; Cava, R. J.; Lotsch, B. V. $Li_{0.6}[Li_{0.2}Sn_{0.8}S_2]$ - a layered lithium superionic conductor. *Energy Environ. Sci.* **2016**, *9*, 2578–2585.

(4) Kato, Y.; Hori, S.; Saito, T.; Suzuki, K.; Hirayama, M.; Mitsui, A.; Yonemura, M.; Iba, H.; Kanno, R. High-power all-solid-state batteries using sulfide superionic conductors. *Nat. Energy* **2016**, *1*, 16030.

(5) Bron, P.; Johansson, S.; Zick, K.; Schmedt auf der Günne, J.; Dehnen, S.; Roling, B. $Li_{10}SnP_2S_{12}$: An Affordable Lithium Superionic Conductor. *J. Am. Chem. Soc.* **2013**, *135*, 15694–15697.

(6) Kuhn, A.; Duppel, V.; Lotsch, B. V. Tetragonal $Li_{10}GeP_2S_{12}$ and Li_7GePS_8 – exploring the Li ion dynamics in LGPS Li electrolytes. *Energy Environ. Sci.* **2013**, *6*, 3548.

(7) Kamaya, N.; Homma, K.; Yamakawa, Y.; Hirayama, M.; Kanno, R.; Yonemura, M.; Kamiyama, T.; Kato, Y.; Hama, S.; Kawamoto, K.; Mitsui, A. A lithium superionic conductor. *Nat. Mater.* **2011**, *10*, 682–686.

(8) Hori, S.; Taminato, S.; Suzuki, K.; Hirayama, M.; Kato, Y.; Kanno, R. Structure-property relationships in lithium superionic conductors having a $Li_{10}GeP_2S_{12}$-type structure. *Acta Crystallogr. Sect. B Struct. Sci. Cryst. Eng. Mater.* **2015**, *71*, 727–736.

(9) West, A. R.; Bruce, P. G. Tetragonal-Packed Crystal Structures. *Acta Crystallogr.* **1982**, *38*, 1891–1896.

(10) Wang, Y.; Richards, W. D.; Ong, S. P.; Miara, L. J.; Kim, J. C.; Mo, Y.; Ceder, G. Design principles for solid-state lithium superionic conductors. *Nat. Mater.* **2015**, *14*, 1026–1031.

(11) Kuhn, A.; Köhler, J.; Lotsch, B. V. Single-crystal X-ray structure analysis of the superionic conductor $Li_{10}GeP_2S12$. *Phys. Chem. Chem. Phys.* **2013**, *15*, 11620.

(12) Hori, S.; Kato, M.; Suzuki, K.; Hirayama, M.; Kato, Y.; Kanno, R. Phase Diagram of the Li_4GeS_4 – Li_3PS_4 Quasi-Binary System Containing the Superionic Conductor $Li_{10}GeP_2S_{12}$. *J. Am. Ceram. Soc.* **2015**, *98*, ed. by Sprenkle, V., 3352–3360.

(13) Kanno, R.; Murayama, M. Lithium Ionic Conductor Thio-LISICON: The Li_2S - GeS_2 - P_2S_5 System. *J. Electrochem. Soc.* **2001**, *148*, A742.

(14) Ong, S. P.; Mo, Y.; Richards, W. D.; Miara, L.; Lee, H. S.; Ceder, G. Phase stability, electrochemical stability and ionic conductivity of the $Li_{10\pm1}MP_2X_{12}$ (M = Ge, Si, Sn, Al or P, and X = O, S or Se) family of superionic conductors. *Energy Environ. Sci.* **2013**, *6*, 148–156.

(15) Kuhn, A.; Gerbig, O.; Zhu, C.; Falkenberg, F.; Maier, J.; Lotsch, B. V. A new ultrafast superionic Li-conductor: ion dynamics in $Li_{11}Si_2PS_{12}$ and comparison with other tetragonal LGPS-type electrolytes. *Phys. Chem. Chem. Phys.* **2014**, *16*, 14669–14674.

(16) Whiteley, J. M.; Woo, J. H.; Hu, E.; Nam, K.-W.; Lee, S.-H. Empowering the Lithium Metal Battery through a Silicon-Based Superionic Conductor. *J. Electrochem. Soc.* **2014**, *161*, A1812–A1817.

(17) Kato, Y.; Saito, R.; Sakano, M.; Mitsui, A.; Hirayama, M.; Kanno, R. Synthesis, structure and lithium ionic conductivity of solid solutions of $Li_{10}(Ge_{1-x}M_x)P_2S_{12}$ (M = Si, Sn). *J. Power Sources* **2014**, *271*, 60–64.

(18) Bron, P.; Dehnen, S.; Roling, B. $Li_{10}Si_{0.3}Sn_{0.7}P_2S_{12}$ – A low-cost and low-grain-boundary-resistance lithium superionic conductor. *J. Power Sources* **2016**, *329*, 530–535.

(19) Wenzel, S.; Randau, S.; Leichtweiß, T.; Weber, D. A.; Sann, J.; Zeier, W. G.; Janek, J. Direct Observation of the Interfacial Instability of the Fast Ionic Conductor $Li_{10}GeP_2S12$ at the Lithium Metal Anode. *Chem. Mater.* **2016**, *28*, 2400–2407.

(20) Zhu, Y.; He, X.; Mo, Y. First principles study on electrochemical and chemical stability of solid electrolyte-electrode interfaces in all-solid-state Li-ion batteries. *J. Mater. Chem. A* **2016**, *4*, 3253–3266.

(21) Dietrich, C.; Sadowski, M.; Sicolo, S.; Weber, D. A.; Sedlmaier, S. J.; Weldert, K. S.; Indris, S.; Albe, K.; Janek, J.; Zeier, W. G. Local Structural Investigations, Defect Formation, and Ionic Conductivity of the Lithium Ionic Conductor $Li_4P_2S_6$. *Chem. Mater.* **2016**, *28*, 8764–8773.

(22) Kahlaoui, R.; Arbi, K.; Sobrados, I.; Jimenez, R.; Sanz, J.; Ternane, R. Cation Miscibility and Lithium Mobility in NASICON $Li_{1+x}Ti_{2-x}Sc_x(PO_4)_3$ ($0 \leq x \leq 0.5$) Series: A Combined NMR and Impedance Study. *Inorg. Chem.* **2017**, *56*, 1216–1224.

(23) Coelho, A. A. Topas Academic, 2012.

(24) Sheldrick, G. M. A short history of SHELX. *Acta Crystallogr. Sect. A Found. Crystallogr.* **2008**, *64*, 112–122.

(25) Tanner, J. E. Use of the Stimulated Echo in NMR Diffusion Studies. *J. Chem. Phys.* **1970**, *52*, 2523–2526.

(26) Stejskal, E. O.; Tanner, J. E. Spin Diffusion Measurements: Spin Echoes in the Presence of a Time-Dependent Field Gradient. *J. Chem. Phys.* **1965**, *42*, 288–292.

(27) Mercier, R.; Malugani, J.-P.; Fahys, B.; Robert, G.; Douglade, J. Structure du tetrathiophosphate de lithium. *Acta Crystallogr. Sect. B Struct. Crystallogr. Cryst. Chem.* **1982**, *38*, 1887–1890.

(28) Matsushita, Y.; Kanatzidis, M. G. Synthesis and Structure of Li_4GeS_4. *Z. Naturforsch. B* **1998**, *53*, 23–30.

(29) Murayama, M. Synthesis of New Lithium Ionic Conductor Thio-LISICON—Lithium Silicon Sulfides System. *J. Solid State Chem.* **2002**, *168*, 140–148.

(30) Shannon, R. D. Revised effective ionic radii and systematic studies of interatomic distances in halides and chalcogenides. *Acta Crystallogr. Sect. A* **1976**, *32*, 751–767.

(31) Einstein, A. Investigations on the theory of the Brownian motion. *Ann. d. Phys.* **1905**, 549.

(32) Kwon, O.; Hirayama, M.; Suzuki, K.; Kato, Y.; Saito, T.; Yonemura, M.; Kamiyama, T.; Kanno, R. Synthesis, structure, and conduction mechanism of the lithium superionic conductor $Li_{10+\delta}Ge_{1+\delta}P_{2-\delta}S_{12}$. *J. Mater. Chem. A* **2015**, *3*, 438–446.

(33) Mo, Y.; Ong, S. P.; Ceder, G. First Principles Study of the $Li_{10}GeP_2S_{12}$ Lithium Super Ionic Conductor Material. *Chem. Mater.* **2012**, *24*, 15–17.

(34) Liang, X.; Wang, L.; Jiang, Y.; Wang, J.; Luo, H.; Liu, C.; Feng, J. In-Channel and In-Plane Li Ion Diffusions in the Superionic Conductor $Li_{10}GeP_2S_{12}$ Probed by Solid-State NMR. *Chem. Mater.* **2015**, *27*, 5503–5510.

(35) Weber, D. A.; Senyshyn, A.; Weldert, K. S.; Wenzel, S.; Zhang, W.; Kaiser, R.; Berendts, S.; Janek, J.; Zeier, W. G. Structural Insights and 3D Diffusion Pathways within the Lithium Superionic Conductor $Li_{10}GeP_2S_{12}$. *Chem. Mater.* **2016**, *28*, 5905–5915.

(36) Krauskopf, T.; Culver, S. P.; Zeier, W. G. Bottleneck of Diffusion and Inductive Effects in $Li_{10}Ge_{1-x}Sn_xP_2S_{12}$. *Chem. Mater.* **2018**, *30*, 1791–1798.

(37) Marcolongo, A.; Marzari, N. Ionic correlations and failure of Nernst-Einstein relation in solid-state electrolytes. *Phys. Rev. Mater.* **2017**, *1*, 025402.

(38) Irvine, J. T. S.; Sinclair, D. C.; West, A. R. Electroceramics: Characterization by Impedance Spectroscopy. *Adv. Mater.* **1990**, *2*, 132–138.

(39) Lasia, A. In *Mod. Asp. Electrochem.* Kluwer Academic Publishers: Boston, 2002, pp 143–248.

(40) Macdonald, J. R.; Johnson, W. B. In *Impedance Spectrosc.* John Wiley & Sons, Inc.: Hoboken, NJ, USA, 2005, pp 1–26.

(41) Raistrick, I. D.; Franceschetti, D. R.; Macdonald, J. R. In *Impedance Spectrosc.* John Wiley & Sons, Inc.: Hoboken, NJ, USA, 2005, p 36.

(42) Lvovich, V. F., *Impedance Spectroscopy*; John Wiley & Sons, Inc.: Hoboken, NJ, USA, 2012.

(43) Brug, G.; van den Eeden, A.; Sluyters-Rehbach, M.; Sluyters, J. The analysis of electrode impedances complicated by the presence of a constant phase element. *J. Electroanal. Chem. Interfacial Electrochem.* **1984**, *176*, 275–295.

(44) Gao, W.; Sammes M., S., *An Introduction to Electronic and Ionic Materials*; World Scientific: 1999.

(45) Fleig, J.; Maier, J. Finite-Element Calculations on the Impedance of Electroceramics with Highly Resistive Grain Boundaries: I, Laterally Inhomogeneous Grain Boundaries. *J. Am. Ceram. Soc.* **1999**, *82*, 3485–3493.

Chapter 4

Chemical modification on *tetra*-LSiPS

4.1 Aliovalent substitution in *tetra*-$Li_{7+x}Si_{1-x}Al_xPS_8$

Sascha Harm, Anna-Katharina Hatz, Carla Hoefer, Max Plaß, Bettina V. Lotsch

Published in: *unpublished results*

In this section the results of the aliovalent substitution attempts on *tetra*-LSiPS to form $Li_{7+x}Si_{1-x}Al_xPS_8$ are presented. Substitution of Si^{+IV} by Al^{+III} is supposed to increase the lithium content of the compound and therefore to increase charge carrier density and decrease the activation energy of lithium hopping by providing a bigger more polarizable anion. Both the increase in charge carrier density and the decrease in activation energy should positively impact the ionic conductivity of this solid solution series (cf. chapter 1.3). This assumption is also corroborated by *ab initio* molecular dynamics (AIMD) simulations performed by Ceder *et al.*, showing that a substitution of the tetrel atom in the tetragonal LGPS structure by aluminum would both increase the ionic conductivity and decrease the activation energy of the resulting compound.[1] This work shows that a substitution of silicon by aluminum in *tetra*-LSiPS can be achieved, however, only up to $x = 0.15$ in $Li_{7+x}Si_{1-x}Al_xPS_8$ with retention of a homogenous phase. Furthermore, a decrease in total conductivity from $2 \cdot 10^{-3}\,S\,cm^{-1}$ to $4 \cdot 10^{-4}\,S\,cm^{-1}$ was observed for samples with $x \geq 0.10$ which is attributed to a compositional change of the amorphous side phase observed in unsubstituted *tetra*-LSiPS (cf. chapter 3).

4.1.1 Experimental procedure

If not stated otherwise, the experimental procedures, sample and data handling was similar as stated in chapter 3.

Synthesis

Stoichiometric amounts of Li_2S (Alfa Aesar, 99.9%), Si (Alfa Aesar, 99.999%), Al_2S_3 (Alfa Aesar, 99.9%), red P (Merck, 99%) and S (sublimed *in vacuo*) were thoroughly ground in an agate mortar and filled in glassy carbon crucibles. The powder was compacted by a steel rod, sealed in quartz glass ampoules under vacuum and heated to 950 °C at a heating rate of 50 °C h^{-1}. The ampoules were then quenched in ice water and annealed at 525 °C for five days. The resulting samples were extremely moisture sensitive orange to yellow powders. All sample handling was performed in an argon filled glovebox.

Electrochemical Impedance Spectroscopy

For electrochemical impedance spectroscopy (EIS) measurements the samples were ground thoroughly and compacted to a pellet of about 0.5 mm thickness and 5 mm diameter by uniaxial cold pressing (500 MPa). For EIS, the pellets were put in between two indium foil sheets (Alfa Aesar, 0.127 mm thick, 99.99%) to enhance the contact with the stainless steel electrodes of the cells. No reaction between In and the samples was observed. EIS measurements were performed with an Ivium compactstat.h (24 bit instrument) in a two-electrode setup using a rhd Instruments Microcell HC cell stand loaded with rhd Instruments TSC Battery cells performing measurements between 25 °C and −20 °C inside a glovebox under argon atmosphere. The spectra were recorded in a frequency range of 1 MHz - 0.1 Hz and an applied rms AC voltage of 10 mV. The analysis of the impedance spectra was carried out with the RelaxIS3 software from rhd Instruments. The linearity, stability and causality was checked by applying the Kramers-Kronig-relation before fitting the data.

The measurement uncertainties arise from the error propagation of the uncertainties in pellet thickness, area and in obtained resistance.

Solid-state Nuclear Magnetic Resonance Spectroscopy

Solid-state NMR spectra were measured on a Bruker Avance III 500 instrument at a magnetic field of $B_0 = 11.74\ T$. Magic-angle spinning (MAS) experiments were performed in zirconia spinners at a spinning speed of 10 kHz using a Bruker 4 mm triple-channel probe. ^{27}Al, ^{29}Si and ^{31}P spectra were referenced indirectly to ^{1}H in 0.1% TMS at 0.00 ppm.

Bond Valence Energy Landscape Calculations

Bond valence energy landscape (BVEL) calculations were performed with the program 3Dbvsmapper.[2] The cutoff distance was fixed to a maximum value of 8 Å. The images were created with VESTA.[3]

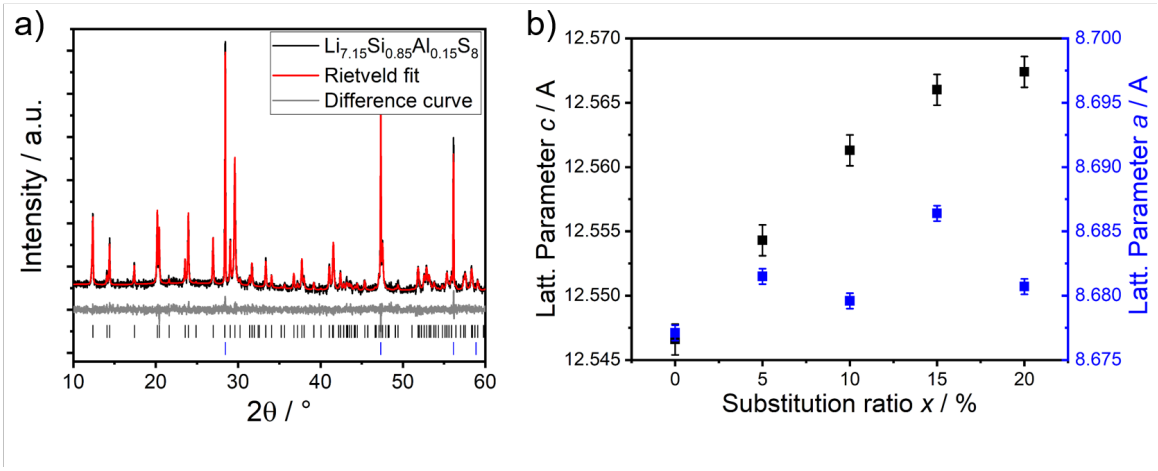

Figure 4.1: **a**: Exemplary Rietveld refinement on the substitution series $Li_{7+x}Si_{1-x}Al_xPS_8$ with $0 \leq x \leq 0.2$. Black and blue vertical lines depict reflection markers of *tetra*-LSiPS and silicon respectively; **b**: Dependance of the lattice parameters a and c in tetragonal $Li_{7+x}Si_{1-x}Al_xPS_8$ on the substitution ratio x obtained by Rietveld refinement with Si as an internal standard.

4.1.2 Results and Discussion

Powder X-ray diffraction

Powder X-ray diffraction data reveal that samples with a substitution ratio of $x = 0.2$ show the appearance of additional side phases, mostly Li_7PS_6, which is accompanied by a decrease in conductivity (cf. 4.1.2). It was expected that even higher substitution ratios would give similar results as in the aliovalent substitution series $Li_{10+x}Ge_{1-x}Al_xP_2S_{12}$ performed by Amaresh *et al.*,[4] who showed that higher substitution ratios give an increasing amount of side phases decreasing the conductivity. Therefore, higher substitution ratios than $x = 0.2$ were not studied.

However, the PXRDs of samples with $x \leq 0.15$ show only reflections of *tetra*-LSiPS. Rietveld refinements on these samples including silicon powder as an internal standard reveal a linear dependence of the c lattice parameter on the substitution ratio x (Fig. 4.1). The lattice parameter a however shows a rather erratic dependence hinting at a more complex behaviour of the system than was observed for the substitution of silicon by aluminum in $Na_{4+x}Si_{1-x}Al_xS_4$ (cf. chapter 5). Although, the dependence of the volume on the substitution value x is not strictly linear and therefore not Vegard-like,[5] the overall trend is an increase in volume, hinting at a successful substitution.

Nuclear magnetic resonance spectroscopy

To confirm the assumption of a successful substitution of silicon by aluminum, ^{27}Al, ^{29}Si and ^{31}P MAS NMR spectra of a sample with $x = 0.1$ were measured. The appearance of only one signal in the ^{27}Al spectrum with a chemical shift of 133 ppm suggest that the sample is single-phase and is in good agreement with the data reported in chapter 5, confirming a tetrahedral coordination of Al by sulfur (Fig. 4.2). Comparing the ^{31}P spectra (Fig. 4.3a) of $Li_{7.1}Si_{0.9}Al_{0.1}PS_8$ closely with spectra of the unsubstituted compound shown in chapter 3 and A reveals some minor differences. On the one hand, substitution of silicon by aluminum causes a compositional change in the amorphous side phase, which is evident by a shift in the relative intensities of the ^{31}P signals observed for the amorphous phase (cf. A). And on the other hand, a shift of all signals of the tetragonal phase by approximately -0.3 *ppm* can be observed. A similar shift combined with a broadening of the signal can also be observed in the ^{29}Si spectrum of $Li_{7.1}Si_{0.9}Al_{0.1}PS_8$ compared to the unsubstituted *tetra*-LSiPS depicted in black or orange, respectively, in Figure 4.3b. Both the shift and broadening of the signal are in accordance with the assumption of a successful substitution of Si by Al in the crystalline compound.

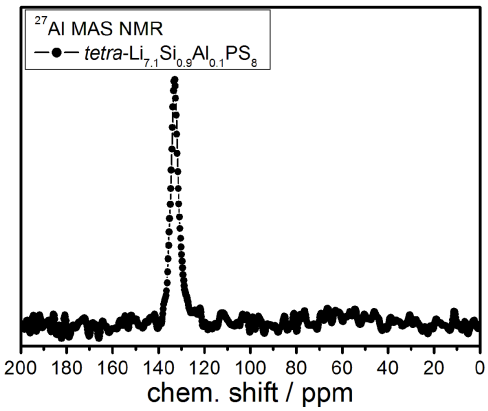

Figure 4.2: ^{27}Al MAS NMR spectrum of $Li_{7.1}Si_{0.9}Al_{0.1}PS_8$.

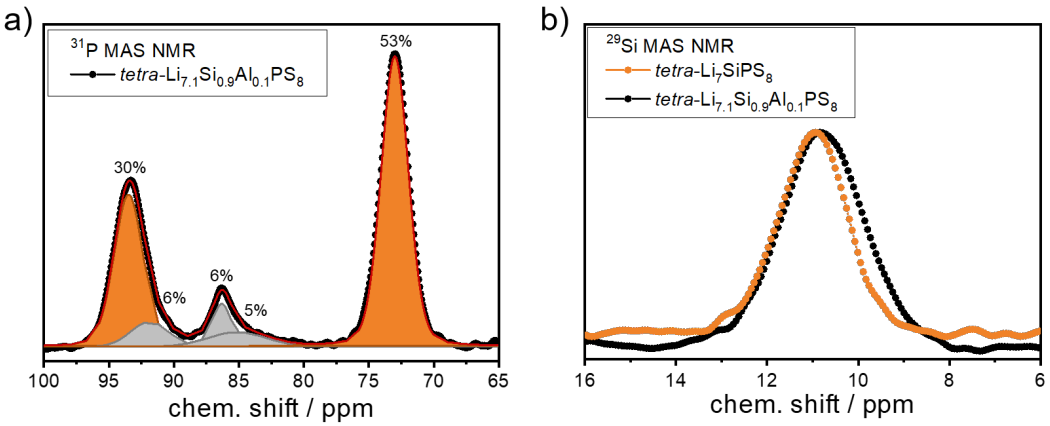

Figure 4.3: **a**: Deconvoluted ^{31}P MAS NMR spectra of $Li_{7.1}Si_{0.9}Al_{0.1}PS_8$ (black). The red line denotes the overall fit, colored peaks denote signals of tetragonal $Li_{7.1}Si_{0.9}Al_{0.1}PS_8$ (orange) and amorphous side phases (gray), respectively. **b**: ^{29}Si MAS NMR spectra of unsubstituted *tetra*-LSiPS (orange) and $Li_{7.1}Si_{0.9}Al_{0.1}PS_8$ (black).

The increased electron count and therefore increased shielding of the atoms stemming from additional lithium being incorporated into the structure to maintain charge neutrality causes a shift to lower ppm. This shift however is minute being an effect of the second coordination sphere and the total increase in charge carriers is only around 2%. The broadening can be explained by the increased static disorder and strain on the sulfur lattice introduced by substitution, resulting in a broader distribution of local chemical environments for the silicon atoms.

Electrochemical impedance spectroscopy

Electrochemical impedance spectroscopy (EIS) measurements were performed to access the ionic conductivities and the respective activation energies of the samples with $0 \leq x \leq 0.15$ in $Li_{7+x}Si_{1-x}Al_xPS_8$ (Fig. 4.4 and Fig. C.1). Regarding the obtained activation energies no drastic change can be observed, suggesting the fundamental mechanism of ion hopping of *tetra*-LSiPS does not change with substitution. Comparing the obtained data with the data reported in chapter 3 it is obvious that within the measurement error a substitution of silicon by aluminum has no large effect on the total conductivity in tetragonal $Li_{7+x}Si_{1-x}Al_xPS_8$. Higher substitution values ($x \geq 0.1$) slightly reduce the conductivity to approximately $4 \cdot 10^{-4}\,\mathrm{S\,cm^{-1}}$. This observation could be related to the small change in the amorphous side phase, which was discussed above. Since the same limitation of the ionic conductivity by the amorphous side phase that was observed for pristine *tetra*-LSiPS should also affect the Al substituted samples, changes in the composition of the amorphous side phase which impact its conductivity would also affect the total conductivity of the samples.

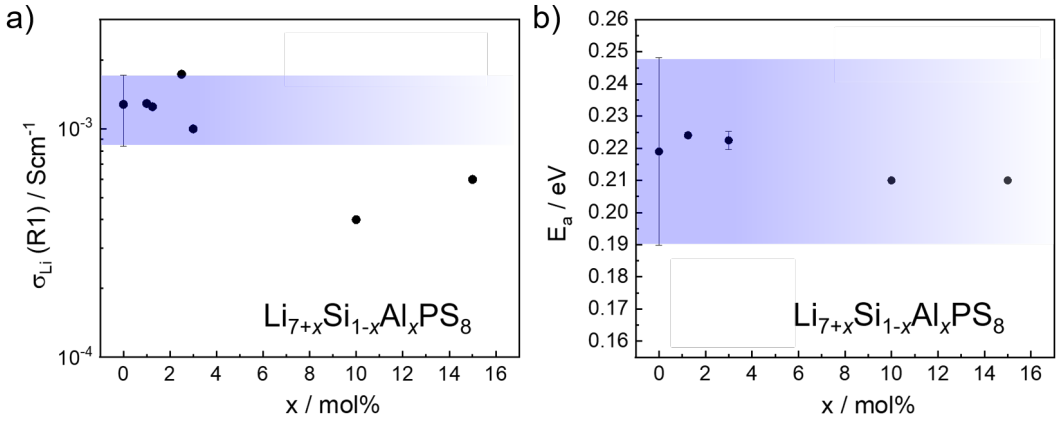

Figure 4.4: **a**: Total room temperature conductivities of samples in the $Li_{7+x}Si_{1-x}Al_xPS_8$ ($0 \leq x \leq 0.15$) substitution series. **b**: Measured activation energies for ion conduction of samples in the $Li_{7+x}Si_{1-x}Al_xPS_8$ ($0 \leq x \leq 0.15$) substitution series. Blue bars depict the typical measurement error of unsubstituted *tetra*-LSiPS.

To clarify if this assumption is correct one has to deconvolute the different contributions to the measured total impedance. On LGPS-like compounds this was so far only achieved by EIS below −100 °C, which will be conducted in further studies.

Bond valence energy landscape calculations

To assess the influence of partial substitution of silicon by aluminum on the crystalline phase, BVEL calculations on the unsubstituted *tetra*-LSiPS and tetragonal $Li_{7.1}Si_{0.9}Al_{0.1}PS_8$ were performed using experimental data obtained by Rietveld refinement for the respective compounds. Cross-sections through the BVEL map of the main lithium diffusion paths parallel to c are depicted in Figure 4.5. Low energy sections (blue areas) coincide very well with crystallographic lithium atom positions, which were therefore omitted from the figure for clarity. The obtained diffusion paths for lithium (BVEL map cut-off level at -4.4 eV) correspond to the calculated paths for isotypic tetragonal LGPS by Ceder *et al.*.[6] The BV calculations on both compounds give very similar results as listed in Table 4.1. A slightly lower activation energy of ion hopping for tetragonal $Li_{7.1}Si_{0.9}Al_{0.1}PS_8$ was obtained, being in line with the trend of decreased activation energy with increased lattice parameters obtained by AIMD simulations by Ceder *et al.* for a series of LMPX compounds including theoretical '$Li_{11}AlP_2S_{12}$'.[1] The obtained difference of about 4 meV however, is well below the margin of error achievable in EIS measurements. Since a decrease in activation energy and an increase in charge carrier concentration should result in an increase in bulk conductivity of the tetragonal $Li_{7+x}Si_{1-x}Al_xPS_8$ phase, the decrease in total conductivity measured by EIS with increasing x is therefore attributed to the change in composition of the amorphous side phase observed by MAS NMR.

Table 4.1: Results of BVEL calculations performed on *tetra*-LSiPS and tetragonal $Li_{7.1}Si_{0.9}Al_{0.1}PS_8$. The activation energy for ion migration is defined as $E_{a,BV} = |E_{min}^{path} - E_{mig}^{path}|$.

Structure	$E_{a,BV}$	E_{mig}^{path}	E_{min}^{path}	E_{min}^{global}
tetra-Li_7SiPS_8	0.7113 eV	-4.8010 eV	-5.5123 eV	-6.1325 eV
tetra-$Li_{7.1}Si_{0.9}Al_{0.1}PS_8$	0.7075 eV	-4.7894 eV	-5.4969 eV	-6.1341 eV

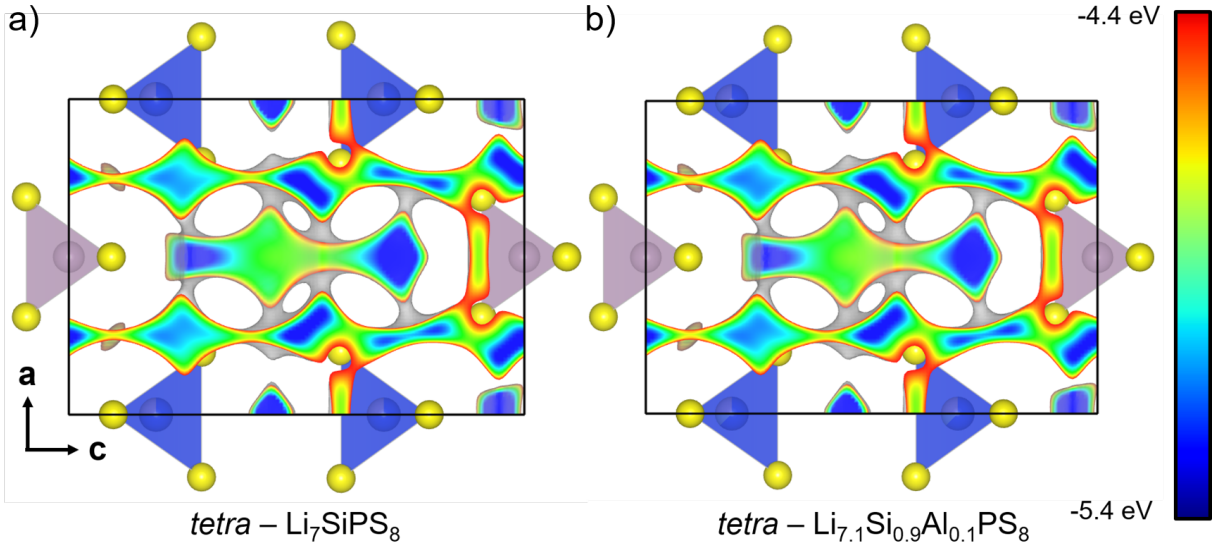

Figure 4.5: Comparison of the calculated BVEL maps for **a**: *tetra*-LSiPS and **b**: tetragonal $Li_{7.1}Si_{0.9}Al_{0.1}PS_8$. [Si/P/Al−$S_4$]-tetrahedra are depicted in blue, [P−S_4]-tetrahedra are depicted in gray, Si is depicted in blue, P in gray, Al in turquoise and S in yellow. Li atom positions were omitted for clarity. The depicted BVEL isosurface (gray) cutoff energy is -4.4 eV. Its cross sections parallel to the main diffusion paths in the *ac*-plane at $y = 0.5$ and $y = 0.75$ are colored dependent on the calculated BV energy from blue (-5.4 eV) to red (-4.4 eV).

4.1.3 Conclusion and Outlook

In this work we show the successful substitution of Si^{+IV} by Al^{+III} up to a substitution ratio of $x = 0.15$ in tetragonal $Li_{7+x}Si_{1-x}Al_xPS_8$ by PXRD and subsequent Rietveld refinement and MAS NMR spectroscopy. DFT calculations by Ceder *et al.* predict a decrease in activation energy for lithium ion diffusion followed by an increase in conductivity in aluminum containing tetragonal LGPS-like compounds.[1] These findings are corroborated by BVEL calculations performed on crystalline materials obtained in this work. However, experimental data from EIS show little influence of the substitution ratio x on both the total conductivity and the activation energy. Substitutional ratios of $x = 0.10$ and more lead to a decrease in total conductivity from $2 \cdot 10^{-3}\,\mathrm{S\,cm^{-1}}$ to $4 \cdot 10^{-4}\,\mathrm{S\,cm^{-1}}$ which is attributed to a change in composition of the amorphous side phase present in this class of materials (cf. chapter 3) which further reduces the measured conductivities compared to unsubstitutted *tetra*-LSiPS. However, subsequent studies including low-temperature EIS measurements are needed to confirm this hypothesis. Furthermore, similar to the solid solution series $Na_{5-x}Al_{1-x}Si_xS_4$ (c.f. chapter 5) a substitution of silicon by aluminum should increase the compounds stability against reduction at the Li anode. This and to what extent the amorphous side phases influence the stabilities will be subject to further studies on these materials.

Author Contributions

SH, AKH and BVL conceived and designed this study; SH, CaH and MP conducted the synthesis; SH, AKH, CaH and MP were responsible for measuring PXRD, NMR and EIS; SH performed Rietveld analysis and BVEL calculations; AKH analysed measured EIS data; SH interpreted the data and wrote the manuscript.

4.2 Impact of LiCl on the phase composition in *tetra*-LSiPS

Sascha Harm, Anna-Katharina Hatz, Carla Hoefer, Lucas Balzat, Verena Langowski, Bettina V. Lotsch

Published in: *unpublished results*

As was already briefly discussed in chapter 1.3.1, the fastest lithium ion solid electrolyte to date was found by Kanno *et al.* with a composition of $Li_{9.54}Si_{1.74}P_{1.44}S_{11.7}Cl_{0.3}$.[7] This compound was synthesized by mixing stoichiometric amounts of LiCl and the respective sulfides by ball milling and forming the tetragonal LGPS-like crystalline material by annealing the compound at 500 °C. By Rietveld analysis of neutron powder diffraction data the authors determined a mixed occupation of the three atomic positions occupied by sulfur with 2 – 4 % Cl, which is in good agreement with the total composition. However, they also report a lithium argyrodite (Li_6PS_5Cl) side phase in addition to the tetragonal LGPS-like phase with a phase fraction of approximately 18 w%. This additional phase covers more than the total mass fraction of chlorine in the compound. This observation in combination with the fact that phosphorous chalcogen halogenides are very reactive and tend to decompose in the presence of a Lewis-acid or at elevated temperatures,[8,9] suggests that additional LiCl reacts to the lithium-argyrodite at the given synthesis conditions. Therefore, a different mechanism is proposed by which the high ionic conductivities of $Li_{9.54}Si_{1.74}P_{1.44}S_{11.7}Cl_{0.3}$ could be explained:
It was shown in chapter 3 that the ionic conductivity of tetragonal LSiPS compounds is impeded by an additional, hitherto undetected, amorphous side phase of approximate composition Li_3PS_4. LiCl, in the presence of Li_2S, could react with this side phase to form the Li_6PS_5Cl observed by Kanno *et al.*. Since this lithium argyrodite phase exhibits a much higher ionic conductivity than the amorphous side phase, the overall conductivity of this phase mixture should increase, especially considering that silicon doping could increase the conductivity of the argyrodite phase even more.[10,11] A scheme of the overall proposed reaction is given in Figure 4.6.

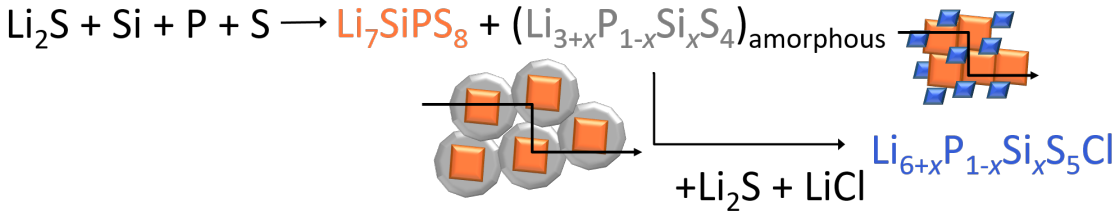

Figure 4.6: Scheme of the proposed reaction between the amorphous side phase (gray) observed in *tetra*-LSiPS (orange) and additional Li_2S and LiCl to form lithium argyrodite side phase (blue), increasing the overall conductivity.

4.2.1 Experimental procedure

Samples were similarly prepared, handled and measured as described in chapter 3. The annealing temperature was set to 525 °C. To calculate the amount of additional Li_2S and LiCl (Alfa Aesar, 99%) different amounts of amorphous side phase of composition Li_3PS_4 were assumed and weighed according to the reaction equation given in Figure 4.6. Since the assumed weight percent of an amorphous phase is the common denominator to describe the amount of additional Li_2S and LiCl, it is chosen in the following to designate specific samples.

4.2.2 Results and discussion

Powder X-ray diffraction

PXRD measurements and subsequent Rietveld refinements with an internal silicon standard were performed for all samples. These show (Fig. 4.7) the expected occurrence of the lithium argyrodite phase with the addition of Li_2S and LiCl. Samples with 8 assumed weight percent amorphous Li_3PS_4 (8 *awt*%), which is an average value for *tetra*-LSiPS samples (cf. chapter 3), shows a negligible amount of amorphous phase within the error limits of the method. However, increasing amounts of *ortho*-LSiPS are present in samples up to 8 awt% which is decreased at 15 *awt*% in combination with a dramatic increase in the phase fraction of an additional amorphous side phase. Furthermore, the addition of Li_2S and LiCl is accompanied by a decrease in unit cell volume of the *tetra*-LSiPS phase (Fig. 4.7b), hinting at a decrease in the Si:P-ratio, since the ionic radius of Si^{IV} is bigger than that of P^V. The Si:P-ratio is decisive for the stability of the tetragonal phase. Preliminary experiments showed that at the given annealing temperature of 525 °C only the composition Li_7SiPS_8 resulted in *tetra*-LSiPS being the only crystalline phase. Other compositions between $\frac{1}{3} \leq x \leq \frac{2}{3}$ in $Li_{3+x}Si_xP_{1-x}S_4$ resulted in additional *ortho*-LSiPS with the given synthesis conditions. It can be assumed, that, similar to LGPS, the tetrel to phosphorous ratio influences the temperature stability of the tetragonal phase resulting in a lower temperature needed for A decomposition of the tetragonal phase to the orthorhombic,[12] which could explain the occurrence of *ortho*-LSiPS in the given samples.

Electrochemical Impedance Spectroscopy

Temperature dependent EIS measurements were performed for all samples to assess their total ionic conductivity and the respective activation energies. The obtained results are depicted in Figure 4.8 and representative EIS spectra measured at −20 °C are given in Figure C.2. Regarding total conductivity, no clear trend can be observed within the margin of error. However, the sample with 15 *awt*% shows the highest total conductivity of 4 mS/cm. The activation energy for ion conduction extracted from the total conductivity by addition of Li_2S and LiCl is first slightly increased with 0.26 eV compared to the usually obtained 0.22(3) eV for *tetra*-LSiPS, decreases however with increasing addition of Li_2S and LiCl to 0.17 eV. Both increase in total conductivity and decrease in activation energy

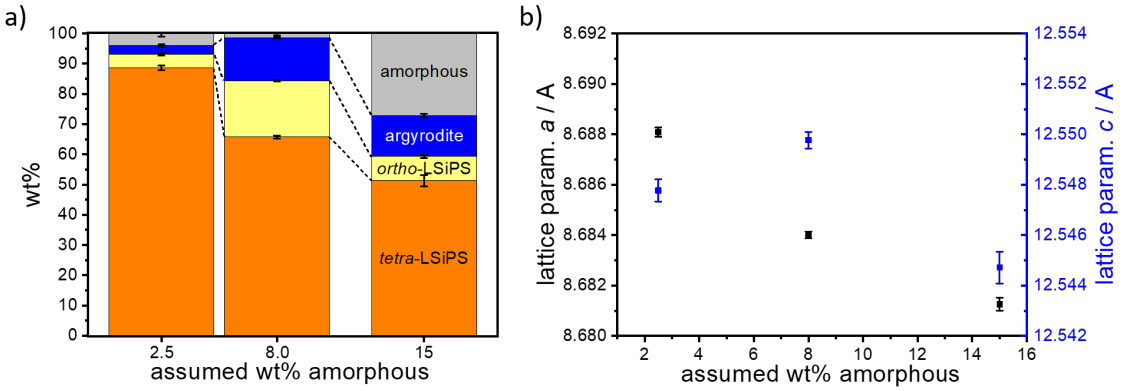

Figure 4.7: Results from Rietveld refinements from *tetra*-LSiPS samples with different amounts of additional Li_2S and LiCl. a): Extracted phase fractions by quantitative phase analysis with an internal silicon standard; b): Lattice parameters *a* and *c* of *tetra*-LSiPS.

cannot be sufficiently explained by the occurence of the Li-argyrodite Li_6PS_5Cl alone and can also not just be correlated to the amount of amorphous side phase determined by PXRD and subsequent Rietveld refinement. However, the disappearance and reappearance of an amorphous phase with increasing Li_2S and LiCl content suggests that the sample with 15 *awt*% shows a different amorphous secondary phase as usually observed for *tetra*-LSiPS.

MAS NMR spectroscopy

To validate the assumption of a change in the amorphous side phase by addition of Li_2S and LiCl a ^{31}P MAS NMR spectrum was measured, deconvoluted and compared to the spectrum of a pure *tetra*-LSiPS sample (Fig. 4.9). The measured ^{31}P MAS NMR spectrum shows four distinct peaks, which were attributed to crystalline *tetra*-LSiPS, *ortho*-LSiPS and Li_6PS_5Cl or an amorphous phase. The signal for *ortho*-LSiPS shows a shift from 88 ppm to 90 ppm (cf. Chapter 3). Since, Rietveld refinement of the obtained PXRD data with internal standard suggests that the amorphous phase shows a higher weight fraction than the lithium argyrodite phase and Li_6PS_5Cl itself shows numerous broad signals between 81 and 85 ppm according to literature,[13] the broad signal observed between 79 and 88 ppm is most likely caused by a broad distribution of amorphous lithium argyrodite like phases and crystalline Li_6PS_5Cl which cannot be deconvoluted.

4.2.3 Conclusion and Outlook

In this preliminary work the impact of an addition of Li_2S and LiCl on the phase composition and overall conductivity of *tetra*-LSiPS was studied. It could be shown that the formation of an amorphous side phase, which usually impedes the predicted high conductivity of *tetra*-LSiPS, could be suppressed. However, the specific ionic conductivity does

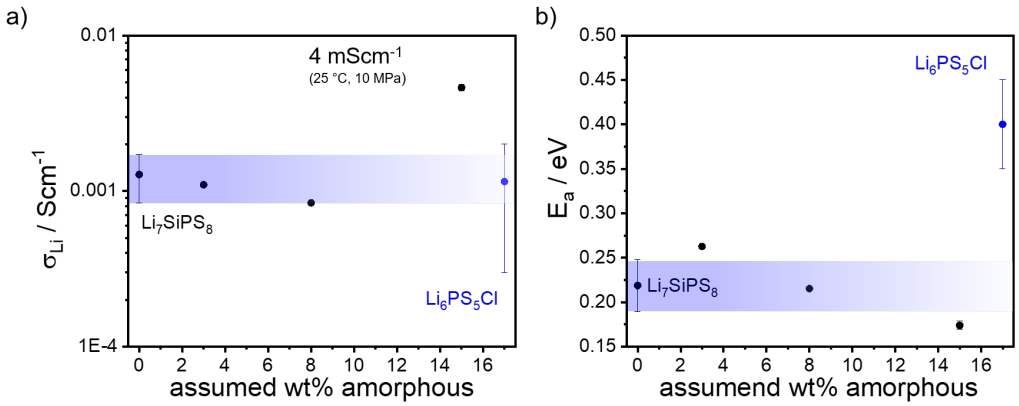

Figure 4.8: **(a)**: Total conductivities and **(b)**: activation energies for ion conduction of samples with increasing Li_2S and LiCl content. Blue bars depict the estimated deviation for the specific ionic conductivity and activation energy for different tetra-LSiPS samples. As a reference the respective values for the lithium argyrodite Li_6PS_5Cl are also depicted.

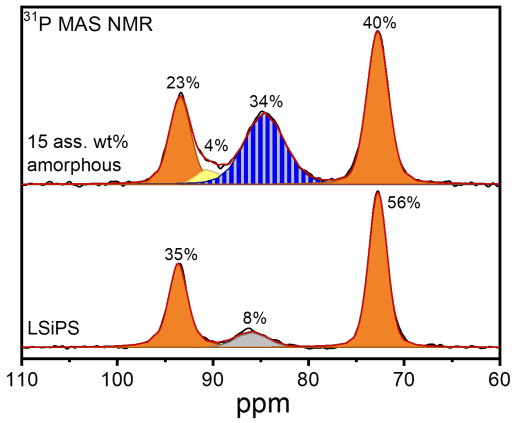

Figure 4.9: Deconvoluted ^{31}P MAS NMR spectra of a sample with 15 awt% amorphous Li_3PS_4 and a typical *tetra*-LSiPS sample. Deconvoluted peaks are color coded to their respective phase. Orange represents crystalline tetra-LSiPS, yellow ortho-LSiPS, blue the Li-argyrodite and gray an amorphous phase. The percentage of the respective integrated areas is given for each peak. The envelope of the overall fit function is depicted in red. Measured data is given as a black line.

not change within the margin of error, which is most likely due to the emergence of other additional side phases, like *ortho*-LSiPS, at increasing ratios of additional lithium sulfide and chloride. Interestingly, by exceeding the assumed amount of Li_2S and LiCl needed to suppress the amorphous side phase, an approximate doubling in conductivity of the resulting mixture is observed from 2 mS/cm for *tetra*-LSiPS to 4 mS/cm, combined with a deacrease in activation energy for ion conduction to 0.17 eV. This change was attributed to the formation of yet unidentified amorphous side phase, which either enables better contact between the *tetra*-Li_7SiPS_8 grains or is a very fast ionic conductor itself, or both. Further investigations will focus on the role of this secondary amorphous phase and the influence of heavier halides such as bromine on this phase system.

Author Contributions

SH, AKH, VL and BVL conceived and designed this study; SH, CH and LB conducted the synthesis; SH, AKH, CaH and LB were responsible for measuring PXRD, NMR and EIS; SH performed Rietveld analysis; AKH analysed measured EIS data; SH interpreted the data and wrote the manuscript.

Bibliography

(1) Ong, S. P.; Mo, Y.; Richards, W. D.; Miara, L.; Lee, H. S.; Ceder, G. Phase stability, electrochemical stability and ionic conductivity of the $Li_{10\pm1}MP_2X_{12}$ (M = Ge, Si, Sn, Al or P and X = O, S or Se) family of superionic conductors. *Energy Environ. Sci.* **2013**, *6*, 148–156.

(2) Sale, M.; Avdeev, M. *3DBVSMAPPER*: a program for automatically generating bond-valence sum landscapes. *J. Appl. Cryst.* **2012**, *45*, 1054–1056.

(3) Momma, K.; Izumi, F. *VESTA3* for three-dimensional visualization of crystal, volumetric and morphology data. *J. Appl. Cryst.* **2011**, *44*, 1272–1276.

(4) Amaresh, S.; Karthikeyan, K.; Kim, K. J.; Lee, Y. G.; Lee, Y. S. Aluminum based sulfide solid lithium ionic conductors for all solid state batteries. *Nanoscale* **2014**, *6*, 6661–6667.

(5) Vegard, L. Die Konstitution der Mischkristalle und die Raumfüllung der Atome. *Z. Phys.* **1921**, *5*, 17–26.

(6) Mo, Y.; Ong, S. P.; Ceder, G. First Principles Study of the $Li_{10}GeP_2S_{12}$ Lithium Super Ionic Conductor Material. *Chem. Mater.* **2012**, *24*, 15–17.

(7) Hori, S.; Suzuki, K.; Hirayama, M.; Kato, Y.; Kanno, R. Lithium Superionic Conductor $Li_{9.42}Si_{1.02}P_{2.1}S_{9.96}O_{2.04}$ with $Li_{10}GeP_2S_{12}$-Type Structure in the Li_2S - P_2S_5 – SiO_2 Pseudoternary System: Synthesis, Electrochemical Properties, and Structure–Composition Relationships. *Front. Energy Res.* **2016**, *4*, 38.

(8) Müller, U.; Mohammed, A. T. Darstellung und Schwingungsspektren von Dichloro- und Dibromodithiophosphat Die Kristallstrukturen von $[PPh_3Me]$ $[PS_2Cl_2]$ und $[PPh_4]$ $[PS_2Br_2]$. *Z. anorg. allg. Chem.* **1984**, *514*, 164–170.

(9) Hoppe, D. Phosphorchalkogenid-Molekülverbindungen, Ph.D. Thesis, Universität Regensburg, 2009.

(10) Kraft, M. A.; Ohno, S.; Zinkevich, T.; Koerver, R.; Culver, S. P.; Fuchs, T.; Senyshyn, A.; Indris, S.; Morgan, B. J.; Zeier, W. G. Inducing High Ionic Conductivity in the Lithium Superionic Argyrodites $Li_{6+x}P_{1-x}Ge_xS_5I$ for All-Solid-State Batteries. *J. Am. Chem. Soc.* **2018**, *140*, 16330–16339.

(11) Zhang, Z.; Sun, Y.; Duan, X.; Peng, L.; Jia, H.; Zhang, Y.; Shan, B.; Xie, J. Design and synthesis of room temperature stable Li-argyrodite superionic conductors via cation doping. *J. Mater. Chem. A* **2019**, *7*, 2717–2722.

(12) Hori, S.; Kato, M.; Suzuki, K.; Hirayama, M.; Kato, Y.; Kanno, R. Phase Diagram of the Li_4GeS_4 – Li_3PS_4 Quasi-Binary System Containing the Superionic Conductor $Li_{10}GeP_2S_{12}$. *J. Am. Ceram. Soc.* **2015**, *98*, ed. by Sprenkle, V., 3352–3360.

(13) Hanghofer, I.; Brinek, M.; Eisbacher, S. L.; Bitschnau, B.; Volck, M.; Hennige, V.; Hanzu, I.; Rettenwander, D.; Wilkening, H. M. R. Substitutional disorder: structure and ion dynamics of the argyrodites Li_6PS_5Cl, Li_6PS_5Br and Li_6PS_5I. *Phys. Chem. Chem. Phys.* **2019**, *21*, 8489–8507.

Chapter 5

Finding the right blend: Interplay between structure and sodium ion conductivity in the system Na_5AlS_4 – Na_4SiS_4

Sascha Harm, Anna-Katharina Hatz*, Christian Schneider, Carla Hoefer, Constantin Hoch, Bettina V. Lotsch*
*These authors contributed equally to this work

Published in: *Frontiers in Chemistry*, **2020**, *8*:90.
DOI: 10.3389/fchem.2020.00090
https://www.frontiersin.org/articles/10.3389/fchem.2020.00090/full

5.1 Abstract

The rational design of high performance sodium solid electrolytes is one of the key challenges in modern battery research. In this work, we identify new sodium ion conductors in the substitution series $Na_{5-x}Al_{1-x}Si_xS_4$ ($0 \leq x \leq 1$), which are entirely based on earth-abundant elements. These compounds exhibit conductivities ranging from $1.64 \cdot 10^{-7}\,S\,cm^{-1}$ for Na_4SiS_4 to $2.04 \cdot 10^{-5}\,S\,cm^{-1}$ for $Na_{8.5}(AlS_4)_{0.5}(SiS_4)_{1.5}$ ($x = 0.75$). We determined the crystal structures of the Na^+-ion conductors Na_4SiS_4 as well as hitherto unknown Na_5AlS_4 and $Na_9(AlS_4)(SiS_4)$. Na^+-ion conduction pathways were calculated by bond valence energy landscape (BVEL) calculations for all new structures highlighting the influence of the local coordination symmetry of sodium ions on the energy landscape within this family. Our findings show that the interplay of charge carrier concentration and low site symmetry of sodium ions can enhance the conductivity by several orders of magnitude.

5.2 Introduction

In recent years, all-solid-state batteries (ASSB) have garnered attention as promising candidates for future battery applications in large scale mobility systems such as electric vehicles.[1–3] This is due to safety issues arising from liquid electrolytes applied in conventional lithium-ion batteries. Implementing solid electrolytes is thought to provide a more stable battery system, both thermally and mechanically. ASSBs can even pair this advantage with improved energy density through the use of Li or Na metal anodes and bipolar stacking. In prospect, the application of sodium containing materials produced from cheap and abundant sources could effectively cut down costs of ASSBs, thus enabling large-scale energy storage system solutions independent of limited lithium resources.[4] One central component of an ASSB is the solid electrolyte. To be applicable for battery systems, the implemented solid electrolytes are required to show high ionic and low electronic conductivity, along with high electrochemical and structural stability, as well as low production costs.[5] Regarding conductivity, the group of sulfides includes some of the best solid electrolytes to date. Especially thiophosphates, e.g. $Li_{10}GeP_2S_{12}$ (LGPS), Li_6PS_5X (X = Cl, Br, I) and Na_3PS_4, are promising materials due to their high ionic conductivities and soft mechanical nature enabling cold pressing of the electrolyte instead of high temperature sintering.[6–12] These high ionic conductivities compared to most oxide solid electrolytes are supposed to stem from the high polarizability of the sulfide or thiophosphate anion lattice, facilitating Li or Na ion hopping in the bulk.[13,14] However, Zeier et. al. showed that a softer lattice cannot only lower the migration barrier for charge carriers, but also affects the entropy of migration, which can negatively influence the overall ionic conductivity.[15,16] This 'softness' of the lattice is commonly tuned by isovalent or aliovalent substitution to obtain materials with even higher ionic conductivities. Isovalent substitution is typically employed to introduce softer, more polarizable anions, and to widen diffusion pathways as was studied recently for the solid electrolyte Na_3PS_4. In its 'cubic' phase, Na_3PS_4 exhibits a room temperature ionic conductivity of up to $4.6 \cdot 10^{-4}\,\mathrm{S\,cm^{-1}}$.[17,18] By substitution of S with Se, values up to $1.16 \cdot 10^{-3}\,\mathrm{S\,cm^{-1}}$ can be achieved for Na_3PSe_4.[15,19,20] In addition to isovalent substitution, aliovalent substitution can be used to not only alter the polarizability of the lattice and influence the size of diffusion pathways, but also to tune the charge carrier concentration. Similar to the LGPS system,[3,6,11,12,21–27] tetrel elements were employed in the $Na_{3+x}T_xP_{1-x}S_4$ (T = Si, Sn) system to increase the charge carrier density and increase the overall ionic conductivity. The Sn-containing compounds are structurally very similar to the LGPS-like $Li_{10}SnP_2S_{12}$ and show conductivities of $4 \cdot 10^{-5}\,\mathrm{S\,cm^{-1}}$ for $Na_{10}SnP_2S_{12}$ and the highest measured sodium ionic conductivity at room temperature for sulfides of $4 \cdot 10^{-3}\,\mathrm{S\,cm^{-1}}$ for $Na_{11}Sn_2PS_{12}$.[22,28,29] Aliovalent silicon substitution studies were also conducted for the Na_3PS_4 phase achieving a maximum conductivity of $7.4 \cdot 10^{-4}\,\mathrm{S\,cm^{-1}}$ for a glass ceramic of composition $94(Na_3PS_4) \cdot 6(Na_4SiS_4)$.[30] The authors showed the presence of two ion conducting, hitherto unknown crystalline phases in this $Na_{3+x}Si_xP_{1-x}S_4$ system with formal compositions '$Na_{11}Si_2PS_{12}$' and 'Na_4SiS_4'. However, no structural information was given nor the reason for the large increase in conductivity of the amorphous ball-milled product ($\sigma = 10^{-5}\,\mathrm{S\,cm^{-1}}$) compared to the crystalline products ($\sigma = 10^{-7}\,\mathrm{S\,cm^{-1}}$). In

this work we expand the materials space of sodium thio-ortho-tetrelates and -trielates by aliovalent substitution of Si in the aforementioned Na_4SiS_4 by Al, therefore increasing the number of charge carriers and expanding the lattice by a larger cation with reduced charge ($r(Si^{4+}_{Tetr.}) = 0.26\,\text{Å}, r(Al^{3+}_{Tetr.}) = 0.39\,\text{Å}$)[31] to enhance sodium ion conductivity. We present the crystal structures of Na_5AlS_4, Na_4SiS_4 and $Na_9(AlS_4)(SiS_4)$ and investigate their Na^+-ion migration pathways by bond valence energy landscape (BVEL) calculations. While Na_5AlS_4 was mentioned by Brown *et al.* and Na_4SiS_4 was reported recently by Tanibata *et al.*, no crystallographic data have been reported as yet.[30,32] In this work we map out the ionic conductivity of the aliovalent substitution series $Na_{5-x}Al_{1-x}Si_xS_4$ ($0 \leq x \leq 1$) and show that the conductivities can be significantly enhanced by tuning the charge carrier or defect concentration. Hereby, the more complex structure of $Na_{8.5}(AlS_4)_{0.25}(SiS_4)_{0.75}$ shows a flatter energy landscape and a jump to a higher conductivity by two orders of magnitude ($2.04 \cdot 10^{-5}\,\text{S cm}^{-1}$) compared to the border phases Na_4SiS_4 and Na_5AlS_4.

5.3 Experimental Section

5.3.1 Synthesis

Stoichiometric amounts of Na_2S (Alfa Aesar, 99%), Al_2S_3 (Alfa Aesar, 99%), Si (ball milled, Alfa Aesar, 99.999%), and S (Grüssing, sublimed *in vacuo*) were used as starting materials. An excess of 5 *wt*% sulfur was added to the mixture to ensure an oxidizing atmosphere during the reaction. Samples were prepared by thoroughly mixing and grinding the starting materials in an agate mortar. The resulting fine powders were transferred into glassy carbon crucibles, compacted and sealed under vacuum into quartz glass ampoules. The ampoules were subsequently transferred into a tube furnace and heated at 50 °C h^{-1} to 600 °C and annealed for 3 d. Subsequently, the furnace was turned off. The ampoules were removed from the furnace when the temperature was below 100 °C and transferred to a glovebox. Na_5AlS_4 and Na_4SiS_4 samples are off-white to yellow powders, probably from excess sulfur. $Na_{8.5}(AlS_4)_{0.25}(SiS_4)_{0.75}$ crystals were colorless cuboids of about 200 µm diameter embedded in an orange amorphous material, presumably solidified sodium polysulfide melt.

5.3.2 Powder X-ray Diffraction

From all samples powder X-ray diffractograms (PXRDs) were measured on a Stoe STADI P diffractometer (Ge-(111) monochromator, Dectris Mythen 1 K detector) utilizing Mo-$K_{\alpha 1}$ or Cu-$K_{\alpha 1}$ radiation in Debye-Scherrer geometry. All samples were sealed in glass capillaries with diameters of 0.3 to 0.5 mm under argon atmosphere in a glovebox. Indexing of PXRD data, structure solution by charge flipping and subsequent Rietveld refinements were carried out with the program Topas Academic v. 5.[33,34]

5.3.3 Single Crystal X-ray Diffraction

f Single crystals of $Na_{8.5}(AlS_4)_{0.25}(SiS_4)_{0.75}$ were isolated under paraffin oil outside the glovebox and sealed in glass capillaries under oil. Single crystal X-ray diffraction (SCXRD) experiments were carried out with a Bruker D8 Quest diffractometer using Mo-K_α radiation. Data handling, including a multi-scan absorption correction with the program SADABS, was done utilizing the Bruker Apex 3 software package.[35] The structure solution and refinement were performed with the programs SHELXS97 and SHELXL97, respectively.[36]

5.3.4 Solid-state Nuclear Magnetic Resonance Spectroscopy

Solid-state NMR spectra were measured on a Bruker Avance III 500 instrument at a magnetic field of $B_0 = 11.74\ T$. Magic-angle spinning (MAS) experiments were performed in zirconia spinners at a spinning speed of 10 kHz using a Bruker 4 mm triple-channel probe. ^{27}Al and ^{29}Si spectra were referenced indirectly to ^{1}H in 0.1% TMS at 0.00 ppm.

5.3.5 Differential Scanning Calorimetry

For differential scanning calorimetry (DSC) measurement samples were sealed in small quartz ampoules (5 mm outer diameter, 10 – 15 mm length) under argon. To improve heat-flow the quartz ampoules were put in Pt-crucibles (6 mm diameter, 10 mm height). Measurements were then carried out using a Netzsch STA 449 F5 Jupiter with an Argon flow of $40\,mL\,min^{-1}$ in a temperature range between room temperature and 900 °C and heating/cooling rates between 1 and $10\,K\,min^{-1}$. Data handling was performed with the Netzsch Proteus software package.

5.3.6 Energy Dispersive X-Ray Analysis

Elemental composition was determined by energy-dispersive X-ray spectroscopy (EDX; detector: Oxford Instruments Inca Energy) and an image of the morphology was obtained using a Jeol JSM 6500 F scanning electron microscope (SEM; field emission gun, acceleration voltage 20 kV).

5.3.7 Bond Valence Energy Landscape Calculations

Bond valence energy landscape (BVEL) calculations were performed with the program 3Dbvsmapper.[37] The BV method calculates the bond valence sum (BVS) for a tested ion at each voxel grid point of a three-dimensional mesh in a unit cell. For a sodium ion at its equilibrium site relative to the other ions in the structure (often equal to the crystallographic site of the sodium ion) the bond valence sum should be equal to its oxidation state (+1). Deviations of the BVS display possible migration pathways for the tested ion.[38] For a detailed description of the method see the SI. Here, the BVEL method uses

soft-bond-valence parameters and additional (penalty) terms to account for Coulombic attraction/repulsion terms.[39] The cutoff distance was fixed to a maximum value of 8 Å. The images were created with VESTA.[40]

5.3.8 Electrochemical Impedance Spectroscopy

Electrochemical impedance spectroscopy and galvanostatic polarization measurements were performed with an Ivium compactstat.h (24 bit instrument) in a two-electrode setup using a rhd Instruments Microcell HC cell stand loaded with rhd Instruments TSC Battery cells performing measurements between 25 °C and 75 °C inside the glovebox under argon atmosphere. The spectra were recorded in a frequency range of 1 MHz - 0.1 Hz and an applied rms AC voltage between 30 mV and 100 mV. The analysis of the impedance spectra was carried out with the RelaxIS3 software from rhd Instruments. The linearity, stability and causality was checked by applying the Kramers-Kronig-relation before fitting the data. Before measuring, the samples were ground thoroughly and compacted to a pellet of about 0.5 mm thickness and 5 mm diameter by uniaxial cold pressing (500 MPa). The obtained densities of the pellets were between 76-91% with an error of 6% (cf. Table S13). For impedance spectroscopy, the pellets were sandwiched between indium foil (Alfa Aesar, 0.127 mm thick, 99.99%) to enhance the contact with the stainless steel electrodes of the cells. No reaction between In and the samples was observed. Every sample was measured twice, and for each sample several temperature cycles were conducted. The measurement uncertainties arise from the error propagation of the uncertainties in pellet thickness, area and in obtained resistance. For the galvanostatic polarization measurements stainless steel electrodes were used.

5.4 Results and Discussion

5.4.1 X-Ray Diffraction

From all samples in the $Na_{5-x}Al_{1-x}Si_xS_4$ ($0 \leq x \leq 1$) aliovalent substitution series PXRDs were measured to study the crystallinity and phase composition (additional crystallographic data for all structures are given in the supplementary information). Figure 5.1B shows that no complete solid solution is formed. Instead, three separate phases crystallize as a function of the degree of substitution x.

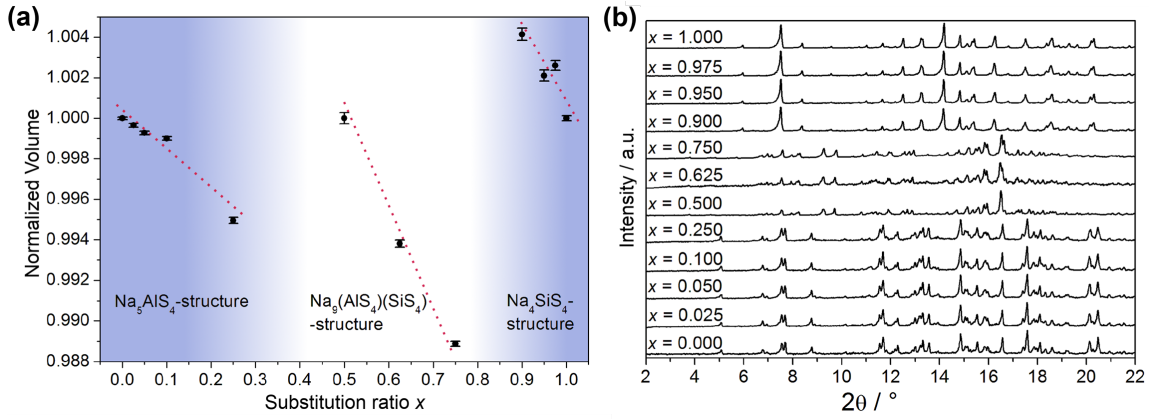

Figure 5.1: **(a)**: Normalized volume of the observed crystalline phases obtained by Rietveld refinement displayed against substitution value x; error bars represent 3σ and the red lines are a guide to the eye to illustrate the Vegard-like dependence on x. **(b)**: PXRDs (Mo-$K_{\alpha 1}$ radiation) of all samples in the $Na_{5-x}Al_{1-x}Si_xS_4$ ($0 \leq x \leq 1$) substitution series.

This is consistent with the fact that the pseudo-binary border phases Na_5AlS_4 and Na_4SiS_4 do not crystallize isotypically as shown below. Regarding the volume of the respective crystalline phases depicted in Figure 5.1A, a Vegard-like dependence on the substitution value x for all phases can be observed and therefore partial miscibility within the respective phases can be assumed.[41]

Crystal Structure of Na_5AlS_4.

Since no suitable single crystals were obtained, the crystal structure of Na_5AlS_4 was determined using powder X-ray data. The PXRD of Na_5AlS_4 was indexed in the orthorhombic space group *Pbca* (No. 61) with $a = 12.0130(12)$ Å, $b = 7.052\,63(7)$ Å and $c = 21.5605(2)$ Å. The structure was solved by charge-flipping implemented in Topas Academic v.5 and refined with the Rietveld algorithm (Figure 5.2A). The structure is depicted in Figure 5.2. The compound crystallizes in the Na_5FeO_4 structure type and is composed of isolated $[AlS_4]$-tetrahedra and distorted $[NaS_4]$-tetrahedra and $[NaS_6]$-octahedra.[42] The packing of the Al^{3+} atoms and therefore the packing of the $(AlS_4)^{5-}$-anions can be regarded as a

slightly distorted α-uranium packing as was stated for isotypic Rb_5GaO_4.[43] The BVEL calculations (cf. below) show that most likely the Na2 atom does not take part in the sodium ion conduction and can therefore be considered as being part of the lattice. Hence, the lattice can be regarded as hexagonally packed infinite chains of face-sharing [$Na2S_6$]-octahedra connected via a common face to [AlS_4]-tetrahedra which alternate back and forth along a (Figure 5.2C).

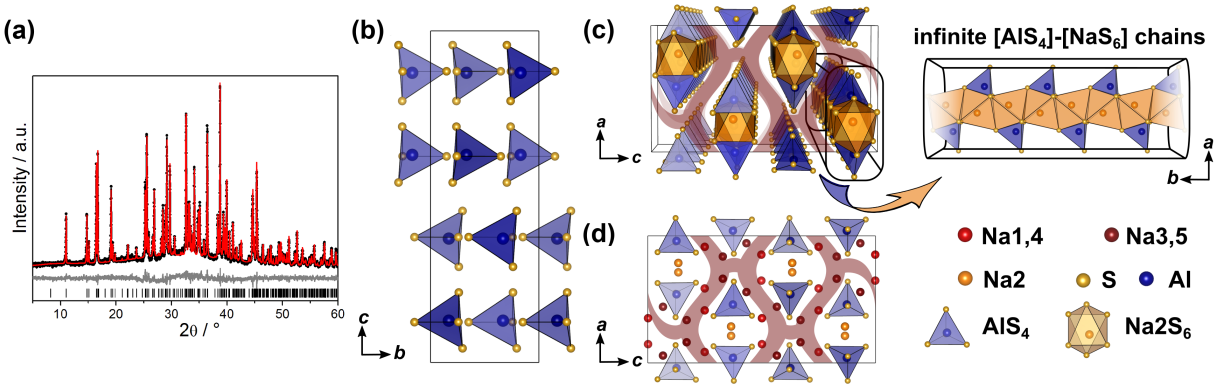

Figure 5.2: **(a)**: Rietveld refinement of Na_5AlS_4 ($x = 0$) measured using Cu-$K_{\alpha 1}$ radiation; black dots depict the measured data, red lines the Rietveld fit, gray lines the difference plot and black lines the respective reflection positions. **(b)**: [AlS_4]-tetrahedral sublattice in Na_5AlS_4 viewed along a. **(c)**: Perspective view of the [AlS_4]-tetrahedral and [$Na2S_6$] octrahedral arrangement parallel to b. **(d)**: Complete Na_5AlS_4 structure with [AlS_4]-tetrahedral arrangement viewed along b; maroon curved lines represent sodium ion diffusion pathways determined by BVEL calculations.

Crystal Structure of Na_4SiS_4.

The structure of Na_4SiS_4 was also determined from PXRD data. The diffractogram was indexed in the orthorhombic space group $P2_12_12_1$ (No. 19) with $a = 13.6765(3)$ Å, $b = 8.7839(2)$ Å and $c = 6.889\,40(15)$ Å, solved using charge-flipping and refined by Rietveld refinement (Figure 5.3A). The structure is comprised of isolated $[SiS_4]$-tetrahedra which are edge- and corner-sharing to distorted $[NaS_6]$-octahedra (5+1 coordination, cf. below). The sulfur atom arrangement constitutes a distorted hexagonal close packing (hcp). Therefore, the structure can be regarded as a hcp of S^{2-}-anions with Si^{4+} and Na^+ filling $\frac{1}{8}$ tetrahedral and all octahedral voids, respectively. This highlights the similarity of this compound's structure with the thio-LiSICON family.[5] However, this structure model does not account for the weak reflection at $2\Theta \approx 5°$, marked in Figure 5.3a. It stems from an elongation of the a-axis by a factor of three ($i3$ transition) to $a = 41.0301(7)$ Å and an ordering of sodium atoms Na10, Na11 and Na12 to form $[NaS_5]$-pyramids in a one-up-two-down-pattern, leading to the superstructure shown in Figure 5.3.

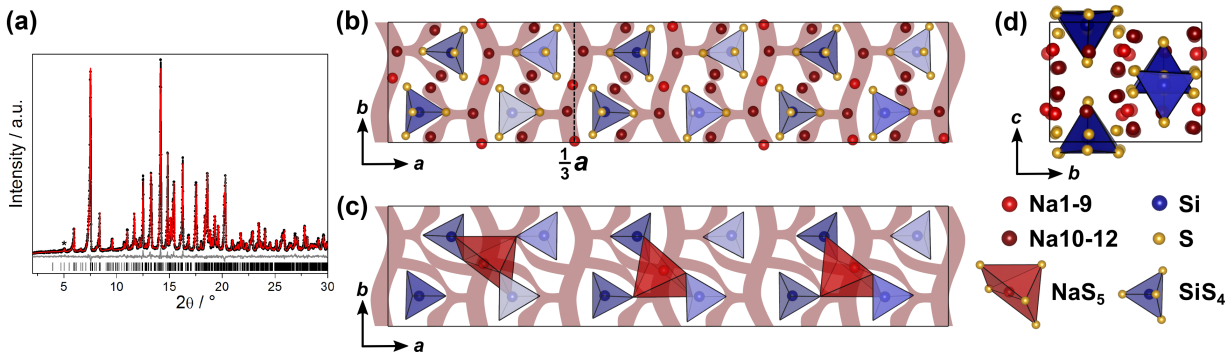

Figure 5.3: **(a)**:Rietveld refinement of Na_4SiS_4 ($x = 1$) measured using Mo-$K_{\alpha 1}$ radiation, the super-structure reflection is marked by an asterisk; black dots depict the measured data, red lines the Rietveld fit, gray lines the difference plot and black lines the respective reflection positions. **(b)**: Na_4SiS_4 crystal structure parallel to c; **(c)**: Na_4SiS_4 structure viewed along a; **(d)**: $[SiS_4]$-tetrahedra (blue) and $[NaS_5]$-pyramidal (red) arrangement viewed parallel to c, showing the $[NaS_5]$-pyramids in a one-up-two-down-pattern; maroon curved lines represent sodium ion diffusion pathways determined by BVEL calculations.

Crystal structure of $Na_9(AlS_4)(SiS_4)$.

The double salt $Na_{10-2x}(AlS_4)_{2-2x}(SiS_4)_{2x}$ could be obtained in a compositional range of $0.5 \leq x \leq 0.75$. Samples with $x = 0.75$ yielded suitable crystals for SCXRD measurements, presumably because a poly-sulfide melt serves as a solvent for the compound at temperatures exceeding 300 °C as shown by thermal analysis (cf. Figure S3). $Na_{8.5}(AlS_4)_{0.5}(SiS_4)_{1.5}$ ($x = 0.75$) crystallizes in the monoclinic space group Cc (No. 9), with $a = 17.5673(6)$ Å,

$b = 13.5408(5)$ Å, $c = 14.2543(5)$ Å, and $\beta = 93.3683(13)°$. Its crystal structure is comprised of isolated [Al/SiS_4]-tetrahedra, and distorted tetrahedrally, trigonal-bipyramidally, square-pyramidally or octahedrally coordinated [NaS_4]-, [NaS_5]-, or [NaS_6]-units (Figure 5.4, Figure S1). Additionally, the anion sublattice shows pseudo-inversion symmetry, which is broken by the sodium cations. Since BVEL calculations show that Na13 requires the highest energy to take part in ion migration (cf. below), it can be considered as part of the lattice. Therefore, the topology of the structure can be described as a distorted hexagonal packing of rods comprised of [Na13S_6] corner-sharing to four [Al/SiS_4]-tetrahedra and interconnected by two corner-sharing [Al/SiS_4]-tetrahedra parallel to c (Figure 5.4A). In contrast, for Na cations Na4, Na12, Na15 and Na18 (cf. Table S8) not taking part in the lattice, large anisotropic displacement parameters are found (see Table S9 and Figure S1). They occupy positions best described as two half-filled face-sharing [NaS_4]-tetrahedra constituting an unresolved split position, which therefore explains the elongated shapes. The occupancy of Si *vs.* Al was not refined because of the similar atomic form factors of both elements, yet the Si/Al ratio was confirmed to be 3/1 by EDX measurements (cf. Table S11).

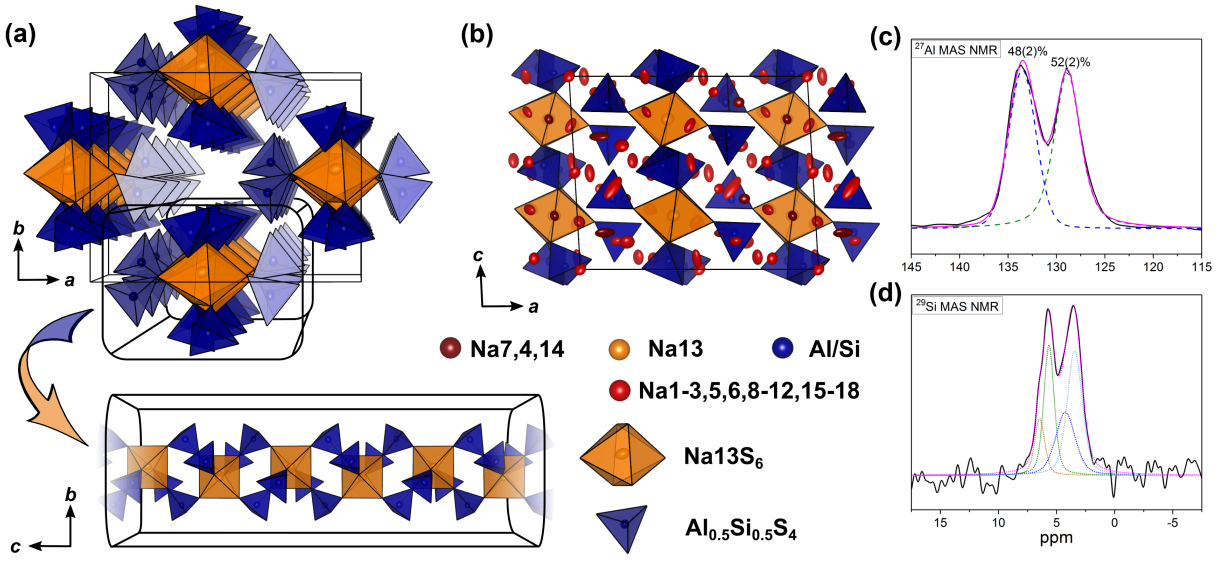

Figure 5.4: **(a)**: [Si/AlS_4]-tetrahedral and [Na13S_6]-octahedral arrangement viewed along c and infinite [Si/AlS_4]-[Na13S_6]-rods viewed parallel to a. **(b)**: $Na_9(AlS_4)(SiS_4)$ crystal structure viewed along b; blue polyhedra depict [Si/AlS_4]-tetrahedra, orange polyhedra depict [Na13S_6]-octahedra, red, dark red and yellow atoms depict Na, and blue atoms depict Si/Al; ellipsoids were drawn at 80% probability. **(c)**: Deconvoluted ^{27}Al MAS NMR spectrum of $Na_9(AlS_4)(SiS_4)$ ($x = 0.5$); purple line shows the overall fit, colored dashed lines represent the contributing pseudo-Voigt peaks, relative intensities are given with their respective standard deviation in parentheses. **(d)**:^{29}Si MAS NMR spectrum of $Na_9(AlS_4)(SiS_4)$; colored dotted lines show a tentative signal distribution.

The mean Al/Si–S-distances (cf. Table S10) of all four atomic sites of 2.147(3) Å ($Si1S_4$), 2.165(3) Å ($Si2S_4$), 2.166(3) Å ($Si3S_4$), and 2.160(3) Å ($Si4S_4$) are in between the distance expected for tetrahedrally coordinated Si^{4+}–S of 2.10 Å and Al^{3+}–S of 2.23 Å.[31] This suggests that all Al/Si sites are occupied by silicon and aluminum with Si1 having a slightly higher Si/Al ratio than the other three sites. Since the single crystal was obtained from a sample with $x = 0.75$, the occupancy of sodium atoms was expected to be less than one to maintain charge neutrality. Therefore, the occupancy of all sodium atoms was freely refined (cf. Table S8) insofar as their occupancy factor was significantly ($\geq 3\sigma$) lower than one, yielding a total number of sodium atoms per unit cell of 66.9(2), which is in good agreement with the nominal value of 68.

5.4.2 NMR spectroscopy

To verify the assumption of a mixed occupancy of all four atomic Al/Si sites in the compound $Na_9(AlS_4)(SiS_4)$, ^{27}Al and ^{29}Si magic-angle spinning (MAS) NMR spectra were collected (Figure 5.4C, D). Both spectra show two clearly separated peaks with noticeable shoulders, especially in the ^{29}Si spectrum. Although four signals in each spectrum are expected due to the four crystallographically independent Al/Si sites, the occurrence of only two peaks in each spectrum is in good agreement with the crystal structure by taking into account that the $[Al/SiS_4]$ sub-lattice shows pseudo-inversion symmetry and therefore the chemical shifts of the respective nuclei should be very similar (or accidentally equal), resulting in two sets of two overlapping signals, which is apparent in the ^{29}Si spectrum and, to a lesser extent, also in the ^{27}Al spectrum. Additionally, the appearance of shoulders in the spectra suggests slightly different Si/Al occupancies for the atomic sites with pseudo-inversion symmetry, which is also corroborated by the mean Al/Si – S distances from SCXRD data.

5.4.3 Bond Valence Energy Landscape Calculations

BVEL calculations were performed in order to elucidate the minimum energy trajectories of the sodium ions and their dimensionalities in the three structures Na_5AlS_4, $Na_9(AlS_4)(SiS_4)$, and Na_4SiS_4. The bond valence approach was proven to be a valid starting point for discussing ion migration pathways in crystalline (ionic) solid electrolytes and electrode materials. The method provides reasonable pathways, comparable to those obtained by density functional theory (DFT) or molecular dynamics (MD) simulations.[44,45] During ion migration (here Na^+) from one equilibrium site Na_i (often a crystallographic site) to an adjacent site Na_j, sodium surpasses one (or multiple) transition state(s). Meta-stable sites along the path are considered to be interstitial sites for sodium ions. In this work, we denote the calculated global minimum energy E_{min}^{global}, the minimum energy within the infinitely connected pathway E_{min}^{path} and the energy at which a infinitely connected pathway is formed E_{mig}^{path}. The energy required for overcoming the ion migration barrier height Δ is calculated by $\Delta E = |E_{min}^{path} - E_{mig}^{path}|$. Subscript abbreviations denote the dimensionality of the pathway. Keeping in mind, that these calculated barrier heights for ion migration are

overestimated, due to not taking lattice relaxations and coulombic repulsion of Na^+–Na^+ into account, the BV method provides elucidating insights into probable ion migration pathways in a new structure.

BVEL calculations for Na_5AlS_4.

In Figure 5.5 the result of the BVEL calculation of Na_5AlS_4 is depicted. To better decipher the individual, spatially distinct components of the overall Na ion trajectory, we introduce sections **A** and **B** in Figure 5.5A, and separately discuss each section. In section **A** tetrahedrally coordinated Na1 form a 2D-like conduction pathway in the *ac* plane. Two adjacent [$Na1S_4$] tetrahedra are connected *via* shared faces of an [$\square S_6$]-octahedron, creating a dumbbell-like conduction network between two Na1 sites as shown in Figure 5.5C. Unoccupied tetrahedral sites (see Figure 5.5C) loosely connect the Na1–Na1 dumbbells. Each of these dumbbells is connected to two Na3, which are residing in peninsular-like side pockets.

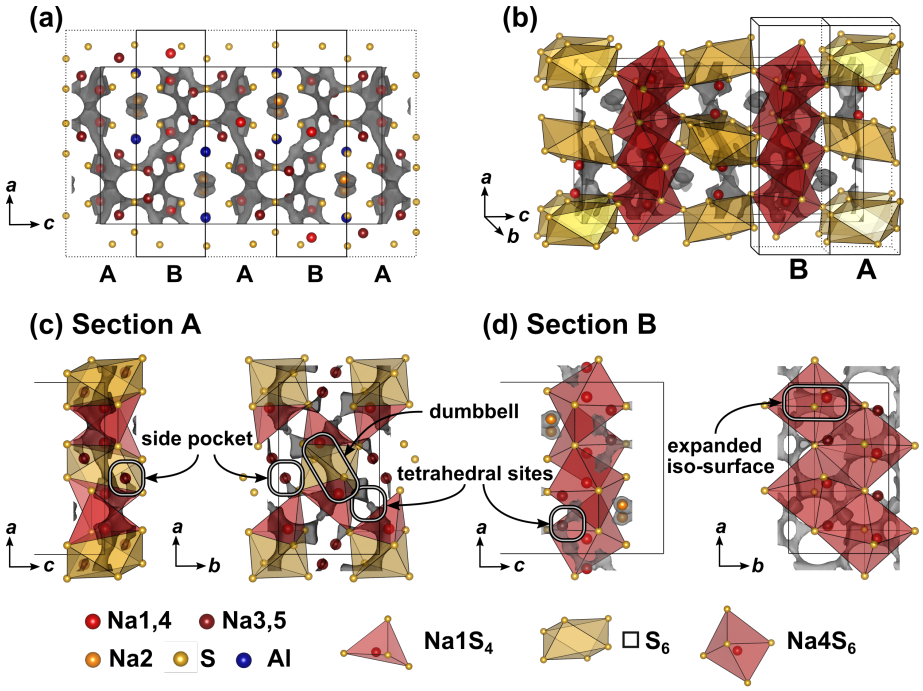

Figure 5.5: **(a)**: Na_5AlS_4 crystal structure viewed along b direction. Bond valence energy landscape at isoenergy value of $-2.40\,\text{eV}$ ($E_{min}^{global} = -3.71\,\text{eV}$, $E_{min}^{path} = -3.43\,\text{eV}$, $E_{mig}^{path} = -2.58\,\text{eV}$,$\Delta E_{3D} = 0.83\,\text{eV}$). The unit cell is divided along the crystallographic c direction into alternating sections **A** and **B**. **(b)**: Na_5AlS_4 unit cell with sections **A** and **B**. **(c)**: Section **A** ($c = 0.9 - 1.1$) viewed along b and c. **(d)**: Section **B** ($c = 0.6 - 0.9$) viewed along b and c.

Section **B** comprises a two-dimensional network composed of larger areas of low sodium ion bond valence energy (expanded isosurface) connected *via* unoccupied tetrahedral sites. These rectangular shaped areas, residing inside an octahedral cavity created by six sulfide ions (red octahedron, Figure 5.5D), display regions in which sodium can migrate freely without passing through high energy bottlenecks. This region is visible at low bond valence isoenergy of −3.0 eV in Figure S4 in the SI. Na4 resides in one of the corners of the expanded isosurface, thus creating a [$Na4S_6$] coordination polyhedron. The [$Na4S_6$] octahedra are connected *via* unoccupied tetrahedral sites forming a percolating network. The infinite [AlS_4]-[NaS_6] chains obstruct ion conduction along the crystallographic c direction, but allow connection of both sections **A** and **B** at the gap between two chains as depicted with the maroon colored curved lines in Figure 5.2C, D forming a zig-zag pattern along c and a two-dimensional pattern in the ab plane. Consequently, despite its more dominant 2D conduction pathways in ab plane, Na_5AlS_4 is expected to be a three-dimensional ion conductor.

BVEL calculations for Na_4SiS_4.

For simplification, the orthorhombic structure with a shorter a axis in Figure S5 instead of the superstructure of Na_4SiS_4 in Figure 5.3 was used to calculate the bond valence energy landscape for Na_4SiS_4. This does not lead to an appreciably different BVEL outcome, since the superstructure is a result of sodium atom ordering. The anionic lattice remains the same in both structure models. Figure 5.6 depicts the structure of Na_4SiS_4 together with bond valence energy surfaces of different isoenergy values.

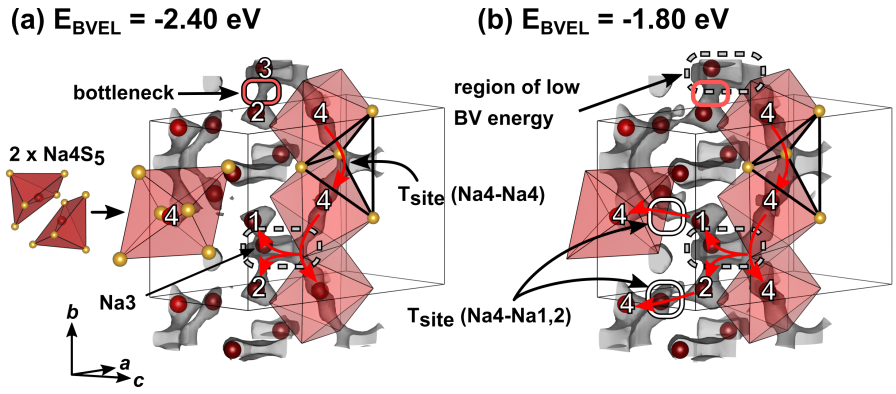

Figure 5.6: Crystal structure of Na_4SiS_4 (simplified model without superstructure) with sodium atoms drawn in red and sulfur atoms drawn in yellow. Bond valence energy landscape at isoenergy values of **(a)**: −2.40 eV and **(b)**: −1.80 eV are drawn in gray ($E_{min}^{global} = -3.73\,\text{eV}$, $E_{min}^{path} = -3.73\,\text{eV}$, $E_{mig}^{path} = -2.68\,\text{eV}, \Delta E_{2D} = 1.05\,\text{eV}$). Red arrows depict sodium ion diffusion pathways. Numbers denote crystallographic sodium sites.

A more detailed illustration of the evolution of BVE isosurfaces can be found in Figure S5. As depicted in Figure 5.6, Na4 occupies a distorted square pyramid. Two base-sharing pyramids form a larger octahedron with Na4 preferentially occupying one half of the octahedron. In a short range, hopping through the common base of two adjacent square pyramids is energetically facile for Na4. For long-range diffusion, Na4 can hop *via* a tetrahedral site spanned by two [$Na4S_6$] units into an expanded region of low bond valence energy (up or down along b). Na3 resides close to one of the [$Na4S_6$] unit's corners. Despite being connected to this low energy site as well, Na1 and Na2 have to pass a bottleneck when diffusing to this site. Therefore, mainly Na4 and Na3 form a quasi-one-dimensional, channel-like structure in b direction. At slightly higher bond valence energies tetrahedral sites between Na4-Na1 and Na4-Na2 are accessible through small bottlenecks (see Figure 5.6B, gray isosurface marked with red ellipses). The resulting network percolates the unit cell in all crystallographic directions, resulting in 3D ion migration at higher energies ($\Delta_{3D} \approx 1.6\,\mathrm{eV}$).

BVEL calculations for $Na_9(AlS_4)(SiS_4)$.

Compared to Na_5AlS_5 and Na_4SiS_4, the double salt $Na_9(AlS_4)(SiS_4)$ is structurally more complex, since it features 18 sodium sites hosted in mostly distorted coordination polyhedra. Only Na13 resides in a rather ordered [$Na13S_6$]-octahedron, which is bridged in c direction by corner-sharing $[AlS_4]^{5-}/[SiS_4]^{4-}$-tetrahedra (cf. Figure 5.7 and Figure 5.4).
In terms of conduction pathways, the sodium ions in $Na_9(AlS_4)(SiS_4)$ can be divided into isolated and migrating sodium ions. Migrating sodium ions, depicted as red spheres in Figure 5.7, reside inside the calculated BVEL network at isoenergy E_{mig}^{path}. Most of the sodium ions contributing to the three-dimensional conduction are mainly square-pyramidally coordinated, but also trigonal bipyramidal, tetrahedral or octahedral coordinated. Presumably, the low local coordination symmetry of those sodium ions and the therefore asymmetric charge distribution leads to less coulombic attraction facilitating ion hopping.

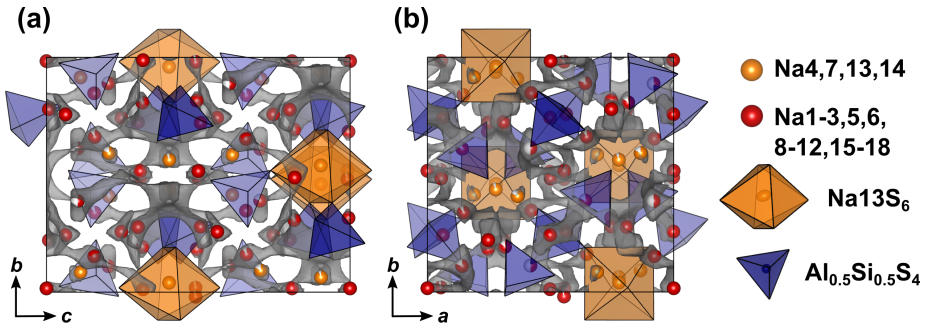

Figure 5.7: Crystal structure of $Na_9(AlS_4)(SiS_4)$ along **(a)**: a and **(b)**: c direction. The bond valence energy landscape at isoenergy value of $-2.60\,\mathrm{eV}$ is drawn in gray ($E_{min}^{global} = -4.02\,\mathrm{eV}$, $E_{min}^{path} = -3.86\,\mathrm{eV}$, $E_{mig}^{path} = -2.64\,\mathrm{eV}$, $\Delta E_{3D} = 1.22\,\mathrm{eV}$).

However, the either trigonal bipyramidally (Na4,7), tetrahedrally (Na14) or octahedrally (Na13) coordinated sodium ions are not connected to the conduction network at E_{mig}^{path} and thus are considered to be members of the rigid framework (cf. Figure S6). At noticeably higher energy all sodium ions but Na13 connect to a large, expanded network. Summarizing, at E_{mig}^{path} a very flat three-dimensional isoenergy surface with only a few bottle necks occupies a large volume fraction of the unit cell. Compared to Na_5AlS_4 and Na_4SiS_4, in terms of conduction pathways, the sodium ions in $Na_9(AlS_4)(SiS_4)$ are expected to show higher mobility due to higher versatility in the sodium ion coordination and the resulting flatter potential energy surface for sodium ion migration.

5.4.4 Electrochemical Impedance Spectroscopy

Electrochemical impedance spectroscopy in the temperature range 25 – 75 °C was conducted on cold pressed samples of all members in the series $Na_{5-x}Al_{1-x}Si_xS_4$ with ($0 \leq x \leq 1$). As depicted in Figure 5.8, they show averaged sodium ion conductivities ranging from $1.64 \cdot 10^{-7}\,S\,cm^{-1}$ for Na_4SiS_4 up to $2.04 \cdot 10^{-5}\,S\,cm^{-1}$ for $Na_{8.5}(AlS_4)_{0.5}(SiS_4)_{1.5}$. Galvanostatic polarization measurements (cf. Figure S7) confirm the mainly ion conducting nature of the materials with transference numbers of about 0.9998, thus being suitable as solid electrolyte in a battery. The conductivities in Figure 5.8 represent the total conductivities of the samples, modelled by a capacitor or constant phase element (CPE) and a resistance (R) in parallel. Where necessary, a second R-CPE-element was added, and in each spectrum the polarization of ions at the interface of the blocking electrode was modelled by a CPE. Exemplary impedance spectra and equivalent circuits of each sample as well as the respective capacitances and ideality factors (α) are given in the SI in Figure S8 and Table S12. The effective capacitances (C_{eff}) were calculated by the Brug formula[46] $C_{eff}=(R(CPE))^{1/\alpha}/R$. The best conducting sample $Na_{8.5}(AlS_4)_{0.5}(SiS_4)_{1.5}$ shows only one semicircle with a capacitance of about $2 \cdot 10^{-10}\,F$. The capacitances of the high frequency semicircle of all other samples are of the same order of magnitude, suggesting the same underlying processes. According to literature, the capacitance of $1 \cdot 10^{-10}\,F$ corresponds to grain boundary contributions.[47] Thus, the high frequency arc contains the information about the bulk and grain boundaries, but the exact bulk contributions can not be deconvoluted. In some spectra a second semicircle at lower frequencies with capacitances of about $8 \cdot 10^{-8}\,F - 6 \cdot 10^{-7}\,F$ is present. The activation energies of this process, calculated according to $\sigma = \sigma_0/T \cdot e^{-E_a/k_BT}$ (with σ_0 being the prefactor, E_a the activation energy, k_B the Boltzmann constant and T the temperature), are higher than the activation energies obtained from the high frequency semicircles (cf. Table S14 and Table S15). Consequently, this semicircle may stem from an inhomogeneity in composition or an additional resistive layer on the surface.[47,48] Interestingly, the low frequency semicircle is absent for the best conducting sample $Na_{8.5}(AlS_4)_{0.5}(SiS_4)_{1.5}$ pointing to an easier handling of this material. To avoid a mingling of processes, only the data from the high frequency semicircle is applied for discussing the trends in activation energy and prefactor in the following. A plot only including conductivities calculated from the high frequency semicircles is given in Figure S9. It exhibits the same trend as in Figure 5.8 with $Na_{8.5}(AlS_4)_{0.5}(SiS_4)_{1.5}$ being

the best conducting member of the series.

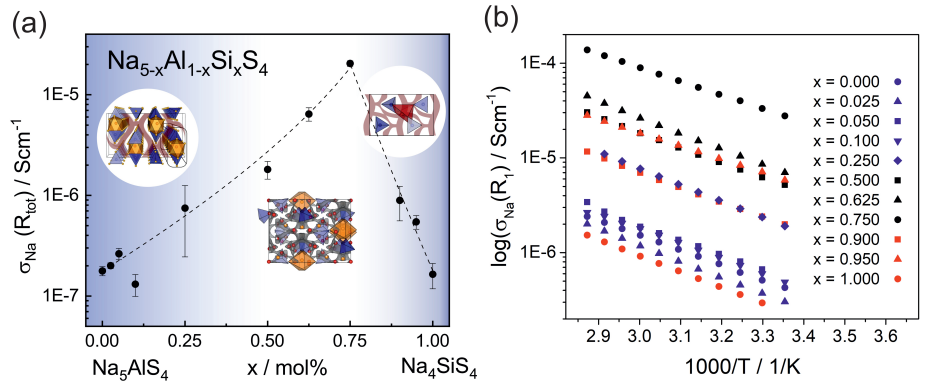

Figure 5.8: **(a)**: Sodium ion conductivity in the phase system $Na_{5-x}Al_{1-x}Si_xS_4$ with ($0 \leq x \leq 1$) as a function of the substitution factor x (visualized by dashed line). In the range of $x = 0.50$ – 0.75, where the material crystallizes in the $Na_9(AlS_4)(SiS_4)$-structure, the highest average conductivity of $2.04 \cdot 10^{-5}\,S\,cm^{-1}$ was observed. The unsubstituted phases Na_5AlS_4 and Na_4SiS_4 show a significantly lower ionic conductivity of $1.64 \cdot 10^{-7}\,S\,cm^{-1}$-$1.77 \cdot 10^{-7}\,S\,cm^{-1}$, respectively. The error bars include the standard deviation of the sample and the error of the measurement of about 8%. **(b)**: Temperature dependent sodium ion conductivities calculated from R1 of all phases for a selection of measurements (all parameters for these particular measurements are given in Table S12 and Table S13). The different colors indicate the different crystal structures: Na_5AlS_4-structure (blue), $Na_9(AlS_4)(SiS_4)$-structure (black) and Na_4SiS_4-structure (red)

5.4.5 Discussion

Taking a closer look at Figure 5.8 and S9 reveals the strong influence of the number of charge carriers on the conductivity of each material. Going from the poor ionic conductor Na_5AlS_4 along the isotypic phases up to $x = 0.25$, the substitution of Al^{3+} with Si^{4+} introduces sodium vacancies, which increases the conductivity. On the other end of the series, Na_4SiS_4 shows a σ_{Na} in line with findings from.[30] Here, the amount of sodium ions is increased in the form of interstitials by substitution with Al^{3+}. The BVEL analysis suggests an occupation of tetrahedral sites between Na4-Na1 and Na4-Na2 as interstitial positions for the sodium ions (cf. Figure 5.6). This would be consistent with more efficient 3D ion migration in the structure and overall facilitation of the ion transport.
In the range of $x = 0.50 - 0.75$, where the $Na_9(AlS_4)(SiS_4)$-structure is stable, the highest conductivities are found. The topology of $Na_9(AlS_4)(SiS_4)$ does not resemble the one of Na_4SiS_4 but shows similarities to Na_5AlS_4 with a distorted hexagonal packing of $[Al/SiS_4]$-$[Na2S_6]$-chains. The structure features (migrating) Na ions whose highly distorted coordination polyhedra are connected to other sodium sites mostly *via* faces and edges, which facilitates ion hopping and approximates 3D diffusion.[49] In this sense, the double salt

$Na_9(AlS_4)(SiS_4)$ thus shows similarities to the well known tetragonal LGPS-phase which shows exceptionally high ionic conductivity that is in part attributable to the low energy barrier for lithium diffusion between face-sharing $[LiS_4]$-tetrahedra.[25,50] Additionally, the BVEL analysis of $Na_9(AlS_4)(SiS_4)$ indicates a similar situation to the frustrated energy landscape leading to superionic diffusion in $LiTi_2(PS_4)_3$:[51] The sodium coordination environments are more diverse and the coordination polyhedra more distorted in the double salt $Na_9(AlS_4)(SiS_4)$ compared to the border phases of the substitution series $Na_{5-x}Al_{1-x}Si_xS_4$. This low local coordination symmetry of sodium and connection of its coordination polyhedra lead to a flat energy landscape for sodium cations in $Na_9(AlS_4)(SiS_4)$, which is beneficial for ion transport.

By further exchanging $[AlS_4]^{5-}$ anions by $[SiS_4]^{4-}$ anions in $Na_9(AlS_4)(SiS_4)$, sodium vacancies are introduced. Within the series $Na_{5-x}(AlS_4)_{1-x}(SiS_4)_x$ the value $x = 0.75$ ($Na_{8.5}(AlS_4)_{0.5}(SiS_4)_{1.5}$) constitutes the optimum for the observed ionic conductivity of $2.04 \cdot 10^{-5}\,S\,cm^{-1}$ and the lowest activation energy in the series of 0.30 eV as shown in Table S15, reflecting the flattening of the energy landscape proposed by the BVEL calculations. For all other members of the series the activation energies are rather similar within their standard deviation, at around 0.35 – 0.40 eV (cf. Figure S10). Besides, the prefactors σ_0 of the best conducting members of the series exceed the prefactors of the end members by one to two orders of magnitude (cf. Table S13), although the activation energy is lowered (cf. Figure S10). The prefactor takes into account the charge carrier density of mobile ions, the entropy of migration, the jump distance and the attempt frequency, among others. Recently, Kraft *et al.* systematically increased the lattice softness in a series of ionic conductors and noted that a decrease in activation energy is accompanied by a decrease in prefactor, which is in line with the Meyer-Nedel-rule.[16] Accordingly, in cases where this rule applies, possible conductivity improvements via lattice softness engineering are inherently limited. However,[51] showed for $LiTi_2(PS_4)_3$ that the highly distorted coordination polyhedra of lithium lead to a frustrated energy landscape, lowering the energy barrier, but increasing the prefactor due to longer jump distances and a higher entropy for the transition state. In $Na_{8.5}(AlS_4)_{0.5}(SiS_4)_{1.5}$ a similar influence on the prefactor as in $LiTi_2(PS_4)_3$ can be inferred due to the flattening of the energy landscape by the highly distorted sodium coordination polyhedra. However, the high prefactor for the sample $x = 0.95$ compared to the composition with the highest conductivity at $x = 0.75$ could hint to an even more complicated situation in this series of compounds, necessitating further studies on the complex interplay between structural factors and the energetics of ion transport in these systems.

Performance-wise, $Na_{8.5}(AlS_4)_{0.5}(SiS_4)_{1.5}$ with an ionic conductivity of $2.04 \cdot 10^{-5}\,S\,cm^{-1}$ and an activation energy of 0.30 eV is comparable to compounds such as $Na_{10}SnP_2S_{12}$,[28] silicon substituted Na_3PS_4,[30] and HT$-NaSi_2P_3$.[52] As can be concluded from the absence of additional resistances at lower frequencies, this material presumably shows an advantageous microstructure or pressing behavior. Furthermore, the smaller electron affinities of Al^{3+} and Si^{4+} may result in increased electrochemical stability at low potentials compared to thiophosphates such as Na_3PS_4, which will be the subject of future studies.

5.5 Conclusion

We have presented the crystal structures and Na ion conductivities in the novel substitution series $Na_{5-x}Al_{1-x}Si_xS_4$ with $(0 \leq x \leq 1)$, containing exclusively low-cost, earth-abundant and lightweight elements. For the best conducting compound $Na_{8.5}(AlS_4)_{0.5}(SiS_4)_{1.5}$ ($x = 0.75$), a relatively high sodium ion conductivity of $2.04 \cdot 10^{-5}\,S\,cm^{-1}$ at room temperature with an activation energy of 0.30 eV was found, putting this material on par with typical sodium solid electrolytes such as silicon substituted Na_3PS_4[30] and $Na_{10}SnP_2S_{12}$.[28] Our analysis of impedance and BVEL data for the substitution series $Na_{5-x}Al_{1-x}Si_xS_4$ $(0 \leq x \leq 1)$ unveils probable sodium ion migration paths and highlights the enhancement of the conductivity by the low local coordination symmetry of the sodium ions flattening out the potential energy landscape and the increase of sodium ion vacancies in $Na_{8.5}(AlS_4)_{0.5}(SiS_4)_{1.5}$. Concluding, the right blend of the cations Al^{3+} and Si^{4+} entails an optimized structure as well as optimal amount of charge carriers for fast sodium ion conduction.

Author Contributions

SH, AKH and BVL conceived and designed this study; SH and CaH conducted the synthesis; SH, AKH and CaH were responsible for measuring SCXRD, PXRD, NMR and EIS; SH performed structure determination; CoH helped in interpretation of crystal structure data; CS performed the calculation and interpretation of BVEL data; AKH analysed measured EIS data; SH, AKH and CS wrote sections of the manuscript; All authors wrote and commented on the manuscript.

Funding

Financial support was granted by the German Federal Ministry of Research and Education (BMBF), project 03XP0177B (FestBatt), the Cluster of Excellence e-conversion, and the Center for NanoScience (CeNS).

Acknowledgments

We would like to thank Christian Minke for his assistance in measuring solid state NMR spectra, Juliane Stahl for her assistance in measuring SEM/EDX data and Arthur Haffner for his assistance in measuring SCXRD data.

Supplemental Data

Electronic Supplementary Information (ESI) available: additional crystallographic data, thermal analysis, EDX measurements and SEM micrographs, supplementary data for BVEL calculations and electrochemical characterization. See DOI: 10.3389/fchem.2020.00090.

Bibliography

(1) Goodenough, J. B. Rechargeable batteries: challenges old and new. *J. Solid State Electrochem.* **2012**, *16*, 2019–2029.

(2) Janek, J.; Zeier, W. G. A solid future for battery development. *Nat. Energy* **2016**, *1*, 16141.

(3) Kato, Y.; Hori, S.; Saito, T.; Suzuki, K.; Hirayama, M.; Mitsui, A.; Yonemura, M.; Iba, H.; Kanno, R. High-power all-solid-state batteries using sulfide superionic conductors. *Nat. Energy* **2016**, *1*, 16030.

(4) Yabuuchi, N.; Kubota, K.; Dahbi, M.; Komaba, S. Research Development on Sodium-Ion Batteries. *Chem. Rev.* **2014**, *114*, 11636–11682.

(5) Lotsch, B. V.; Maier, J. Relevance of solid electrolytes for lithium-based batteries: A realistic view. *J. Electroceram.* **2017**, *38*, 128–141.

(6) Kamaya, N.; Homma, K.; Yamakawa, Y.; Hirayama, M.; Kanno, R.; Yonemura, M.; Kamiyama, T.; Kato, Y.; Hama, S.; Kawamoto, K.; Mitsui, A. A lithium superionic conductor. *Nat. Mater.* **2011**, *10*, 682–686.

(7) Rao, R. P.; Adams, S. Studies of lithium argyrodite solid electrolytes for all-solid-state batteries. *Phys. status solidi* **2011**, *208*, 1804–1807.

(8) Jansen, M.; Henseler, U. Synthesis, structure determination, and ionic conductivity of sodium tetrathiophosphate. *J. Solid State Chem.* **1992**, *99*, 110–119.

(9) Hayashi, A.; Noi, K.; Sakuda, A.; Tatsumisago, M. Superionic glass-ceramic electrolytes for room-temperature rechargeable sodium batteries. *Nat. Commun.* **2012**, *3*, 855–856.

(10) Holzmann, T.; Schoop, L. M.; Ali, M. N.; Moudrakovski, I.; Gregori, G.; Maier, J.; Cava, R. J.; Lotsch, B. V. $Li_{0.6}[Li_{0.2}Sn_{0.8}S_2]$ - a layered lithium superionic conductor. *Energy Environ. Sci.* **2016**, *9*, 2578–2585.

(11) Kuhn, A.; Gerbig, O.; Zhu, C.; Falkenberg, F.; Maier, J.; Lotsch, B. V. A new ultrafast superionic Li-conductor: ion dynamics in $Li_{11}Si_2PS_{12}$ and comparison with other tetragonal LGPS-type electrolytes. *Phys. Chem. Chem. Phys.* **2014**, *16*, 14669–14674.

(12) Kuhn, A.; Köhler, J.; Lotsch, B. V. Single-crystal X-ray structure analysis of the superionic conductor $Li_{10}GeP_2S12$. *Phys. Chem. Chem. Phys.* **2013**, *15*, 11620.

(13) Wakamura, K. Roles of phonon amplitude and low-energy optical phonons on superionic conduction. *Phys. Rev. B* **1997**, *56*, 11593–11599.

(14) Bachman, J. C.; Muy, S.; Grimaud, A.; Chang, H.-H.; Pour, N.; Lux, S. F.; Paschos, O.; Maglia, F.; Lupart, S.; Lamp, P.; Giordano, L.; Shao-Horn, Y. Inorganic Solid-State Electrolytes for Lithium Batteries: Mechanisms and Properties Governing Ion Conduction. *Chem. Rev.* **2016**, *116*, 140–162.

(15) Krauskopf, T.; Pompe, C.; Kraft, M. A.; Zeier, W. G. Influence of Lattice Dynamics on Na^+ Transport in the Solid Electrolyte $Na_3PS_{4-x}Se_x$. *Chem. Mater.* **2017**, *29*, 8859–8869.

(16) Kraft, M. A.; Culver, S. P.; Calderon, M.; Bo, F.; Krauskopf, T.; Senyshyn, A.; Dietrich, C.; Zevalkink, A.; Janek, J.; Zeier, W. G. Influence of Lattice Polarizability on the Ionic Conductivity in the Lithium Superionic Argyrodites Li_6PS_5X (X = Cl, Br, I). *J. Am. Chem. Soc.* **2017**, *139*, 10909–10918.

(17) Hayashi, A.; Noi, K.; Tanibata, N.; Nagao, M.; Tatsumisago, M. High sodium ion conductivity of glass–ceramic electrolytes with cubic Na_3PS_4. *J. Power Sources* **2014**, *258*, 420–423.

(18) Krauskopf, T.; Culver, S. P.; Zeier, W. G. Local Tetragonal Structure of the Cubic Superionic Conductor Na_3PS_4. *Inorg. Chem.* **2018**, *57*, 4739–4744.

(19) Zhang, L.; Yang, K.; Mi, J.; Lu, L.; Zhao, L.; Wang, L.; Li, Y.; Zeng, H. Na_3PSe_4: A Novel Chalcogenide Solid Electrolyte with High Ionic Conductivity. *Adv. Energy Mater.* **2015**, *5*, 1501294.

(20) Krauskopf, T.; Muy, S.; Culver, S. P.; Ohno, S.; Delaire, O.; Shao-Horn, Y.; Zeier, W. G. Comparing the Descriptors for Investigating the Influence of Lattice Dynamics on Ionic Transport Using the Superionic Conductor $Na_3PS_{4-x}Se_x$. *J. Am. Chem. Soc.* **2018**, *140*, 14464–14473.

(21) Kuhn, A.; Duppel, V.; Lotsch, B. V. Tetragonal $Li_{10}GeP_2S_{12}$ and Li_7GePS_8 – exploring the Li ion dynamics in LGPS Li electrolytes. *Energy Environ. Sci.* **2013**, *6*, 3548.

(22) Bron, P.; Johansson, S.; Zick, K.; Schmedt auf der Günne, J.; Dehnen, S.; Roling, B. $Li_{10}SnP_2S_{12}$: An Affordable Lithium Superionic Conductor. *J. Am. Chem. Soc.* **2013**, *135*, 15694–15697.

(23) Kato, Y.; Saito, R.; Sakano, M.; Mitsui, A.; Hirayama, M.; Kanno, R. Synthesis, structure and lithium ionic conductivity of solid solutions of $Li_{10}(Ge_{1-x}M_x)P_2S_{12}$ (M = Si, Sn). *J. Power Sources* **2014**, *271*, 60–64.

(24) Hori, S.; Taminato, S.; Suzuki, K.; Hirayama, M.; Kato, Y.; Kanno, R. Structure-property relationships in lithium superionic conductors having a $Li_{10}GeP_2S_{12}$-type structure. *Acta Crystallogr. Sect. B Struct. Sci. Cryst. Eng. Mater.* **2015**, *71*, 727–736.

(25) Hori, S.; Kato, M.; Suzuki, K.; Hirayama, M.; Kato, Y.; Kanno, R. Phase Diagram of the Li_4GeS_4 – Li_3PS_4 Quasi-Binary System Containing the Superionic Conductor $Li_{10}GeP_2S_{12}$. *J. Am. Ceram. Soc.* **2015**, *98*, ed. by Sprenkle, V., 3352–3360.

(26) Bron, P.; Dehnen, S.; Roling, B. $Li_{10}Si_{0.3}Sn_{0.7}P_2S_{12}$ – A low-cost and low-grain-boundary-resistance lithium superionic conductor. *J. Power Sources* **2016**, *329*, 530–535.

(27) Harm, S.; Hatz, A.-K.; Moudrakovski, I.; Eger, R.; Kuhn, A.; Hoch, C.; Lotsch, B. V. Lesson Learned from NMR: Characterization and Ionic Conductivity of LGPS-like Li_7SiPS_8. *Chem. Mater.* **2019**, *31*, 1280–1288.

(28) Richards, W. D.; Tsujimura, T.; Miara, L. J.; Wang, Y.; Kim, J. C.; Ong, S. P.; Uechi, I.; Suzuki, N.; Ceder, G. Design and synthesis of the superionic conductor $Na_{10}SnP_2S_{12}$. *Nat. Commun.* **2016**, *7*, 11009.

(29) Duchardt, M.; Ruschewitz, U.; Adams, S.; Dehnen, S.; Roling, B. Vacancy-Controlled Na^+ Superion Conduction in $Na_{11}Sn_2PS_{12}$. *Angew. Chemie Int. Ed.* **2018**, *57*, 1351–1355.

(30) Tanibata, N.; Noi, K.; Hayashi, A.; Tatsumisago, M. Preparation and characterization of highly sodium ion conducting Na_3PS_4 – Na_4SiS_4 solid electrolytes. *RSC Adv.* **2014**, *4*, 17120–17123.

(31) Shannon, R. D. Revised effective ionic radii and systematic studies of interatomic distances in halides and chalcogenides. *Acta Crystallogr.* **1976**, *A32*, 751–767.

(32) Brown, A. P.; Tani, B. S. Powder X-ray diffraction identification of some new phases in the Na_2S – Al_2S_3 system. *Mater. Res. Bull.* **1987**, *22*, 1029–1037.

(33) Coelho, A. A. TOPAS and TOPAS-Academic : an optimization program integrating computer algebra and crystallographic objects written in C++. *J. Appl. Crystallogr.* **2018**, *51*, 210–218.

(34) Oszlányi, G.; Sütő, A. The charge flipping algorithm. *Acta Crystallogr.* **2008**, *A64*, 123–134.

(35) Krause, L.; Herbst-Irmer, R.; Sheldrick, G. M.; Stalke, D. Comparison of silver and molybdenum microfocus X-ray sources for single-crystal structure determination. *J. Appl. Crystallogr.* **2015**, *48*, 3–10.

(36) Sheldrick, G. M. A short history of SHELX. *Acta Crystallogr. Sect. A Found. Crystallogr.* **2008**, *64*, 112–122.

(37) Sale, M.; Avdeev, M. *3DBVSMAPPER*: a program for automatically generating bond-valence sum landscapes. *J. Appl. Cryst.* **2012**, *45*, 1054–1056.

(38) Nishitani, Y.; Adams, S.; Ichikawa, K.; Tsujita, T. Evaluation of magnesium ion migration in inorganic oxides by the bond valence site energy method. *Solid State Ionics* **2018**, *315*, 111–115.

(39) Adams, S.; Rao, R. P. High power lithium ion battery materials by computational design. *Phys. Status Solidi A* **2011**, *208*, 1746–1753.

(40) Momma, K.; Izumi, F. *VESTA3* for three-dimensional visualization of crystal, volumetric and morphology data. *J. Appl. Cryst.* **2011**, *44*, 1272–1276.

(41) Vegard, L. Die Konstitution der Mischkristalle und die Raumfüllung der Atome. *Z. Phys.* **1921**, *5*, 17–26.

(42) Brachtel, G.; Hoppe, R. Neue Oxoferrate(III). Zur Kenntnis von Na_5FeO_4. *Z. anorg. allg. Chem.* **1978**, *446*, 77–86.

(43) Bender, J.; Wohlfarth, A.; Hoch, C. Crystal Structures of New Alkali Metal-rich Oxometallates: Rubidium Aluminate Tetrahydroxide, $Rb_9(AlO_4)(OH)_4$, Rubidium Orthogallate, Rb_5GaO_4, Caesium bis-Chromate(IV) Oxide, $Cs_{10}(CrO_4)_2O$, and Caesium Diindate, $Cs_8In_2O_7$. *Z. Naturforsch. B* **2010**, *65*, 1416–1426.

(44) Xiao, R.; Li, H.; Chen, L. High-throughput design and optimization of fast lithium ion conductors by the combination of bond-valence method and density functional theory. *Sci. Rep.* **2015**, *5*, 14227.

(45) Avdeev, M.; Sale, M.; Adams, S.; Rao, R. P. Screening of the alkali-metal ion containing materials from the Inorganic Crystal Structure Database (ICSD) for high ionic conductivity pathways using the bond valence method. *Solid State Ionics* **2012**, *225*, 43–46.

(46) Brug, G.; van den Eeden, A.; Sluyters-Rehbach, M.; Sluyters, J. The analysis of electrode impedances complicated by the presence of a constant phase element. *J. Electroanal. Chem. Interfacial Electrochem.* **1984**, *176*, 275–295.

(47) Irvine, J. T. S.; Sinclair, D. C.; West, A. R. Electroceramics: Characterization by Impedance Spectroscopy. *Adv. Mat.* **1990**, *2*, 132–138.

(48) Bruce, P. G.; West, A. R. The A-C Conductivity of Polycrystalline LISICON, $Li_{2+2x}Zn_{1-x}GeO_4$, and a Model for Intergranular Constriction Resistances. *J. Electrochem. Soc.* **1983**, *130*, 662–669.

(49) West, A. R.; Bruce, P. G. Tetragonal-Packed Crystal Structures. *Acta Crystallogr.* **1982**, *38*, 1891–1896.

(50) Wang, Y.; Richards, W. D.; Ong, S. P.; Miara, L. J.; Kim, J. C.; Mo, Y.; Ceder, G. Design principles for solid-state lithium superionic conductors. *Nat. Mater.* **2015**, *14*, 1026–1031.

(51) Di Stefano, D.; Miglio, A.; Robeyns, K.; Filinchuk, Y.; Lechartier, M.; Senyshyn, A.; Ishida, H.; Spannenberger, S.; Prutsch, D.; Lunghammer, S.; Rettenwander, D.; Wilkening, M.; Roling, B.; Kato, Y.; Hautier, G. Superionic Diffusion through Frustrated Energy Landscape. *Chem.* **2019**, *5*, 2450–2460.

(52) Haffner, A.; Hatz, A.-K.; Moudrakovski, I.; Lotsch, B. V.; Johrendt, D. Fast Sodium-Ion Conductivity in Supertetrahedral Phosphidosilicates. *Angew. Chem. Int. Ed.* **2018**, *57*, 6155–6160.

Chapter 6

Summary and Outlook

The scope of this work was to find, characterize and optimize new sulfide based lithium and sodium ion conductors utilizing earth abundant main group elements, to expand the field of low-cost solid electrolyte materials.

In chapter 3 two new compounds, tetragonal and orthorhombic Li_7SiPS_8, were presented. The latter crystallizes homeotypically to the pseudo-binary border phases β–Li_3PS_4 and Li_4SiS_4 showing a distorted *hcp* of sulfur atoms with the cations occupying the tetrahedral and octahedral voids and therefore falls into the class of LISICON materials. It exhibits a total ionic conductivity of $1.3 \cdot 10^{-4}\,\mathrm{S\,cm^{-1}}$ with an activation energy of 0.29 eV. Tetragonal Li_7SiPS_8 on the other hand exhibits a total conductivity of $2 \cdot 10^{-3}\,\mathrm{S\,cm^{-1}}$ with an activation energy of 0.27 eV. It crystallizes homeotypically to the well known superionic conductor LGPS ($Li_{10}GeP_2S_{12}$) and shows a phase transformation to the orthorhombic modification at temperatures exceeding 550 °C. While being a fast ion conductor in absolute terms, the total conductivity of tetragonal Li_7SiPS_8 is unexpectedly low considering not only the theoretical studies by Ceder *et al.*[1] but also the diffusivity measurements performed in this work. Using a combination of electrochemical impedance spectroscopy, powder X-ray diffraction (PXRD) and different solid-state NMR techniques, it could be shown that tetragonal Li_7SiPS_8, although appearing phase pure in PXRD, is a glassy ceramic. The additional amorphous phases of proposed composition $Li_{3.2}Si_{0.2}P_{0.8}S_4$ significantly impede the total ionic conductivity. The bulk conductivity of tetragonal Li_7SiPS_8 was determined by pulsed field gradient solid-state NMR to be at least $5 \cdot 10^{-3}\,\mathrm{S\,cm^{-1}}$ not considering correlation effects. These should however, assuming typical Haven ratios for other LGPS-like compounds, increase its conductivity well beyond $10^{-2}\,\mathrm{S\,cm^{-1}}$.

Furthermore, as described in chapter 4.1, it was possible to substitute silicon by aluminum in tetragonal Li_7SiPS_8, resulting in the partial solid solution series $Li_{7+x}Si_{1-x}Al_xPS_8$ with $0 \leq x \leq 0.15$. Although this substitution increases the charge carrier concentration and size of the lithium diffusion channels and should therefore increase the conductivity, a marginal decrease of the total conductivity can be observed. This observation was attributed to a change in the composition of the amorphous side phases described above. It

is therefore of utmost importance to understand the reason why these amorphous phases form and how their formation can be suppressed to further improve this very promising solid electrolyte.
In this regard, first investigations, described in chapter 4.2, showed that upon addition of lithium chloride and lithium sulfide the formation of the amorphous side phases can almost completely be inhibited by forming lithium argyrodite $Li_{7+x-y}P_{1-x}Si_xS_{6-y}Cl_y$. However, although the amorphous side phase is removed, no dramatic increase in conductivity was observed. This was attributed to the formation of additional, less conductive orthorhombic $Li_{7-x}Si_{1-x}P_xS_8$. However, further addition of LiCl and Li_2S leads to the formation of another amorphous Li argyrodite-like phase, increasing the conductivity of the resulting mixture to $4 \cdot 10^{-3}\,\mathrm{S\,cm^{-1}}$ with an activation energy of 0.17 eV.
The optimization of tetragonal Li_7SiPS_8 by tuning its microstructure using lithium chloride and sulfide to form lithium argyrodites is very promising. Further studies should also include heavier halides due to their increased polarizability, which typically decreases the activation energy for ion conduction. Additionally, investigation to inhibit the formation of amorphous side phases could lead to very promising solid electrolyte materials. For an application of the new solid electrolytes, further research should include evaluation of the electrochemical stability against typical cathode materials and lithium metal, followed by full cell assemblies to determine their long-term performance in a battery.

In chapter 5 the solid solution series $Na_{5-x}Si_{1-x}Al_xS_4$ with $(0 \leq x \leq 1)$ was introduced. These solid sodium electrolytes crystallize in three new crystal structures and exhibit ionic conductivities ranging from $2 \cdot 10^{-7}\,\mathrm{S\,cm^{-1}}$ ($E_a = 0.35\ eV$) for the pseudo-binary border phases Na_5AlS_4 and Na_4SiS_4 to $2 \cdot 10^{-5}\,\mathrm{S\,cm^{-1}}$ ($E_a = 0.30\ eV$) for the double salt $Na_{8.5}(AlS_4)_{0.5}(SiS_4)_{1.5}$. Na_4SiS_4 can be described as a *hcp* of sulfur with silicon occupying tetrahedral and sodium octahedral voids, showing its close relation to the LISICON family. Since Na_5AlS_4 crystallizes isotypic to Na_5FeO_4 and therefore shows a different sulfur packing, it is unsurprising that only partial miscibility of the two pseudo-binary border phases exists, which however substantially increases their ionic conductivity through the introduction of sodium vacancies or the occupation of sodium interstitial sites, respectively. The double salt $Na_{10-2x}(AlS_4)_{2-2x}(SiS_4)_{2x}$ resulting from higher degrees of substitution $(0.5 \leq x \leq 0.75)$ crystallizes in its own structure type and shows the highest total sodium ion conductivity in this substitution series. Utilizing bond valence energy landscape calculations probable sodium ion migration paths for all three structures were identified. These calculations revealed a flattened energy landscape for sodium ions in the double salt compared to the pseudo-binary border phases caused by the low local coordination symmetry of sodium ions. This does not only decrease the activation energy for ion migration but also affects the entropy of migration, ultimately increasing the ionic conductivity of the double salt.
Further studies on these materials should focus on the introduction of defects by e.g. ball milling. Increasing the defect concentration could be beneficial for the total ion conductivity of these materials, especially for $Na_{8.5}(AlS_4)_{0.5}(SiS_4)_{1.5}$, as was already shown for Na_4SiS_4.[2] Since the presented materials could act as a model system to study the com-

bined effect of substitution by a less electronegative element and structural change on the stability against sodium metal in sulfides, electrochemical stability investigations on this substitution series should be performed.

Putting the findings of this work in a bigger picture, the materials discussed in this work follow the established trend of increasing total ionic conductivity and decreasing activation energy for ion conduction due to the softening of the anion lattice. Sulfide based isolated tetrahedral anions have proven to be beneficial for achieving high ionic conductivities. In this sense, thio-phosphates are the most promising due to the high covalency of the P-S bond. This assumption is also confirmed by the findings in this work by tetragonal Li_7SiPS_8 competing with state-of-the-art lithium solid electrolytes. Additionally, this work highlights the importance of microstructure on conductivity especially the presence of an amorphous side phase. Thiophosphates in particular tend to form glassy ceramics which is often overlooked. This work lays the foundation for a tuning of the microstructure, which is indispensable for achieving outstanding performance of solid electrolytes. However, this is not the only influencing factor for achieving high ionic conductivity. In this sense, this work points to static disorder of the anion sublattice that can be found in certain double salts as being beneficial for flattening out the energy landscape, similar to tetragonal LGPS and lithium argyrodites. Furthermore, the results on the sodium electrolytes show the influence of the local site symmetry of alkali cations on the energy landscape and the entropy of migration, enhancing the ion conductivity. These high ionic conductivities are essential for fast charging of emerging all-solid-state batteries, bringing us one step closer to a solely renewable energy based society.

Appendix A

Supporting Information for "A Lesson learned from NMR: characterization and ionic conductivity of LGPS-like Li_7SiPS_8"

A.1 Crystallographic Data

Table A.1: Crystallographic information and data for the structure solution and refinement of orthorhombic Li_7SiPS_8 on the basis of single crystal data. Standard deviation values are given in parentheses

Li_7SiPS_8	
Crystal system	orthorhombic
Space group	*Pnma*, (Nr. 62)
Lattice parameters	$a = 13.348(3)$ Å
	$b = 7.970(2)$ Å
	$c = 6.1343(12)$ Å
V [Å^3]	652.6(2)
Formula units, Z	2
Calculated density [gcm^{-3}]	1.853
Diffractometer	STOE IPDS-II, MoK_α radiation
	graphite monochromator
Temperature [K]	295
Absorption coefficient [mm^{-1}]	1.530
ϑ-range [°]	3.66-31.64
Indexing range	$-19 \leq h \leq 19$,
	$-11 \leq k \leq 11$,
	$-8 \leq l \leq 9$
Observed reflections	7121
Independent reflections	1165
Independent reflections ($I \geq 2\sigma(I)$)	945
R_{int}	3.36%
R_σ	2.28%
$F(000)$	356
Corrections	Lorentz, polarization, absorption
Absorption correction	multi scan
Structure solution	direct, SHELXS97[3]
Structure refinement	Least-Squares on F^2, SHELXL97[3]
Parameters	73
GooF	0.883
R values for reflections with $I \geq 2\sigma(I)$)	$R1 = 2.37\%$, $wR2 = 4.84\%$
R values (all data)	$R1 = 3.83\%$, $wR2 = 5.24\%$
Residual electron density [$e^-/\AA^3$]	0.304/-0.261
Extinction coefficient	0.0049(11)

Table A.2: Fractional atomic coordinates[4] in standardized setting[4] and equivalent isotropic displacement parameters [Å^2] of orthorhombic Li_7SiPS_8. The equivalent isotropic displacement parameters is defined as $\frac{1}{3}$ times the trace of the anisotropic displacement parameter. Standard deviations are given in parantheses

Atom	Occupation factor	Wyckoff position	x	y	z	U_{equiv}
Li1	0.433(11)	$8d$	0.0072(8)	0.5384(11)	0.0539(14)	0.051(3)
Li2	0.263(14)	$8d$	0.1661(10)	0.005(2)	0.192(3)	0.047(5)
Li3	0.764(13)	$8d$	0.1707(3)	0.0274(6)	0.3754(10)	0.043(2)
S1	1	$8d$	0.34585(3)	0.03271(5)	0.27451(6)	0.02551(10)
S2	1	$4c$	0.06088(4)	1/4	0.23174(9)	0.02143(11)
Li4	0.24(3)	$4c$	0.071(2)	1/4	0.809(5)	0.037(7)
Li5	0.34(3)	$4c$	0.0869(14)	1/4	0.655(5)	0.054(8)
S3	1	$4c$	0.40241(4)	1/4	0.51834(8)	0.02517(13)
P1	0.50	$4c$	0.41261(4)	1/4	0.15554(8)	0.01657(11)
Si1	0.50	$4c$	0.41261(4)	1/4	0.15554(8)	0.01657(11)

Table A.3: Anisotropic displacement parameters [Å^2] of orthorhombic Li_7SiPS_8. U_{ij} is defined as $U_{ij} = exp\{-2\pi^2[U_{11}(ha^*)^2 + ... + 2U_{21}hka^*b^*]\}$. Standard deviations are given in parantheses

Atom	U_{11}	U_{22}	U_{33}	U_{23}	U_{13}	U_{12}
Li1	0.045(5)	0.058(6)	0.050(6)	0.028(4)	-0.003(5)	0.011(4)
Li2	0.049(8)	0.027(6)	0.065(13)	-0.009(6)	-0.010(7)	-0.001(5)
Li3	0.031(2)	0.041(2)	0.057(4)	-0.016(2)	-0.007(2)	-0.001(2)
S1	0.0233(2)	0.0248(2)	0.0285(2)	0.00506(13)	-0.00020(14)	-0.00423(12)
S2	0.0196(2)	0.0202(2)	0.0245(2)	0	-0.0019(2)	0
Li3	0.033(10)	0.041(10)	0.04(2)	0	0.006(8)	0
Li4	0.050(10)	0.036(8)	0.08(2)	0	0.032(10)	0
S3	0.0352(3)	0.0230(2)	0.0173(2)	0	-0.0039(2)	0
P1	0.0171(2)	0.0168(2)	0.0158(2)	0	-0.0013(2)	0
Si1	0.0171(2)	0.0168(2)	0.0158(2)	0	-0.0013(2)	0

Table A.4: Interatomic distances in orthorhombic Li_7SiPS_8
(*i*: x, -y+$\frac{1}{2}$, z; *ii*: -x, y+$\frac{1}{2}$, -z+2; *iii*: -x, -y, -z+2; *iv*: -x, -y, -z+1; *v*: -x, y+$\frac{1}{2}$, -z+1; *vi*: x-$\frac{1}{2}$, y, -z+$\frac{3}{2}$; *vii*: x+$\frac{1}{2}$, y, -z+$\frac{3}{2}$; *viii*: -x+$\frac{1}{2}$, -y, z-$\frac{1}{2}$; *ix*: x, -y-$\frac{1}{2}$, z; *x*: -x, y-$\frac{1}{2}$, -z+1; *xi*: -x, y-$\frac{1}{2}$, -z+2; *xii*: -x+$\frac{1}{2}$, -y, z+$\frac{1}{2}$)

Atom1	Atom2	distance [Å]	Atom1	Atom2	distance [Å]
S1	Si1	2.0964(8)		S3	2.504(6)^{iv}
	Li5	2.419(13)^{i}		Li3	2.71(2)^{iv}
	Li5	2.419(13)		Li5	2.93(2)^{viii}
	Li1	2.465(4)^{i}		Li2	2.988(11)
	Li1	2.465(4)		Si1	3.013(4)^{iv}
	Li2	2.596(9)^{ii}		P1	3.013(4)^{iv}
	Li2	2.596(9)^{iii}		Li4	3.46(3)^{iv}
	Li4	2.60(3)^{iii}	Li2	Li2	0.92(2)^{iii}
	Li3	2.62(3)^{iv}		Li4	2.16(2)
	Li2	2.644(9)^{i}		Li5	2.31(2)
	Li2	2.644(9)		S1	2.596(9)^{iii}
Si1	S2	2.0730(8)		S3	2.605(10)^{iii}
	S3	2.0799(5)		S2	2.633(9)^{iv}
	S3	2.0799(5)^{i}		Li3	2.76(3)
	Li3	3.01(2)^{iv}		Li5	2.77(2)^{iii}
	Li1	3.013(4)^{iv}		Li4	2.88(2)^{iii}
	Li1	3.013(4)^{v}	Li3	Li4	0.97(3)
	Li2	3.156(8)^{ii}		S2	2.47(2)^{iv}
	Li2	3.156(8)^{iii}		S3	2.533(8)^{ix}
	Li2	3.171(8)^{i}		S1	2.62(3)^{iv}
	Li2	3.171(8)		Li1	2.71(2)^{x}
S3	Li1	2.419(4)^{vi}		Li1	2.71(2)^{iv}
	Li5	2.462(14)^{vi}		Li2	2.76(3)^{ix}
	Li2	2.463(10)		Si1	3.01(2)^{iv}
	Li1	2.504(6)^{iv}		P1	3.01(2)^{iv}
	Li4	2.520(9)		Li2	3.52(2)^{iii}
	Li3	2.533(8)	Li4	Li2	2.16(2)^{ix}
	Li5	2.58(2)^{iii}		S2	2.38(2)^{iv}
	Li2	2.605(10)^{iii}		S3	2.520(9)^{ix}
S2	Li5	2.358(12)^{iv}		S1	2.60(3)^{iii}
	Li5	2.358(12)^{v}		Li2	2.88(2)^{iii}
	Li4	2.38(2)^{iv}		Li2	2.88(2)^{xi}
	Li1	2.442(5)^{iv}		Li5	3.31(3)^{iii}

Continued on next page

Continuation of table A.4

Atom1	Atom2	distance [Å]	Atom1	Atom2	distance [Å]
	Li1	$2.442(5)^{v}$		Li5	$3.31(3)^{xi}$
	Li3	$2.47(2)^{iv}$		Li1	$3.46(3)^{x}$
	Li2	$2.633(9)^{iv}$	Li5	S2	$2.358(12)^{iv}$
	Li2	$2.633(9)^{v}$		S3	$2.462(14)^{vii}$
Li1	Li5	1.14(2)		S3	$2.58(2)^{iii}$
	S3	$2.419(4)^{vii}$		Li2	$2.77(2)^{iii}$
	S2	$2.442(5)^{iv}$		Li1	$2.93(2)^{xii}$
				Li4	$3.31(3)^{iii}$

Table A.5: Fractional atomic coordinates and equivalent isotropic displacement parameters for *tetra*-Li_7SiPS_8 from Rietveld refinement. Standard deviations for refined parameters are given in parentheses.

Atom	occupation factor	Wyckoff position	x	y	z	B_{eq}
Li1	0.50(3)	16h	0.249(4)	0.2663(4)	0.192(3)	7(2)
Li2	0.90(4)	4d	0	1/2	0.939(3)	6(2)
Li3	0.85(7)	8f	0.239(3)	$=x$	0	20(4)
Li4	0.65(5)	4c	0	0	0.250(3)	1(2)
Si1	0.75	4d	0	1/2	0.6914(4)	0.68(12)
P1	0.25	4d	0	1/2	0.6914(4)	0.68(12)
P2	1	2b	0	0	1/2	1.1(2)
S1	1	8g	0	0.1901(3)	0.4069(3)	2.12(8)
S2	1	8g	0	0.2979(3)	0.0976(3)	0.96(8)
S3	1	8g	0	0.6977(4)	0.7912(2)	1.09(8)

Table A.6: Interatomic distances in tetragonal Li_7SiPS_8 (*i*: -x+$\frac{1}{2}$, -y+$\frac{1}{2}$, -z+$\frac{1}{2}$; *ii*: -y+1, -x, -z+1; *iii*: y-$\frac{1}{2}$, -x+$\frac{1}{2}$, z-$\frac{1}{2}$; *iv*: -y+$\frac{1}{2}$, -x+$\frac{1}{2}$, z-$\frac{1}{2}$; *v*: x, -y+1, z; *vi*: x, y, z+1; *vii*: x, -y+1, z+1; *viii*: -y+$\frac{1}{2}$, -x+$\frac{1}{2}$, z+$\frac{1}{2}$; *ix*: y-$\frac{1}{2}$, -x+$\frac{1}{2}$, z+$\frac{1}{2}$; *x*: -y, -x+1, -z+1; *xi*: -x, y, z+1; *xii*: y, -x+1, -z+1; *xiii*: y, x, -z; *xiv*: y, -x, -z; *xv*: x, y, z-1; *xvi*: x, -y, z; *xvii*: y-1, -x, -z+1; *xviii*: x-$\frac{1}{2}$, -y+$\frac{1}{2}$, -z+$\frac{1}{2}$; *xix*: -x+$\frac{1}{2}$, y-$\frac{1}{2}$, -z+$\frac{1}{2}$; *xx*: x-$\frac{1}{2}$, y-$\frac{1}{2}$, -z+$\frac{1}{2}$; *xxi*: y-$\frac{1}{2}$, x+$\frac{1}{2}$, z+$\frac{1}{2}$; *xxii*: -y+$\frac{1}{2}$, x+$\frac{1}{2}$, z+$\frac{1}{2}$; *xxiii*: -y, -x, -z+1; *xxiv*: y, -x, -z+1; *xxv*: y-$\frac{1}{2}$, x-$\frac{1}{2}$, z+$\frac{1}{2}$; *xxvi*: -x, y, z;)

Atom1	Atom2	distance [Å]	Atom1	Atom2	distance [Å]
Li1	Li1	1.46(8)^{i}		Li1	2.96(3)^{xxi}
	S3	2.37(3)^{ii}		Li1	2.96(3)^{xxii}
	S3	2.41(4)^{iii}		Li1	2.96(3)^{ix}
	Li3	2.43(4)		Li2	3.09(4)
	S2	2.48(3)		Li2	3.18(4)^{iv}
	S1	2.54(3)^{i}	P1	Si1	0.00000
	P1	2.96(3)^{iv}		S2	2.110(4)^{viii}
	Si1	2.96(3)^{iv}		S2	2.110(4)^{ix}
	Li4	3.06(3)^{i}		S3	2.123(4)^{v}
Li2	S3	2.52(3)		S3	2.123(4)
	S3	2.52(3)^{v}		Li1	2.96(3)^{viii}
	S2	2.66(3)^{vi}		Li1	2.96(3)^{xxi}
	S2	2.66(3)^{vii}		Li1	2.96(3)^{xxii}
	S1	2.717(7)^{viii}		Li1	2.96(3)^{ix}
	S1	2.717(7)^{ix}		Li2	3.09(4)
	P1	3.09(4)		Li2	3.18(4)^{iv}
	Si1	3.09(4)	P2	S1	2.021(3)
	Li3	3.166(10)^{vi}		S1	2.021(3)^{xxiii}
	Li3	3.166(10)^{x}		S1	2.021(3)^{xxiv}
	Li3	3.166(10)^{xi}		S1	2.021(3)^{xvi}
	Li3	3.166(10)^{xii}		Li4	3.14(3)
	P1	3.18(4)^{viii}		Li4	3.14(3)^{xxiii}
	Si1	3.18(4)^{viii}		Li3	3.20(3)^{xix}
Li3	Li1	2.43(4)^{xiii}		Li3	3.20(3)^{ix}
	Li1	2.43(4)		Li3	3.20(3)^{i}
	S2	2.46(2)		Li3	3.20(3)^{xxv}
	S2	2.46(2)^{xiv}	S1	P2	2.021(3)
	S1	2.62(2)^{iv}		Li1	2.54(3)^{i}
	S1	2.62(2)^{i}		Li1	2.54(3)^{xviii}

Continued on next page

Continuation of table A.6

Atom1	Atom2	distance [Å]	Atom1	Atom2	distance [Å]
	Li2	$3.166(10)^{ii}$		Li4	2.57(3)
	Li2	$3.166(10)^{xv}$		Li3	$2.62(2)^{ix}$
	P2	$3.20(3)^{i}$		Li3	$2.62(2)^{i}$
Li4	S1	$2.57(3)^{xvi}$		Li2	$2.717(7)^{iv}$
	S1	2.57(3)	S2	Si1	$2.110(4)^{iv}$
	S3	$2.672(8)^{ii}$		P1	$2.110(4)^{iv}$
	S3	$2.672(8)^{xvii}$		Li3	2.46(2)
	Li1	$3.06(3)^{xviii}$		Li3	$2.46(2)^{xxvi}$
	Li1	$3.06(3)^{xix}$		Li1	$2.48(3)^{xxvi}$
	Li1	$3.06(3)^{xx}$		Li1	2.48(3)
	Li1	$3.06(3)^{i}$		Li2	$2.66(3)^{xv}$
	P2	3.14(3)	S3	P1	2.123(4)
Si1	P1	0.00000		Si1	2.123(4)
	S2	$2.110(4)^{viii}$		Li1	$2.37(3)^{x}$
	S2	$2.110(4)^{ix}$		Li1	$2.37(3)^{xii}$
	S3	$2.123(4)^{v}$		Li1	$2.41(4)^{xxii}$
	S3	2.123(4)		Li1	$2.41(4)^{xxi}$
	Li1	$2.96(3)^{viii}$		Li2	2.52(3)

A.2 Energy-dispersive X-ray Analysis

Results of elemental analysis with energy-dispersive X-ray (EDX) spectroscopy for *tetra*-LSiPS samples are given in table A.7. The data show a slightly higher silicon content than is expected from the targeted stoichiometry. The observed sulfur content of the samples is systematically too low due to hydrolysis reactions during the sample transfer into the SEM.

Table A.7: EDX measurements on *tetra*-LSiPS. All data are given in relative atom%

Measurement	Si	P	S
M1	11.0	9.9	79.1
M2	11.2	9.6	79.3
M3	11.3	10.1	78.6
M4	11.2	10.1	78.8
M5	10.7	10.5	78.9
M6	12.1	10.3	77.7
average:	11.2	10.1	78.7
stand. dev.:	0.5	0.3	0.6
calculated:	10	10	80
mean error:	1.2	0.1	1.3

A.3 Scanning Electron Microscopy

A scanning electron microscopy image of *tetra*-LSiPS is shown in figure A.1. The material is not stable under long illumination with the electron beam.

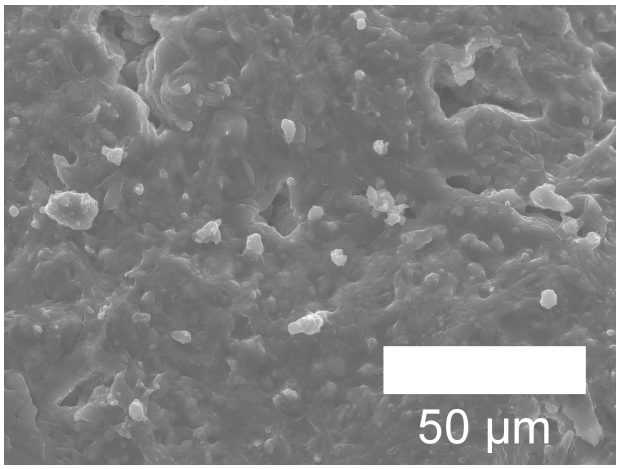

Figure A.1: SEM image of *tetra*-LSiPS with an acceleration voltage of 20.0 kV showing a morphology resembling a glassy matrix with embedded crystallites.

A.4 Quantitative phase analysis

For converting P atom percent obtained from deconvolution of ^{31}P MAS NMR spectra to weight percent of the amorphous side phase, two assumptions were made. First, its composition was assumed to be Li_3PS_4, which is reasonable in light of the chemical shift and the low silicon content of this phase. The second assumption is that the total molar mass of all phases is equal to the target phase Li_7SiPS_8: $w\%(amorphous, NMR) = atom\%(P_{amorphous,NMR}) \cdot \frac{M(Li_3PS_4)}{M(Li_7SiPS_8)}$. The thereby introduced absolute error is estimated to be around 2%.

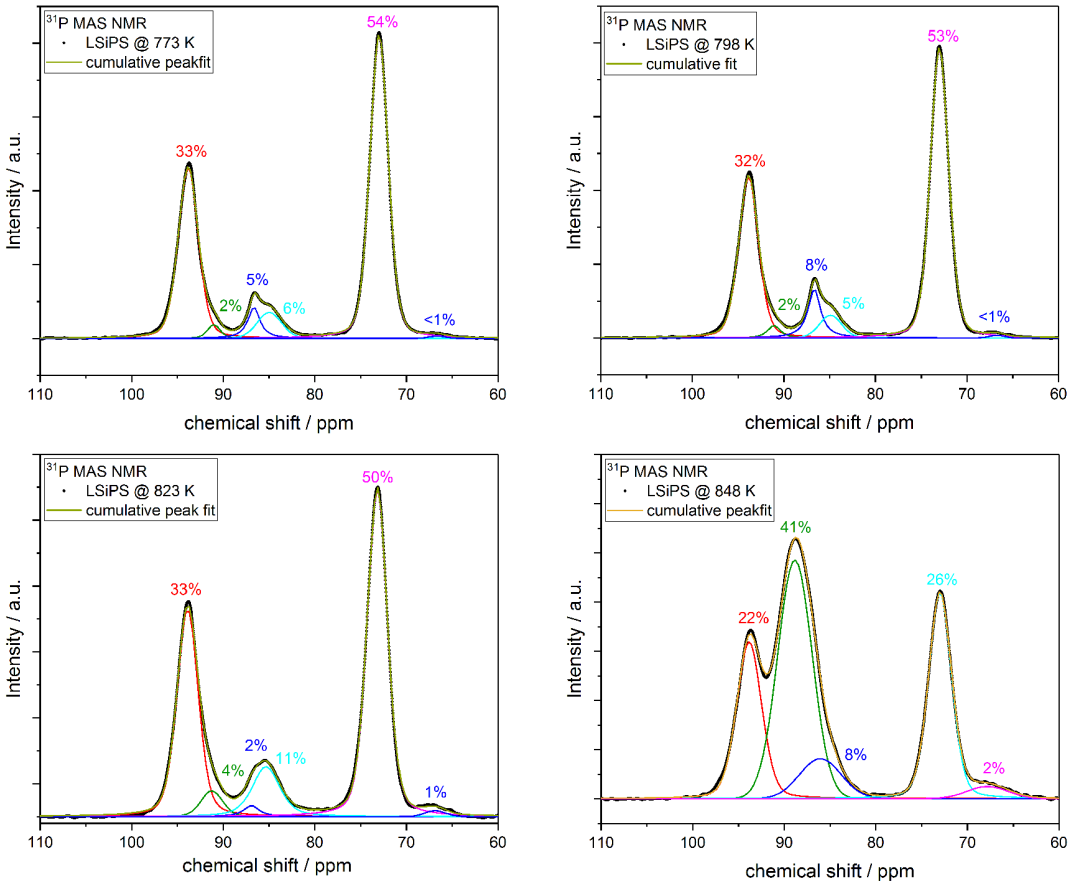

Figure A.2: ^{31}P MAS NMR spectra and peak deconvolutions for all samples containing *tetra*-LSiPS. Relative intensity values were extracted from peak areas and are given in the respective images as percentage values.

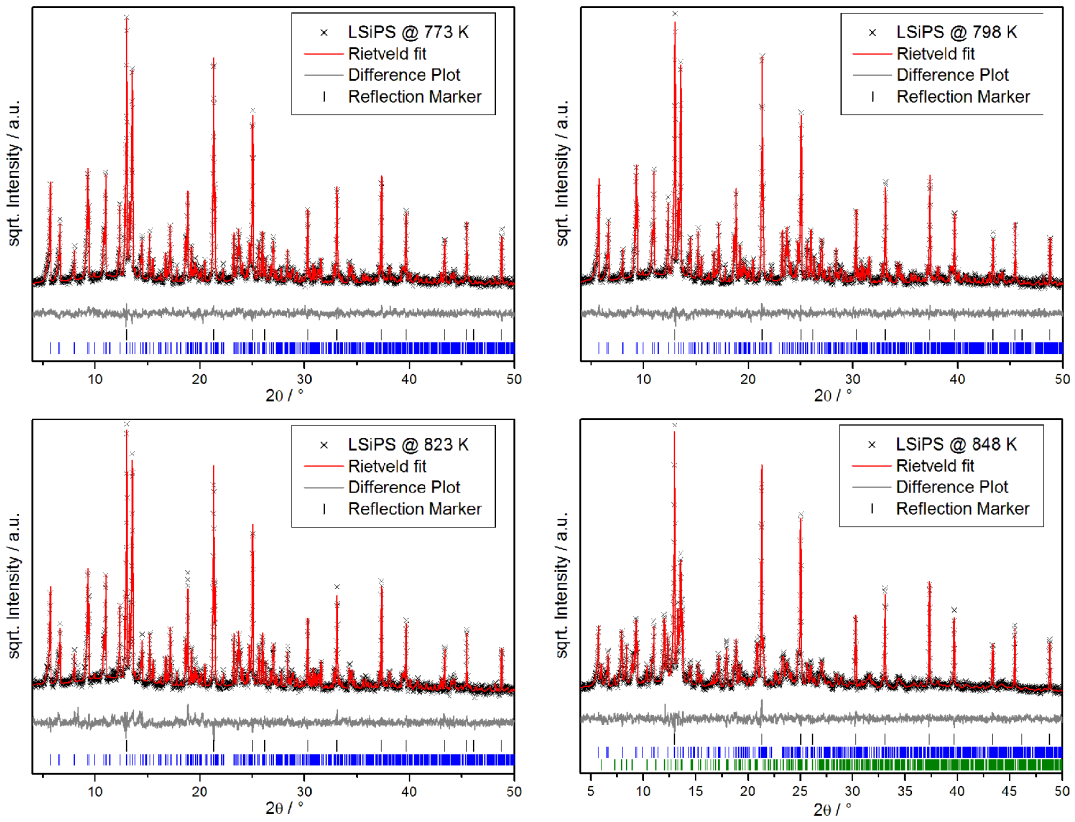

Figure A.3: Rietveld fits for all samples containing *tetra*-LSiPS. Black reflection markers indicate peak positions of the internal standard Si, blue markers of *tetra*-LSiPS and green markers of *ortho*-LSiPS. The square root of the intensity is shown for better visibility of all phases.

A.5 Raman spectroscopy

Raman spectroscopy was performed on *tetra*-LSiPS and *ortho*-LSiPS samples (Fig. A.4). The resulting spectrum of *tetra*-LSiPS is typical for a *tetra*-LGPS like material.[5] A shift of the symmetric SiS_4 'breathing' vibration in contrast to the SnS_4 vibration to higher wave-numbers is notable, which is expected to be around 400 cm^{-1} due to the stronger covalent bonding and the lower mass of Si.[6,7] Raman spectroscopy was intended to reveal characteristic vibrational bands of the amorphous side phase. Yet, no distinct vibrational bands can be assigned to this phase. Only the broad PS_4 vibrational band could originate from this observed second phase, hinting at thio-orthophosphate anions being the main component of the amorphous side phase. This assumption would also be in accordance with the proposed composition of this phase.

Table A.8: Observed Raman modes of *tetra*-LSiPS compared with vibrational modes of tetragonal LGPS-like $Li_{10}SnP_2S_{12}$ and orthorhombic β-Li_3PS_4. All values are given in wavenumbers cm^{-1}

vib. Mode	$\bar{\nu}$(Li-S)	$\bar{\nu}$(Li-S)	$\bar{\nu}$(P-S)	$\bar{\nu}$(Sn-S)	$\bar{\nu}$(Si-S)	$\bar{\nu}$(P-S)	$\bar{\nu}$(P-S)	$\bar{\nu}$(P-S)	$\bar{\nu}$(P-S)
tetra-LSiPS	140 w	195 m, br	291 m, br	-	403 s	424 s	443 s	521 w, br	590 w
$Li_{10}SnP_2S_{12}$[5]	128 w	168 m, br	276 m, br	345 s	-	416 s	427 s	548 w	570 w, br
ortho-LSiPS	176 m	198 m, br	254 m, br*	-	422 s	422 s	-	545 w, br	590 w
β-Li_3PS_4[8, 9]	-	-	270 m, br	-	-	418 s	-	550 w	570 w, br

*exhibits a shoulder at about 270 cm^{-1}

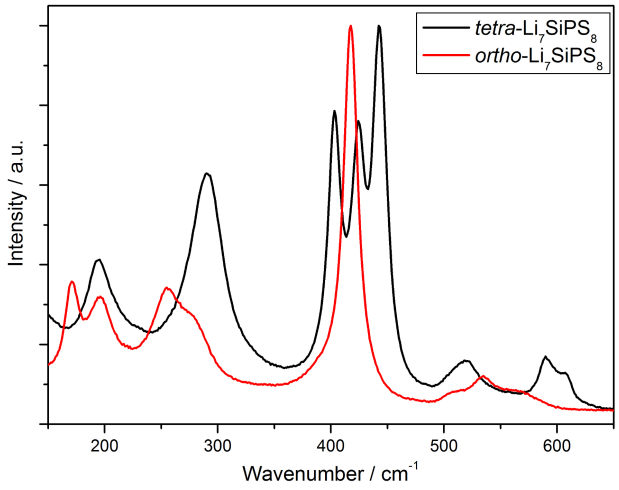

Figure A.4: Raman spectra of *tetra*-LSiPS (black) and *ortho*-LSiPS (red).

A.6 Estimation of the electronic contribution to the conductivity

To determine the electronic contribution to the conductivity, DC galvanostatic polarization measurements with ion-blocking electrodes (Platinum metal) were conducted. A current of 5 nA was applied for at least 14 h (each data point was collected in an interval of 0.1 s). As visible in Figure S2, even after such a long time the samples did not reach a steady state, and the estimation of the electronic conductivity represents only an upper limit. According to Maier[10] the processes in an ionic and electronic conducting sample between two ion blocking electrodes can be usefully approximated with the equivalent circuit model shown in Figure A.5 as parallel arrangement of electronic R_{eon} and ionic resistance R_{ion} with the bulk capacitor C_{bulk} and the ion-blocking capacitor C_{block} in series with an RC element representing grain boundary processes (GB).

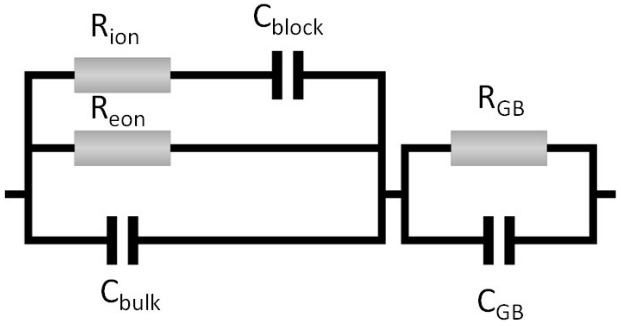

Figure A.5: Equivalent circuit model of an ionic and electronic conducting sample with a grain boundary process between two ion blocking electrodes.

After a long time of current flow (all capacitors are charged) the saturation voltage U_e is obtained which can be assigned to the sum of the electronic resistance and the grain boundary resistance ($U_e = U_{eon} + U_{GB}$)). As the bulk ionic conductivity of the compounds is not known and only the grain boundary conductivity was measured by EIS, the following approximations were assumed in order to calculate an electronic transference number t_e as defined in equation A.1. For *ortho*-LSiPS the grain boundary resistance is about 6000 Ω, equivalent to a voltage of $2.98 \cdot 10^{-5}$ V. In comparison to the voltage resulting from the electronic resistance (0.878 V) U_{GB} is negligible, thus following $U_e + U_{GB} \approx U_e$. For the ionic conductivity (σ_{ion}) in equation A.1, the grain boundary conductivity was used ($\sigma_{GB} = 0.13\, mScm^{-1}$) as the real bulk ionic conductivity should be even higher. Therefore, this is a cautious approximation of the electronic transference number. For *tetra*-LSiPS the same reasoning was applied with a σ_{GB} of 2 $mScm^{-1}$. In general, for a good ionic conductor, the electronic transference number is ideally close to zero.

$$t_e = \frac{\sigma_{eon}}{\sigma_{eon} + \sigma_{ion}} \tag{A.1}$$

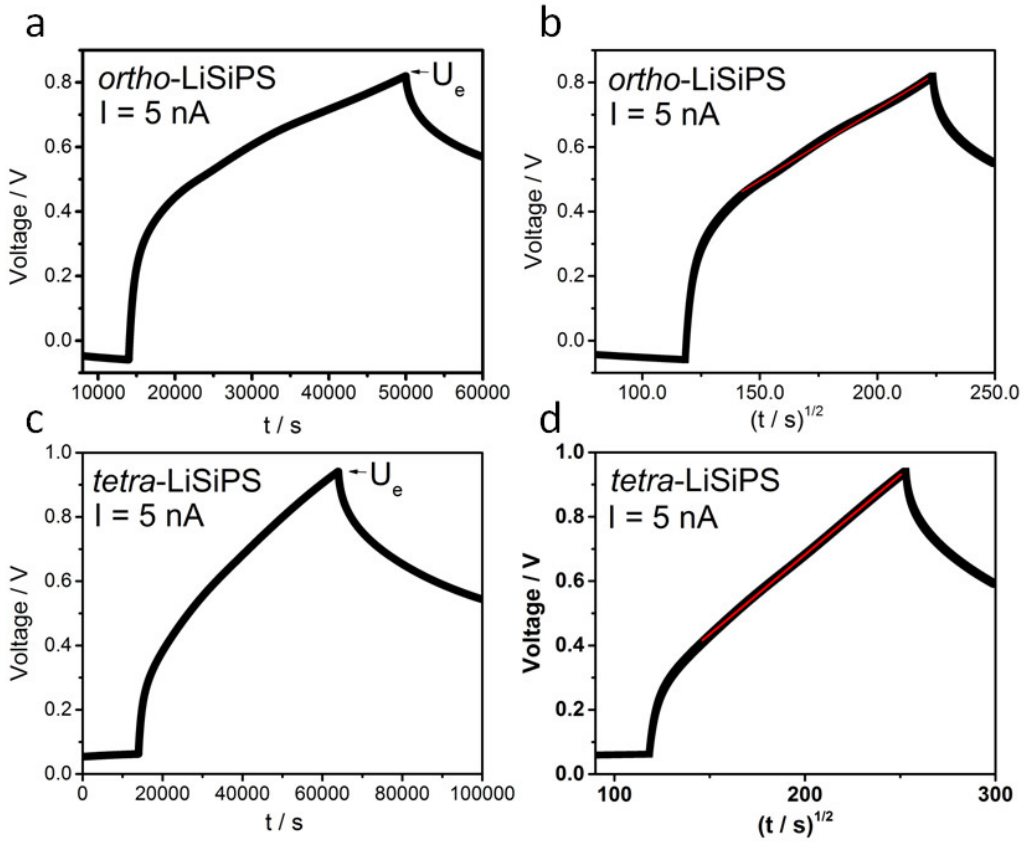

Figure A.6: *a)* and *b)* DC galvanostatic polarization measurements of *ortho-* and *tetra*-LSiPS performend at 298 K with blocking electrodes Pt|LSiPS|Pt
. *c)* and *d) Voltage as function of the square root of time according to equation A.2.*

By the DC measurements shown in Figure A.6 an upper limit of t_e of 10^{-5} for *ortho*-LSiPS and 10^{-6} for *tetra*-LSiPS was estimated. This in accordance with the transference numbers of other known fast Li^+-ion conductors.[11,12] Another way of estimating the electronic conductivity is to plot the voltage as function of the square root of time and to estimate σ_{eon} according to formula A.2 from the slope of the linear region.[10–12] Equation A.2 for the transient describing the semi-infinite chemical diffusion holds for $t < \tau^\delta$ (τ^δ is in general the characteristic chemical diffusion time and here the lower limit of τ^δ the time of applied current). I is the applied current (5 nA), L the diffusion length (thickness of the sample of about 1 mm) and σ is the total conductivity, approximated as $\sigma \approx \sigma_{ion}$. The upper limit of the electronic conductivity of about 10^{-9} Scm^{-1} obtained with this method is in accordance to the considerations above and results in the same t_e.

$$U - U_{GB} = \frac{IL}{\sigma} + \frac{\sigma_{ion}}{\sigma}\frac{IL}{\sigma_{eon}}\frac{4}{pi^{3/2}}\sqrt{\frac{t}{\tau^\delta}} \tag{A.2}$$

A.7 Comparison of different fitting models for the impedance spectrum of *tetra*-LSiPS at -80°C

In Figure A.7 a fit with a single R1-CPE1 element plus a CPE2 in series (model #1), a fit with two R-CPE elements plus a CPE2 (model #2) in series and a fit with one RC, two R-CPE elements and a CPE for the polarization in series (model #3) are displayed. The fit of model #1 is apparently worse in comparison to model #2 and #3, and especially in the low frequency region the deviations are significant. Model #2 and #3 fit the data over the whole frequency range very well and the total quality of the fit expressed in terms of the sum of squares of regression decreases from the simple model to the more advanced model (model #1: 0.23, model #2: 0.056 and model #3: 0.024). Moreover, the extrapolated room temperature conductivity of model #3 with 1.5±2 mS/cm matches the measured ionic conductivity of 2 mS/cm best (model #1: 1.13±2 mS/cm and model #2: 0.90±5 mS/cm). Therefore, even Model #2 does not sufficiently describe the situation. It must be noted that the large capacitances (expected capacitance of the bulk of a non ferroelectric material is in the pF range) of model #3 show that the bulk process cannot be deconvoluted from the spectrum even if that many circuit elements are included. The impedance is completely dominated by the grain boundary phenomena and the amorphous side phase. Using a model with even more parameters does not improve the quality of the fit and only leads to highly correlated parameters.

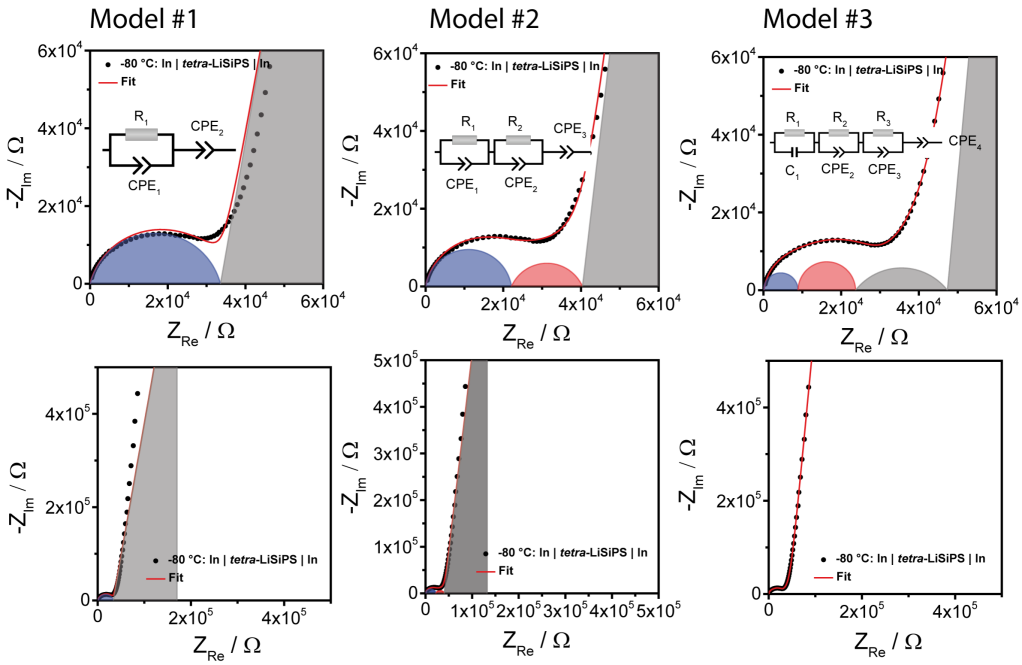

Figure A.7: Comparison of three different models of the impedance spectrum of *tetra*-LSiPS at -80 °C showing that model #3 fits the data best.

A.8 Room-temperature EIS measurements of *tetra*-LSiPS

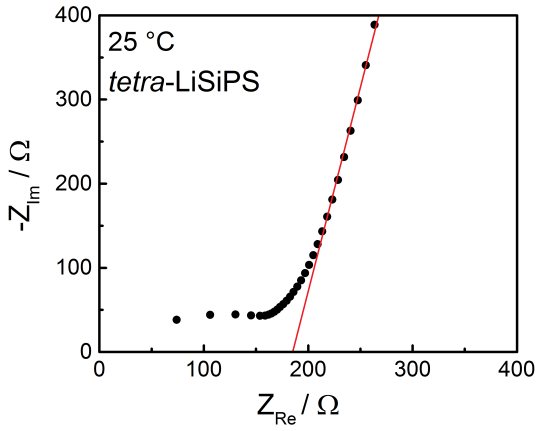

Figure A.8: Room-temperature impedance spectrum of *tetra*-LSiPS showing a total resistance of about 180 Ω resulting in an ionic conductivity of 2 $mScm^{-1}$.

Appendix B

Supporting Information for "Finding the right blend: Interplay between structure and sodium ion conductivity in the system Na_5AlS_4 – Na_4SiS_4"

B.1 Crystallographic data for Na_5AlS_4

Table B.1: Crystallographic data and information for the structure solution and refinement from powder X-ray diffraction data for Na_5AlS_4. Standard deviations are given in parentheses. These data were deposited in the Cambridge Crystallographic Data Centre and were given the deposition number CCDC 1980422.

Na_5AlS_4		
crystal system		orthorhombic
space group		*Pbca*, (Nr. 61)
lattice params.	a	12.01930(12) Å
	b	7.05236(7) Å
	c	21.5605(2) Å
V [Å^3]		1827.56(3)
Z		8
calc. density [gcm^{-3}]		1.96398(3)
diffractometer		STOE STADI P, Cu$K_{\alpha 1}$-radiation
		Debye-Scherrer geometry
temperature [K]		295
absorption coefficient [mm^{-1}]		12.1231(2)
refined 2ϑ region [°]		3 – 90
R_{exp}		6.054
R_p		5.187
R_{wp}		6.604
Goof		1.091
R_{Bragg}		1.949
number of refined params.		60
number of background params.		12

Table B.2: Standardized fractional atomic coordinates[4] and isotropic displacement parameters [Å^2] for Na_5AlS_4. Standard deviations are given in parentheses.

Atom	occupation-factor	Wyckoff-position	x	y	z	B_{iso}
S1	1	8c	0.3713(4)	0.2046(6)	0.9571(3)	2.58(15)
S2	1	8c	0.4477(3)	0.8520(5)	0.3783(3)	2.50(12)
S3	1	8c	0.1402(3)	0.2426(6)	0.6222(4)	3.29(12)
S4	1	8c	0.6317(4)	0.7610(6)	0.2113(3)	3.4(2)
Al1	1	8c	0.0399(3)	0.8312(5)	0.8737(3)	2.70(14)
Na1	1	8c	0.3521(5)	0.9080(9)	0.5013(3)	3.8(2)
Na2	1	8c	0.2869(4)	0.5531(8)	0.3658(3)	3.6(2)
Na3	1	8c	0.5579(6)	0.5658(9)	0.4332(3)	4.6(2)
Na4	1	8c	0.5863(5)	0.3809(10)	0.2501(3)	4.3(2)
Na5	1	8c	0.8373(5)	0.1078(9)	0.8294(3)	2.9(2)

Table B.3: Interatomic distances in Na_5AlS_4. Standard deviations are given in parentheses.
i: -x+$\frac{1}{2}$, y-$\frac{1}{2}$, z; ii: -x+1, y-$\frac{1}{2}$, -z+$\frac{3}{2}$; iii: x, -y+$\frac{1}{2}$, z+$\frac{1}{2}$; iv: x, -y+$\frac{3}{2}$, z+$\frac{1}{2}$; v: -x+$\frac{1}{2}$, -y+1, z+$\frac{1}{2}$; vi: -x+$\frac{1}{2}$, -y+2, z-$\frac{1}{2}$; vii: -x+1, y+$\frac{1}{2}$, -z+$\frac{1}{2}$; viii: -x+$\frac{3}{2}$, -y+1, z-$\frac{1}{2}$; ix: -x+$\frac{1}{2}$, y+$\frac{1}{2}$, z; x: -x, y-$\frac{1}{2}$, -z+$\frac{3}{2}$; xi: x-$\frac{1}{2}$, -y+$\frac{1}{2}$, -z+1; xii: x-$\frac{1}{2}$, y, -z+$\frac{3}{2}$; xiii: -x+1, y+$\frac{1}{2}$, -z+$\frac{3}{2}$; xiv: x+$\frac{1}{2}$, -y+$\frac{3}{2}$, -z+1; xv: x+$\frac{1}{2}$, y, -z+$\frac{1}{2}$; xvi: x-$\frac{1}{2}$, -y+$\frac{3}{2}$, -z+1; xvii: -x+$\frac{1}{2}$, -y+2, z+$\frac{1}{2}$; xviii: -x, y+$\frac{1}{2}$, -z+$\frac{3}{2}$; xix: x, -y+$\frac{3}{2}$, z-$\frac{1}{2}$; xx: -x+$\frac{1}{2}$, -y+1, z-$\frac{1}{2}$; xxi: -x+1, y-$\frac{1}{2}$, -z+$\frac{1}{2}$; xxii: x, -y+$\frac{1}{2}$, z-$\frac{1}{2}$; xxiii: x-$\frac{1}{2}$, y, -z+$\frac{1}{2}$; xxiv: x+$\frac{1}{2}$, -y+$\frac{1}{2}$, -z+1; xxv: -x+$\frac{3}{2}$, -y+1, z+$\frac{1}{2}$; xxvi: x+$\frac{1}{2}$, y, -z+$\frac{3}{2}$

Atom1	Atom2	distance [Å]	Atom1	Atom2	distance [Å]
S1	Al1	2.274(8)^{i}		S2	2.241(5)^{xvii}
	Na3	2.696(8)^{ii}		S3	2.255(6)^{xviii}
	Na2	2.864(8)^{iii}		S1	2.274(8)^{ix}
	Na1	2.902(8)^{iv}		Na2	3.084(7)^{iv}
	Na1	2.958(8)^{v}	Na1	S3	2.857(10)^{ix}
	Na3	2.989(8)^{iii}		S1	2.902(8)^{xix}
S2	Al1	2.241(5)^{vi}		S2	2.918(8)
	Na3	2.689(8)		S1	2.958(8)^{xx}
	Na4	2.804(9)^{vii}	Na2	S4	2.822(8)^{xxi}
	Na5	2.805(7)^{viii}		S1	2.864(8)^{xxii}
	Na2	2.873(7)		S2	2.873(7)
	Na1	2.918(8)		S4	2.898(8)^{xxiii}
	Na2	3.168(6)^{ix}		Al1	3.084(7)^{xix}
S3	Al1	2.255(6)^{x}		S2	3.168(6)^{i}
	Na3	2.672(8)^{xi}	Na3	S3	2.672(8)^{xxiv}
	Na5	2.757(7)^{xii}		S2	2.689(8)
	Na5	2.792(8)^{xiii}		S1	2.696(8)^{xiii}
	Na1	2.857(10)^{i}		S1	2.989(8)^{xxii}
	Na4	2.961(10)^{xi}	Na4	S2	2.804(9)^{xxi}
S4	Al1	2.236(9)^{xiv}		S4	2.861(8)
	Na5	2.736(8)^{viii}		S4	2.876(8)^{xxi}
	Na2	2.822(8)^{vii}		S3	2.961(10)^{xxiv}
	Na4	2.861(8)	Na5	S4	2.736(8)^{xxv}
	Na4	2.876(8)^{vii}		S3	2.757(7)^{xxvi}
	Na2	2.898(8)^{xv}		S3	2.792(8)^{ii}
Al1	S4	2.236(9)^{xvi}		S2	2.805(7)^{xxv}

B.2 Crystallographic data for Na_4SiS_4

Table B.4: Crystallographic data and information for the structure solution and refinement from powder X-ray diffraction data for Na_4SiS_4. Standard deviations are given in parentheses. These data were deposited in the Cambridge Crystallographic Data Centre and were given the deposition number CCDC 1980423.

Na_4SiS_4		
crystal system		orthorhombic
space group		$P2_12_12_1$, (Nr. 19)
lattice params.	a	41.0301(7) Å
	b	8.78409(14) Å
	c	6.88962(12) Å
V [Å^3]		2483.10(7)
Z		12
calc. density [gcm^{-3}]		1.99260(6)
diffractometer		STOE STADI P, Mo$K_{\alpha1}$-radiation
		Debye-Scherrer geometry
temperature [K]		295
absorption coefficient [mm^{-1}]		1.42581(4)
refined 2ϑ region [°]		2 – 50
R_{exp}		5.390
R_p		4.127
R_{wp}		5.377
Goof		0.998
R_{Bragg}		1.825
number of refined params.		109
number of background params.		10

Table B.5: Standardized fractional atomic coordinates[4] and isotropic displacement parameters [Å^2] for Na_4SiS_4. Standard deviations are given in parentheses.

Atom	occupation-factor	Wyckoff-position	x	y	z	B_{iso}
S1	1	4a	0.0315(5)	0.056(3)	0.908(3)	0.8(2)
S2	1	4a	0.3654(5)	0.065(3)	0.904(3)	0.8(2)
S3	1	4a	0.6993(5)	0.051(3)	0.907(3)	0.8(2)
S4	1	4a	0.0621(5)	0.758(3)	0.436(3)	1.54(10)
S5	1	4a	0.3963(5)	0.748(3)	0.447(3)	1.54(10)
S6	1	4a	0.7289(5)	0.752(3)	0.430(3)	1.54(10)
S7	1	4a	0.1346(5)	0.548(3)	0.422(4)	1.5(2)
S8	1	4a	0.4662(5)	0.537(3)	0.434(3)	1.5(2)
S9	1	4a	0.8019(5)	0.548(3)	0.408(3)	1.5(2)
S10	1	4a	0.2185(4)	0.249(3)	0.669(3)	1.37(10)
S11	1	4a	0.5436(4)	0.247(3)	0.662(3)	1.37(10)
S12	1	4a	0.8813(5)	0.246(3)	0.667(4)	1.37(10)
Si1	1	4a	0.2216(6)	0.246(4)	0.962(3)	1.58(10)
Si2	1	4a	0.5555(6)	0.248(4)	0.973(4)	1.58(10)
Si3	1	4a	0.8868(5)	0.245(4)	0.980(3)	1.58(10)
Na1	1	4a	0.2394(6)	0.048(4)	0.386(5)	2.0(3)
Na2	1	4a	0.5763(7)	0.045(4)	0.406(5)	2.0(3)
Na3	1	4a	0.9051(6)	0.056(4)	0.408(4)	2.0(3)
Na4	1	4a	0.2435(6)	0.443(4)	0.381(5)	0.9(3)
Na5	1	4a	0.5760(6)	0.452(4)	0.384(5)	0.9(3)
Na6	1	4a	0.9166(5)	0.433(3)	0.379(3)	0.9(3)
Na7	1	4a	0.1518(7)	0.241(5)	0.256(5)	3.2(2)
Na8	1	4a	0.4840(7)	0.242(5)	0.244(5)	3.2(2)
Na9	1	4a	0.8199(7)	0.241(5)	0.255(5)	3.2(2)
Na10	1	4a	-0.0079(6)	1.036(4)	0.235(4)	3.4(2)
Na11	1	4a	0.3330(9)	1.011(5)	0.238(7)	3.4(2)
Na12	1	4a	0.6706(8)	0.979(4)	0.270(6)	3.4(2)

Table B.6: Interatomic distances in Na_4SiS_4. Standard deviations are given in parentheses.
i: x-$\frac{1}{2}$, -y+$\frac{1}{2}$, -z+2; ii: x-$\frac{1}{2}$, -y+$\frac{1}{2}$, -z+1; iii: x, y-1, z+1; iv: -x+1, y-$\frac{1}{2}$, -z+$\frac{3}{2}$; v: -x+$\frac{1}{2}$, -y, z+$\frac{1}{2}$; vi: x+$\frac{1}{2}$, -y+$\frac{1}{2}$, -z+2; vii: x+$\frac{1}{2}$, -y+$\frac{1}{2}$, -z+1; viii: -x+$\frac{3}{2}$, -y, z+$\frac{1}{2}$; ix: -x+1, y+$\frac{1}{2}$, -z+$\frac{3}{2}$; x: -x+1, y+$\frac{1}{2}$, -z+$\frac{1}{2}$; xi: -x+$\frac{1}{2}$, -y+1, z+$\frac{1}{2}$; xii: x-$\frac{1}{2}$, -y+$\frac{3}{2}$, -z+1; xiii: -x, y-$\frac{1}{2}$, -z+$\frac{1}{2}$; xiv: -x+$\frac{3}{2}$, -y+1, z+$\frac{1}{2}$; xv: x+$\frac{1}{2}$, -y+$\frac{3}{2}$, -z+1; xvi: -x+1, y-$\frac{1}{2}$, -z+$\frac{1}{2}$; xvii: -x+$\frac{1}{2}$, -y, z-$\frac{1}{2}$; xviii: -x+$\frac{3}{2}$, -y, z-$\frac{1}{2}$; xix: -x+$\frac{1}{2}$, -y+1, z-$\frac{1}{2}$; xx: -x+$\frac{3}{2}$, -y+1, z-$\frac{1}{2}$; xxi: x, y+1, z-1; xxii: -x, y+$\frac{1}{2}$, -z+$\frac{1}{2}$;

Atom1	Atom2	distance [Å]	Atom1	Atom2	distance [Å]
S1	Si2	2.15(4)^{i}	Si2	S5	2.05(3)^{iv}
	Na5	2.72(4)^{ii}		S1	2.15(4)^{vi}
	Na10	2.78(4)^{iii}		S8	2.15(4)^{iv}
	Na6	2.80(3)^{iv}		S11	2.20(3)
	Na8	2.83(4)^{ii}		Na6	3.10(4)^{xiv}
	Na8	2.92(5)^{v}		Na3	3.15(5)^{viii}
S2	Si3	2.05(4)^{i}	Si3	S2	2.05(4)^{vi}
	Na11	2.70(5)^{iii}		S7	2.06(4)^{iv}
	Na9	2.76(4)^{ii}		S12	2.17(3)
	Na6	2.87(3)^{ii}		S4	2.18(3)^{iv}
	Na7	2.96(5)^{v}		Na2	3.01(4)^{viii}
	Na5	2.98(4)^{iv}		Na5	3.14(5)^{xiv}
S3	Si1	2.19(4)^{vi}	Na1	S9	2.64(4)^{xvi}
	Na4	2.69(4)^{vii}		S10	2.77(4)
	Na12	2.84(4)^{iii}		S6	2.95(5)^{ii}
	Na9	2.88(5)^{viii}		S9	3.05(4)^{ii}
	Na7	2.89(4)^{vii}		Si1	3.08(5)^{xvii}
	Na4	2.92(3)^{iv}		S6	3.11(4)^{xvi}
S4	Si3	2.18(3)^{ix}	Na2	S7	2.80(4)^{vii}
	Na6	2.80(3)^{x}		S11	2.84(4)
	Na8	2.84(4)^{xi}		S8	2.92(4)^{xvi}
	Na5	2.89(4)^{xii}		S4	2.93(4)^{vii}
	Na2	2.93(4)^{ii}		Si3	3.01(4)^{xviii}
	Na10	3.18(4)^{xiii}	Na3	S12	2.63(4)
S5	Si2	2.05(3)^{ix}		S7	2.80(4)^{xvi}
	Na3	2.88(4)^{ii}		S8	2.85(3)^{vii}
	Na7	2.90(4)^{xi}		S5	2.88(4)^{vii}
	Na5	3.11(4)^{x}		Si2	3.15(5)^{xviii}

Continued on next page

Continued from table B.6

Atom1	Atom2	distance [Å]	Atom1	Atom2	distance [Å]
	Na6	$3.16(4)^{xii}$	Na4	S3	$2.69(4)^{ii}$
S6	Si1	$2.16(3)^{ix}$		S10	2.81(4)
	Na1	$2.95(5)^{vii}$		S3	$2.92(3)^{ix}$
	Na4	$2.95(4)^{x}$		S6	$2.95(4)^{xvi}$
	Na9	$3.01(4)^{xiv}$		S6	$3.04(4)^{xii}$
	Na4	$3.04(4)^{xv}$		Si1	$3.13(5)^{xix}$
	Na1	$3.11(4)^{x}$	Na5	S1	$2.72(4)^{vii}$
S7	Si3	$2.06(4)^{ix}$		S4	$2.89(4)^{xv}$
	Na12	$2.60(4)^{xii}$		S11	2.95(4)
	Na2	$2.80(4)^{ii}$		S2	$2.98(4)^{ix}$
	Na3	$2.80(4)^{x}$		S5	$3.11(4)^{xvi}$
	Na9	$2.80(4)^{x}$		Si3	$3.14(5)^{xx}$
	Na7	3.01(5)	Na6	S4	$2.80(3)^{xvi}$
S8	Si2	$2.15(4)^{ix}$		S1	$2.80(3)^{ix}$
	Na10	$2.60(4)^{xv}$		S2	$2.87(3)^{vii}$
	Na3	$2.85(3)^{ii}$		S12	2.95(3)
	Na2	$2.92(4)^{x}$		Si2	$3.10(4)^{xx}$
	Na8	2.99(4)		S5	$3.16(4)^{xv}$
	Na8	$2.99(4)^{x}$	Na7	S9	$2.79(4)^{xvi}$
S9	Si1	$2.18(4)^{ix}$		S3	$2.89(4)^{ii}$
	Na1	$2.64(4)^{x}$		S5	$2.90(4)^{xix}$
	Na7	$2.79(4)^{x}$		S2	$2.96(5)^{xvii}$
	Na11	$2.80(5)^{xv}$		S7	3.01(5)
	Na9	2.98(5)	Na8	S1	$2.83(4)^{vii}$
	Na1	$3.05(4)^{vii}$		S4	$2.84(4)^{xix}$
S10	Si1	2.02(3)		S1	$2.92(5)^{xvii}$
	Na1	2.77(4)		S8	2.99(4)
	Na4	2.81(4)		S8	$2.99(4)^{xvi}$
	Na12	$3.13(4)^{xii}$	Na9	S2	$2.76(4)^{vii}$
	Na11	$3.14(5)^{xi}$		S7	$2.80(4)^{xvi}$
S11	Si2	2.20(3)		S3	$2.88(5)^{xviii}$
	Na2	2.84(4)		S9	2.98(5)
	Na10	$2.92(4)^{xi}$		S6	$3.01(4)^{xx}$
	Na10	$2.94(4)^{xv}$	Na10	S8	$2.60(4)^{xii}$
	Na5	2.95(4)		S1	$2.78(4)^{xxi}$
S12	Si3	2.17(3)		S11	$2.92(4)^{xix}$
	Na3	2.63(4)		S11	$2.94(4)^{xii}$
	Na6	2.95(3)		S4	$3.18(4)^{xxii}$
	Na11	$2.98(5)^{xv}$	Na11	S2	$2.70(5)^{xxi}$

Continued on next page

Continued from table B.6

Atom1	Atom2	distance [Å]	Atom1	Atom2	distance [Å]
	Na12	$2.99(4)^{xiv}$		S9	$2.80(5)^{xii}$
Si1	S10	2.02(3)		S12	$2.98(5)^{xii}$
	S6	$2.16(3)^{iv}$		S10	$3.14(5)^{xix}$
	S9	$2.18(4)^{iv}$	Na12	S7	$2.60(4)^{xv}$
	S3	$2.19(4)^{i}$		S3	$2.84(4)^{xxi}$
	Na1	$3.08(5)^{v}$		S12	$2.99(4)^{xx}$
	Na4	$3.13(5)^{xi}$		S10	$3.13(4)^{xv}$

B.3 Crystallographic data for $Na_{8.5}(AlS_4)_{0.5}(SiS_4)_{1.5}$

Table B.7: Crystallographic data and information for the structure solution and refinement from powder X-ray diffraction data for $Na_{8.5}(AlS_4)_{0.5}(SiS_4)_{1.5}$. Standard deviations are given in parentheses. These data were deposited in the Cambridge Crystallographic Data Centre and were given the deposition number CCDC 1980426.

$Na_{16.76(6)}(AlS_4)(SiS_4)_3$		
crystal system		monoclinic
space group		Cc, (Nr. 9)
lattice params.	a	17.5673(6) Å
	b	13.5408(5) Å
	c	14.2543(5) Å
	β	93.3683(13)°
V [Å^3]		3384.9(2)
Z		8
calculated density [gcm^{-3}]		1.982
diffractometer		Bruker D8 Quest (microfocus), MoK_α-radiation, Göbel mirror optics
temperature [K]		295
absorption coefficient [mm^{-1}]		1.382
ϑ-range [°]		2.32 – 27.50
indexing range		-22 $\leq h \leq$ 22, -17 $\leq k \leq$ 17, -18 $\leq l \leq$ 18
number of measured reflexions		66764
number of independent reflexions		7778
number of independent reflexions ($I \geq 2\sigma(I)$)		6660
R_{int}		0.0532
R_σ		0.0302
$F(000)$		1984
corrections		Lorentz-, polarization-, absorption-effects
absorption correction		multi-scan (SADABS)[13]
structure solution		direct methods, SHELXS97[3]
structure refinement		least-squares on F^2, SHELXL97[3]
number of free params.		350
Goof		1.040
R values (reflexions satisfying $I \geq 2\sigma(I)$)		$R1 = 0.0348$, $wR2 = 0.0814$
R values (all data)		$R1 = 0.0448$, $wR2 = 0.0863$
residual electron density [$e^-/\AA^{-3}$]		0.625/-0.499
twin law		(-1 0 0, 0 -1 0, 0 0 -1)
batch scale factor		0.46

Table B.8: Standardized fractional atomic coordinates[4] and equivalent isotropic displacement parameters [Å^2] for $Na_{8.5}(AlS_4)_{0.5}(SiS_4)_{1.5}$. Standard deviations are given in parentheses.

Atom	occupation-factor	Wyckoff-position	x	y	z	$U_{equiv.}$
Na1	1	4a	0.0000(2)	0.0160(3)	0.0160(3)	0.0403(8)
Na2	1	4a	0.0079(2)	0.2210(4)	0.2467(3)	0.0558(11)
S1	1	4a	0.04013(12)	0.0236(2)	0.31978(15)	0.0379(5)
S2	1	4a	0.04982(12)	0.2071(2)	0.05134(14)	0.0389(5)
Na3	1	4a	0.0627(2)	0.2428(3)	0.4983(4)	0.0610(12)
S3	1	4a	0.07158(13)	0.4809(2)	0.24654(15)	0.0352(5)
Na4	1	4a	0.1121(3)	0.0854(3)	0.6894(2)	0.0776(14)
S4	1	4a	0.14462(12)	0.5680(2)	0.03750(13)	0.0360(5)
Si1	1	4a	0.15165(12)	0.07480(14)	0.36658(15)	0.0250(4)
Si2	1	4a	0.15633(12)	0.57514(15)	0.19140(14)	0.0255(4)
Na5	0.895(8)	4a	0.1588(2)	0.3388(3)	0.1468(2)	0.0488(10)
S5	1	4a	0.16361(13)	0.0715(2)	0.51778(14)	0.0450(6)
S6	1	4a	0.16354(13)	0.2241(2)	0.3200(2)	0.0492(6)
Na6	0.805(14)	4a	0.2040(3)	0.1103(4)	0.1413(3)	0.067(2)
Na7	0.823(7)	4a	0.2062(2)	0.4083(2)	0.3655(2)	0.0318(8)
S7	1	4a	0.23822(13)	0.0183(2)	0.8137(2)	0.0394(5)
Na8	1	4a	0.2465(2)	0.2575(3)	0.5632(3)	0.0551(10)
S8	1	4a	0.25849(12)	0.2932(2)	0.00555(15)	0.0384(5)
S9	1	4a	0.26822(12)	0.5230(2)	0.23772(15)	0.0409(5)
Na9	1	4a	0.3017(2)	0.7230(4)	0.3090(3)	0.0563(11)
Na10	1	4a	0.3087(2)	0.4838(3)	0.0561(2)	0.0400(8)
Na11	0.848(7)	4a	0.3162(2)	0.1925(3)	0.3152(2)	0.0421(10)
Na12	1	4a	0.3179(2)	0.0119(4)	0.4977(3)	0.0756(15)
S10	1	4a	0.36523(10)	0.35601(14)	0.44868(12)	0.0274(4)
S11	1	4a	0.36644(13)	0.11952(15)	0.13820(14)	0.0355(5)
Si3	1	4a	0.37248(11)	0.24120(15)	0.04104(14)	0.0251(4)
S12	1	4a	0.38285(11)	0.19002(15)	0.63956(13)	0.0315(4)
Na13	1	4a	0.4038(3)	0.03996(10)	0.7780(4)	0.0429(3)
Na14	0.931(5)	4a	0.4046(3)	0.43673(10)	0.2774(3)	0.0344(5)
S13	1	4a	0.42616(11)	0.8087(2)	0.41727(14)	0.0355(5)
Si4	1	4a	0.43545(11)	0.24254(14)	0.51666(13)	0.0200(4)
S14	1	4a	0.44125(12)	0.11958(15)	0.41900(13)	0.0336(4)
S15	1	4a	0.44322(10)	0.35692(15)	0.10912(12)	0.0280(4)
Na15	0.934(8)	4a	0.4911(2)	0.0193(4)	0.0547(4)	0.070(2)
Na16	1	4a	0.4949(2)	0.1838(3)	0.2455(2)	0.0511(9)
Na17	0.498(12)	4a	0.6027(3)	0.1125(4)	0.4185(4)	0.029(2)
S16	1	4a	0.64521(14)	0.2255(2)	0.2408(2)	0.0464(6)
Na18	1	4a	0.6571(3)	0.3469(3)	0.4219(3)	0.101(2)

Table B.9: Anisotropic displacement coefficients [Å^2] for $Na_{8.5}(AlS_4)_{0.5}(SiS_4)_{1.5}$. U_{ij} is defined by: $U_{ij} = exp{-}2\pi^2[U_{11}(ha^*)^2 + ... + 2U_{21}hka^*b^*]$. Standard deviations are given in parentheses.

Atom	U_{11}	U_{22}	U_{33}	U_{23}	U_{13}	U_{12}
Na1	0.041(2)	0.038(2)	0.043(2)	0.0120(15)	0.009(2)	0.000(2)
Na2	0.039(2)	0.086(3)	0.041(2)	0.011(2)	-0.003(2)	0.012(2)
S1	0.0258(12)	0.0487(12)	0.0387(11)	-0.0098(9)	-0.0018(9)	-0.0132(9)
S2	0.0284(11)	0.0524(13)	0.0350(10)	-0.0109(10)	-0.0057(9)	0.0035(10)
Na3	0.030(2)	0.053(2)	0.100(3)	0.011(2)	-0.001(2)	0.001(2)
S3	0.0316(12)	0.0352(10)	0.0392(11)	-0.0022(8)	0.0046(8)	-0.0031(9)
Na4	0.119(3)	0.087(3)	0.0269(15)	0.0142(15)	0.008(2)	-0.040(2)
S4	0.0289(10)	0.0538(12)	0.0249(9)	0.0074(8)	-0.0008(7)	0.0046(9)
Si1	0.0206(10)	0.0213(9)	0.0330(10)	-0.0008(8)	0.0009(8)	-0.0006(8)
Si2	0.0203(10)	0.0303(11)	0.0260(9)	0.0073(8)	0.0013(8)	0.0007(8)
Na5	0.047(2)	0.074(2)	0.0256(12)	-0.0047(12)	0.0054(11)	-0.0092(15)
S5	0.0284(11)	0.076(2)	0.0312(10)	-0.0177(10)	0.0022(8)	-0.0026(11)
S6	0.0266(11)	0.0288(10)	0.091(2)	0.0030(11)	-0.0079(11)	0.0033(8)
Na6	0.065(4)	0.086(4)	0.050(3)	-0.018(2)	0.006(2)	0.010(3)
Na7	0.0388(14)	0.0251(13)	0.032(2)	-0.0004(11)	0.0026(11)	0.0020(11)
S7	0.0337(12)	0.0322(10)	0.0539(13)	-0.0034(9)	0.0157(10)	-0.0032(9)
Na8	0.033(2)	0.062(3)	0.070(2)	0.018(2)	0.00(2)	0.012(2)
S8	0.0236(11)	0.0520(13)	0.0390(11)	-0.0186(10)	-0.0022(8)	0.0085(9)
S9	0.0276(12)	0.0585(14)	0.0365(11)	0.0045(10)	0.0017(9)	0.0085(10)
Na9	0.039(2)	0.093(3)	0.036(2)	0.003(2)	-0.0061(15)	-0.026(2)
Na10	0.035(2)	0.040(2)	0.045(2)	0.0006(15)	0.003(2)	0.005(2)
Na11	0.027(2)	0.058(2)	0.040(2)	-0.0115(15)	-0.0123(13)	0.0148(15)
Na12	0.033(2)	0.125(4)	0.069(2)	0.063(2)	-0.002(2)	0.001(2)
S10	0.0272(10)	0.0257(9)	0.0289(9)	-0.0001(7)	-0.0013(7)	0.0009(7)
S11	0.0433(13)	0.0315(10)	0.0313(10)	0.0022(8)	-0.0002(9)	-0.0068(9)
Si3	0.0210(10)	0.0280(10)	0.0261(9)	-0.0030(8)	0.0008(8)	-0.0011(9)
S12	0.0267(10)	0.0409(10)	0.0273(8)	0.0101(8)	0.0049(7)	-0.0030(8)
Na13	0.0519(8)	0.0342(7)	0.0429(7)	0.001(2)	0.0052(6)	0.008(2)
Na14	0.0247(7)	0.0494(9)	0.0287(7)	0.000(2)	-0.0015(5)	-0.002(2)
S13	0.0248(10)	0.0508(12)	0.0307(9)	0.0101(9)	-0.0009(7)	0.0016(9)
Si4	0.0194(10)	0.0236(9)	0.0168(8)	0.0016(7)	0.0001(7)	0.0010(8)
S14	0.0388(12)	0.0319(10)	0.0302(10)	-0.0038(8)	0.0037(8)	0.0041(8)
S15	0.0256(10)	0.0310(9)	0.0272(9)	-0.0072(7)	-0.0016(7)	-0.0052(8)
Na15	0.026(2)	0.074(3)	0.108(4)	-0.053(2)	-0.007(2)	-0.001(2)
Na16	0.042(2)	0.049(2)	0.065(2)	-0.0140(15)	0.0269(15)	-0.0106(13)
Na17	0.031(3)	0.027(3)	0.029(3)	0.002(2)	0.004(2)	0.014(2)
S16	0.0368(13)	0.0221(9)	0.079(2)	-0.0110(10)	-0.0073(11)	0.0018(8)
Na18	0.105(3)	0.056(2)	0.151(4)	0.057(2)	0.085(3)	0.032(2)

Table B.10: Interatomic distances in $Na_{8.5}(AlS_4)_{0.5}(SiS_4)_{1.5}$. Standard deviations are given in parentheses.
i: x, -y, z-$\frac{1}{2}$; ii: x-$\frac{1}{2}$, y-$\frac{1}{2}$, z; iii: x-$\frac{1}{2}$, -y+$\frac{1}{2}$, z-$\frac{1}{2}$; iv: x, -y, z+$\frac{1}{2}$; v: x, -y+1, z+$\frac{1}{2}$; vi: x-$\frac{1}{2}$, -y+$\frac{1}{2}$, z+$\frac{1}{2}$; vii: x-$\frac{1}{2}$, y+$\frac{1}{2}$, z; viii: x, -y+1, z-$\frac{1}{2}$; ix: x+$\frac{1}{2}$, y+$\frac{1}{2}$, z; x: x+$\frac{1}{2}$, -y+$\frac{1}{2}$, z+$\frac{1}{2}$; xi: x+$\frac{1}{2}$, -y+$\frac{1}{2}$, z-$\frac{1}{2}$; xii: x+$\frac{1}{2}$, y-$\frac{1}{2}$, z;

Atom1	Atom2	distance [Å]	Atom1	Atom2	distance [Å]
Na1	S1	2.756(4)^{i}		Na10	2.808(4)
	S2	2.815(4)		Na18	2.818(5)^{iii}
	S15	2.870(4)^{ii}		Na9	2.954(4)^{viii}
	S10	2.990(4)^{iii}		Na17	3.203(6)^{iii}
	S5	3.105(4)^{i}	S9	Na14	2.696(5)
	Si4	3.474(4)^{iii}		Na10	2.775(4)
	Na4	3.526(5)^{i}		Na9	2.939(5)
	Na10	3.528(2)^{ii}	Na9	S13	2.848(4)
	Na14	3.557(5)^{iii}		S16	2.862(5)^{vii}
	Na18	3.559(5)^{iii}		S8	2.954(4)^{v}
	Na3	3.674(5)^{i}		S12	3.108(4)^{viii}
	Na6	4.205(6)		Si3	3.498(4)^{v}
Na2	S12	2.866(4)^{iii}		Na18	3.513(6)^{vii}
	S6	2.869(4)		Na8	3.590(5)^{viii}
	S1	2.912(5)		Na13	3.716(5)^{viii}
	S2	2.929(4)		Na2	3.779(2)^{ix}
	S13	3.129(5)^{ii}		Na17	4.188(7)^{vii}
	Na5	3.470(6)	Na10	S10	2.866(4)^{viii}
	Si4	3.483(4)^{iii}		S15	2.984(4)
	Na3	3.670(6)		Si3	3.482(4)
	Na13	3.756(6)^{iii}		Na7	3.490(5)^{viii}
	Na9	3.779(2)^{ii}		Na1	3.528(2)^{ix}
	Na6	4.121(7)		Na14	3.546(5)
S1	Si1	2.147(3)		Na8	3.672(5)^{viii}
	Na14	2.692(5)^{ii}		Na17	4.220(6)^{iii}
	Na4	2.739(4)^{i}	Na11	S14	2.758(4)
	Na1	2.756(4)^{iv}		S11	2.895(4)
S2	Si4	2.151(3)^{iii}		S10	3.012(4)
	Na18	2.811(4)^{iii}		S7	3.165(5)^{i}
	Na5	2.896(4)		Na16	3.350(2)
	Na6	3.208(6)		Si4	3.520(4)
	Na17	3.259(6)^{iii}		Na13	3.557(5)^{i}

Continued on next page

Continued from table B.10

Atom1	Atom2	distance [Å]	Atom1	Atom2	distance [Å]
Na3	S13	2.750(4)^{ii}		Na12	3.570(5)
	S5	2.922(5)	Na12	S11	2.775(4)^{iv}
	S4	2.975(5)^{v}		S14	2.892(5)
	S15	3.020(5)^{vi}		S7	2.928(5)^{i}
	S6	3.192(5)		Na15	3.130(2)^{iv}
	Na8	3.311(2)		S12	3.307(6)
	Si1	3.389(5)		Na6	3.378(6)^{iv}
	Si3	3.439(4)^{vi}		Na13	3.624(7)^{i}
	Na4	3.527(6)		Na18	3.712(7)^{ii}
	Na15	3.567(7)^{vi}	S10	Si4	2.164(3)
	Na1	3.674(5)^{iv}		Na14	2.799(5)
S3	Si2	2.145(3)		Na10	2.866(4)^{v}
	Na5	2.886(4)		Na1	2.990(4)^{x}
	Na7	2.994(4)	S11	Si3	2.159(3)
	Na13	3.020(6)^{iii}		Na12	2.775(4)^{i}
	Na15	3.049(6)^{vii}		Na16	2.790(4)
	Na17	3.053(6)^{vii}		Na15	2.890(5)
	Na16	3.060(4)^{vii}		Na13	2.985(4)^{i}
Na4	S5	2.665(4)	Si3	S13	2.158(3)^{viii}
	S16	2.717(5)^{vi}		S15	2.191(3)
	S1	2.739(4)^{iv}		Na3	3.439(4)^{xi}
	S7	2.901(5)		Na9	3.498(4)^{viii}
	Na6	3.199(7)^{iv}	S12	Si4	2.149(3)
	S15	3.212(5)^{vi}		Na13	2.841(4)
	Si1	3.370(4)^{iv}		Na2	2.866(4)^{x}
	Na18	3.485(6)^{vi}		Na9	3.108(4)^{v}
	Na1	3.526(5)^{iv}	Na13	S13	2.864(4)^{v}
	Na8	3.840(6)		S11	2.985(4)^{iv}
	Na16	3.851(6)^{vi}		S14	2.998(4)^{iv}
S4	Si2	2.193(3)		S3	3.020(6)^{x}
	Na7	2.756(4)^{viii}		Na16	3.471(4)^{iv}
	Na15	2.802(5)^{vii}		Na11	3.557(5)^{iv}
	Na8	2.974(5)^{viii}		Na12	3.624(7)^{iv}
	Na3	2.975(5)^{viii}		Na15	3.700(8)^{iv}
	Na17	3.040(6)^{iii}		Na9	3.716(5)^{v}
	Na10	3.095(4)		Na2	3.756(6)^{x}
Si1	S6	2.143(3)	Na14	S1	2.692(5)^{ix}
	S7	2.146(3)^{i}		S15	2.752(5)
	S5	2.154(3)		Na1	3.557(5)^{x}

Continued on next page

Continued from table B.10

Atom1	Atom2	distance [Å]	Atom1	Atom2	distance [Å]
	Na18	3.185(4)^{ii}		Na16	3.813(4)
	Na4	3.370(4)^{i}		Na4	3.934(7)^{xi}
	Na11	3.418(5)	S13	Si3	2.158(3)^{v}
	Na6	3.426(5)		Na3	2.750(4)^{ix}
	Na12	3.480(4)		Na13	2.864(4)^{viii}
Si2	S9	2.155(3)		Na2	3.129(5)^{ix}
	S16	2.167(3)^{vii}		Na15	3.209(6)^{v}
	Na5	3.264(5)	Si4	S2	2.151(3)^{x}
	Na16	3.325(4)^{vii}		S14	2.176(3)
	Na8	3.365(5)^{viii}		Na1	3.474(4)^{x}
	Na7	3.431(4)		Na2	3.483(4)^{x}
	Na17	3.461(5)^{vii}	S14	Na15	2.801(4)^{iv}
	Na15	3.483(5)^{vii}		Na16	2.835(4)
Na5	S8	2.814(4)		Na17	2.838(6)
	S6	2.913(4)		Na13	2.998(4)^{i}
	Na6	3.196(7)	S15	Na1	2.870(4)^{ix}
	Na7	3.316(4)		Na3	3.020(5)^{xi}
	S9	3.363(5)		Na16	3.145(4)
	Na17	3.408(6)^{iii}		Na4	3.212(5)^{xi}
	Na10	3.586(5)	Na15	S14	2.801(4)^{i}
	Na15	3.991(6)^{vii}		S4	2.802(5)^{xii}
S5	Na12	2.859(5)		S3	3.049(6)^{xii}
	Na8	2.961(5)		Na12	3.130(2)^{i}
	Na6	3.085(6)^{iv}		S13	3.209(6)^{viii}
	Na1	3.105(4)^{iv}		Na17	3.354(7)^{i}
	Na18	3.333(5)^{ii}		Si2	3.483(5)^{xii}
S6	Na7	2.673(4)		Na16	3.513(5)
	Na11	2.721(4)		Na3	3.567(7)^{xi}
	Na6	3.095(6)		Na13	3.700(8)^{i}
Na6	S11	2.859(6)		Na5	3.991(6)^{xii}
	S7	3.044(6)^{i}	Na16	S16	2.705(4)
	S5	3.085(6)^{i}		S3	3.060(4)^{xii}
	Na4	3.199(7)^{i}		Na17	3.171(6)
	Na18	3.238(7)^{iii}		Si2	3.325(4)^{xii}
	Na11	3.270(6)		Na13	3.471(4)^{i}
	S8	3.318(6)		Na4	3.851(6)^{xi}
	Na12	3.378(6)^{i}	Na17	S4	3.040(6)^{x}
Na7	S9	2.674(4)		S3	3.053(6)^{xii}
	S4	2.756(4)^{v}		S16	3.088(6)

Continued on next page

Continued from table B.10

Atom1	Atom2	distance [Å]	Atom1	Atom2	distance [Å]
	S10	3.053(4)		S8	3.203(6)^{x}
	Na17	3.418(5)^{vii}		S2	3.259(6)^{x}
	Na10	3.490(5)^{v}		Na18	3.315(7)
	Na8	3.518(5)		Na15	3.354(7)^{iv}
	Na11	3.599(5)		Na5	3.408(6)^{x}
	Na14	3.793(6)		Na7	3.418(5)^{xii}
S7	Si1	2.146(3)^{iv}		Si2	3.461(5)^{xii}
	Na18	2.828(4)^{vi}	S16	Si2	2.167(3)^{xii}
	Na12	2.928(5)^{iv}		Na4	2.717(5)^{xi}
	Na13	2.997(6)		Na9	2.862(5)^{xii}
	Na6	3.044(6)^{iv}		Na18	3.058(6)
	Na11	3.165(5)^{iv}		Na8	3.187(5)^{xi}
Na8	S12	2.730(4)	Na18	S2	2.811(4)^{x}
	S4	2.974(5)^{v}		S8	2.818(5)^{x}
	S10	3.032(4)		S7	2.828(4)^{xi}
	S16	3.187(5)^{vi}		Si1	3.185(4)^{ix}
	Si2	3.365(5)^{v}		Na6	3.238(7)^{x}
	Si4	3.429(4)		S5	3.333(5)^{ix}
	Na9	3.590(5)^{v}		Na4	3.485(6)^{xi}
	Na10	3.672(5)^{v}		Na9	3.513(6)^{xii}
	Na12	3.694(7)		Na1	3.559(5)^{x}
S8	Si3	2.155(3)		Na12	3.712(7)^{ix}

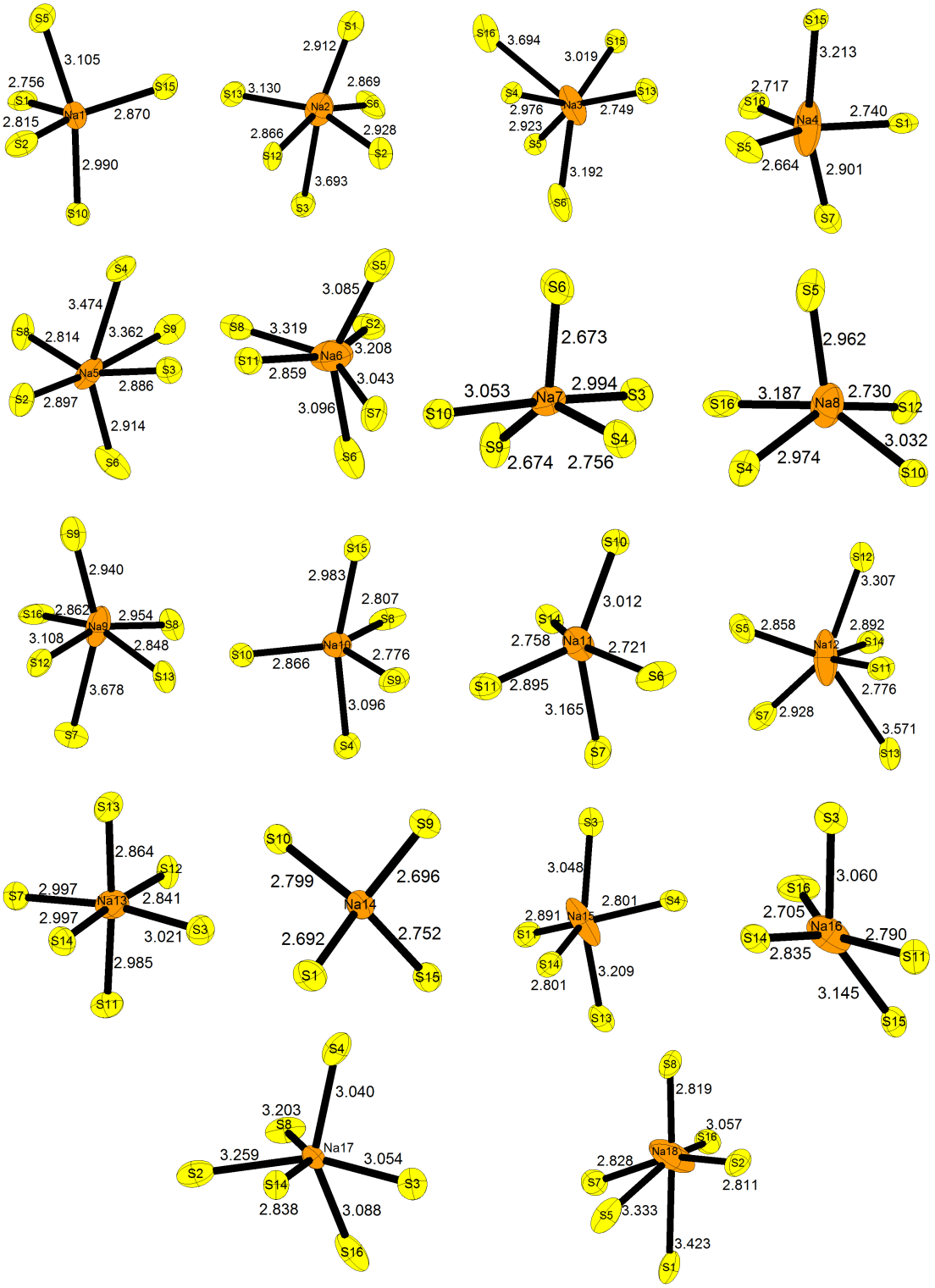

Figure B.1: Sodium ion coordination in $Na_{8.5}(AlS_4)_{0.5}(SiS_4)_{1.5}$. Na–S-distances are given in Å. Sodium atoms are depicted in orange, sulfur atoms in yellow. Ellipsoids are drawn at 80% probability.

B.4 Thermal analysis

Due to the occurrence of crystalline side phases in Na_5AlS_4 samples, the synthesis conditions had to be optimized. Therefore, DSC measurements were done for the pseudo-binary border phases Na_4SiS_4 and Na_5AlS_4. Both compounds were synthesized in small (6 mm diameter) sealed carbon coated quartz ampoules at 600 °C suited for DSC measurements and annealed for 3 h. The subsequent DSC measurements are depicted in figure B.2. Both compounds show broad endothermic signals during heating at 608 °C (Na_4SiS_4) and 722 °C (Na_5AlS_4), respectively, which are attributed to a complicated multi-step melting process of the materials. In the case of Na_5AlS_4, this is presumed to be a decomposition reaction which also takes place at lower temperatures, albeit at a slower rate, since samples synthesized at 650 °C and above showing increasing amounts of an unknown crystalline side phase. This decomposition behaviour, at least to crystalline side phases, was not observed for Na_4SiS_4. However, the maximum synthesis temperatures were chosen to be below the onset of melting of Na_4SiS_4 at 600 °C, which was suitable for all products.

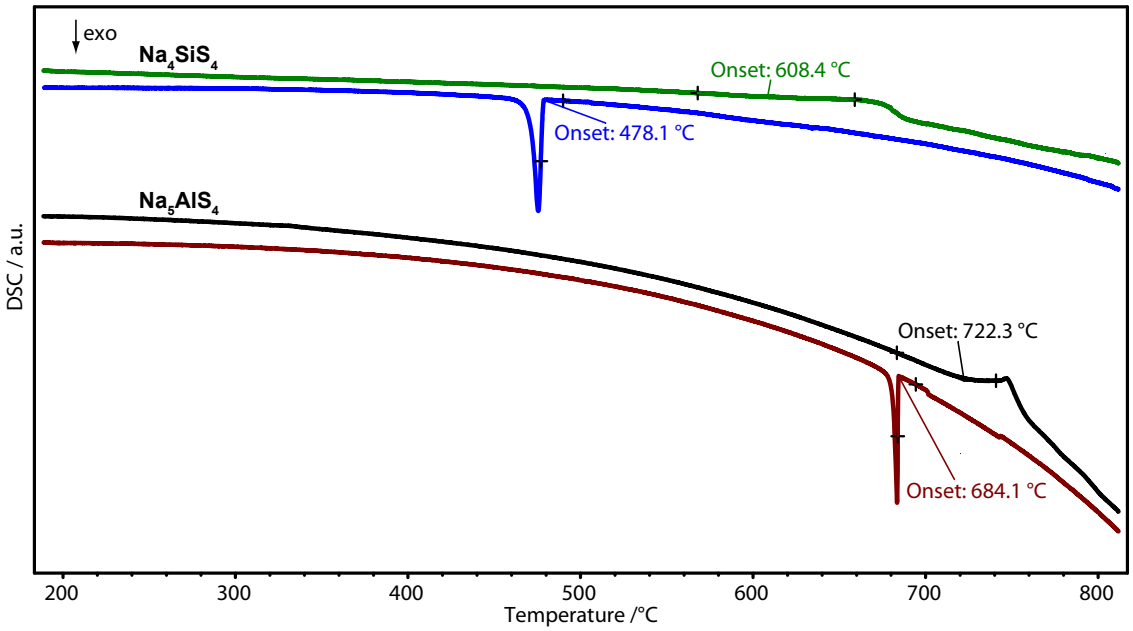

Figure B.2: DSC measurement of Na_4SiS_4 and Na_5AlS_4; green and blue lines represent the heating and cooling ramps of Na_4SiS_4, respectively, measured at 5 $Kmin^{-1}$, black and red lines represent the heating and cooling ramps of Na_5AlS_4, respectively, measured at 2 $Kmin^{-1}$.

In addition, we were interested why the only sample showing big single crystals ($d \approx 200\ \mu m$) was with $x = 75\%$ for $Na_{5-x}Al_{1-x}Si_xS_4$. Therefore, the synthesis conditions were mimicked by heating the precursors to 600 °C for 3 h directly in the DSC machine and measuring the thermal signals during subsequent cooling. The DSC curve (cf. Fig.

B.3) shows two distinct exothermic signals at 542 °C and 299 °C. The first signal probably corresponds to the crystallization of $Na_{8.5}(AlS_4)_{0.5}(SiS_4)_{1.5}$ from the melt and the latter is in good accordance with the melting point of sodium tetrasulfide (Na_2S_4, m.p.=300 °C).[14] The signal's broad nature also suggests the presence of sodium polysulfides with higher chain lengths. This polysulfide melt could be beneficial for crystal growth by acting as a solvent for the targeted phase $Na_{8.5}(AlS_4)_{0.5}(SiS_4)_{1.5}$. Since there are no indications of crystalline polysulfides in the PXRD or isolated sodium and sulfur rich areas in SEM/EDX measurements, we suppose that the polysulfide melt forms from unreacted Na_2S and excess S during the reaction and gets gradually consumed with progressing reaction time.

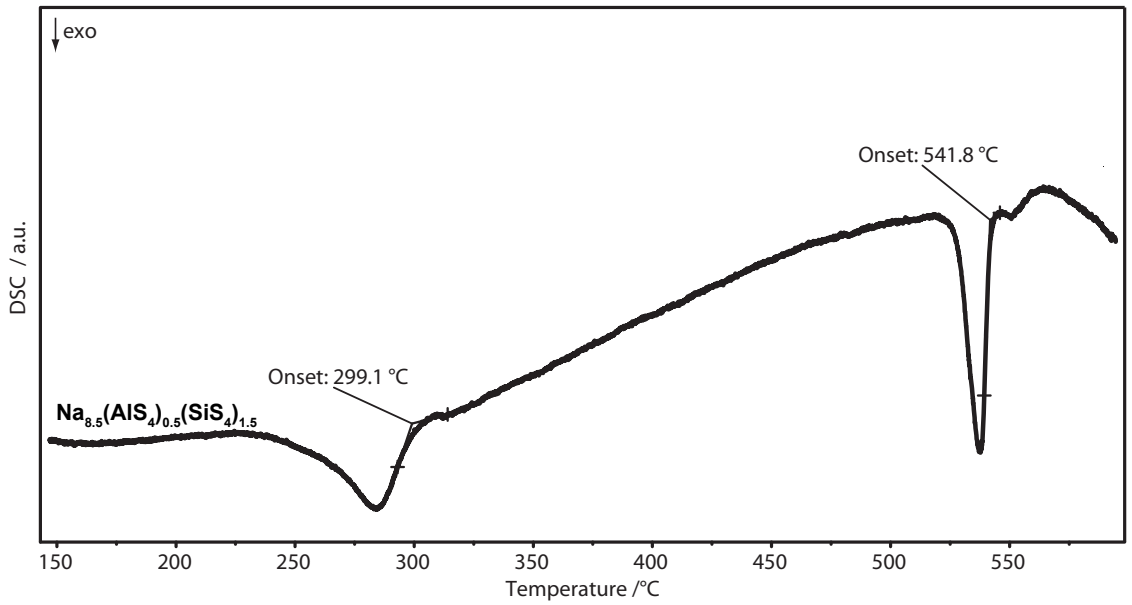

Figure B.3: DSC measurement of $Na_{5-x}Al_{1-x}Si_xS_4$, $x = 75\%$; the measurement corresponds to the cooling of the sample at a rate of 5 $Kmin^{-1}$ after annealing it at 600 °C for 3 h.

B.5 Electron microscopy

Since the Al/Si occupancy for the single crystal data of $Na_{8.5}Al_{0.5}Si_{1.5}S_8$ ($x = 0.75$) could not be refined because of the similar atomic form factors of the two elements, EDX spectroscopy was used to determine the composition. Table B.11 shows the normalized results, averages, the respective standard deviations for O, Na, Al, Si and S, as well as SEM micrographs depicting the positions on the sample. From the SEM micrographs and the values for oxygen it is evident that the sample was partially hydrolyzed on the surface by being in contact with air although exposure time was less than 30 s. While the values for Na and S are systematically too low and show a large spread supposedly due to hydrolysis and the strongly hygroscopic behavior of the sample, Al/Si ratios are within a small error margin and show a slightly lower Al/Si ratio as expected from the weighted precursors, which is in good accordance with the data obtained from SCXRD.

Table B.11: Results of EDX measurements for $Na_{8.5}Al_{0.5}Si_{1.5}S_8$ ($x = 0.75$) in atom% normalized to the sum of Al and Si being 4. SEM micrographs depict the positions on the sample.

Position	O	Na	Al	Si	S
SHA089 1	4.693	15.884	0.998	3.002	11.717
SHA089 2	8.492	12.860	1.076	2.924	11.379
SHA089 3	10.782	12.075	0.722	3.278	17.440
SHA089 4	8.844	15.756	0.928	3.072	15.796
SHA089 5	7.596	13.464	1.022	2.978	12.397
SHA089 6	12.085	14.975	0.730	3.270	18.945
SHA089 7	7.760	12.525	1.070	2.930	10.467
SHA089 8	6.326	14.372	0.915	3.085	10.921
SHA089 9	18.805	14.123	0.832	3.168	11.439
SHA089 10	8.225	13.775	0.857	3.143	12.760
SHA089 11	5.089	14.522	0.881	3.119	11.512
SHA089 12	7.019	13.404	0.985	3.015	11.388
SHA089 13	6.663	10.975	1.025	2.975	10.186
SHA089 14	6.982	11.258	0.974	3.026	9.481
SHA089 15	8.892	12.715	1.012	2.988	12.023
SHA089 16	2.589	15.593	0.902	3.098	11.485
average	8	14	0.9	3.1	12
std. deviation	4	2	0.1	0.1	3

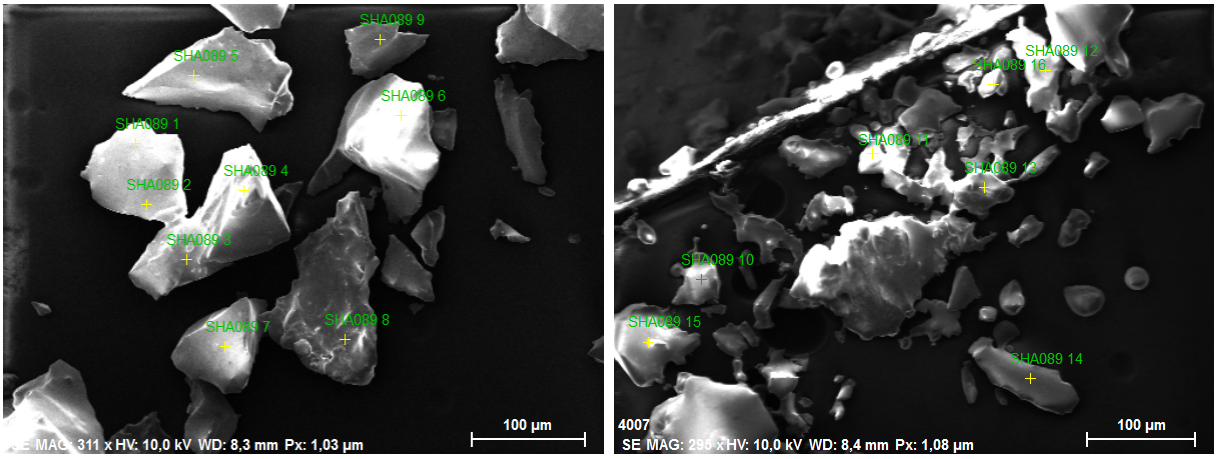

B.5.1 BVEL calculations

Description of BVEL calculations

In this section we describe the general procedure of calculating bond valence sums and bond valence energy landscapes using the program 3DBVSMAPPER. We also discuss the limitations of this method.
In practice, the program 3DBVSMAPPER executes the following procedure:
(i) Removal of all atoms of low occupancy ($SOF < 0.05$).
(ii) Removal of the tested ion (here Na^+).
(iii) Creation of equal size voxel points across the unit cell (here: 0.2 Å).
(iv) Calculation of the BVEL at each point in real space.
(v) Analysis of the volumetric data: calculation of the global minimum energy E_{min}^{global}, the minimum energy within the infinitely connected pathway E_{min}^{path} and the energy E_{mig}^{path}, at which a infinitely connected pathway is formed.
(vi) Generation of a periodic grid file (*.grd).

The output file of *.grd extension can be used as a volumetric data input for VESTA.[15] Although the BV approach used in this work provides quite accurate insights into ion migration pathways in possible crystalline solid ion conductors, some factors are not considered in this method. In DFT and molecular dynamics calculations the relaxation of the anionic lattice during ion migration through a bottleneck is usually considered. This relaxation, however, is lowering the potential energy of the transition sate and therefore lowering E_{mig}, compared to the energy of the transition state calculated by the BV approach. Additionally, coulombic repulsion of Na^+–Na^+ is not included in this model, since all tested ions are removed from the structure before calculation. This can lead to underestimating the energy at real space points of higher test ion probability (e.g. along the conduction pathway), since the BV calculated energy landscape mimics a migration network for one test ion per unit cell. This is less important for materials with low concentrations of the migrating ion but plays a more crucial role in materials with high mobile ion concentrations. Pathways might be clogged by repulsion of ions with the same charge, may they be of the same or different kind, thus increasing E_{mig}. Additionally, the BV method is restricted to mostly ionic compounds, excluding compounds with a more covalent bonding character and metals. Despite these methodological drawbacks, calculated bond valence energy landscapes provide fast and computationally cheap access for investigating ion migration pathways in crystalline (ionic) solids.

B.5.2 BVEL calculations of Na_5AlS_4

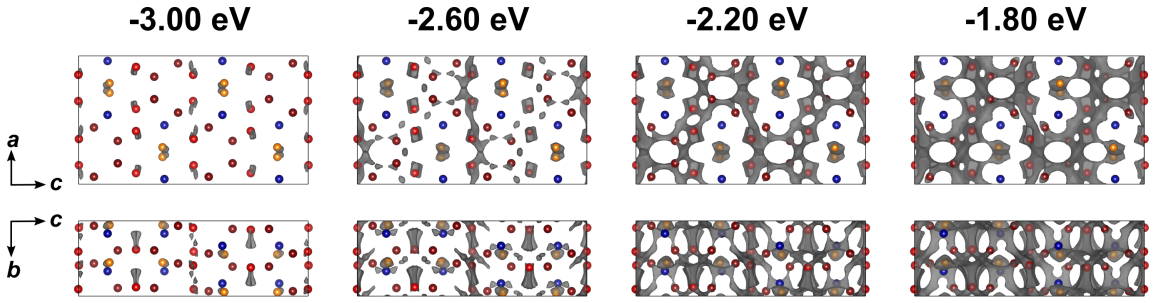

Figure B.4: Crystal structure of Na_5AlS_4 with Na atoms drawn in red (migrating ions) and orange (isolated ions), Al atoms drawn in blue and sulfur atoms depicted in yellow. Bond valence energy landscape at different isoenergy values are drawn in grey.

B.5.3 BVEL calculations of Na_4SiS_4

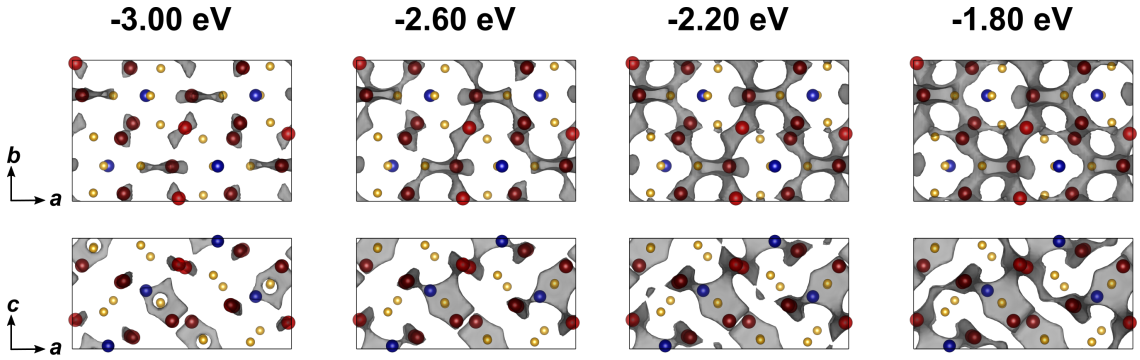

Figure B.5: Crystal structure of Na_4SiS_4 with Na atoms drawn in red, Si atoms drawn in blue and sulfur depicted in yellow. Bond valence energy landscape at different isoenergy values are drawn in grey.

B.5.4 BVEL calculations of $Na_9(AlS_4)(SiS_4)$

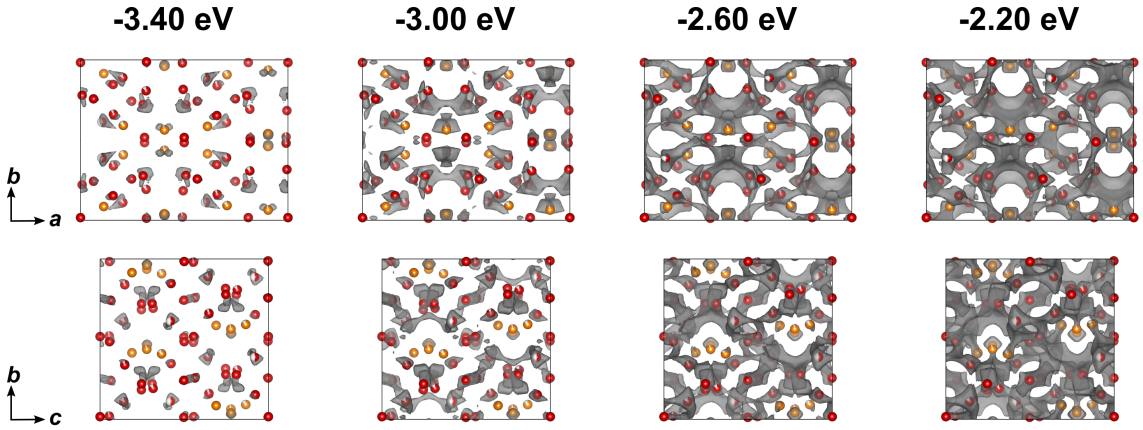

Figure B.6: Crystal structure of $Na_9(AlS_4)(SiS_4)$ with Na atoms drawn in red (migrating ions) and orange (isolated ions). Bond valence energy landscape at different isoenergy values are drawn in grey.

B.6 Electrochemical characterization

B.6.1 Galvanostatic polarization measurements

A transference number t_{ion} of 0.9998 of an representative sample ($Na_{5-x}Al_{1-x}Si_xS_4$ with x = 0.05) was determined by direct current galvanostatic polarization measurements using blocking-electrodes (stain less steel). The material is thus a mainly ionic conductor.[10,16]

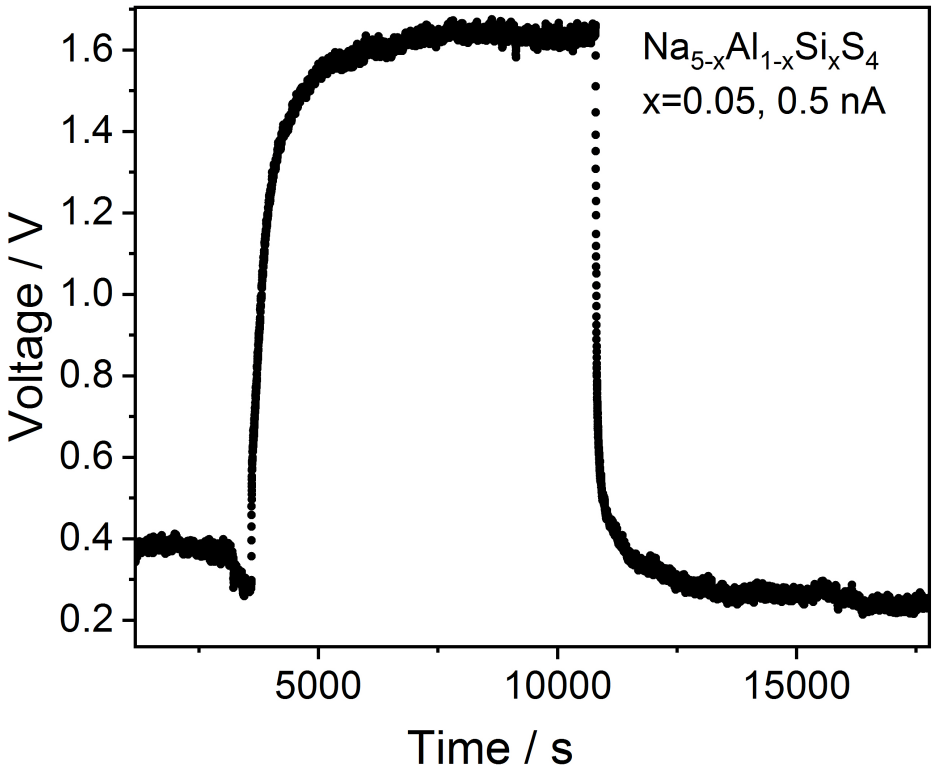

Figure B.7: Galvanostatic polarization measurement of $Na_{5-x}Al_{1-x}Si_xS_4$ with $x = 0.05$ with a current of 0.5 nA shows an electronic conductivity of $6x10^{-11} S\,cm^{-1}$ and a transference number of 0.9998. The material is clearly a mainly ionic conducting material.

B.7 Electrochemical impedance spectroscopy

Table B.12: Ionic conductivities calculated from R_1 and R_{Tot} (=R_1+R_2) and the respective capacitances of representative measurements shown in Figure B.8 at 25 °C of $Na_{5-x}Al_{1-x}Si_xS_4$ with ($0 \leq x \leq 1$). The electrode area was 0.20 cm^2 and the thickness of the pellets in the range of 0.35-0.75 mm.

x	σ_{R1} / S cm^{-1}	σ_{RTot} / S cm^{-1}	Ceff$_1$ / F	CPE$_1$	α_1	Ceff$_2$ / F	CPE$_2$	α_2
0.00	4.27E-7	1.52E-7	2.26E-10	3.11E-10	0.96	1.75E-8	8.46E-8	0.59
0.025	3.72E-7	2.18E-7	1.86E-10	3.15E-10	0.94	2.35E-8	1.54E-7	0.59
0.05	6.41E-7	2.86E-7	1.96E-10	2.77E-10	0.96	2.02E-8	1.63E-7	0.50
0.10	4.81E-7	1.27E-7	2.19E-10	5.55E-10	0.90	3.44E-7	6.29E-7	0.42
0.25	1.82E-6	5.47E-7	2.22E-10	-	-	2.48E-8	8.48E-8	0.76
0.50	5.19E-6	2.76E-6	2.06E-10	-	-	5.11E-8	4.53E-7	0.63
0.625	7.14E-6	-	2.41E-10	3.63E-10	0.97	-	-	-
0.75	2.78E-5	-	1.86E-10	-	-	-	-	-
0.90	2.31E-6	1.46E-6	2.00E-10	-	-	4.56E-8	1.53E-7	0.78
0.95	5.83E-6	7.64E-7	2.75E-10	-	-	2.81E-8	1.59E-7	0.67
1.00	2.85E-7	-	1.58E-10	-	-	-	-	-

Table B.13: Pellet density of $Na_{5-x}Al_{1-x}Si_xS_4$ with ($0 \leq x \leq 1$) samples shown in Figure B.8 and their activation energies with prefactor σ_0 averaged over several temperature cycles.

x	pellet density	$E_a(R1)$ / eV	standard deviation (E_a)	σ_0 / KS cm^{-1}	standard deviation (σ_0)
0.00	0.87	0.35	0.01	118	39
0.025	0.81	0.36	0.02	154	99
0.05	0.91	0.37	0.01	288	74
0.10	0.86	0.35	0.01	116	26
0.25	0.80	0.37	0.003	1059	154
0.50	0.87	0.35	0.01	1106	278
0.625	0.87	0.36	0.01	2954	681
0.75	0.88	0.31	0.001	1684	59
0.90	0.88	0.34	0.01	394	86
0.95	0.80	0.40	0.01	4389	1603
1.00	0.76	0.36	0.01	78	24

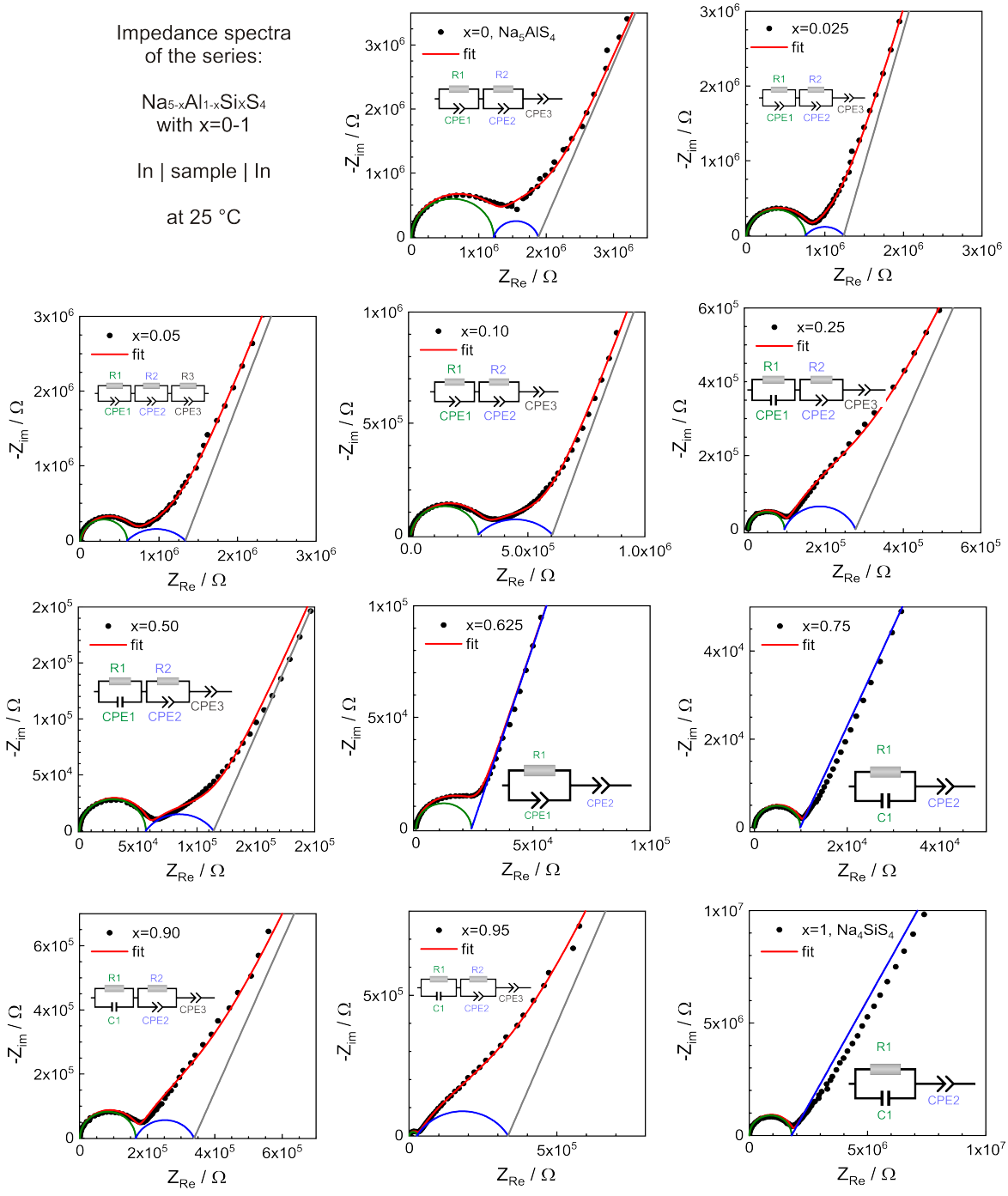

Figure B.8: For each member of the series $Na_{5-x}Al_{1-x}Si_xS_4$ with $(0 \leq x \leq 1)$ a representative impedance spectrum with fit and equivalent circuit model at 25 °C is given. The according values for conductivity, capacitance, activation energy and the prefactor are given in TableB.12 and TableB.13. For x=0.625,0.75and1.00 the inclusion of a low frequency semicircle into the model leads to overfitting. Thus, the best fitting model consists only of one RC- or RCPE-element in series to an CPE.

Table B.14: Ionic conductivity data calculated from R_{Tot} and averaged over all samples measured for each member of the series $Na_{5-x}Al_{1-x}Si_xS_4$ with $(0 \leq x \leq 1)$ at 25 °C. The activation energies $\sigma(R_{Tot})$ were averaged over all samples and several temperature cycles for each sample. The electrode area was 0.20 cm^2 and the thickness of the pellet in the range of 0.35-0.75 mm.

x	$\sigma_{R_{Tot}}$ / Scm^{-1}	Standard deviation and error	$E_a(R_2)$ / eV	Standard deviation
0.00	1.68E-07	1.91E-08	0.38	0.09
0.025	2.01E-07	1.35E-08	0.50	0.04
0.05	2.63E-07	3.35E-08	0.42	0.04
0.10	1.31E-07	3.22E-08	0.46	0.04
0.25	7.49E-07	5.04E-07	0.39	0.04
0.50	1.81E-06	3.63E-07	0.37	0.08
0.625	-	-	-	-
0.75	-	-	-	-
0.90	8.93E-07	3.34E-07	0.36	0.04
0.95	5.46E-07	8.57E-08	0.63	0.03
1.00	-	-	-	-

Table B.15: Ionic conductivity data calculated from R_1 and averaged over all samples measured for each member of the series $Na_{5-x}Al_{1-x}Si_xS_4$ with $(0 \leq x \leq 1)$ at 25 °C. The activation energies $\sigma(R_1)$ were averaged over all samples and several temperature cycles for each sample. The electrode area was 0.20 cm^2 and the thickness of the pellet in the range of 0.35-0.75 mm.

x	σ_{R1} / Scm^{-1}	Standard deviation and error	E_a / eV	Standard deviation
0.00	3.20E-07	3.12E-08	0.35	0.01
0.025	3.07E-07	3.65E-08	0.39	0.02
0.05	6.42E-07	8.99E-08	0.37	0.02
0.10	1.29E-06	8.20E-08	0.37	0.01
0.25	2.06E-06	1.38E-07	0.38	0.01
0.50	7.04E-06	4.23E-07	0.36	0.01
0.625	6.44E-06	2.69E-07	0.33	0.02
0.75	2.04E-05	1.32E-06	0.31	0.01
0.90	1.89E-06	2.04E-07	0.33	0.01
0.95	4.49E-06	1.16E-06	0.37	0.01
1.00	1.64E-07	4.64E-08	0.38	0.01

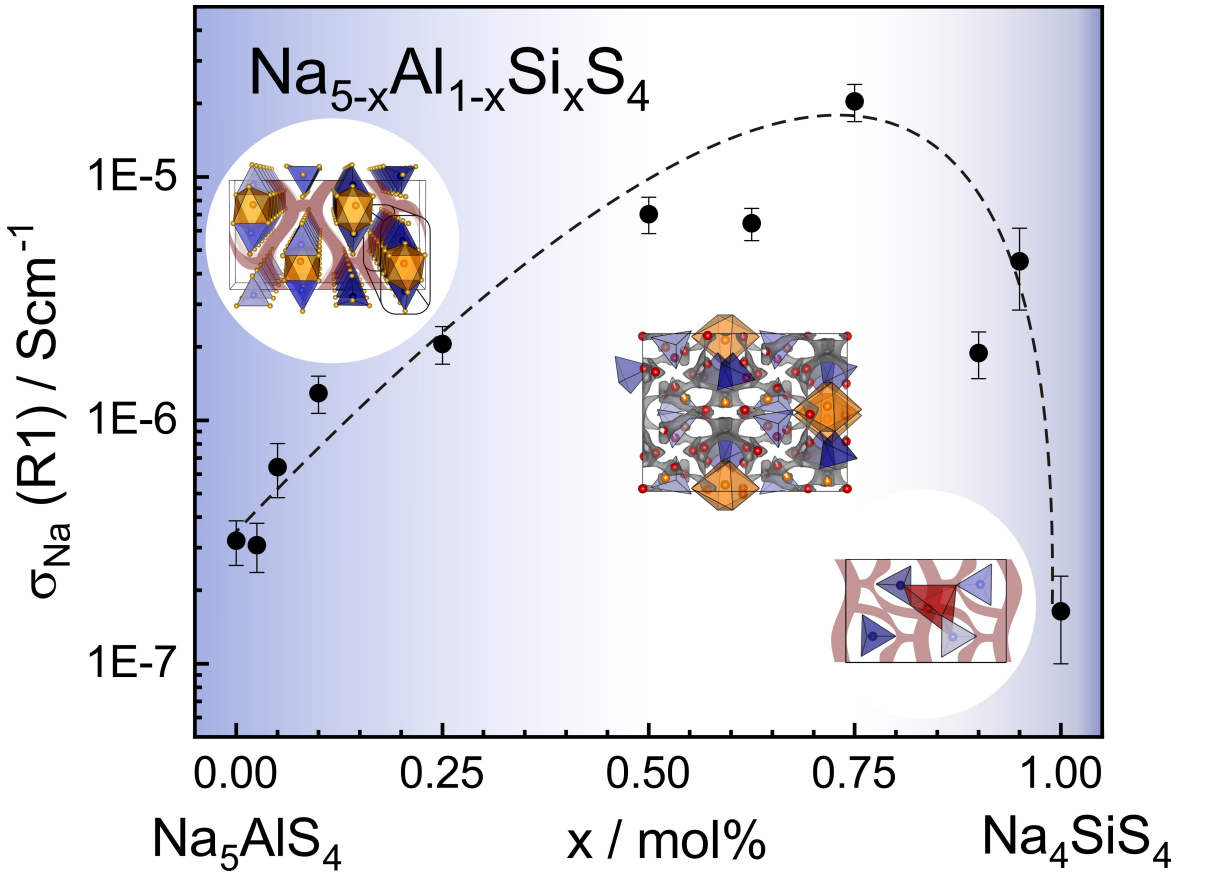

Figure B.9: Ionic conductivities calculated exclusively from the resistance of the high frequency semicircle (R1) excluding resistive processes occurring for some member of in $Na_{5-x}Al_{1-x}Si_xS_4$ with $(0 \leq x \leq 1)$. The error bars denote the error and the standard deviation of the values.

B.7.1 Activation Energies

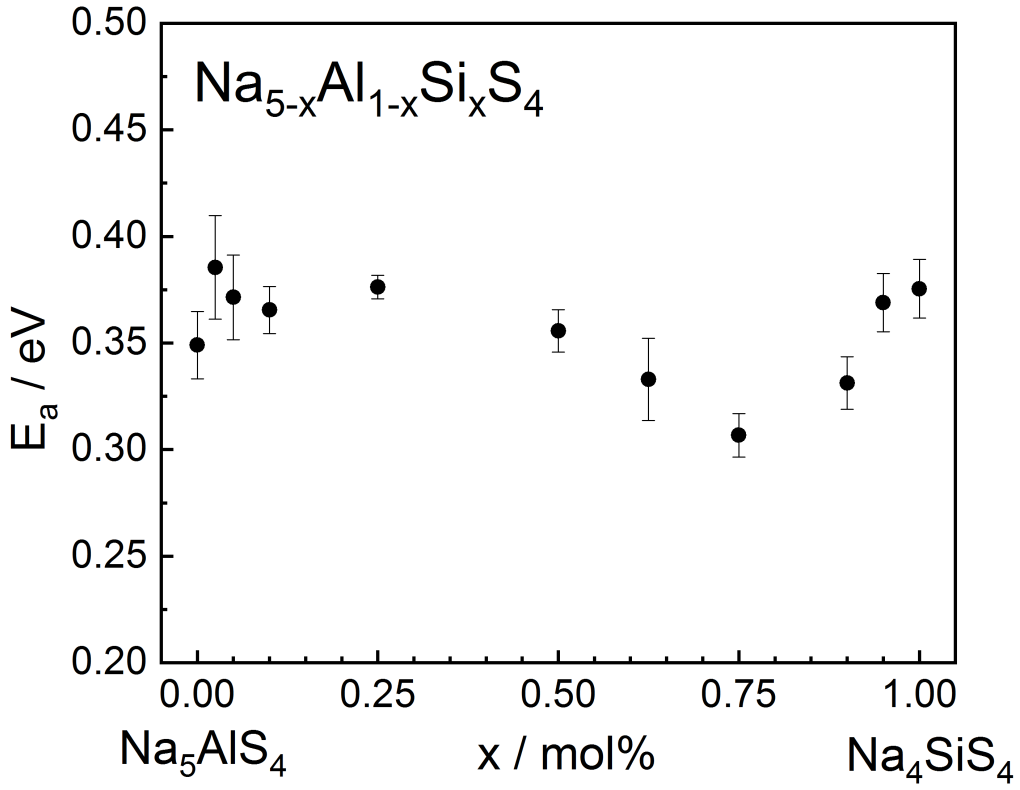

Figure B.10: The measured activation energies range from 0.30-0.38 eV for the whole substitution range of $Na_{5-x}Al_{1-x}Si_xS_4$ with ($0 \leq x \leq 1$). The lowest activation energy can be found in the double salt at x=0.75. The error bars denote the error and the standard deviation of the values.

Appendix C

Additional supporting information

C.1 Additional data for Chapter 1

Table C.1: Total ionic conductivities at room temperature and the respective activation energies for selected lithium solid electrolytes. This data was used to create Figure 1.3.

Solid electrolyte	Composition	Total Li ion conductivity (RT) $/mS\ cm^{-1}$	E_a $/meV$	Reference
LSiPSCl	$Li_{9.54}Si_{1.74}P_{1.44}S_{11.7}Cl_{0.3}$	25	238	[17]
LGPS	$Li_{10}GeP_2S_{12}$	12	249	[18]
LSnPS	$Li_{10}SnP_2S_{12}$	5.5	259	[19]
LLZO	$Li_7La_3Zr_2O_{12}$	0.24	310	[20]
LPS	Li_3PS_4	0.16	356	[21]
LSiPSO	$Li_{9.42}Si_{1.02}P_{2.1}S_{9.96}O_{2.04}$	0.11	238	[22]
LLTO	$Li_{0.34}La_{0.56}TiO_3$	0.07	420	[23]
$LiPON_{0.46}$	$Li_{2.98}PO_{3.30}N_{0.46}$	$3.3 \cdot 10^{-3}$	540	[24]

C.2 Additional data for Chapter 4.1

C.2.1 Electrochemical impedance data

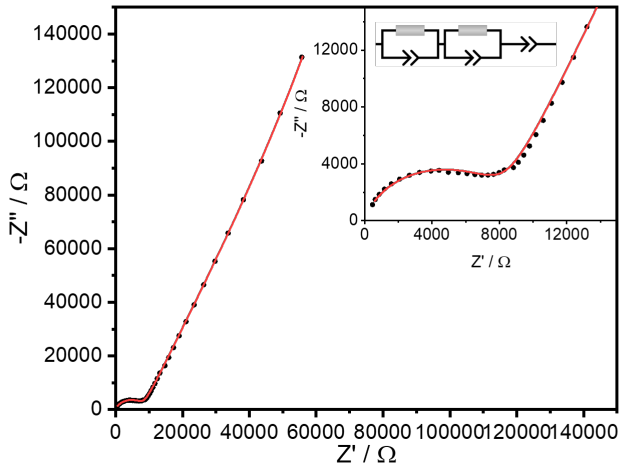

Figure C.1: Representative Nyquist plot of electrochemical impedance spectra measured at $-70\,^{\circ}\mathrm{C}$ of $Li_{7+x}Si_{1-x}Al_xPS_8$ ($x = 15\%$). Black dots depict the measured data, red lines represent the fit of the equivalent circuit model depicted in the insets.

C.2.2 Crystallographic data

Table C.2: Crystallographic data and information on the Rietveld refinement from powder X-ray diffraction data for $Li_{7.05}Si_{0.95}Al_{0.05}PS_8$ using Si as an internal standard. Standard deviations are given in parentheses.

$Li_{7.05}Si_{0.95}Al_{0.05}PS_8$		
crystal system		tetragonal
space group		$P4_2/nmc$, (Nr. 137)
lattice params.	a	8.68153(15) Å
	c	12.5543(4) Å
V [Å^3]		946.21(4)
Z		4
calc. density [gcm^{-3}]		1.90471(9)
diffractometer		STOE STADI P, Cu$K_{\alpha 1}$-radiation
		Debye-Scherrer geometry
temperature [K]		295
absorption coefficient [mm^{-1}]		14.749(7)
refined 2ϑ region [°]		10 – 93
R_{exp}		14.361
R_p		10.196
R_{wp}		13.104
Goof		0.912
R_{Bragg}		3.367
number of refined params.		38
number of background params.		12

Table C.3: Crystallographic data and information on the Rietveld refinement from powder X-ray diffraction data for $Li_{7.1}Si_{0.9}Al_{0.1}PS_8$ using Si as an internal standard. Standard deviations are given in parentheses.

$Li_{7.1}Si_{0.9}Al_{0.1}PS_8$		
crystal system		tetragonal
space group		$P4_2/nmc$, (Nr. 137)
lattice params.	a	8.67954(15) Å
	c	12.5613(4) Å
V [Å^3]		946.30(4)
Z		4
calc. density [gcm^{-3}]		1.90490(8)
diffractometer		STOE STADI P, Cu$K_{\alpha 1}$-radiation
		Debye-Scherrer geometry
temperature [K]		295
absorption coefficient [mm^{-1}]		14.111(4)
refined 2ϑ region [°]		10 – 93
R_{exp}		15.278
R_p		10.684
R_{wp}		14.042
Goof		0.919
R_{Bragg}		3.387
number of refined params.		38
number of background params.		12

Table C.4: Crystallographic data and information on the Rietveld refinement from powder X-ray diffraction data for $Li_{7.15}Si_{0.85}Al_{0.15}PS_8$ using Si as an internal standard. Standard deviations are given in parentheses.

$Li_{7.15}Si_{0.85}Al_{0.15}PS_8$		
crystal system		tetragonal
space group		$P4_2/nmc$, (Nr. 137)
lattice params.	a	8.6864(2) Å
	c	12.5658(4) Å
V [Å^3]		948.15(5)
Z		4
calc. density [gcm^{-3}]		1.90099(8)
diffractometer		STOE STADI P, Cu$K_{\alpha 1}$-radiation
		Debye-Scherrer geometry
temperature [K]		295
absorption coefficient [mm^{-1}]		14.7201(7)
refined 2ϑ region [°]		10 – 93
R_{exp}		14.777
R_p		10.804
R_{wp}		13.999
Goof		0.947
R_{Bragg}		3.233
number of refined params.		38
number of background params.		12

Table C.5: Crystallographic data and information on the Rietveld refinement from powder X-ray diffraction data for $Li_{7.2}Si_{0.8}Al_{0.2}PS_8$ using Si as an internal standard. Standard deviations are given in parentheses.

$Li_{7.2}Si_{0.8}Al_{0.2}PS_8$		
crystal system		tetragonal
space group		$P4_2/nmc$, (Nr. 137)
lattice params.	a	8.68059(15) Å
	c	12.5679(4) Å
V [Å^3]		947.02(4)
Z		4
calc. density [gcm^{-3}]		1.90326(8)
diffractometer		STOE STADI P, Cu$K_{\alpha 1}$-radiation
		Debye-Scherrer geometry
temperature [K]		295
absorption coefficient [mm^{-1}]		14.7376(6)
refined 2ϑ region [°]		10 – 93
R_{exp}		15.707
R_p		11.218
R_{wp}		14.564
Goof		0.927
R_{Bragg}		3.944
number of refined params.		44
number of background params.		12

C.3 Additional data for Chapter 4.2

C.3.1 Electrochemical impedance data

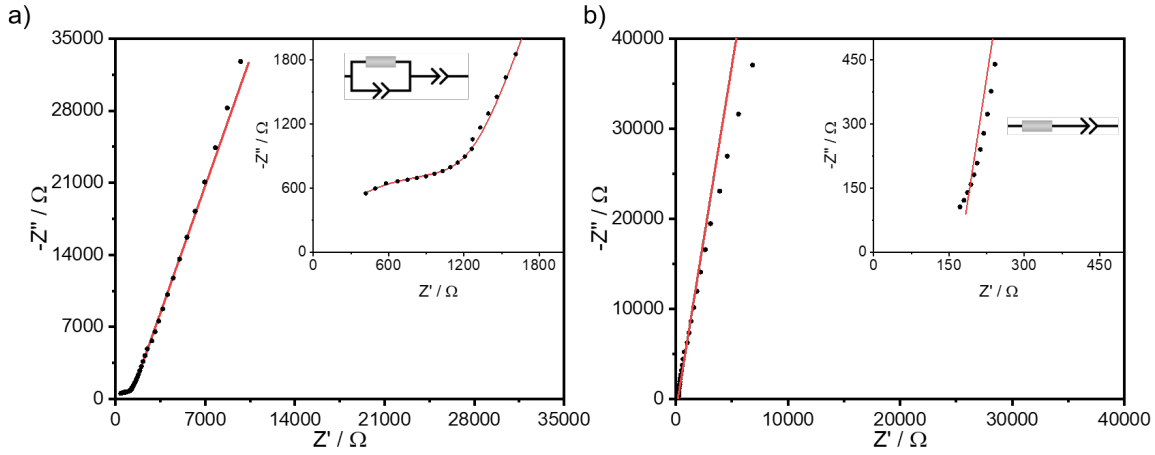

Figure C.2: Representative Nyquist plots of electrochemical impedance spectra measured at −20 °C of **(a)**: a sample with 8 awt% amorphous and **(b)**: 15 awt% amorphous. Black dots depict the measured data, red lines represent the fit of the equivalent circuit model depicted in the insets.

C.3.2 Crystallographic data

Table C.6: Crystallographic data and information on the Rietveld refinement from powder X-ray diffraction data for a LSiPSCl sample, assuming 2.5 wt% amorphous content, using Si as an internal standard. The phase content of the internal standard was omitted and the given data scaled accordingly. Standard deviations are given in parentheses.

2.5 wt% assumed amorphous		
diffractometer		STOE STADI P, Mo$K_{\alpha 1}$-radiation Debye-Scherrer geometry
temperature [K]		295
absorption coefficient [mm^{-1}]		15.233(3)
refined 2ϑ region [°]		4 – 56
R_{exp}		8.824
R_p		6.195
R_{wp}		8.165
Goof		0.925
number of refined params.		47
number of background params.		12
Phase / weight%	*tetra*-LSiPS	88.5(8) wt%
space group		$P4_2/nmc$, (Nr. 137)
lattice params.	a	8.6880(2) Å
	c	12.5477(4) Å
V [Å^3]		947.14(5)
R_{Bragg}		2.599
Phase / weight%	*ortho*-LSiPS	4.5(4) wt%
space group		$Pnma$, (Nr. 62)
lattice params.	a	13.49(2) Å
	b	7.889(11) Å
	c	6.125(9) Å
V [Å^3]		652(2)
R_{Bragg}		1.881
Phase / weight%	Li_6PS_5Cl	3.0(3) wt%
space group		$F\bar{4}3m$, (Nr. 216)
lattice params.	a	9.875(6) Å
V [Å^3]		962(2)
R_{Bragg}		1.983

Table C.7: Crystallographic data and information on the Rietveld refinement from powder X-ray diffraction data for a LSiPSCl sample, assuming 8 wt% amorphous content, using Si as an internal standard. The phase content of the internal standard was omitted and the given data scaled accordingly. Standard deviations are given in parentheses.

8 wt% assumed amorphous		
diffractometer		STOE STADI P, Mo$K_{\alpha 1}$-radiation
		Debye-Scherrer geometry
temperature [K]		295
absorption coefficient [mm^{-1}]		1.5249(3)
refined 2ϑ region [°]		4 – 56
R_{exp}		3.716
R_p		4.845
R_{wp}		6.237
Goof		1.678
number of refined params.		47
number of background params.		12
Phase / weight%	*tetra*-LSiPS	65.7(5) wt%
space group		$P4_2/nmc$, (Nr. 137)
lattice params.	a	8.68400(14) Å
	c	12.5498(3) Å
V [Å^3]		946.40(4)
R_{Bragg}		3.309
Phase / weight%	*ortho*-LSiPS	18.6(2) wt%
space group		$Pnma$, (Nr. 62)
lattice params.	a	13.562(2) Å
	b	7.8358(13) Å
	c	6.1268(5) Å
V [Å^3]		651.0(2)
R_{Bragg}		3.747
Phase / weight%	Li_6PS_5Cl	14.2(2) wt%
space group		$F\bar{4}3m$, (Nr. 216)
lattice params.	a	9.8729(6) Å
V [Å^3]		962.3(2)
R_{Bragg}		4.099

Table C.8: Crystallographic data and information on the Rietveld refinement from powder X-ray diffraction data for a LSiPSCl sample, assuming 15 wt% amorphous content, using Si as an internal standard. The phase content of the internal standard was omitted and the given data scaled accordingly. Standard deviations are given in parentheses.

15 wt% assumed amorphous		
diffractometer		STOE STADI P, Mo$K_{\alpha 1}$-radiation
		Debye-Scherrer geometry
temperature [K]		295
absorption coefficient [mm^{-1}]		15.8731(15)
refined 2ϑ region [°]		4 – 56
R_{exp}		8.462
R_p		7.178
R_{wp}		9.377
Goof		1.108
number of refined params.		45
number of background params.		12
Phase / weight%	*tetra*-LSiPS	51.5(6) wt%
space group		$P4_2/nmc$, (Nr. 137)
lattice params.	a	8.6813(3) Å
	c	12.5444(6) Å
V [Å^3]		945.43(7)
R_{Bragg}		3.424
Phase / weight%	*ortho*-LSiPS	7.8(3) wt%
space group		$Pnma$, (Nr. 62)
lattice params.	a	13.551(5) Å
	b	7.842(3) Å
	c	6.128(2) Å
V [Å^3]		651.2(4)
R_{Bragg}		3.417
Phase / weight%	Li_6PS_5Cl	13.4(3) wt%
space group		$F\bar{4}3m$, (Nr. 216)
lattice params.	a	9.8501(6) Å
V [Å^3]		955.7(2)
R_{Bragg}		6.171

Appendix D

List of publications and author contributions

1. **Title:** Benzimidazolium Lead Halide Perovskites: Effects of Anion Substitution and Dimensionality on the Bandgap
   Authors: Claudia Lermer, Sascha P. Harm, Susanne T. Birkhold, Julian A. Jaser, Christopher M. Kutz, Peter Mayer, Lukas Schmidt-Mende, Bettina V. Lotsch
   Published in: *Z. Anorg. Allg. Chem.* **2016**, *642* (23), 1369-1376.
   Author contributions: CL wrote the main part of the manuscript, did the literature research, created the figures(unless otherwise noted), conceived the syntheses and evaluated the NMR and PXRD data. CL and JAJ performed the syntheses of the benzimidazolium lead halides. SH carried out the Rietveld refinements and was involved in designing the figures. STB performed the absorption and PL measurements, provided the respective figures and contributed to writing the manuscript. PM carried out the single-crystal X-ray diffraction measurements and also solved and refined the crystal structures. JAJ took the photographs of the benzimidazolium lead halide powders. BVL and LSM directed and supervised the work. All authors revised the manuscript.

2. **Title:** A Lesson learned from NMR: characterization and ionic conductivity of LGPS-like Li_7SiPS_8
   Authors: Sascha Harm, Anna-Katharina Hatz, Igor Moudrakovski, Roland Eger, Alexander Kuhn, Constantin Hoch, Bettina V. Lotsch
   Published in: *Chem. Mater.*, **2019**, *31*, 1280-1288.
   Author contributions: SH, CoH and BVL conceived and designed this study; SH conducted the synthesis, measured PXRD and performed Rietveld analysis; SH and AKH were responsible for measuring EIS; AKH analysed measured EIS data; IM performed ssNMR spectroscopy; SH and IM analysed obtained ssNMR data; RE and AK were responsible for growing single crystals of *ortho*-LSiPS; AK performed the structure determination from SCXRD data; CoH helped in interpretation of crystal structure data; SH and AKH wrote sections of the manuscript; All authors wrote

and commented on the manuscript.

3. **Title:** Finding the right blend: Interplay between structure and sodium ion conductivity in the system Na_5AlS_4 – Na_4SiS_4
Authors: Sascha Harm, Anna-Katharina Hatz, Christian Schneider, Carla Hoefer, Constantin Hoch, Bettina V. Lotsch
Published in: *Front. Chem.*, **2020**, *8*:90.
Author contributions: SH, AKH and BVL conceived and designed this study; SH and CaH conducted the synthesis; SH, AKH and CaH were responsible for measuring SCXRD, PXRD, NMR and EIS; SH performed structure determination; CoH helped in interpretation of crystal structure data; CS performed the calculation and interpretation of BVEL data; AKH analysed measured EIS data; SH, AKH and CS wrote sections of the manuscript; All authors wrote and commented on the manuscript.

4. **Title:** Aliovalent substitution in *tetra*-$Li_{7+x}Si_{1-x}Al_xPS_8$
Authors: Sascha Harm, Anna-Katharina Hatz, Carla Hoefer, Max Plaß, Bettina V. Lotsch
Published in: *to be submitted*
Author contributions: SH, AKH and BVL conceived and designed this study; SH, CaH and MP conducted the synthesis; SH, AKH, CaH and MP were responsible for measuring PXRD, NMR and EIS; SH performed Rietveld analysis and BVEL calculations; AKH analysed measured EIS data; SH interpreted the data and wrote the manuscript.

5. **Title:** Impact of LiCl on the phase composition in *tetra*-LSiPS
Authors: Sascha Harm, Anna-Katharina Hatz, Carla Hoefer, Lucas Balzat, Verena Langowski, Bettina V. Lotsch
Published in: *to be submitted*
Author contributions: SH, AKH, VL and BVL conceived and designed this study; SH, CH and LB conducted the synthesis; SH, AKH, CaH and LB were responsible for measuring PXRD, NMR and EIS; SH performed Rietveld analysis; AKH analysed measured EIS data; SH interpreted the data and wrote the manuscript.

Appendix E

List of presentations

E.1 Oral presentations

1. **Title:** Rehydratisierung von Zinkphosphat im wasserfreien Milieu?
   Authors: Sascha Harm, Pamina Hirler, Constantin Hoch, Bettina V. Lotsch
   Occasion: Hirschegg-Seminar, 27.05.2016

2. **Title:** Novel solid electrolytes for Li-ion and Li-metal batteries
   Authors: Sascha Harm, Matteo Cococcioni, Anna-Katharina Hatz, Constantin Hoch, Bettina V. Lotsch
   Occasion: 5. MPI-EPFL Science Day , 13.10.2016

3. **Title:** Tetragonal Li_7SiPS_8
   Authors: Sascha Harm, Anna-Katharina Hatz, Igor Moudrakovski, Roland Eger, Alexander Kuhn, Constantin Hoch, Bettina V. Lotsch
   Occasion: 2. FestBatt cluster meeting, 19.05.2019

E.2 Poster presentations

1. **Title:** Neue Kathodenmaterialien für Lithiumionen-Batterien: $LiZnPO_4 \cdot H_2O$
   Authors: Sascha Harm, C. Hoch
   Occasion: 15. European Conference on Solid State Chemistry, Vienna, Austria, 24.08.2015

2. **Title:** A new LGPS-type superionic conductor – synthesis and characterization of Li_7SiPS_8
   Authors: Sascha Harm, Giuliano Gregori, Igor Moudrakovski, Bettina V. Lotsch
   Occasion: MPI Scientific Advisory Board meeting, Stuttgart, Germany, 09.11.2015

3. **Title:** A new LGPS-type superionic conductor – synthesis and characterization of Li_7SiPS_8

Authors: Sascha Harm, Anna-Katharina Hatz, Igor Moudrakovski, Robert E. Usiskin, Joachim Maier, Bettina V. Lotsch
Occasion: 21. solid state ionics conference, Padua, Italy, 19.06.2017

4. **Title:** A new LGPS-type superionic conductor – synthesis and characterization of Li_7SiPS_8
Authors: Sascha Harm, Anna-Katharina Hatz, Igor Moudrakovski, Robert E. Usiskin, Joachim Maier, Bettina V. Lotsch
Occasion: NIM summer retreat, 31.07.2017

Bibliography

(1) Ong, S. P.; Mo, Y.; Richards, W. D.; Miara, L.; Lee, H. S.; Ceder, G. Phase stability, electrochemical stability and ionic conductivity of the $Li_{10\pm1}MP_2X_{12}$ (M = Ge, Si, Sn, Al or P and X = O, S or Se) family of superionic conductors. *Energy Environ. Sci.* **2013**, *6*, 148–156.

(2) Tanibata, N.; Noi, K.; Hayashi, A.; Tatsumisago, M. Preparation and characterization of highly sodium ion conducting Na_3PS_4 – Na_4SiS_4 solid electrolytes. *RSC Adv.* **2014**, *4*, 17120–17123.

(3) Sheldrick, G. M. A short history of SHELX. *Acta Crystallogr. Sect. A Found. Crystallogr.* **2008**, *64*, 112–122.

(4) Parthé, E.; Gelato, L. M. The standardization of inorganic crystal-structure data. *Acta Crystallogr. Sect. A Found. Crystallogr.* **1984**, *40*, 169–183.

(5) Bron, P.; Johansson, S.; Zick, K.; Schmedt auf der Günne, J.; Dehnen, S.; Roling, B. $Li_{10}SnP_2S_{12}$: An Affordable Lithium Superionic Conductor. *J. Am. Chem. Soc.* **2013**, *135*, 15694–15697.

(6) Litvinchuk, A. P.; Dzhagan, V. M.; Yukhymchuk, V. O.; Valakh, M. Y.; Babichuk, I. S.; Parasyuk, O. V.; Piskach, L. V.; Gordan, O. D.; Zahn, D. R. T. Electronic structure, optical properties, and lattice dynamics of orthorhombic Cu_2CdGeS_4 and Cu_2CdSiS_4 semiconductors. *Phys. Rev. B* **2014**, *90*, 165201.

(7) Shibao, R. K.; Srdanov, V. I.; Hay, M.; Eckert, H. Remote Plasma-Enhanced Chemical Vapor Deposited $a - SiS_x : H$. Characterization by Raman and Solid-State NMR Spectroscopies and Relationship to the Structure of Vitreous SiS_2. *Chem. Mater.* **1994**, *6*, 306–310.

(8) Muramatsu, H.; Hayashi, A.; Ohtomo, T.; Hama, S.; Tatsumisago, M. Structural change of Li_2S - P_2S_5 sulfide solid electrolytes in the atmosphere. *Solid State Ionics* **2011**, *182*, 116–119.

(9) Tachez, M.; Malugani, J.; Mercier, R.; Robert, G. Ionic conductivity of and phase transition in lithium thiophosphate Li_3PS_4. *Solid State Ionics* **1984**, *14*, 181–185.

(10) Maier, J., *Physical Chemistry of Ionic Materials: Ions and Electrons in Solids*; John Wiley & Sons, Inc.: Chichester England, 2004, pp 419–462.

(11) Kuhn, A.; Gerbig, O.; Zhu, C.; Falkenberg, F.; Maier, J.; Lotsch, B. V. A new ultrafast superionic Li-conductor: ion dynamics in $Li_{11}Si_2PS_{12}$ and comparison with other tetragonal LGPS-type electrolytes. *Phys. Chem. Chem. Phys.* **2014**, *16*, 14669–14674.

(12) Holzmann, T.; Schoop, L. M.; Ali, M. N.; Moudrakovski, I.; Gregori, G.; Maier, J.; Cava, R. J.; Lotsch, B. V. $Li_{0.6}[Li_{0.2}Sn_{0.8}S_2]$ - a layered lithium superionic conductor. *Energy Environ. Sci.* **2016**, *9*, 2578–2585.

(13) Krause, L.; Herbst-Irmer, R.; Sheldrick, G. M.; Stalke, D. Comparison of silver and molybdenum microfocus X-ray sources for single-crystal structure determination. *J. Appl. Crystallogr.* **2015**, *48*, 3–10.

(14) D'Ans; Lax, *D'Ans-Lax Taschenbuch für Chemiker und Physiker*, 3rd ed.; Blachnik, R., Ed.; Springer: Berlin, Heidelberg, 1998.

(15) Momma, K.; Izumi, F. *VESTA3* for three-dimensional visualization of crystal, volumetric and morphology data. *J. Appl. Cryst.* **2011**, *44*, 1272–1276.

(16) Harm, S.; Hatz, A.-K.; Moudrakovski, I.; Eger, R.; Kuhn, A.; Hoch, C.; Lotsch, B. V. Lesson Learned from NMR: Characterization and Ionic Conductivity of LGPS-like Li_7SiPS_8. *Chem. Mater.* **2019**, *31*, 1280–1288.

(17) Kato, Y.; Hori, S.; Saito, T.; Suzuki, K.; Hirayama, M.; Mitsui, A.; Yonemura, M.; Iba, H.; Kanno, R. High-power all-solid-state batteries using sulfide superionic conductors. *Nat. Energy* **2016**, *1*, 16030.

(18) Kamaya, N.; Homma, K.; Yamakawa, Y.; Hirayama, M.; Kanno, R.; Yonemura, M.; Kamiyama, T.; Kato, Y.; Hama, S.; Kawamoto, K.; Mitsui, A. A lithium superionic conductor. *Nat. Mater.* **2011**, *10*, 682–686.

(19) Bron, P.; Dehnen, S.; Roling, B. $Li_{10}Si_{0.3}Sn_{0.7}P_2S_{12}$ – A low-cost and low-grain-boundary-resistance lithium superionic conductor. *J. Power Sources* **2016**, *329*, 530–535.

(20) Murugan, R.; Thangadurai, V.; Weppner, W. Fast Lithium Ion Conduction in Garnet-Type $Li_7La_3Zr_2O_{12}$. *Angew. Chem. Int. Ed.* **2007**, *46*, 7778–7781.

(21) Liu, Z.; Fu, W.; Payzant, E. A.; Yu, X.; Wu, Z.; Dudney, N. J.; Kiggans, J.; Hong, K.; Rondinone, A. J.; Liang, C. Anomalous High Ionic Conductivity of Nanoporous β-Li_3PS_4. *J. Am. Chem. Soc.* **2013**, *135*, 975–978.

(22) Hori, S.; Suzuki, K.; Hirayama, M.; Kato, Y.; Kanno, R. Lithium Superionic Conductor $Li_{9.42}Si_{1.02}P_{2.1}S_{9.96}O_{2.04}$ with $Li_{10}GeP_2S_{12}$-Type Structure in the Li_2S - P_2S_5 – SiO_2 Pseudoternary System: Synthesis, Electrochemical Properties, and Structure–Composition Relationships. *Front. Energy Res.* **2016**, *4*, 38.

(23) Inaguma, Y.; Liquan, C.; Itoh, M.; Nakamura, T.; Uchida, T.; Ikuta, H.; Wakihara, M. High ionic conductivity in lithium lanthanum titanate. *Solid State Commun.* **1993**, *86*, 689–693.

(24) Yu, X.; Bates, J. B.; Jellison, G. E.; Hart, F. X. A Stable Thin-Film Lithium Electrolyte: Lithium Phosphorus Oxynitride. *J. Electrochem. Soc.* **1997**, *144*, 524–532.